BRNO UNIVERSITY OF TECHNOLOGY

FACULTY OF ELECTRICAL ENGINEERING AND COMMUNICATION

# HABILITATION THESIS

Field of Research
ELECTRONICS AND COMMUNICATION

# Nonlinear Dynamical Systems

Proceedings of Original Scientific and Research Papers
from Years (2010 – 2018)

## Tomas GOTTHANS

BRNO 2018

**Abstract**

The habilitation thesis is oriented in the field of non-linear dynamical systems. It is composed as commented proceedings of author's most important research papers, published in peer reviewed international conferences or international journals in the years 2010 – 2018. The research papers are organized in two dominant topics, each forming a single part of the thesis: The topics included are (1) Lineariation and Modelling of Non-linear Power Amplifiers, (2) Advanced Modelling on Non-linear Dynamical Systems. For completeness, also the educational activities of the author are summarized in the thesis.

**Keywords**

Linearisation, power amplifier, Volterra series, polynomial series, digital predistortion, dynamical systems, ordinary differential equations, chaotic systems, Lyapunov exponents.

**Acknowledgment**

First of all, I would like to express my deepest gratitude to my two previous supervisors: prof. Geneviève Baudoin and Doc. Jiří Petržela. They have inspired me by the high standards and by their deep devotion to their work. Your professional and patient attitude helped me to better understand countless research problems. Thank you also for encouraging, exciting and thoughtful discussions and for your friendly attitude that greatly contributed to my professional development.

Many thanks belong definitely to prof. Roman Maršálek, who introduced me to the research team at ESIEE Paris and at Brno University of Technology and took me as a member of his fruitful research team. Without his support and expert advices, this work could not have started.

Another key person in motivating me to finish my habilitation thesis was prof. Tomáš Kratochvíl, the head of Department of Radio Electronics, Brno University of Technology, Faculty of Electrical Engineering and Communication.

I have had the pleasure to supervise several Bachelor and Master level students in the work on their theses. One of them, Jan Král, became my first Ph.D. student, always open minded and there when needed.

I would like to express my gratitude for support in submitting this work to Doc. Martin Slanina.

Last, but truly not least, I would also like to express my deepest gratitude to my wife Eliška and son Vincent for being my source of inspiration and beatitude. Thank you for your patience during the time I was home and far away from home.

# Contents

# Part I

# General Introduction, Problem Statement, Terminology

# 1. Introduction

It is common situation that nonlinear devices are simulated using computers. There can be complex models modeling physical phenomenas of each electronic part. Models on physical level are usually very complex and difficult to handle even with modern computers. Another approach can be modeling systems in fact as a black-box device.

Another aspect of non-linear systems is the reduction and modeling of inconvenient effects connected with a real characteristic of many real-world parts [2], especially the modeling aspects connected with non-linear power amplifiers (PA) used in wireless communications and broadcasting.

Power amplifiers are critical elements of mobile communication and broadcasting systems because their efficiency conditions the autonomy and the weight of mobile handset batteries and their linearity influences on performance of the communication. In practice, PAs are not perfectly linear and present memory effects, i.e. the output signal is a function of the current and of previous input signal values. And a compromise must be achieved between the efficiency and the linearity of the PA [3].

The aim of this work is to bring new innovative solutions to improve the performance of RF power transmitters.

The work conducted in this thesis is a part of work for the project AMBRUN (FUI project with partners: Thales, TeamCast, Supélec and ESIEE Paris). The project aims to improve the radio performance of the amplification of multiplexed signals using adaptive algorithms for dual applications: tactical communication and broadcasting VHF band. The originality and ambition of the project lie in the bandwidths of processed signals (above 40 MHz) the involved powers (up to 100W) and the non-stationarity of tactical multiplex signals.

An increasing demands on communications system with every generation of devices. One may observe, that in 1985 for AMPS systems the required bandwidth of signal was 30kHz. Comparing for example with the latest LTE Advanced, that can require 100MHz of bandwidth. The LTE Advanced requires approximatively 3400 times larger bandwidth than AMPS systems. That is also challenging in terms of signal processing.

# 2. Generalities on Radio Frequency Power Amplifiers

In this chapter we would like to introduce some generalities related with power amplifiers. The following section brings overview of performance evaluation methods. Finally the last section introduces generalities on linearization of power amplifiers.

## 2.1  Signal Crest Factor - PAPR

The crest factor of a signal is defined as the ratio between peak amplitude input and its root mean square (RMS) value:

$$C = \frac{|x|_{peak}}{x_{rms}}. \tag{2.1}$$

A derived measure from Crest factor is the peak-to-average power ratio (PAPR). The PAPR is usually used in signal processing applications. It is defined as power ratio:

$$PAPR = \frac{|x|^2_{peak}}{x^2_{rms}} = C^2. \tag{2.2}$$

Usually the PAPR is expressed in decibels (dB). The knowledge of PAPR is important, because it is a measure of the envelope dynamics.

The PAPR can be measured on radio-frequency (RF) or baseband complex envelope signals. There is a 3dB difference between the two definitions.

Widely used Orthogonal Frequency-Division Multiplexing (OFDM) signals have quite high PAPR (approx. 12dB in RF) unlike sine wave which has $3.01dB$. The PAPR is an important signal parameter for a PA, because it leads to using large back-off to preserve linearity whilst the efficiency is degraded.

In order to have good efficiency, the operating point of PA needs to be set close to saturation area, but the higher the operating point is, the worst the linearity. Usually we need to set a certain compromise between linearity and efficiency. Therefore a back-off is used. The value of the back-off is of the same order as the PAPR ($Back-off \approx PAPR$).

## 2.2 System performance evaluation: ACPR, EVM, NMSE

There are several parameters used to evaluate the influence of PA non-linearity on system performance in the case of modulated signals, in particular ACPR and EVM.

### 2.2.1 Adjacent Channel Power Ration - ACPR

The imperfections and non-linearities usually results in some adjacent channel spectral regrowth. This phenomenon can be quantified with the parameter ACPR that is defined as a bandwidth limited ratio between the power in the main channel and the power in one adjacent channel. Therefore we can define this property for left and right adjacent channel. The right and left channel ACPRs are defined by:

$$
\begin{aligned}
ACPR_R[dB] &= 10\log\left(\frac{\int_{-B/2}^{B/2} P_y(f)df}{\int_{B/2}^{3B/2} P_y(f)df}\right) \tag{2.3}\\
ACPR_L[dB] &= 10\log\left(\frac{\int_{-B/2}^{B/2} P_y(f)df}{\int_{-3B/2}^{-B/2} P_y(f)df}\right),
\end{aligned}
$$

where $B$ represents the bandwidth of the signal and $P_y(f)$ is power spectral density.

## 2.3 Normalized Mean Square Error - NMSE

For the quantification of performance we can also use Normalized Mean Square Error (NMSE)[5]. It is an estimator of the overall deviations between predicted and measured values. For two complex vectors $\mathbf{x}$ and $\mathbf{y}$ of N samples the NMSE is defined as:

$$
NMSE(\mathbf{x}, \mathbf{y})[dB] = 10\log\left(\frac{(\mathbf{x}-\mathbf{y})^H(\mathbf{x}-\mathbf{y})}{\mathbf{x}^H\mathbf{x}}\right). \tag{2.4}
$$

Where $(.)^H$ stands for transposed complex conjugation of vector also so-called Hermitian transpose.

The NMSE is a global measure of quality. But it does not distinguish between linear and non-linear distortion.

For example bad NMSE could be due to time shift between signals and/or bad gain alignment.

## 2.4 Error Vector Magnitude - EVM

Error vector magnitude (EVM) is a measurement of performance in the presence of impairments. The measured symbol location obtained after decimating the recovered waveform at the demodulator output are compared with the ideal symbol locations of

constellation points. EVM is defined as normalized average value of the vector error. It is usually estimated on a window of $N$ samples. The measured symbol location is given by $w$. However, the ideal symbol location (using the symbol map) is given by $v$. Therefore, the resulting error vector is the difference between the actual measured and ideal symbol vectors defined as $e = w - v$.

The EVM is calculated after compensation of simple constellation determination: offset and complex gain. Analytically, RMS EVM is defined as:

$$EVM = \frac{E(|v - c_1 w - c_0|^2)}{E(|v|^2)},\tag{2.5}$$

where E(.) represents the average value, $c_0$ and $c_1$ are the optimal values of gain and offset. Using ergodic properties, it is estimated on $N$ symbols by (in the case where $c_0 = 0$ and $c_1 = 1$):

$$EVM = \frac{\sum_{j=1}^{N} \left[ (I_j - I_j^{meas})^2 + (Q_j - Q_j^{meas})^2 \right]}{\sum_{j=1}^{N} |I_j^2 + Q_j^2|} \; 100\%.\tag{2.6}$$

# 3. Generalities on post-OFDM Modulation Techniques

In today communication systems orthogonal frequency division multiplexing signals (OFDM) with cyclic prefix are widely used. It was proved that using multicarrier modulations (MCM) is an efficient way of transmission and has better resistance to multi-path channels than single carrier modulations. In multi-carrier systems, information is commonly transmitted through orthogonal pulses which overlap in time and frequency. On of the main advantage is that these pulses occupy (mostly) only a small bandwidth. CP-OFDM (Cyclic-Prefix OFDM) is the most prominent multicarrier scheme that is nowadays applied. It employs rectangular transmit and receive pulses, which greatly reduce the computational complexity. Furthermore, the CP guarantees orthogonality in frequency selective channels. Unfortunately of the biggest disadvantages of OFDM or CP-OFDM is its poor spectral behavior, caused by the rectangular prototype filters. Furthermore CP simplifies equalization in frequency-selective channels reducing the spectral efficiency. Comparison between contemplated modulation can be seen in Fig.3.1.

## 3.1 Filter Bank Multi-carrier Modulation - FBMC

There does not exist a unique definition for FBMC-QAM. We can sacrifice frequency localization, and have unsatisfying OOB emissions, or we can sacrifice orthogonality in order to have a time-frequency localization. Due to properties of prototype filter in the FBMC systems, offset quadrature amplitude modulation (OQAM) is used. Offset means the in-phase and quadrature components are time staggered by half of symbol period. The baseband model of FBMC/OQAM transmitter can be written

$$x[t] = \sum_{m=-\infty}^{+\infty} \sum_{k=0}^{N-1} (\theta^k \Re\{X_k[m]\} h[t - m\ N] +$$

$$\theta^{k+1} \Im\{X_k[m]\} h[t - m\ N - \frac{N}{2}])\ e^{j\frac{2\pi}{N}k(t-mN)} \tag{3.1}$$

where $X_k$ is a modulation part of a symbol, $\theta^{k+1}$ is real part phase rotation vector for the imaginary part $\theta^k$ respectively, $h[.]$ is general prototype filter for each sub-carrier with impulse response length $L = KN$ with $K$ so-called overlapping factor and $N$ number of sub-carriers.

There exists several approaches implementing FBMC modulator/demodulator such as NK-IFFTs operating in parallel, two N-IFFTs and polyphase filtering and with lower complexity single N-FFT and polyphase filtering. The last mentioned method was implemented in this paper. The principle of computing the discrete inverse Fourier transform of two real functions simultaneously is used. Such approach is beneficial because then the concept can be easily reconfigured as OFDM transmitter.

The input signal of IFFT can be expressed as $\Re\{X_k[m]\}\theta^k + j\Im\{X_k[m]\}\theta^k$ where multiplication with a vector $\theta^k = e^{j\frac{2\pi}{4}k}$ in frequency domain induce circular shift of $\frac{N}{4}$ in the time domain. The principle is commonly named as folding scheme.

## 3.2    Generalised Frequency Division Multiplex - GFDM

The Generalized Frequency Division Multiplex (GFDM) is based on the circular shifted prototype filter in time and frequency domain. Hence the OOB emission is significantly suppressed. This fact allows that the modulation scheme is well suited for transmission on non-contiguous frequency bands with strict spectral mask constraints.
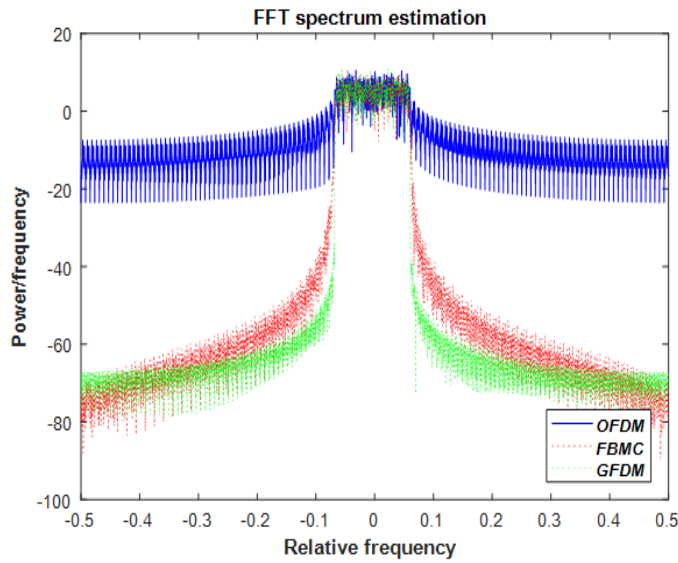


Figure 3.1: Comparison of sectral properties: OFDM (blue curve), FBMC (red curve), GFDM (green curve).

## 3.3    I/Q Imbalance Model for Wireless Transciever

I/Q imbalance is a performance-limiting issue in the design of direct conversion receivers. IQ imbalances occur due to mismatches between the parallel sections of the transceiver chain dealing with the in-phase (I) and quadrature (Q) signal paths. The local oscillator (LO) generates a sinewave (can be influenced with offset, noise, gain change, etc.), and a copy of that sine-wave that is delayed by 90 degrees (this principle is called quadrature modulator). When the direct LO output is mixed with the original signal, this produces the I signal, whereas when the delayed LO output is mixed with the original signal, that produces the Q signal. In the analog domain, the delay is never exactly 90 degrees. Similarly, analog gain is never perfectly matched for each of the signal paths. In this paragraph, we would like to show that I/Q imbalance is in general imperfection that have to be neglected.

Suppose first that we can neglect the noise and thus the received passband signal in the receiver path is identical to the transmitted signal with the baseband components

$$y(t) = y_r(t) + jy_i(t), \tag{3.2}$$

$$y_{RF}(t) = \Re\left\{y(t)e^{j\omega t}\right\} = y_r(t)cos(\omega t) - y_i(t)sin(\omega t). \tag{3.3}$$

Multiplying the passband signal by the two local oscillator signals and passing through a pair of low-pass filters, one obtains the demodulated baseband signals. After rearrangements we can write the symmetrical model burdened by I/Q imbalance:

$$\begin{aligned} y(t)'_r &= (1+\epsilon)\left[y_r(t)cos(\phi) - y_i(t)sin(\phi)\right] \\ y(t)'_i &= (1-\epsilon)\left[y_i(t)cos(\phi) - y_r(t)sin(\phi)\right], \end{aligned} \tag{3.4}$$

where $\epsilon$ is a gain imbalance and $\phi$ is a phase imbalance.

# 4. Techniques For Analyzing And Modeling Non-linear Systems

## 4.1 Introduction

This chapter presents the principals models that can be used for modelling PA or for digital predistortion (DPD). It is composed of two main parts: first the description of the models, then the methods for identification of the models. It focuses on models that can be used in the case of PA linearization.

There are several models used in modeling the PA (or used for DPD) from the simplest models modelling just the amplitude distortions to the most general form known as Volterra series and its derivatives.

We may distinguish the models to three basic categories: memoryless or static, quasi-static and dynamic (or memory) models. For memoryless models, the output at time $t$ only depends on input at time $t$ and it can be shown that the system introduces only amplitude distortions. These amplitude distortions only depends on the magnitude of the input signal. Quasi-static models can also model phase distortions depending on the signal magnitude.

The third category is called dynamic, because these models are able to model memory effects.

## 4.2 Static and Quasi-static models

### 4.2.1 Memoryless RF Polynomial Series

One of the most straightforward models are the polynomial series. We can define the RF model for power amplifier as:

$$y_{RF}(t) = \sum_{n=1}^{N} a_n x_{RF}^n(t). \tag{4.1}$$

The coefficients of models can be obtained from simple measurements such as $P_{L1dB}$, IP3; etc. Let us establish the baseband equivalent model of the RF polynomial series.

Let us investigate the behavior in the presence of $n$-th order nonlinearity [11]:

$$x_{RF}^n(t) \quad = \quad \frac{1}{2^n} \left[ x(t)e^{j\omega_0 t} + x^*(t)e^{-j\omega_0 t} \right]^n \tag{4.2}$$

$$= \quad \frac{1}{2^n} \sum_{k=0}^n \binom{n}{k} x(t)^k x^*(t)^{(n-k)} e^{j\omega_0(2k-n)t}.$$

We are interested by $y_{RF1}(t)$ that is the component at frequency $\pm f_0$. So we look for component for which:

$$(2k - n) = \pm 1. \tag{4.3}$$

For $n$ even, $(2k - n)$ never equals 1, therefore $\omega_0(2k - n)$ is always out of band. For $n$ odd the frequencies can be in-band. Hence (for $-\omega_0$) we may write:

$$k \quad = \quad \frac{n-1}{2}, \tag{4.4}$$

$$(n - k) \quad = \quad \frac{n-1}{2} + 1.$$

Then using (4.5) we may define:

$$x(t)^k x^*(t)^{n-k} \quad = \quad x(t)^{\frac{n-1}{2}} x^*(t)^{\frac{n-1}{2}+1} \tag{4.5}$$

$$= \quad |x(t)|^{n-1} x(t)^*.$$

Similarly for frequency $+f_0$ for $(2k - n) = 1$ we obtain:

$$x(t)^k x^*(t)^{n-k} \quad = \quad |x(t)|^{n-1} x(t). \tag{4.6}$$

Using these results the baseband output is defined as:

$$y(t) = \sum_{\substack{n=1 \\ n \ odd}}^N \frac{a_n}{2^{n-1}} \binom{n}{(n-1)/2} |x(t)|^{n-1} x(t), \tag{4.7}$$

setting

$$b_n = \frac{a_n}{2^{n-1}} \binom{n}{(n-1)/2}. \tag{4.8}$$

This explains why the baseband models are often defined with odd coefficients only. They can be defined as:

$$y(t) = \sum_{\substack{n=1 \\ n \ odd}}^N b_n x(t) |x(t)|^{n-1} = \sum_{k=0}^{\frac{N-1}{2}} b_{2k+1} x(t) |x(t)|^{2k}, \tag{4.9}$$

where $x$ is the input baseband signal of the power amplifier, $y$ is the output baseband signal of PA and $b_n$ are the polynomial coefficients.

Another explanation why equivalent baseband models contain only odd terms can be done using Shimbo formula [12, 13]. For the rest of the thesis we will refer only to baseband models of PA (the PA is followed by bandpass filter).

In practice including even order terms in baseband models can improve performance.

Several models corresponding to modeling the AM/AM and AM/PM characteristic have been given, for example: Saleh, Rapp, quasi-static models. Their general expression is given by:

$$y(t) = A(|x(t)|)e^{j\phi(|x(t)|)}x(t). \tag{4.10}$$

We precise some of them in the following sections.

## 4.3 Dynamical Models Derived From Volterra Series

### 4.3.1 Polynomial series with memory

Polynomial memory series (PMS) were first presented in [27] and are widely used for modeling the non-linearities [28, 11, 29]. They can be interpreted as a special case of a generalized Hammerstein model. The presented series can model the memory effects. In this model, all off-diagonal terms of the Volterra series are set to zero. The series is defined as:

$$\begin{aligned}
y(t) &= \sum_{k=1}^{K}\sum_{q=0}^{Q} b_{kq}\, x(t-q)|x(t-q)|^{k-1} \\
&= \sum_{k=1}^{K}\sum_{q=0}^{Q} b_{k,q}\Phi_{k,q}(x(t)) = \mathbf{\Phi}(t)\mathbf{b},
\end{aligned} \tag{4.11}$$

where

$$\begin{aligned}
\Phi_{k,q}(x(t)) &= |x(t-q)|^{k-1}x(t-q), \tag{4.12} \\
\mathbf{b} &= [b_{1,0}, b_{2,0}, ..., b_{1,1}, ..., b_{1,Q}, ..., b_{K,Q}]^T \tag{4.13} \\
\mathbf{\Phi}(t) &= [\Phi_{1,0}(x(t)), ..., \Phi_{K,Q}(x(t))]. \tag{4.14}
\end{aligned}$$

Their structure is determined by 2 parameters: $K$ the non-linearity order and $Q$ the memory length. The number of coefficients is $K(Q+1)$.

These models have good performance for applications with narrow or medium bandwidths. But they are often insufficient when large bandwidth applications are needed because of their limitation in modeling memory effects. For large bandwidth applications more complicated models are necessary.

### 4.3.2  Dynamic Deviation Reduction Models

To overcome the complexity of the general Volterra series, an effective model pruning method, called dynamic deviation reduction (DDR) [32, 33, 34] was proposed. It is based on the fact that the effects of dynamics tend to fade with increasing nonlinearity order in many real PAs, so that the high-order dynamics can be removed in the model, leading to a significant simplification in model complexity.

Note that this dynamic-order truncation does not affect the nonlinearity or memory truncation in the same way as in the classical series. In other words, it only removes higher order dynamics, preserving the static nonlinearities and low-order dynamics[32].

The 2st-order dynamic truncation of the DDR-based baseband Volterra model in the discrete time can be written as:

$$
\begin{aligned}
y(t) =\ & \sum_{k=0}^{\frac{K-1}{2}} \sum_{i=1}^{Q} g_{2k+1,1}(i)\,|x(t)|^{2k} x(t-i) \\
& + \sum_{k=1}^{\frac{K-1}{2}} \sum_{i=1}^{Q} g_{2k+1,2}(i)\,|x(t)|^{2(k-1)} x^2(t) x^*(t-i) \\
& + \sum_{k=1}^{\frac{K-1}{2}} \sum_{i_1=1}^{Q} \sum_{i_2=1}^{Q} g_{2k+1,3}(i_1,i_2)|x(t)|^{2(k-1)}\, x^*(t)x(t-i_1)x(t-i_2) \\
& + \sum_{k=1}^{\frac{K-1}{2}} \sum_{i_1=1}^{Q} \sum_{i_2=1}^{Q} g_{2k+1,4}(i_1,i_2)|x(t)|^{2(k-1)}\, x(t)x^*(t-i_1)x(t-i_2) \\
& + \sum_{k=1}^{\frac{K-1}{2}} \sum_{i_1=1}^{Q} \sum_{i_2=1}^{Q} g_{2k+1,5}(i_1,i_2)|x(t)|^{2(k-2)}\, x^3(t)x^*(t-i_1)x^*(t-i_2). \quad (4.15)
\end{aligned}
$$

where $x(n)$ and $y(n)$ are the complex envelopes of the input and output of the PA, respectively, and $g_{2k+1,j}$ is the complex Volterra kernel of the system.

A simplified version of the model is defined by:

$$
\begin{aligned}
y(t) =\ & \sum_{k=0}^{\frac{K-1}{2}} \sum_{i=0}^{Q} g_{2k+1,1}(i)\,|x(t)|^{2k} x(t-i) \\
& + \sum_{k=1}^{\frac{K-1}{2}} \sum_{i=1}^{Q} g_{2k+1,2}(i)\,|x(t)|^{2(k-1)} x^2(t) x^*(t-i) \\
& + \sum_{k=1}^{\frac{K-1}{2}} \sum_{i=1}^{Q} g_{2k+1,3}(i)|x(t)|^{2(k-1)}\, x(t)|x(t-i)|^2 \\
& + \sum_{k=1}^{\frac{K-1}{2}} \sum_{i=1}^{Q} g_{2k+1,4}(i)|x(t)|^{2(k-1)}\, x^*(t)x^2(t-i). \quad (4.16)
\end{aligned}
$$

### 4.3.3 Generalized Memory Polynomials

Another model including cross terms is the generalized memory polynomials (GMP)[35]. Inserting a delay of samples between the signal and its exponentiated envelope using positive and negative cross-term time shifts we get:

$$
\begin{aligned}
y(n) \quad = \quad & \sum_{k=0}^{K_a-1} \sum_{l=0}^{L_a-1} a_{k,l} x(n-l) |x(n-l)|^k \\
+ \quad & \sum_{k=1}^{K_b} \sum_{l=0}^{L_b-1} \sum_{m=1}^{M_b} b_{k,l,m} x(n-l) |x(n-l-m)|^k \\
+ \quad & \sum_{k=1}^{K_c} \sum_{l=0}^{L_c-1} \sum_{m=1}^{M_c} c_{k,l,m} x(n-l) |x(n-l+m)|^k,
\end{aligned}
\tag{4.17}
$$

where the structure of GMP models is determined by 8 parameters: $K_a$, $K_b$, $K_c$ non-linearity orders, $L_a$, $L_b$, $L_c$ memory lengths and $M_b$, $M_c$ distances from the diagonal of Volterra series, and $a_{k,l}$, $b_{k,l,m}$ and $c_{k,l,m}$ are the linear coefficients of the equation.

In order to reduce the complexity, it is not necessary in many cases to use all of the coefficients. For example, odd-order nonlinearities usually dominate so that we may only want to consider odd-order terms. Also additionally, depending on the signal bandwidth and sampling rate, it may not be necessary to implement all cross-term time shifts.

## 4.4 Identification of Models

In this section we will focus on models with linear dependency with respect to their coefficients. The interest of these models is that we will obtain a convex minimization problem for the least-squares (LS) criteria for PA modeling and DPD with indirect learning architecture.

In order to identify the coefficients of PA model or DPD coefficients, we use LS optimization criterion:

$$
\mathbf{e} = \min_b ||\mathbf{y} - \mathbf{z}||^2 .
\tag{4.18}
$$

We apply notations defined in Fig.4.1, where for PA modeling $y(t)$ is measured signal (for DPD $x(t)$ is measured signal) and $z(t)$ is the output of the model. We consider here only indirect learning approach for the DPD.

The $||.||^2$ represent the quadratic norm of vector and $\mathbf{z}$ is expressed as:

$$
\mathbf{z} = \mathbf{U}b,
\tag{4.19}
$$

and where a $\mathbf{z}$ is a in vector with dimensions $N \times 1$:

$$
\mathbf{z} = [z(0), ..., z(N-1)]^T .
\tag{4.20}
$$

17
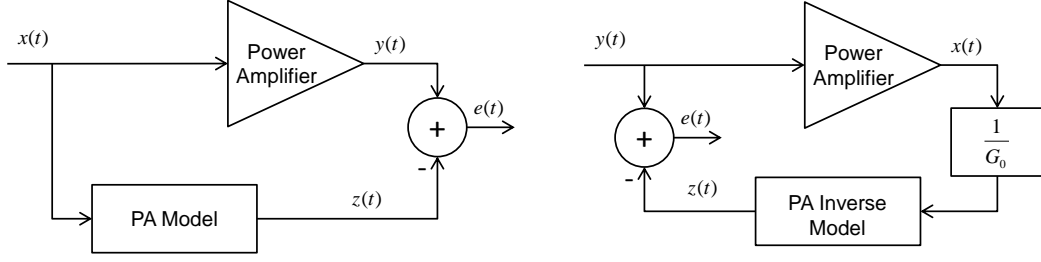
Figure 4.1: Schematic of minimizing problem between measured and modeled signals. The left schematic represents calculation of PA model. The right schematic represents calculation of PA inverse model (note that the input $x(t)$ and output $y(t)$ notation is swapped in order to meet error defined in (4.18).

$$\mathbf{y} = [y(0), ..., y(N-1)]^T. \tag{4.21}$$

$$\mathbf{e} = [e(0), ..., e(N-1)]^T. \tag{4.22}$$

As seen in equation (4.19) $\mathbf{U}$ is a matrix of size $N \times N_c$ (where $N_c$ represents number of coefficients and for example for PMS $N_c = K(Q+1)$):

$$\mathbf{U} = \begin{pmatrix} \boldsymbol{\Phi}(0) \\ \boldsymbol{\Phi}(t) \\ \vdots \\ \boldsymbol{\Phi}(N-1) \end{pmatrix}. \tag{4.23}$$

$\mathbf{b}$ a vector of size $N_c \times 1$

$$\mathbf{b} = [b_0, ..., b_{N_c-1}]^T. \tag{4.24}$$

The optimization problem can be written:

$$\min_{\mathbf{b}}(\mathbf{e}^H\mathbf{e}). \tag{4.25}$$

### 4.4.1 Least Squares one-shot solution

The LS solution minimizing distance between each data point and the space of best fit passing through the data points for (4.19). The criteria $\mathbf{J}$ can be expressed as:

$$\begin{aligned} \mathbf{J(b)} &= ||\mathbf{z} - \mathbf{y}||^2 = \mathbf{e}^H\mathbf{e} = (\mathbf{y} - \mathbf{Ub})^H(\mathbf{y} - \mathbf{Ub}) \tag{4.26} \\[2mm] &= \mathbf{b}^H\mathbf{U}^H\mathbf{Ub} - \mathbf{y}^H\mathbf{Ub} - \mathbf{b}^H\mathbf{U}^H\mathbf{y} + \mathbf{y}^H\mathbf{y} \end{aligned}$$

The solution of (4.27) can be obtained by calculating the gradient and setting it to 0. The gradient is equal to:

$$\frac{\partial \mathbf{J((b))}}{\partial \mathbf{b}} = 2\,\mathbf{U}^H\mathbf{Ub} - 2\,\mathbf{U}^H\mathbf{y}, \tag{4.27}$$

The least square solution yields to:

$$\mathbf{U}^H\mathbf{U}\mathbf{b} - \mathbf{U}^H\mathbf{y} = 0. \tag{4.28}$$

$$\mathbf{b} = (\mathbf{U}^H\mathbf{U})^{-1}\mathbf{U}^H\mathbf{y} = \mathbf{U}^+\mathbf{y}, \tag{4.29}$$

where $\mathbf{U}^+$ denotes Moore - Penrose pseudo-inverse. The LS algorithm is in fact one-shot solution for block of data.

LS one-shot solution is quite good in terms of performance. Nevertheless an interest in adaptive algorithms grows (adaptive filtering, adaptive equalization, etc.). The problem with LS one-shot solution is, that it is not able to track PA variations. Therefore adaptive algorithms have been proposed for the case of DPD identification either.

### 4.4.2 Damped Newton Algorithm

In many applications, adaptive estimation is performed on a block by block basis. There exists method called Damped Newton Algorithm (DNA) that upgrades the LS solution by adding possibility to control the speed of convergence depending on the preceding error. The DNA works block by block and it adapts preceding vector of coefficients to take into account the new block of data with a damping factor. In this section we will describe DNA used for predistortion of PA. The approach for predistortion using DNA was defined in [35].
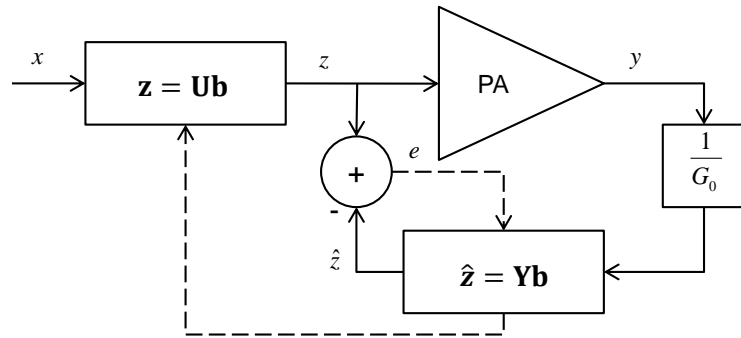


Figure 4.2: Schematic of DNA system.

The initialization vector $\mathbf{b}_0$ is usually chosen to use predistorter as a transparent block as:

$$\mathbf{b}_0 = [1, 0, \cdots, 0]^T. \tag{4.30}$$

According to notation in Fig.4.2 we can describe the algorithm for $n \in 1, 2, 3, ...$, where $n$ represents the block number, with the following equation for block $n$ (each block has $N$ samples):

$$\mathbf{z} = \mathbf{U}\,\mathbf{b}_{n-1}. \tag{4.31}$$

Equivalently as in (4.20-4.23) we define the output matrix $\mathbf{Y}$ from the signal $\frac{y}{G_0}$ as:

$$\hat{\mathbf{z}} = \mathbf{Y}\,\mathbf{b}_{n-1}. \tag{4.32}$$

Then we define the error vector $\mathbf{e}$

$$\mathbf{e} = \mathbf{z} - \hat{\mathbf{z}}. \tag{4.33}$$

The coefficients $\mathbf{b}$ can be updated as:

$$\mathbf{b}_n = \mathbf{b}_{n-1} + \mu \left(\mathbf{Y}^H \mathbf{Y}\right)^{-1} \mathbf{Y}^H\,\mathbf{e}, \tag{4.34}$$

where $\mu$ is a relaxation variable. When setting the relaxation variable $\mu = 1$ the damping is removed and the solution becomes the standard LS solution.

### 4.4.3 LMS algorithm

The Least Mean Square (LMS) algorithm is often used in adaptive systems due its simplicity and relative precision. The algorithm works sample by sample. The algorithm computes instantaneous error and then corrects the actual value of coefficients.

Using any of models defined before with linear relation with respect to their coefficients (for example PMS, OMPS, DDR) we note:

$$\boldsymbol{\Phi}(n) = n^{th}\ row\ of\ matrix\ \mathbf{U}. \tag{4.35}$$

Then the criterion function can be defined as:

$$\begin{aligned} \min J(n) &= \min |e(n)|^2 \\ &= \min |y(n) - \boldsymbol{\Phi}(n)\mathbf{b}(n)|^2\,. \end{aligned} \tag{4.36}$$

The estimated gradient vector becomes:

$$\nabla J(n) = \frac{\partial |e(n)|^2}{\partial \mathbf{b}(n)} \tag{4.37}$$

Because

$$e(n) = z(n) - \boldsymbol{\Phi}(n)\mathbf{b}(n), \tag{4.38}$$

applying equation (4.38) to equation (4.37) we get:

$$\nabla J(n) = -e(n)\boldsymbol{\Phi}^H(n). \tag{4.39}$$

Then using the steepest descent weight update equation we obtain iterative solution:

$$\mathbf{b}(n+1) = \mathbf{b}(n) + \mu e(n)\boldsymbol{\Phi}^H, \tag{4.40}$$

where parameter $\mu$ adjusts the compromise between convergence speed and the error value after convergence.

Due to sensitivity to value $\mu$ that can lead to instability, the algorithm was modified by using a normalization that improves stability of the algorithm. This algorithm is so-called Normalized Least Mean Square (NLMS) defined as:

$$\mathbf{b}(n+1) = \mathbf{b}(n) + \mu\ e(n)\ \frac{\boldsymbol{\Phi}^H}{\boldsymbol{\Phi}\ \boldsymbol{\Phi}^H} \tag{4.41}$$

Both LMS and NLMS suffers from low convergence speed and limited precision.

### 4.4.4 RLS algorithm

For solving the LS criterion optimization problem recursive least squares (RLS) algorithm can also be used. In its adaptive form it converges faster than LMS. Theoretically where the forgetting factor is equal to 1, it achieves the optimal solution (Wiener solution) but it is more complex than LMS. Now defining the input of the system:

$$\mathbf{x}(n) = [x(n), x(n-1), \ldots, x(0)]^T, \tag{4.42}$$

and vector of desired output:

$$\mathbf{y}(n) = [y(n), y(n-1), \ldots, y(0)]^T. \tag{4.43}$$

Then we define line vector $\mathbf{\Phi}(n)$ as before of size $1 \times N_c$ and matrix $\mathbf{\Theta}$ of size $(n+1) \times N_c$ as:

$$\mathbf{\Theta}(n) = \begin{pmatrix} \mathbf{\Phi}(0) \\ \vdots \\ \mathbf{\Phi}(n) \end{pmatrix}. \tag{4.44}$$

Then the output of the system will be:

$$\mathbf{z}(n) = \mathbf{\Theta}(n)\mathbf{b}(n). \tag{4.45}$$

The instantaneous error at time $n$ is:

$$e(n) = y(n) - \mathbf{\Phi}(n)\mathbf{b}(n). \tag{4.46}$$

Now defining the criterion function with a forgetting factor denoted as $\lambda$:

$$
\begin{aligned}
\min_{\mathbf{b}} J(n) &= \sum_{k=0}^{n} \lambda^{n-k} |e(k)|^2 \\
&= \sum_{k=0}^{n} \lambda^{n-k} |y(k) - \mathbf{\Phi}(k)\mathbf{b}(n)|^2 \\
&= \mathbf{e}^H \mathbf{\Lambda} \mathbf{e}(n)
\end{aligned} \tag{4.47}
$$

where:

$$\mathbf{\Lambda} = \mathrm{diag}\left[1, \lambda, \lambda^2, \ldots, \lambda^n\right] \tag{4.48}$$

To use recursive implementation we need to define the correlation matrix $\mathbf{R}(n)$ by a recurrence equation:

$$
\begin{aligned}
\mathbf{R}(n) &= \mathbf{\Theta}^H(n)\mathbf{\Lambda}\mathbf{\Theta}(n) \\
&= \sum_{k=0}^{n} \lambda^{n-k} \mathbf{\Phi}^H(k)\mathbf{\Phi}(k) \\
&= \sum_{k=0}^{n-1} \lambda^{n-k} \mathbf{\Phi}^H(k)\mathbf{\Phi}(k) + \mathbf{\Phi}^H(n)\mathbf{\Phi}(n) \\
&= \lambda\mathbf{R}(n-1) + \mathbf{\Phi}^H(n)\mathbf{\Phi}(n).
\end{aligned} \tag{4.49}
$$

We define the cross-correlation vector of size $N_c \times 1$:

$$
\begin{aligned}
\mathbf{p}(n) &= \mathbf{\Theta}^H(n)\mathbf{\Lambda}\mathbf{y}(n) & (4.50) \\
&= \sum_{k=0}^{n} \lambda^{n-k}\mathbf{\Phi}^H(k)y(k) \\
&= \sum_{k=0}^{n-1} \lambda^{n-k}\mathbf{\Phi}^H(k)y(k) + \mathbf{\Phi}^H(n)y(n) \\
&= \lambda\mathbf{p}(n-1) + \mathbf{\Phi}^H(n)y(n).
\end{aligned}
$$

Defining the recursive solution:

$$
\mathbf{b}(n+1) = \mathbf{R}^{-1}(n)\mathbf{p}(n) = \mathbf{P}(n)\mathbf{p}(n), \tag{4.51}
$$

where defining $\mathbf{P}(n) = \mathbf{R}^{-1}(n)$ and applying the inversion lemma to calculate $\mathbf{R}^{-1}(n)$ yields to:

$$
\mathbf{P}(n) = \lambda^{-1}\mathbf{P}(n-1) - \frac{\lambda^{-2}\mathbf{P}(n-1)\mathbf{\Phi}^H(n)\mathbf{\Phi}(n)\mathbf{P}(n-1)}{1 + \lambda^{-1}\mathbf{\Phi}(n)\mathbf{P}(n-1)\mathbf{\Phi}^H(n)}. \tag{4.52}
$$

Now defining the gain $\mathbf{g}(n)$:

$$
\mathbf{g}(n) = \frac{\lambda^{-1}\mathbf{P}(n-1)\mathbf{\Phi}^H(n)}{1 + \lambda^{-1}\mathbf{\Phi}(n)\mathbf{P}(n-1)\mathbf{\Phi}^H(n)} \tag{4.53}
$$

Then applying (4.53) to $\mathbf{P}(n)$ defined in (4.52) we get:

$$
\mathbf{P}(n) = \lambda^{-1}\mathbf{P}(n-1) - \lambda^{-1}\mathbf{g}(n)\mathbf{\Phi}(n)\mathbf{P}(n-1). \tag{4.54}
$$

To rewrite the recursive weight update algorithm:

$$
\begin{aligned}
\mathbf{g}(n) &= \frac{\lambda^{-1}\mathbf{P}(n-1)\mathbf{\Phi}^H(n)}{1 + \lambda^{-1}\mathbf{\Phi}(n)\mathbf{P}(n-1)\mathbf{\Phi}^H(n)} \\
\mathbf{P}(n) &= \lambda^{-1}\mathbf{P}(n-1) - \lambda^{-1}\mathbf{g}(n)\mathbf{\Phi}(n)\mathbf{P}(n-1) \\
e(n) &= y(n) - \mathbf{\Phi}^T(n)\mathbf{b}(n) \\
\mathbf{b}(n+1) &= \mathbf{b}(n) + \mathbf{g}(n)e(n).
\end{aligned} \tag{4.55}
$$

We define initial conditions as $\mathbf{p}(0) = 0$, $\mathbf{R}(0) = \delta\mathbf{I}$, where $\mathbf{I}$ is identity matrix. The typical value of $\delta$ is usually set as a small positive value equal to $\delta = 10^{-3}$. Then we can define:

$$
\mathbf{P}(0) = \mathbf{R}^{-1}(0) = \delta^{-1}\mathbf{I}. \tag{4.56}
$$

To show the relationship between LS solution and RLS algorithm lets set $\lambda = 1$, we get:

$$
\mathbf{R}(n) = \mathbf{\Theta}^H(n)\mathbf{I}\mathbf{\Theta}(n). \tag{4.57}
$$

$$
\mathbf{p}(n) = \mathbf{\Theta}^H(n)\mathbf{I}\mathbf{z}(n). \tag{4.58}
$$

and using:

$$\begin{aligned} \mathbf{R}(n)\mathbf{b}(n) &= \mathbf{p}(n) \\ \mathbf{\Theta}^H(n)\mathbf{I}\mathbf{\Theta}(n)\mathbf{b}(n) &= \mathbf{\Theta}^H(n)\mathbf{I}\mathbf{z}(n). \end{aligned} \qquad (4.59)$$

we get:

$$\mathbf{b}(n) = \left(\mathbf{\Theta}(n)\mathbf{\Theta}^H(n)\right)^{-1}\mathbf{\Theta}(n)\mathbf{z}(n). \qquad (4.60)$$

We recognize (4.60) for $n = N$ the LS solution for the block of $N$ samples.

Introducing a forgetting factor $\lambda$ leads to an adaptive algorithm. RLS converges faster and is more precise than LMS. The RLS algorithm is more complex than LMS.

## 4.5  Bibliography

[1]  M. M. Rana, "Performance comparison of lms and rls channel estimation algorithms for 4g mimo ofdm systems," in *Computer and Information Technology (ICCIT), 2011 14th International Conference on*, pp. 635–639, 2011.

[2]  E. Ngoya, C. Quindroit, and J. M. Nebus, "On the continuous-time model for nonlinear-memory modeling of rf power amplifiers," *Microwave Theory and Techniques, IEEE Transactions on*, vol. 57, no. 12, pp. 3278–3292, 2009.

[3]  J. Ibanez-Diaz, C. Pantaleon, I. Santamaria, T. Fernandez, and D. Martinez, "Nonlinearity estimation in power amplifiers based on subsampled temporal data," *Instrumentation and Measurement, IEEE Transactions on*, vol. 50, no. 4, pp. 882–887, 2001.

[4]  J. P. Martins, P. M. Cabral, N. B. Carvalho, and J. C. Pedro, "A metric for the quantification of memory effects in power amplifiers," *Microwave Theory and Techniques, IEEE Transactions on*, vol. 54, no. 12, pp. 4432–4439, 2006.

[5]  O. Hammi, M. Younes, and F. M. Ghannouchi, "Metrics and methods for benchmarking of rf transmitter behavioral models with application to the development of a hybrid memory polynomial model," *Broadcasting, IEEE Transactions on*, vol. 56, no. 3, pp. 350–357, 2010.

[6]  H. Seidel, "A microwave feedforward experiment," *Bell Systems Technical Journal*, vol. Vol. 50, pp. 2879–2918, 1971.

[7]  Y. Jaehyok, Y. Youngoo, P. Myungkyu, K. Wonwoo, and B. Kim, "Analog predistortion linearizer for high-power rf amplifiers," *Microwave Theory and Techniques, IEEE Transactions on*, vol. 48, no. 12, pp. 2709–2713, 2000.

[8]  Y. Nagata, "Linear amplification technique for digital mobile communications," in *Vehicular Technology Conference, 1989, IEEE 39th*, pp. 159–164 vol.1, 1989.

[9] J. K. Cavers, "Amplifier linearization using a digital predistorter with fast adaptation and low memory requirements," *Vehicular Technology, IEEE Transactions on*, vol. 39, no. 4, pp. 374–382, 1990.

[10] J. K. Cavers, "A linearizing predistorter with fast adaptation," in *Vehicular Technology Conference, 1990 IEEE 40th*, pp. 41–47, 1990.

[11] L. Ding and G. T. Zhou, "Effects of even-order nonlinear terms on power amplifier modeling and predistortion linearization," *Vehicular Technology, IEEE Transactions on*, vol. 53, no. 1, pp. 156–162, 2004.

[12] O. Shimbo, "Effects of intermodulation, am-pm conversion, and additive noise in multicarrier twt systems," *Proceedings of the IEEE*, vol. 59, no. 2, pp. 230–238, 1971.

[13] A. Saleh, "Intermodulation analysis of fdma satellite systems employing compensated and uncompensated twt's," *Communications, IEEE Transactions on*, vol. 30, no. 5, pp. 1233–1242, 1982.

[14] A. A. M. Saleh, "Frequency-independent and frequency-dependent nonlinear models of twt amplifiers," *Communications, IEEE Transactions on*, vol. 29, no. 11, pp. 1715–1720, 1981.

[15] J. R. Cadenas, M. Valdez, B. Palafox, C. Gontrand, and J. C. N. Perez, "Performance evaluation of a memory-polynomial model for microwave power amplifiers," *Programacion Matematica y Software*, vol. 4, pp. 13–23, 2012.

[16] M. Honkanen and S. G. Haggman, "New aspects on nonlinear power amplifier modeling in radio communication system simulations," in *Personal, Indoor and Mobile Radio Communications, 1997. Waves of the Year 2000. PIMRC '97., The 8th IEEE International Symposium on*, vol. 3, pp. 844–848 vol.3, 1997.

[17] C. Dudak and N. D. Kahyaoglu, "A descriptive study on am-am and am-pm conversion phenomena through evm-snr relation," in *Power Amplifiers for Wireless and Radio Applications (PAWR), 2012 IEEE Topical Conference on*, pp. 69–72, 2012.

[18] A. Ghorbani and M. Sheikhan, "The effect of solid state power amplifiers (sspas) nonlinearities on mpsk and m-qam signal transmission," in *Digital Processing of Signals in Communications, 1991., Sixth International Conference on*, pp. 193–197, 1991.

[19] G. P. White, A. G. Burr, and T. Javornik, "Modelling of nonlinear distortion in broadband fixed wireless access systems," *Electronics Letters*, vol. 39, no. 8, pp. 686–687, 2003.

[20] M. Schoukens, R. Pintelon, and Y. Rolain, "Parametric identification of parallel hammerstein systems," *Instrumentation and Measurement, IEEE Transactions on*, vol. 60, no. 12, pp. 3931–3938, 2011.

[21] D. Silveira, M. Gadringer, H. Arthaber, and G. Magerl, "Rf-power amplifier characteristics determination using parallel cascade wiener models and pseudo-inverse techniques," in *Microwave Conference Proceedings, 2005. APMC 2005. Asia-Pacific Conference Proceedings*, vol. 1, pp. 4 pp.–, 2005.

[22] V. A. Bohara, M. A. Hussein, and O. Venard, "Parameter identification algorithm for multi-stage digital predistorter," in *Proceedings of the 43rd European Microwave Conference*, 2013.

[23] M. E. Gadringer, D. Silveira, and G. Magerl, "Efficient power amplifier identification using modified parallel cascade hammerstein models," in *Radio and Wireless Symposium, 2007 IEEE*, pp. 305–308, 2007.

[24] N. Calinoiu, S. Bachir, and C. Duvanaud, "A power amplifier envelope distortion model using direct calculation of polynomial parameters and delay taps," in *Microwave Integrated Circuits Conference (EuMIC), 2011 European*, pp. 292–295, 2011.

[25] E. G. Lima, T. R. Cunha, H. M. Teixeira, M. Pirola, and J. C. Pedro, "Baseband derived volterra series for power amplifier modeling," in *Microwave Symposium Digest, 2009. MTT '09. IEEE MTT-S International*, 2009.

[26] M. Schetzen, *The Volterra and Wiener Theories of Nonlinear Systems*. Wiley, 1980.

[27] J. Kim and K. Konstantinou, "Digital predistortion of wideband signals based on power amplifier model with memory," *Electronics Letters*, vol. 37, no. 23, pp. 1417–1418, 2001.

[28] L. Ding, G. T. Zhou, D. R. Morgan, M. Zhengxiang, J. S. Kenney, K. Jaehyeong, and C. R. Giardina, "A robust digital baseband predistorter constructed using memory polynomials," *Communications, IEEE Transactions on*, vol. 52, no. 1, pp. 159–165, 2004.

[29] R. Marsalek, P. Jardin, and G. Baudoin, "From post-distortion to pre-distortion for power amplifiers linearization," *Communications Letters, IEEE*, vol. 7, no. 7, pp. 308–310, 2003.

[30] R. Dallinger, H. Ruotsalainen, R. Wichman, and M. Rupp, "Adaptive pre-distortion techniques based on orthogonal polynomials," in *Signals, Systems and Computers (ASILOMAR), 2010 Conference Record of the Forty Fourth Asilomar Conference on*, pp. 1945–1950, 2010.

[31] R. Raich, H. Qian, and G. T. Zhou, "Orthogonal polynomials for power amplifier modeling and predistorter design," *Vehicular Technology, IEEE Transactions on*, vol. 53, no. 5, pp. 1468–1479, 2004.

[32] Z. Anding, J. C. Pedro, and T. J. Brazil, "Dynamic deviation reduction-based volterra behavioral modeling of rf power amplifiers," *Microwave Theory and Techniques, IEEE Transactions on*, vol. 54, no. 12, pp. 4323–4332, 2006.

[33] G. Lei and A. Zhu, "Simplified dynamic deviation reduction-based volterra model for doherty power amplifiers," in *Integrated Nonlinear Microwave and Millimetre-Wave Circuits (INMMIC), 2011 Workshop on*, pp. 1–4, 2011.

[34] Z. Anding, P. Draxler, J. Yan, T. Brazil, D. Kimball, and P. Asbeck, "Open-loop digital predistorter for rf power amplifiers using dynamic deviation reduction-based volterra series," *Microwave Theory and Techniques, IEEE Transactions on*, vol. 56, no. 7, pp. 1524–1534, 2008.

[35] D. R. Morgan, M. Zhengxiang, K. Jaehyeong, M. Zierdt, and J. Pastalan, "A generalized memory polynomial model for digital predistortion of rf power amplifiers," *Signal Processing, IEEE Transactions on*, vol. 54, no. 10, pp. 3852–3860, 2006.

[36] R. E. Kalman, "A new approach to linear filtering and prediction problems," *Journal of Basic Engineering*, vol. 82, p. 35–45, 1960.

[37] M. Djamai, S. Bachir, and C. Duvanaud, "Kalman filtering algorithm for on-line memory polynomial predistortion," in *Microwave Conference, 2008. EuMC 2008. 38th European*, pp. 575–578, 2008.

[38] A. V. Malipatil and H. Yih-Fang, "Amplifier predistortion using unscented kalman filtering," in *Signal Processing Advances in Wireless Communications, 2005 IEEE 6th Workshop on*, pp. 221–225, 2005.

[39] S. Bachir, C. Duvanaud, and D. Djamai, "On-line memory polynomial predistortion based on the adapted kalman filtering algorithm," in *Circuits and Systems and TAISA Conference, 2008. NEWCAS-TAISA 2008. 2008 Joint 6th International IEEE Northeast Workshop on*, pp. 65–68, 2008.

[40] A. Malipatil and H. Yih-Fang, "Amplifier predistortion using unscented kalman filtering," in *Signal Processing Advances in Wireless Communications, 2005 IEEE 6th Workshop on*, pp. 221–225, 2005.

[41] S. Bachir, N. Calinou, and C. Duvanaud, "Linearization of rf power amplifiers using adaptive kalman filtering algorithm," *Journal of Circuits, Systems and Computers*, vol. 20, no. 06, pp. 1001–1018, 2011.

# Part II

# State of the Art Methods for Dynamical Non-linear systems

# 5. Introduction

The idea of deterministic non-linear series has influenced thinking in many research fields of science. Especially the paradigm of chaotic behavior. It is well known, that complex dynamical mathematical objects show rich and surprising structures [1, 2, 3]. Most catching for researchers over forty years in applied sciences is the fact that deterministic systems provide striking explanation for irregular behavior and anomalies in many systems which does not seem to be implicitly stochastic[4].

With a recent massive progress in the overall personal computer performance it turns out that even very complicated multi-level dynamical systems can be modeled and analyzed, in a reasonable amount of computational time. Many of these discovered events have been recently observed and proved by means of the artificial experiments. The excitement about chaos theory rises from the perception that it captures the complex disorganized order of the real world [5]. Meaning that chaotic signal from the macroscopic point of view represents total disorder [6].

Looking closely certain deterministic properties can be revealed. The absence of long-term predictability [7, 8] and the presence of infinitely many unstable periodical orbits makes almost any chaotic subsystem an ideal candidate for the ultra-fast encrypted communication channels. The basic obstacle to be removed in this area lies in the lack of sophisticated algorithms for the higher-order dynamical motion quantification. Due to the absence of closed-form analytical solution of the non-linear dynamical systems the existing routines are based on the numerical analysis and linearizion of continuous vector field near equilibrium points. On the other hand, great efforts are being made to exploit ideas from chaos theory in cases where the system is not necessarily deterministic but the data display more structure than can be captured by traditional methods.

# 6. Mathematical Models and Time Series Analysis

In this chapter several methods for analyzing the non-linear dynamical systems have been presented. Fist section deals with mathematical model analysis. Such methods are usually useful in the case of known mathematical models.

Otherwise in the case of having only measurements, different methods have to be applied. Such method have been presented in second part of this chapter.

## 6.1 Mathematical Model Analysis

The dynamics of linear systems is governed by the paradigm that small causes lead to small changes of a solution. Linear equations can lead to exponentially decaying (growing) or damped periodically oscillating solutions, where all irregular behavior has to be introduced by some random external conditions.

Chaos theory has simply demonstrated that there is no need of being one of the parameters random or stochastic [9], to produce irregular and complicated behavior.

Usually the model of autonomous system is given by the set of ordinary differential equations. The closed-form solution for such set of the equations is impossible to obtain analytically. Actually for modern computer technology it is impossible to find a analytical solution, but even if the solution is be obtained, it probably won't be intelligible.

### 6.1.1 Poincare Sections

The purpose of a Poincare section is to detect some sort of structure in the attractor. It can be defined as an intersection of a state space orbit of a continuous dynamical system with a certain lower dimensional subspace, transversal to the flow of the system.

A Poincare sections can be interpreted as a discrete dynamical system with a state space that is one dimension smaller than the original continuous dynamical system.

$$P : U \to S, \tag{6.1}$$

where $P$ is Poincare map for certain orbit on the Poincare section $S$ and $U$ is an open and connected neighborhood of point on the orbit.

### 6.1.2   Bifurcation Analysis

Bifurcation analysis is used to find certain points, where the system exhibits periodic, aperiodic and chaotic behavior (be aware that there exist also different bifurcation analysis.).

One of the most used methods is made of marginal sight (set) of Poincare sections, by perturbing chosen parameter of the mathematical model. Such typical plot can be seen in the Fig.6.1.
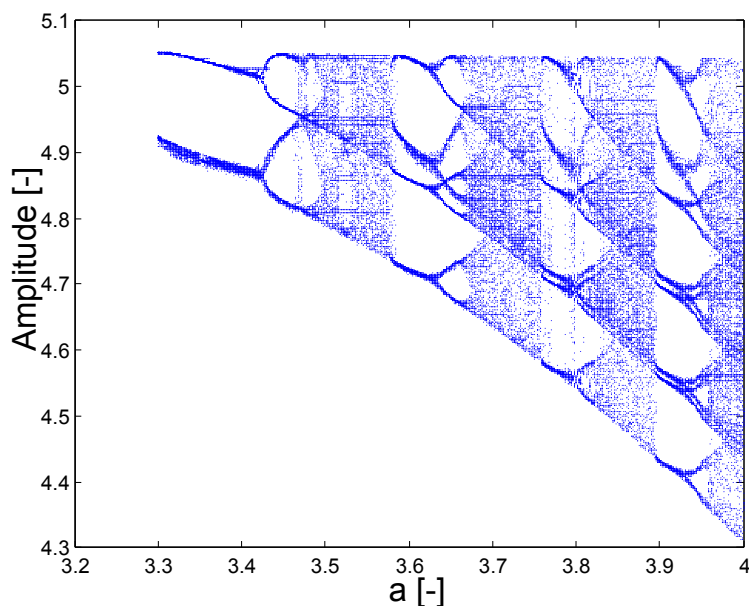


Figure 6.1: Bifurcation analysis of single Hindamarsch-Rose neural model.

### 6.1.3   Lyapunov Exponents

Detecting and quantifying chaotic behavior has become very important task for the non-linear dynamical systems. Almost every article dealing with non-linear systems is using Lyapunov exponents for its analysis [10, 11, 12].

These exponents are used to describe the average exponential rate of divergence or convergence of near arbitrary trajectories in the phase state space. They are also called characteristic exponents. Exponents can be regarded as a measure of sensitivity to initial conditions.

Lyapunov exponents are real numbers that can be advantageously used to classify non-chaotic and chaotic systems. If the system is in an unstable state, one can see that two nearby trajectories of each are moving away faster than a polynomial rate. Any system containing at least one positive Lyapunov exponent is defined to be chaotic. The

LE can be defined as:

$$LE[\mathbf{x}_0, \mathbf{y}_0 \in T_{x(t)}\Re^3] = \lim_{t \to \infty} \frac{1}{t} \frac{\|D_x\phi(t, \mathbf{x}_0)\mathbf{y}_0\|}{\|\mathbf{y}_0\|}, \tag{6.2}$$

where $Tx(t)$ is a tangent space in the point on the fiducial trajectory and $D_x\phi(t, \mathbf{x}_0)\mathbf{y}_0$ is solution of the linearized system.

In order to preserve the orthogonal base of vectors in each iteration step, a Gram-Smith orthogonalization procedure is added to the standard routine for LE calculation.

By sorting and indexing LEs in descending order the mentioned metric dimension called Kaplan-Yorke dimension can be calculated as:

$$D_{KY} = k + \frac{\sum_{i=1}^{k} LE_i}{\|LE_{k+1}\|}, \tag{6.3}$$

where $k$ is the largest integer representing the $k + 1$ state variables. This formula is in accordance with two fundamental mechanisms of chaos generation, i.e. folding and stretching of the state space trajectories.

From definition of the dissipative systems the sum of all LEs has to be negative. It is obvious from that the most common approach for LE evaluation for three dimensional dynamical systems described by ordinary differential equations is based on the numerical integration of the twelve differential equations. The linearization matrix is calculated in each point on the trajectory [13], thus it necessary to have the knowledge about Jacobi matrix (JM) in the symbolic form.

The approach is based on the divergence of neighboring trajectories compared with the fiducial trajectory. The solution was first presented in [14]. It is a method for identifying just the largest Lyapunov exponent, since the quantifying property is sufficient enough. Over time interval $t_2 - t_1$, the rate of divergence of two points that evolve from a spacing $D_1$ to a spacing $D_2$, may be characterized by a quantity:

$$Q = \frac{ln\left(\frac{D_2}{D_1}\right)}{t_2 - t_1}. \tag{6.4}$$

Because the separation must be kept small comparing with the size of the attractor, a new neighbor has to be set periodically for subsequent estimates of the divergence rate. After n repetitions of stretching and re-normalizing the spacing the rates are weighted by fraction of time between each re-normalization. Then they are added to yield an experimental value for the largest Lyapunov exponent as:

$$\lambda_1 = \sum_{i=1}^{n-1} \left\{ \left[ \frac{(t_{i+1} - t_i)}{\sum_{i=1}^{n-1}(t_{i+1} - t_i)} \right] \left[ \frac{ln\left(\frac{D_{i+1}}{D_i}\right)}{(t_{i+1} - t_i)} \right] \right\}. \tag{6.5}$$

Since

$$\sum_{i=1}^{n-1}(t_{i+1} - t_i) = t_n - t_1, \tag{6.6}$$

we have

$$\lambda_1 = \frac{\sum_{i=1}^{n-1} \left( \frac{D_{i+1}}{D_i} \right)}{t_n - t_1}. \tag{6.7}$$
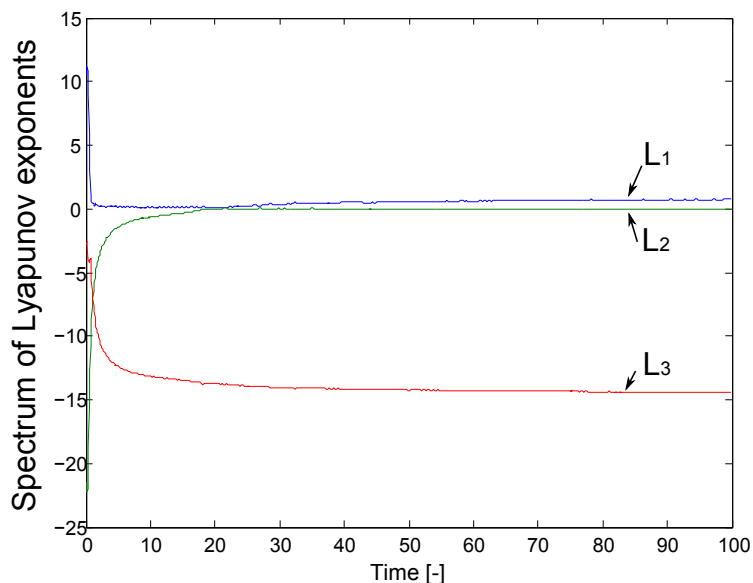


Figure 6.2: The spectrum of Lyapunov exponents for the system (**??**).

The estimated spectrum of Lyapunov exponents for the Lorenz system **??** of ordinary differential equations of third order is in the Fig.6.2.

This method cannot be used if the vector field is discontinuous, especially if the repeated jump functions are involved in the mathematical model [15], since JM contains extreme values [16, 17, 10]. In the article, there are values in the matrix, both infinity (positive as well as negative) and zero [10, 4].

If the transition between two states of the sign function is omitted the standard procedure returns the incorrect results. It is because the linearized flow is uniquely determined by three real negative eigenvalues and form stable node local geometry near the fiducial point. Having this configuration each edge of the volume cube shrinks suggesting that the system possess three negative LEs.

In practice the transition event is not neglected and the corresponding derivative depends on the numerical integration step size. If the extreme values substituted into the Jacobi matrix the entire procedure tends to diverge and fails.

## 6.2   Time Series Approach

One rarely has complete information about all of the degrees of freedom in a complex dynamical system. There are quite few conventional approaches for analyzing time series.

For example for quantifying the behavior, calculation of a correlation dimension can be used. The correlation dimension gives us an estimate of the system complexity [18]. But the methods for dynamical analysis of experimental data have been still developing.

In order to estimate all variables, first the reconstruction of dynamics has to be done. The standard method of reconstruction consists of estimating the degree of freedom, called embedding dimension $m$, reconstruction of dynamics and of determination of certain invariant quantities.

### 6.2.1 Reconstruction Of Dynamics

The reconstruction of a vector state space which is equivalent to the generating state space of the system from a scalar time series is the basis of almost all of the methods. The simplest method to embed scalar data is usage of method of delays.

This can be done by reconstructing the pseudo phase-space from a scalar time series, by using delayed copies of the original time series as components of the reconstruction matrix. It involves sliding a window of length $m$ through the data to form a series of vectors, stacked row-wise in the matrix. Each row of this matrix is a point in the reconstructed phase-space. Setting $\{X_1 \cdots X_n\}$ represent the time series, the reconstruction matrix is then represented as:

$$\mathbf{X} = \begin{pmatrix} X_0 & \cdots & X_{(m-1)\tau} \\ \vdots & \ddots & \vdots \\ X_n & \cdots & X_{n+(m-1)\tau} \end{pmatrix}, \tag{6.8}$$

where $m$ is the embedding dimension and $\tau$ is the embedding delay (in samples). Fixing an optimal value of $m$ and $\tau$ requires domain specific knowledge about the time series being analyzed.

### 6.2.2 Embedded Dimension

In fact there exists several methods for estimating the embedded dimensions. If the attractor is embedded in spaces of increasingly higher dimension it exhibits an increasingly complex structure as it unfolds. This process continues, until the structure's correlation dimension saturates. At this point the fully attractor is revealed.

Another possibility is take advantage of symplectic geometry process, performing symplectic transforms [19].

### 6.2.3 Time Delay $\tau$

For choosing the time delay $\tau$ the geometrical argument has to be applied and the attractor should be unfolded. It means that the extension of the attractor in all space

dimensions should be roughly the same. Statistics such as fill factor or displacement from diagonal are employed to evaluate this argument quantitatively.

Despite this definition the most natural approach is utilizing the autocorrelation function to the time series. It is intimately related to the shape of the state space attractor. Investigating the ellipsoid set containing normally distributed points in the state space.

The lengths of semi-axes of the optimal approximation have been given by the square root eigenvalues of the auto-covariance matrix. In the two dimensional space the two eigenvalues are equal if the autocorrelation function vanishes at the time lag used for the construction of the matrix.

Because there is no simple rule for choosing $\tau$ in all cases, investigators has to adjust $\tau$ until the results seems satisfactory. Autocorrelation based methods have the advantage of short calculation time using the fast Fourier transform (FFT) algorithm.

$$R_{ff}(\tau) = (f(t) * \hat{f}(-t))(\tau) = \int_{-\infty}^{\infty} f(t)\hat{f}(t - \tau)dt \approx 0. \tag{6.9}$$

### 6.2.4 Demonstration of Time Series Analysis

For analyzing the time series the Lorenz equations [5] have been chosen as the generating system. This system has bee chosen, because it is well known and it has been precisely studied by many researchers [20].

Particularly the first variable was stored and the others were discarded. In the real valued measurements, the system under study gives usually one observable, thus the only information about the system, is noisy one-dimensional signal sampled with a finite precision [8]. According to Taken's embedding theorem [21], we can use time series $x_1, x_2, ..., x_n$ to construct a trajectory matrix $X_{m \times d}$ by time delay coordinates method described by (6.8).

The different attractors can be seen in Fig.6.3 for different embedded lag $\tau$. The most appropriate estimation to preserve the dynamics seems to be $\tau = 8$.

To estimate the embedded dimension $m$ a symplectic geometry method is used to determine the appropriate number of variables from a scalar time series. Symplectic geometry has a certain measure and can keep the essential character of the primary time series unchanged when performing symplectic similar transforms. More about this theory can be found in [19]. When using the symplectic geometry approach, the embedded dimension of Lorenz system was estimated to be $m = 4$. In fact that is not exactly correct result, but using higher order of system can also lead to same behavior.

Using method described in [14] for estimation of the largest Lyapunov exponent for the time series, the exponent was estimated as $\lambda_1 = 0.663$. For comparison estimated
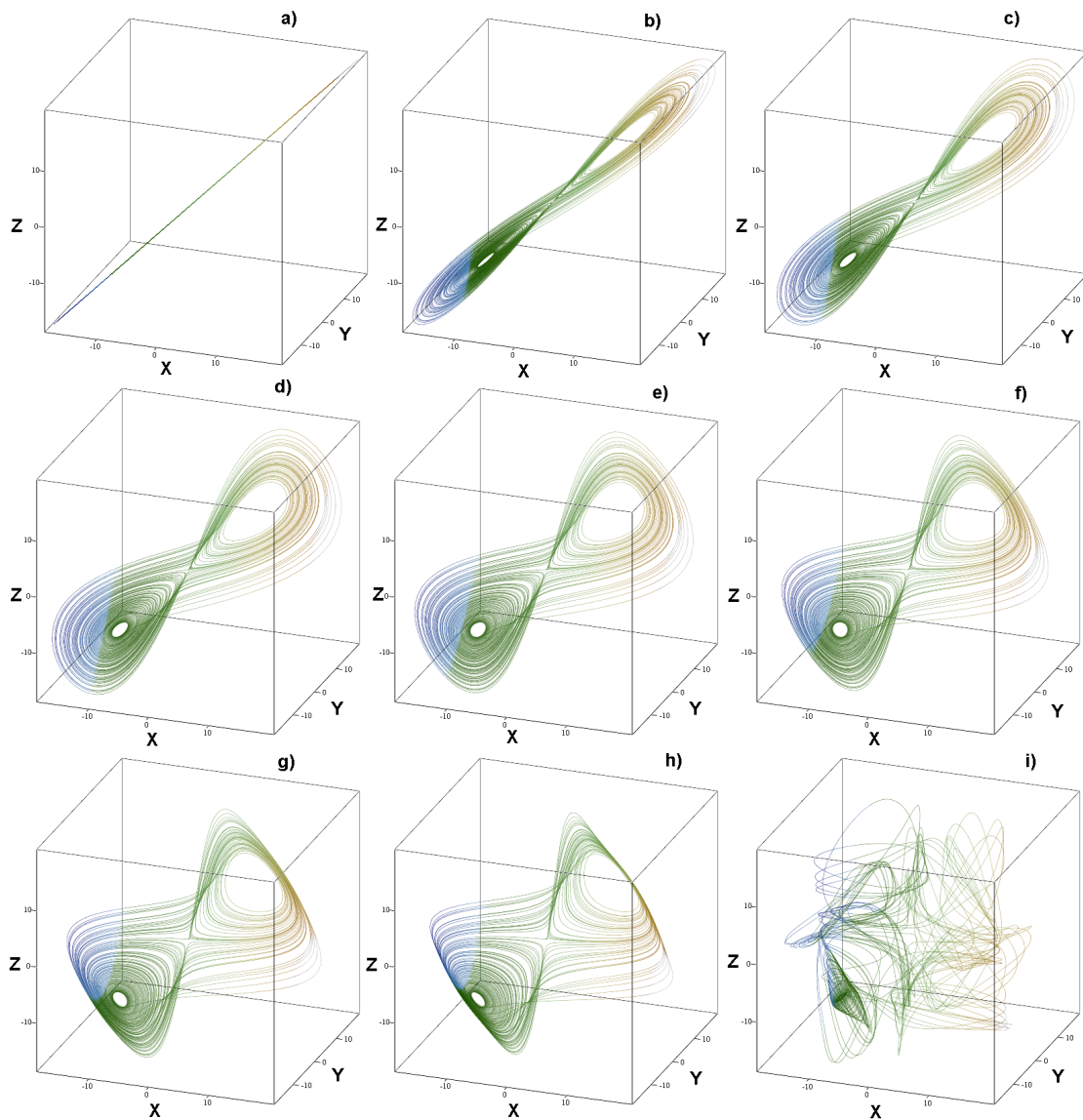
Figure 6.3: Different lag $\tau$ a) $\tau = 0$, b) $\tau = 2$, c) $\tau = 4$, d) $\tau = 6$, e) $\tau = 8$, f) $\tau = 10$, g) $\tau 12$, h) $\tau = 14$, i) $\tau = 98$.

largest Lyapunov exponent from the ODEs is equal to $\lambda_1 = 0.703$.

## 6.3  Bibliography

[1]  E. Zeraoulia and J. C. Sprott, "Some open problems in chaos theory and dynamics," *International Journal of Open Problems in Computer Science and Mathematics*, vol. 4, pp. 1–10, 2011.

[2]  M. Small, *Applied Nonlinear Time Series Analysis: Applications in Physics, Phys-*

*iology and Finance.* World Scientific series in nonlinear science, Series A, World Scientific, 2005.

[3]   D. A. Arroyo-Almanza, A. N. Pisarchik, and F. R. Ruiz-Oliveras, "Route to chaos in a ring of three unidirectionally-coupled semiconductor lasers," *Photonics Technology Letters, IEEE*, vol. 24, no. 7, pp. 605–607, 2012.

[4]   H. G. E. Hentschel and I. Procaccia, "The infinite number of generalized dimensions of fractals and strange attractors," *Physica D Nonlinear Phenomena*, vol. 8, pp. 435–444, Sept. 1983.

[5]   J. C. Sprott, *Chaos and Time-Series Analysis.* Oxford University Press, 2003.

[6]   J. C. Sprott, "Some simple chaotic flows," *Phys. Rev. E*, vol. 50, pp. R647–R650, 1994.

[7]   G. P. Williams, *Chaos Theory Tamed.* London: Taylor and Francis, 1997.

[8]   H. Kantz and T. Schreiber, *Nonlinear Time Series Analysis.* Cambridge nonlinear science series, Cambridge University Press, 2004.

[9]   J. C. Sprott and K. E. Chlouverakis, "Labyrinth chaos," *I. J. Bifurcation and Chaos*, vol. 17, no. 6, pp. 2097–2108, 2007.

[10]  J. Petrzela and J. Prokopec, "Some practical experiments with simple driven dynamical systems," in *Radioelektronika, 2009. RADIOELEKTRONIKA '09. 19th International Conference*, pp. 247–250, 2009.

[11]  J. C. Sprott, *Elegant Chaos: Algebraically Simple Chaotic Flows.* World Scientific, 2010.

[12]  K. Grygiel and P. Szlachetka, "Lyapunov exponents analysis of autonomous and nonautonomous set of ordinary differential equations," *Acta Physica Polonica B*, vol. 26, pp. 1321 – 1331, 1995.

[13]  V. Spany, P. Galajda, M. Guzan, L. Pivka, and M. Olejar, "Chua's singularities: Great miracle in circuit theory.," *I. J. Bifurcation and Chaos*, vol. 20, no. 10, pp. 2993–3006, 2010.

[14]  A. Wolf, J. B. Swift, H. L. Swinney, and J. A. Vastano, "Determining Lyapunov exponents from a time series," *Physica D*, vol. 16, p. 285, 1985.

[15]  N. K. Bari, *A treatise on trigonometric series.* No. v. 1 in A Treatise on Trigonometric Series, Pergamon Press, 1964.

[16]  P. Morters, Y. Peres, O. Schramm, and W. Werner, *Brownian Motion.* Cambridge Series in Statistical and Probabilistic Mathematics, Cambridge University Press, 2010.

[17]  H. Ocampo, S. Paycha, and A. Vargas, *Geometric and Topological Methods for Quantum Field Theory.* Lecture Notes in Physics, Springer, 2005.

[18] P. Grassberger and I. Procaccia, "Characterization of strange attractors," *Physical Review Letters*, vol. 50, pp. 346–349, 1983.

[19] L. Min, W. Zhizhong, and F. Zhengjin, "A method of embedding dimension estimation based on symplectic geometry," *Physics Letters A*, vol. 303, pp. 179–189, 2002.

[20] E. N. Lorenz, "Deterministis nonperiodic flow," *Journal of Atmospheric Sciences*, vol. 1, pp. 130–141, 1963.

[21] F. Takens, "Detecting strange attractors in turbulence dynamical systems and turbulence," *Dynamical Systems and Turbulence*, vol. 898, pp. 366–381, 1981.

# Part III

# Overview of Research Work I

# 7. On the Lower I/Q Imbalance Sensitivity Using Real-valued Feedback of Digital Predistortion

**Abstract**

The adaptive digital predistortion is currently widely used to compensate for the nonlinearities. Usually the observing (feedback) path of the predistorter is required to be very accurate. That means it is compensated for any radio frequency front-end imperfections.

In this paper we demonstrate that recently proposed (real-valued) digital predistortion algorithm employing only one of the signals in the quadrature pair implies the reduced sensitivity of the predistorter adaptation to the I/Q modulator imbalance in the feedback path. The lower sensitivity is demonstrated using both simulation as well as by an experiment conducted using the mm-Wave setup with integrated direct-conversion transceiver with important imbalances in both transmitting (Tx) as well as in receiving (Rx) path.

## 7.1 Introduction

An efficiency and linearity are two important merits for the radio frequency (RF) power amplifiers (PA's). In order to maximize the efficiency, PA's have to be operated close to saturation, where they exhibit strong nonlinear behavior. One of the widely-employed methods for PA linearization is a digital predistortion (DPD) based on the pre-processing the signal by the inverse characteristics of PA, [1]. In order to track the changes of PA characteristics adaptive baseband DPD system is required, the PA output has to be monitored by the dedicated feedback (observation) path, where the part of the signal is down-converted to the baseband in-phase (I) and quadrature (Q) components. Moreover, as has been widely demonstrated [2], the standard DPD adaptation algorithm is sensitive to RF impairments, such as DC offset or I/Q modulator/demodulator imbalances. Recently, the DPD adaptation algorithm, employing only one of the I and Q signals from the quadrature pair of down-converted PA output has been proposed in [3]. In this paper we demonstrate that such algorithm is not only beneficial due to its lower hardware complexity, but we lower sensitivity on I/Q imperfections as well show. The lower sensitivity is demonstrated using both simulation as well as by an experiment conducted using the mm-Wave setup with integrated direct-conversion transceiver with important imbalances in both transmitting (Tx) as well as in in receiving (Rx) path.

## 7.2 Digital Predistortion

Digital predistortion is one of techniques used for overcoming the non-linear behavior of PA. It is well known, [1] the non-linear regime is related with PA efficiency resulting to several undesirable effects such as spectrum widening in the adjacent channel interferences or memory effects, etc. The most general form of predistorters are based on Volterra series models. Nevertheless, for practical reasons, several less complex models derived from Volterra series have been derived in the past. Overcoming the complexity of the general Volterra series, an effective model pruning method, called dynamic deviation reduction (DDR) of 2nd-order was proposed and used in several recent papers [4, 5, 6] to demonstrate its performance in DPD application. The overall model structure determined by 2 parameters: the non-linearity order $K$ and the memory length $M$. The number of coefficients $b$ is thus $2MK + (\frac{K+1}{2})) - M$. Throughout this paper, we use such model to describe the nonlinear function output, i.e., the output of the predistorter $z(t)$ as:

$$
\begin{aligned}
z(t) = {} & \sum_{k=0}^{\frac{K-1}{2}} \sum_{i=0}^{M} b_{2k+1,1}(i) \, |x(t)|^{2k} x(t-i) \\
& + \sum_{k=1}^{\frac{K-1}{2}} \sum_{i=1}^{M} b_{2k+1,2}(i) \, |x(t)|^{2(k-1)} x^2(t) x^*(t-i) \\
& + \sum_{k=1}^{\frac{K-1}{2}} \sum_{i=1}^{M} b_{2k+1,3}(i) |x(t)|^{2(k-1)} \, x(t) |x(t-i)|^2 \\
& + \sum_{k=1}^{\frac{K-1}{2}} \sum_{i=1}^{M} b_{2k+1,4}(i) |x(t)|^{2(k-1)} \, x^*(t) x^2(t-i),
\end{aligned}
$$

(7.1)

with $x(t)$ being the nonlinear function, i.e., predistorter input. The model coefficients as well as its instantaneous input samples can be arranged into vector/matrix using feedback signal $y(t)$. Using the indirect learning architecture [7] of DPD the criteria can be written as:

$$
\mathbf{x} = \mathbf{U}\mathbf{b}. \tag{7.2}
$$

## 7.3 Real-valued Feedback Signal

By splitting the real and imaginary parts, further denoted as $(.)_r$ and $(.)_i$, of equation 13.5 we get

$$
\mathbf{x}_r + j\mathbf{x}_i = (\mathbf{U}_r + j\mathbf{U}_i)(\mathbf{b}_r + j\mathbf{b}_i), \tag{7.3}
$$

$$
\mathbf{x}_r + j\mathbf{x}_i = \mathbf{U}_r\mathbf{b}_r + j\mathbf{U}_i\mathbf{b}_r + j\mathbf{U}_i\mathbf{b}_i - \mathbf{U}_i\mathbf{b}_r. \tag{7.4}
$$

$$
\mathbf{x}_r = \mathbf{U}_r\mathbf{b}_r - \mathbf{U}_i\mathbf{b}_i \quad \wedge \quad \mathbf{x}_i = \mathbf{U}_i\mathbf{b}_r - \mathbf{U}_r\mathbf{b}_i \tag{7.5}
$$

$$
\mathbf{M}_a = [\mathbf{U}_r \;\; -\mathbf{U}_i] \quad \wedge \quad \mathbf{M}_b = [\mathbf{U}_i \;\; \mathbf{U}_r] \tag{7.6}
$$

$$\boldsymbol{\Theta}_a = [\mathbf{b}_r \quad -\mathbf{b}_i] \quad \wedge \quad \boldsymbol{\Theta}_b = [\mathbf{b}_r \ \mathbf{b}_i] \tag{7.7}$$

$$\boldsymbol{\Theta}_a = \left(\mathbf{M}_a^H \mathbf{M}_a\right)^{-1} \mathbf{M}_a^H \mathbf{x}_r \quad \wedge \quad \boldsymbol{\Theta}_b = \left(\mathbf{M}_b^H \mathbf{M}_b\right)^{-1} \mathbf{M}_b^H \mathbf{x}_i, \tag{7.8}$$

where $(.)^H$ represents Hermitian transpose. In the equation (9) we may observe, that on the right-hand side of the equation we have $\mathbf{x}_r$ or $\mathbf{x}_i$. But adventitiously using Iterative learning control (ILC) we may interchange $\mathbf{x}$ and $\mathbf{y}$. ILC, [8] is a widely-recognized technique that can help to obtain the inverse of a system. Fundamentally the approach divides the problem into the two steps – estimation of a model and predistortion. Thus, instead of focusing on identifying the predistorter parameters, an iterative learning algorithm is used to identify the optimal power amplifier (PA) model. Once the optimal PA model is found (we used DDR2 as well), then the parameters of the predistorter are estimated using standard modeling approach such as least squares.

## 7.4 I/Q Imbalance in Feedback Path

In this paragraph, we would like to show that DPD adaptation based on the real/in-phase (or imaginary/quadrature) part of the demodulated signal is less sensitive to Rx quadrature demodulator imbalances than DPD adaptation methods based on standard LS criteria as eq. (13.5). Suppose first that we can neglect the noise and thus the received passband signal in the feedback path of DPD is identical to the transmitted signal with the baseband components $y(t) = y_r(t) + jy_i(t)$:

$$y_{RF}(t) = \Re\left\{y(t)e^{j\omega t}\right\} = y_r(t)cos(\omega t) - y_i(t)sin(\omega t), \tag{7.9}$$

Multiplying the passband signal by the two local oscillator signals and passing through a pair of low-pass filters, one obtains the demodulated baseband signals. After rearrangements we can write the symmetrical model burdened by I/Q imbalance:

$$\begin{aligned} y(t)_r' &= (1+\epsilon)\left[y_r(t)cos(\phi) - y_i(t)sin(\phi)\right] \\ y(t)_i' &= (1-\epsilon)\left[y_i(t)cos(\phi) - y_r(t)sin(\phi)\right] \end{aligned} \tag{7.10}$$

where $\epsilon$ is a gain imbalance and $\phi$ is a phase imbalance. In order to express the performance of the real-valued DPD adaptation method (using only one of the I or Q components) in contrast to the standard complex-valued adaptation method, we may define the error ratio as:

$$E = 10\log_{10}\left(\frac{\sum_{n=1}^{N}(\mathbf{y}(n) - \mathbf{y}'(n))(\mathbf{y}(n) - \mathbf{y}'(n))^*}{\sum_{n=1}^{N}(\Re\{\mathbf{y}(n)\} - \Re\{\mathbf{y}(n)\}')^2}\right), \tag{7.11}$$

with the analytic solution presented in Appendix of this paper. Where $(.)^*$ is complex conjugation and $\Re(.)$ is real and $\Im(.)$ imaginary part and $N$ is length of a vector $\mathbf{x}$.

### 7.4.1 Typical system

To better illustrate the practical benefits of real-valued method, the dependency of the error ratio $E$ on the gain imbalance $\epsilon$ and the phase imbalance $\phi$ is shown in Fig.7.1. On

an example of the selected practical values of imbalances, e.g. $\epsilon = 0.02$ and $\phi = 0.35$ °
the error ratio is equal to $E = 4.5\ dB$, that means that the proposed (i.e. real-valued)
adaptation method is approximately 6.5 times better in term of insensitivity to I/Q
mismatch.
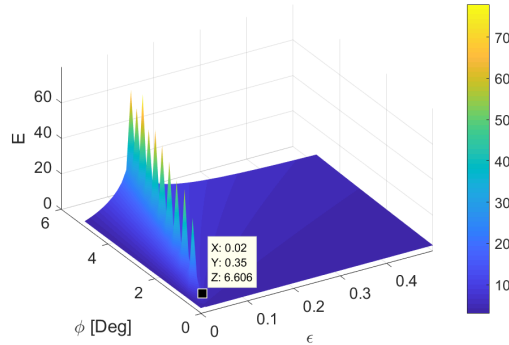


Figure 7.1: Error ratio dependency as function of phase $\phi$ and gain $\epsilon$ imbalances.

## 7.5 Measurement setup

The performance of the DPD adaptation based on the real-valued PA feedback has been
evaluated using the 60 GHz mm-wave measurement setup, with the block structure and
photo shown in Fig. 7.2. This setup is based on the Infineon BGT-60 evaluation board,
CompuGen 4302, a 4-channel 300 MSa/s arbitrary waveform generator board with 12-
bit resolutionand the CompuScope 12400, 2-channel data acquisition card with maximal
sampling speed of 400 MSa/s with 12-bit resolution. The sampling speed 250 MSa/s
was selected. The output of BGT-60 RF in-built PA is, after attenuation by a Quinstar
V-band attenuator visualized on the FSUP spectrum analyzer equipped with FS-Z75
harmonic mixer. A part of the PA output signal is fed back to BGT-60 receiver part
through the in-house fabricated directional coupler.
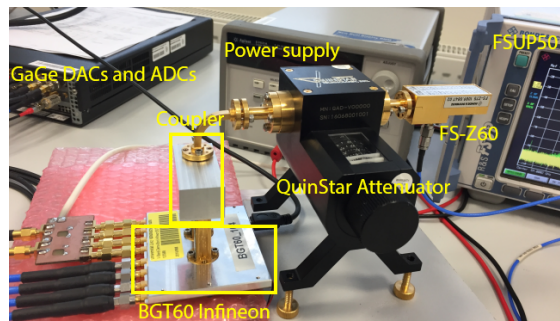


Figure 7.2: Photo of experimental setup for mm-Waves used for testing the digital pre-
distortion.

## 7.6 Results

According to the data-sheet of BGT-60 chipset, the present I/Q demodulator exhibits a phase error of $\phi = 2$ ° and gain mismatch of 0.5 dB. The tests described below have been carried out for the relatively narrow-band (12.5 MHz BW) QAM signals with 16 samples per symbol and root raised cosine shaping with roll-off 0.3. In order to asses the sensitivity of the standard and real-valued feedback DPD adaptation methods, in the first experiment, the I/Q imbalances were left uncompensated. The I/Q imbalance effect on the AM/AM characteristic of the PA are clearly visible in Fig. 7.3. The standard indirect learning DPD adaptation method failed to estimate DPD characteristics due to the presence of I/Q imbalances, nevertheless the real-valued based DPD adaptation method performed well. With the I/Q imbalances of RF front-end compensated (using approach from [9]) both methods were able to find the stable solution of DPD, as demonstrated in Fig. 7.3. The superior performance of the real-valued feedback DPD adaptation (denoted as single-channel DPD) is confirmed as well.
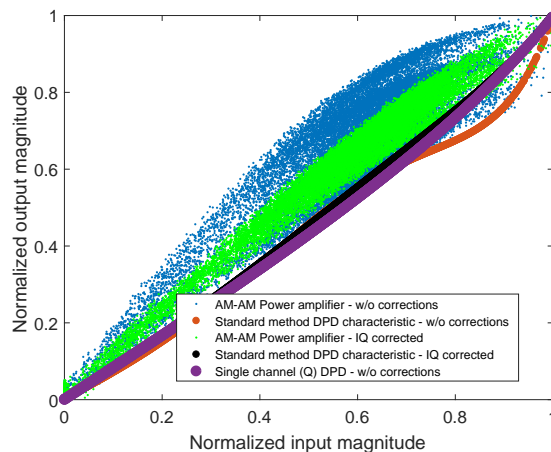


Figure 7.3: AM-AM characteristics without applied I/Q corrections and with applied I/Q Tx and Rx corrections.

## 7.7 Conclusion

We have investigated the performance of a standard (i.e. using both real and imaginary parts of feedback signal) least-squares solution of the digital predistorter coefficients calculation in comparison with the recently proposed method, based on using either real or imaginary part of feedback signal separately. We have demonstrated, both analytically as well as through the practical experiment with the direct conversion mm-wave transceiver system, the lower sensitivity of this recent approach to the uncompensated gain and phase imbalances in the predistorter feedback path. The reason of unsuccessful calculation of DPD coefficients in case of I/Q imbalances can be due an inversion of matrix made of observation samples (measurements).

## 7.8 Appendix

After some manipulations, the instantaneous error ratio $E(n)$ defined in equation (7.11) can be analytically expressed by equation (7.12). For our simulations (visualizations in Fig. 7.1) we expect that the mean value of transmitted signals is close to zero, as can be expected for both multi-carrier as well as single-carrier QAM signals.

$$E(n) = 10\log \frac{[(y(n) - (y(n) + \epsilon y(n)^*)\cos(\phi) - j(\epsilon y(n) - y(n)^*)\sin(\phi)] [y(n) - (y(n) + \epsilon y(n)^*)\cos(\phi)]^* + j(-y(n) + \epsilon y(n)^*)\sin(\phi)}{(1 - \epsilon)[\cos(\phi)\Im(y(n)) - \Re(y(n))\sin(\phi)] + \Re\{y(n) - (1 + \epsilon)\cos(\phi)\Re(y(n)) + (1 + \epsilon)\Im(y(n))\sin(\phi)\}^2} \quad (7.12)$$

## 7.9 Bibliography

[1] J. K. Cavers, "Amplifier linearization using a digital predistorter with fast adaptation and low memory rrequirements," *Vehicular Technology, IEEE Transactions on*, vol. 39, no. 4, pp. 374–382, 1990.

[2] T. Gotthans, R. Marsalek, J. Gotthans, and G. Baudoin, "Influence of filter-bank rf transceiver chain imperfections on digital predistortion performance," in *2016 International Symposium on Wireless Communication Systems (ISWCS)*, Sept 2016, pp. 623–627.

[3] J. Chani-Cahuana, M. Ozen, C. Fager, and T. Eriksson, "Digital predistortion parameter identification for rf power amplifiers using real-valued output data," *IEEE Transactions on Circuits and Systems II: Express Briefs*, vol. PP, no. 99, pp. 1–1, 2017.

[4] A. Zhou, J. C. Pedro, and T. J. Brazil, "Dynamic deviation reduction-based volterra behavioral modeling of rf power amplifiers," *Microwave Theory and Techniques, IEEE Transactions on*, vol. 54, no. 12, pp. 4323–4332, 2006.

[5] T. Gotthans, G. Baudoin, and A. Mbaye, "Comparison of modeling techniques for power amplifiers," in *Radioelektronika (RADIOELEKTRONIKA), 2013 23rd International Conference*, 2013, pp. 232–235.

[6] Z. Anding, P. Draxler, J. Yan, T. Brazil, D. Kimball, and P. Asbeck, "Open-loop digital predistorter for rf power amplifiers using dynamic deviation reduction-based volterra series," *Microwave Theory and Techniques, IEEE Transactions on*, vol. 56, no. 7, pp. 1524–1534, 2008.

[7] J. Chani-Cahuana, C. Fager, and T. Eriksson, "A new variant of the indirect learning architecture for the linearization of power amplifiers," in *2015 European Microwave Conference (EuMC)*, Sept 2015, pp. 1295–1298.

[8] J. Chani-Cahuana, P. N. Landin, C. Fager, and T. Eriksson, "Iterative learning control for rf power amplifier linearization," *IEEE Transactions on Microwave Theory and Techniques*, vol. 64, no. 9, pp. 2778–2789, Sept 2016.

[9] I. Held, O. Klein, A. Chen, and V. Ma, "Low complexity digital iq imbalance correction in ofdm wlan receivers," in *59th IEEE Vehicular Technology Conference. VTC 2004-Spring*, vol. 2, May 2004, pp. 1172–1176 Vol.2.

# 8. Experimental evaluation of digital predistortion with FBMC and OFDM signals

**Abstract**

In this paper we would like to point out one open issue related with filtered bank multi-carrier signals (FBMC). The experiment was trying to give an answer whether the FBMC signals would keep their beneficial properties even whilst real non-linear power amplifiers were employed. As one of the merits that have been used were error vector magnitude (EVM) and adjacent channel power (ACP). Due to higher sensitivity to angle rotations the digital predistortion have been employed in order to evaluate the importance of linearization.

## 8.1 Introduction

In the vision of future radio systems where the amount of transfered data rises, the demands for more efficient technologies arises. In today communication systems orthogonal frequency division multiplexing signals (OFDM) with cyclic prefix are widely used [1]. It was proved that using multi-carrier modulations (MCM) is an efficient way of transmission [2] and has better resistance to multi-path channels than single carrier modulations. The key technologies that have been lately discussed for the future 5G networks are: non-orthogonal multiple access, millimeter frequencies, 3D massive MIMO, cognitive spectrum radio sensing, ultra wideband signals, ultra dense networks (UDN) with heterogeneous cells (HetNet), multiple technology carrier aggregation and filtered bank multi-carrier (FBMC) signals [3], [4].

It was demonstrated that FBMC/OQAM signals are more sensitive to phase rotations than OFDM ones [5]. It was also shown in [5] that the intrinsic interference in FBMC/OQAM will increase the error probability. But in the case of perfect phase correction the FBMC signal the performance is similar as OFDM [6]. Therefore the natural step is to try to use digital predistortion techniques for mitigating the non-linearity and memory effects introduced by power amplifiers (PA). Consequently comparison with OFDM adopted in 4G systems is from authors point of view a great interest.

## 8.2 Brief description of FBMC/OQAM

Due to properties of prototype filter in the FBMC systems, offset quadrature amplitude modulation (OQAM) is used. Offset means the in-phase and quadrature components are time staggered by half of symbol period. According to the above definition and as presented in [7] and [8] the baseband model of FBMC/OQAM transmitter can be written

$$x[t] = \sum_{m=-\infty}^{+\infty} \sum_{k=0}^{N-1} (\theta^k \Re\{X_k[m]\} h[t - m\ N] +$$

$$\theta^{k+1} \Im\{X_k[m]\} h[t - m\ N - \frac{N}{2}]) \ e^{j\frac{2\pi}{N} k(t-mN)} \tag{8.1}$$

where $X_k$ is a modulation part of a symbol, $\theta^{k+1}$ is real part phase rotation vector for the imaginary part $\theta^k$ respectively, $h[.]$ is general prototype filter for each sub-carrier with impulse response length $L = KN$ with $K$ so-called overlapping factor and $N$ number of sub-carriers.

There exists several approaches implementing FBMC modulator/demodulator such as NK-IFFTs operating in parallel, two N-IFFTs and polyphase filtering and with lower complexity single N-FFT and polyphase filtering [7]. The last mentioned method was implemented in this paper. The principle of computing the discrete inverse Fourier transform of two real functions simultaneously is used [7]. Such approach is beneficial because then the concept can be easily reconfigured as OFDM transmitter.

According to [8] the input signal of IFFT can be expressed as $\Re\{X_k[m]\}\theta^k + j\Im\{X_k[m]\}\theta^k$ where multiplication with a vector $\theta^k = e^{j\frac{2\pi}{4} k}$ in frequency domain induce circular shift of $\frac{N}{4}$ in the time domain. The principle is commonly named as folding scheme [1].

## 8.3 Digital predistortion

In order to fulfill the increasing demands of higher data rates, higher energy efficiency of power amplifiers, and better spectral efficiency, the digital predistortion system (DPD) can be used. Unfortunately a drawback of higher efficiency needs is that the PAs are operating in non-linear regime. Non-linearities of PAs usually introduces unwanted signal properties such as compression, memory effects, spectrum regrowth in adjacent channels and intermodulation products.

One of the possible technique for dealing with nonlinearities is usage of digital predistorion (DPD). Usually the predistorter is inserted between power amplifier and transmitter. The digital predistorter monitors output of a PA. The feedback path is usually used for calculation of DPD coefficients [9].

The predistortion principles have been introduced many times, but so far no general rule for choice of proper DPD have not been yet presented.

Demonstrating the DPD and overcoming the complexity of the general Volterra series, an effective model pruning method, called dynamic deviation reduction (DDR) [10, 11,

12] was used. A simplified version of the model is defined by

$$
\begin{aligned}
z(t) = \quad & \sum_{k=0}^{\frac{K-1}{2}} \sum_{i=0}^{M} g_{2k+1,1}(i) \, |x(t)|^{2k} x(t-i) \\
+ \; & \sum_{k=1}^{\frac{K-1}{2}} \sum_{i=1}^{M} g_{2k+1,2}(i) \, |x(t)|^{2(k-1)} x^2(t) x^*(t-i) \\
+ \; & \sum_{k=1}^{\frac{K-1}{2}} \sum_{i=1}^{M} g_{2k+1,3}(i)|x(t)|^{2(k-1)} \, x(t)|x(t-i)|^2 \\
+ \; & \sum_{k=1}^{\frac{K-1}{2}} \sum_{i=1}^{M} g_{2k+1,4}(i)|x(t)|^{2(k-1)} \, x^*(t)x^2(t-i).
\end{aligned}
$$

$$(8.2)$$

where $x(n)$ and $z(n)$ are the complex envelopes of the input and output of the PA, respectively, and $g_{2k+1,j}$ is the complex Volterra kernel of the system.

For the calculation, explanation of principles and closer information the readers could be referred to [11].

## 8.4 Experimental evaluation

In order to prove the concept, the experimental test-bench was assembled. The signal-processing and additional post-processing has been done with Matlab that was communicating with Rohde&Schwarz generator SMU200A and with real-time spectrum analyzer Rohde&Schwarz FSVR. The generator was synchronized with analyzer using 10 MHz reference signal and the beginning of test sequence was triggering the acquisition with signal marker. Then in PC additional processing have been done (such as integer synchronization based on correlation, fractional synchronization based on Farrow filters, etc.). The generated FBMC signal had 1024 sub-carriers and prototype filter of fourth order was used [13]. The total generated data sequence had 16384 samples. For the OFDM signal, the same initial data with similar setup but rectangular filter was used. The signal had oversampling ratio 4, sampling frequency $f_s = 20 \; MHz$, with carrier frequency $f_c = 1 \; GHz$, and with inner OQAM modulation level $M = 4$. Therefore the total bandwidth of transmitted signals was $BW = 5 \; MHz$. The equipment with high dynamical ranges and low noise figures had to be threated very carefully for taking advantage of FBMC properties.

Keeping higher accuracy of the measurements, each point od results was repeated 10 times and then the mean value was used. Also for credibility of the results three different PAs have been used. The are denoted as: Tesla 1, Mini Circuits, Tesla 2 with AM/AM and AM/PM characteristics given if Fig.13.4. We may see that the presented PAs have different non-linear characteristics with different memory effects. For testing the nonlinear order of DPD was chosen as $K = 13$ and memory depth of $M = 1$.

We have been measuring ACP (Fig.14.2) at the output of PA with offset of 5.1 $MHz$
and bandwidth of (5 MHz). The EVM Fig.8.3 after demodulation of all sub-carriers
(without quantification) is also evaluated.   From the results presented in Fig.14.2 and
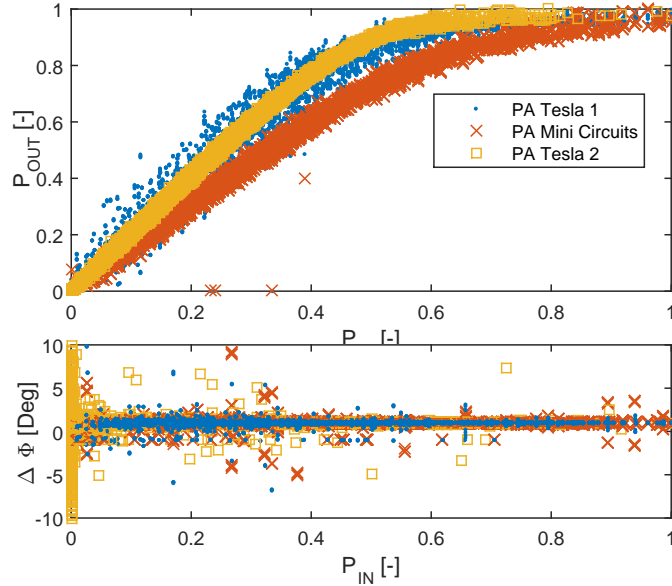


Figure 8.1: Normalized AM/AM characteristics (Top) of three different PAs and corre-
sponding AM/PM characteristics (Bottom).
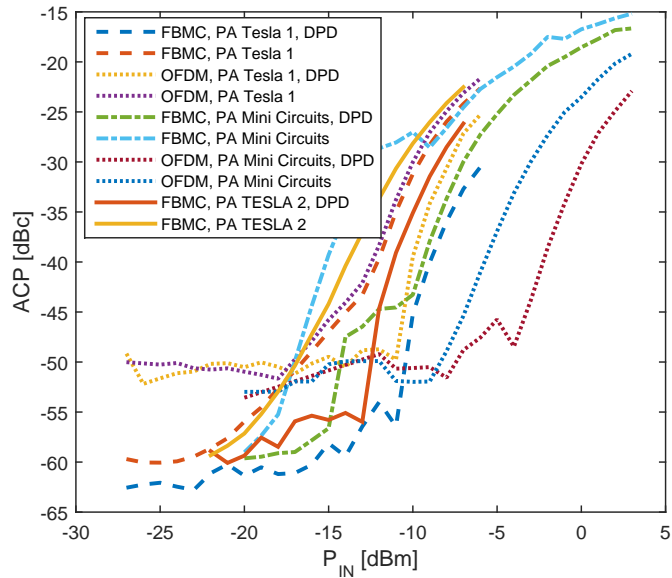


Figure 8.2: The experimentally measured ACP of FBMC and OFDM for three different
PAs depending on the input power $P_{IN}$.

Fig.8.3 we may observe that the FBMC signals have in general 10 dB lower ACP, but as
presented in Fig.8.3 the FBMC signals tend to be more sensitive to non-linear distortions
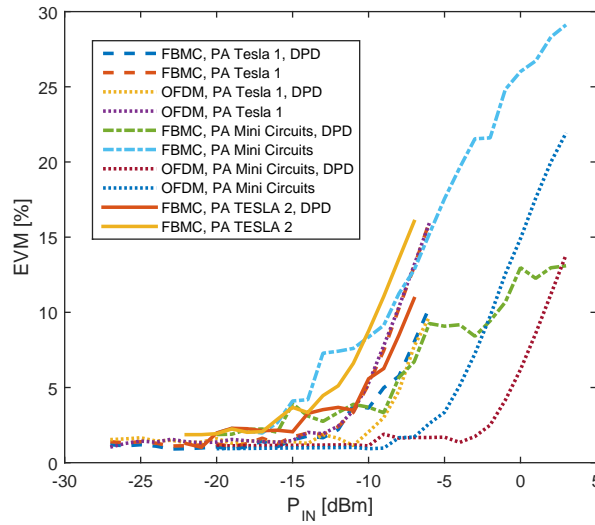
Figure 8.3: The experimentally measured EVM before quantification depending on the input power $P_{IN}$.

than OFDM. Further the figures also demonstrates the necessary need for using DPD. The power spectrum densities can be seen in the Fig.9.6, where the green trace represents FBMC signal without DPD, black signal is FBMC signal with DPD and blue curve is OFDM signal without DPD.



Figure 8.4: The power spectrum density where green trace represents FBMC signal without DPD, black signal is FBMC signal with DPD and blue curve is OFDM signal without DPD. The signals were obtained at the output of PA denoted as Mini Circuits with input power $P_{IN} = -14dBm$.

## 8.5 Conclusion

The FBMC signals are resolutely candidates for future 5G systems. In this brief paper experimental study and comparison of FBMC and OFDM signals distorted by real non-linear power amplifiers have been tested. In order to guarantee higher accuracy of presented results three power amplifiers have been used. In this paper we have experimentally proved that using FBMC signals, lower ACP can be achieved, however lower resistance than OFDM signals to non-linear distortions must be taken into the account. Using DPD systems the immunity of FBMC can be boosted for the undoubted cost of higher complexity. The results indicates, that FBMC modulation can achieve in general better ACP then OFDM signals. The EVM figures shows, that the DPDs can improve the error rate. We tried to prove that the DPD is even more important for FBMC than for OFDM signals.

## 8.6 Bibliography

[1] H. Zhang, D. Le Ruyet, and M. Terre, "Spectral efficiency comparison between ofdm-oqam- and ofdm-based cr networks," *Wirel. Commun. Mob. Comput.*, vol. 9, no. 11, pp. 1487–1501, Nov. 2009. [Online]. Available: http://dx.doi.org/10.1002/wcm.v9:11

[2] J.-B. Dore, V. Berg, N. Cassiau, and D. Ktenas, "Fbmc receiver for multi-user asynchronous transmission on fragmented spectrum," *EURASIP Journal on Advances in Signal Processing*, vol. 2014, no. 1, p. 41, 2014. [Online]. Available: http://asp.eurasipjournals.com/content/2014/1/41

[3] H. Lin and P. Siohan, "Multi-carrier modulation analysis and wcp-coqam proposal," *EURASIP Journal on Advances in Signal Processing*, vol. 2014, no. 1, 2014. [Online]. Available: http://dx.doi.org/10.1186/1687-6180-2014-79

[4] J. Nadal, C. Abdel Nour, A. Baghdadi, and H. Lin, "Hardware prototyping of FBMC/OQAM baseband for 5G mobile communication systems," in *RSP 2014 : IEEE International Symposium on Rapid System Prototyping*, 2014, pp. 135 – 141.

[5] H. Bouhadda, H. Shaiek, D. Roviras, R. Zayani, Y. Medjahdi, and R. Bouallegue, "Theoretical analysis of ber performance of nonlinearly amplified fbmc/oqam and ofdm signals," *EURASIP Journal on Advances in Signal Processing*, vol. 2014, no. 1, p. 60, 2014. [Online]. Available: http://asp.eurasipjournals.com/content/2014/1/60

[6] Y. Medjahdi, M. Terre, D. Le Ruyet, D. Roviras, and A. Dziri, "Performance analysis in the downlink of asynchronous ofdm/fbmc based multi-cellular networks," *Wireless Communications, IEEE Transactions on*, vol. 10, no. 8, pp. 2630–2639, August 2011.

[7] L. Varga and Z. Kollar, "Low complexity fbmc transceiver for fpga implementation," in *Radioelektronika (RADIOELEKTRONIKA), 2013 23rd International Conference*, April 2013, pp. 219–223.

[8]   Z. Kollár and P. Horváth, "Papr reduction of fbmc by clipping and its iterative compensation," *Journal of Computer Networks and Communications*, vol. 2012, 2012.

[9]   J. K. Cavers, "Amplifier linearization using a digital predistorter with fast adaptation and low memory requirements," *Vehicular Technology, IEEE Transactions on*, vol. 39, no. 4, pp. 374–382, 1990.

[10]   Z. Anding, J. C. Pedro, and T. J. Brazil, "Dynamic deviation reduction-based volterra behavioral modeling of rf power amplifiers," *Microwave Theory and Techniques, IEEE Transactions on*, vol. 54, no. 12, pp. 4323–4332, 2006.

[11]   T. Gotthans, G. Baudoin, and A. Mbaye, "Comparison of modeling techniques for power amplifiers," in *Radioelektronika (RADIOELEKTRONIKA), 2013 23rd International Conference*, 2013, pp. 232–235.

[12]   Z. Anding, P. Draxler, J. Yan, T. Brazil, D. Kimball, and P. Asbeck, "Open-loop digital predistorter for rf power amplifiers using dynamic deviation reduction-based volterra series," *Microwave Theory and Techniques, IEEE Transactions on*, vol. 56, no. 7, pp. 1524–1534, 2008.

[13]   T. Ihalainen, A. Viholainen, T. Stitz, and M. Renfors, "Generation of filter bank-based multicarrier waveform using partial synthesis and time domain interpolation," *Circuits and Systems I: Regular Papers, IEEE Transactions on*, vol. 57, no. 7, pp. 1767–1778, July 2010.

# 9. FBMC Filter Bank Optimization for Non-linear Power Amplifiers

**Abstract**

In this paper we would like to point out one open issue related with filtered
bank multi-carrier signals (FBMC). The experiment was trying to calculate filter
coefficients for FBMC signals where non-linear power amplifiers were employed. As
one of the merits that have been used were error vector magnitude (EVM) and
adjacent channel power (ACP). We have demonstrated that proper calculation of
coefficients could improve the merits significantly.

## 9.1 Introduction

The future radio systems where the number of transfered data rises, the demands for
more efficient technologies also arises. In today communication systems orthogonal fre-
quency division multiplexing signals (OFDM) with cyclic prefix are widely used [1]. The
multi-carrier modulations (MCM) is an efficient way of transmission, that was proved in
[2] and it was also shown that MCM has better resistance to multi-path channels than
single carrier modulations.

Technologies that have been lately examined for the future 5G networks are: non-
orthogonal multiple access, millimeter frequencies, 3D massive MIMO, cognitive spec-
trum radio sensing, ultra wide-band signals, ultra dense networks (UDN) with hetero-
geneous cells (HetNet), multiple technology carrier aggregation and filtered bank multi-
carrier (FBMC) signals [3], [4].

It was shown that FBMC/OQAM signals are more sensitive to phase rotations than
OFDM ones [5]. In the case of perfect phase correction the FBMC signal the performance
could be similar as OFDM [6].

The natural step is to try to optimize the filter coefficients for mitigating the non-
linearity and memory effects introduced by power amplifiers (PA).

## 9.2 Brief description of FBMC/OQAM

Due to properties of prototype filter in the FBMC systems, offset quadrature amplitude
modulation (OQAM) is used. Offset means the in-phase and quadrature components

are time staggered by half of symbol period. According to the above definition and as presented in [7] and [8] the baseband model of FBMC/OQAM transmitter can be written

$$x[t] = \sum_{m=-\infty}^{+\infty} \sum_{k=0}^{N-1} (\theta^k \Re\{X_k[m]\}h[t-m\ N] +$$

$$\theta^{k+1}\Im\{X_k[m]\}h[t-m\ N - \frac{N}{2}])\ e^{j\frac{2\pi}{N}k(t-mN)} \tag{9.1}$$

where $X_k$ is a modulation part of a symbol, $\theta^{k+1}$ is real part phase rotation vector for the imaginary part $\theta^k$ respectively, $h[.]$ is general prototype filter for each sub-carrier with impulse response length $L = KN$ with $K$ so-called overlapping factor and $N$ number of sub-carriers. The filter impulse response of fourth order overlap (taken from the PHYDAS [9]) can be written as:

$$h(1+i) = 1 \quad - \quad 2H_1\cos(\frac{\pi i}{2N}) + 2H_2\cos(\frac{\pi i}{N})$$

$$- \quad 2H_3\cos(\frac{3\pi i}{2N}), \tag{9.2}$$

where filter coefficients are $H_1 = 0.972$, $H_2 = \frac{\sqrt{(2)}}{2}$ and $H_3 = 0.235$.

There exists several approaches implementing FBMC modulator/demodulator such as NK-IFFTs operating in parallel, two N-IFFTs and polyphase filtering and with lower complexity single N-FFT and polyphase filtering [7]. The last mentioned method was implemented in this paper. The principle of computing the discrete inverse Fourier transform of two real functions simultaneously is used [7]. Such approach is beneficial because then the concept can be easily reconfigured as OFDM transmitter. According to [8] the input signal of IFFT can be expressed as $\Re\{X_k[m]\}\theta^k + j\Im\{X_k[m]\}\theta^k$ where multiplication with a vector $\theta^k = e^{j\frac{2\pi}{4}k}$ in frequency domain induce circular shift of $\frac{N}{4}$ in the time domain. The principle is commonly named as folding scheme [1]. The general difference between OFDM and FBMC is more obvious from Fig13.1.

## 9.3 Problem statement

It was already experimentally proved [10], that FBMC modulator in the link with real non-linear power amplifier will not keep it's beneficial properties. Due to non-linear effects (such as amplitude and phase distortions), the modulator decrease in performance. As we will further demonstrate, the build-in filter in FBMC can be used to compensate some phenomenas.

## 9.4 Power Amplifier Model

In order to provide relevant results, the model was derived from designed power amplifier with the ADL5610. It is a single-ended RF/IF gain block amplifier, that provides broadband operation from 30 MHz to 6 GHz. The ADL5610 provides a low noise figure of 2.2 dB with a very high OIP3 (at 900 MHz) of more than 38 dBm simultaneously,

**OFDM baseband signal processing blocks**



**FBMC baseband signal processing blocks**
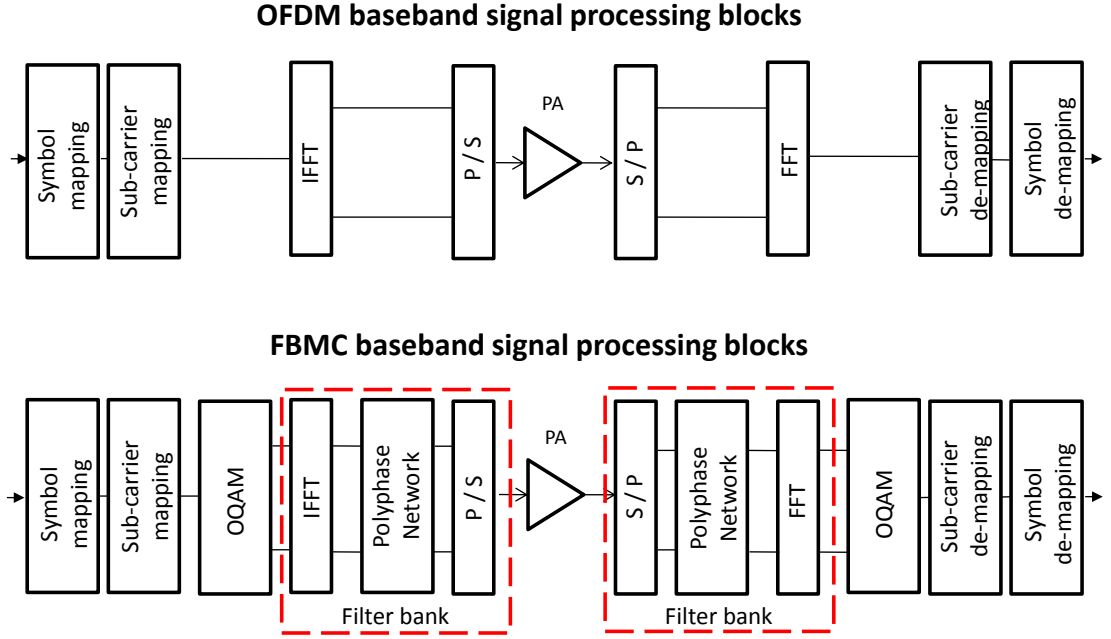


Figure 9.1: General difference between Orthogonal frequency division multiplexing signals (OFDM) with cyclic prefix (Top) and Filter Bank based Multicarrier (FBMC) transmitter (Bottom).

which delivers a high dynamic range. The one-dB compression point is 20.4 dBm at 900 MHz.

First the power amplifier was measured using FBMC signal and then was modeled with orthogonal polynomial memory series expressed as: [11]

$$
\begin{aligned}
y(t) \quad = \quad & \sum_{k=1}^{K} \sum_{m=0}^{M} b_{k,m} \sum_{l=1}^{k} (-1)^{l+k} \cdot \\
& \cdot \frac{(k+l)!}{(l-1)!(l+1)!(k-l)!} |x(t-m)|^{k-1} x(t-m),
\end{aligned}
$$

(9.3)

where $K$ is polynomial order, $M$ is memory depth, $y$ is the output of PA and $x$ is the input. The coefficients $b_{k,m}$ were estimated using least-squares criterion.

## 9.5    A multi-criteria genetic algorithm

The genetic algorithms are well known, therefore further description is intensionally skipped. The process starts by building a population, with individuals (solutions). The populations of next generations are obtained through the application of mutation, selection and crossover operators.
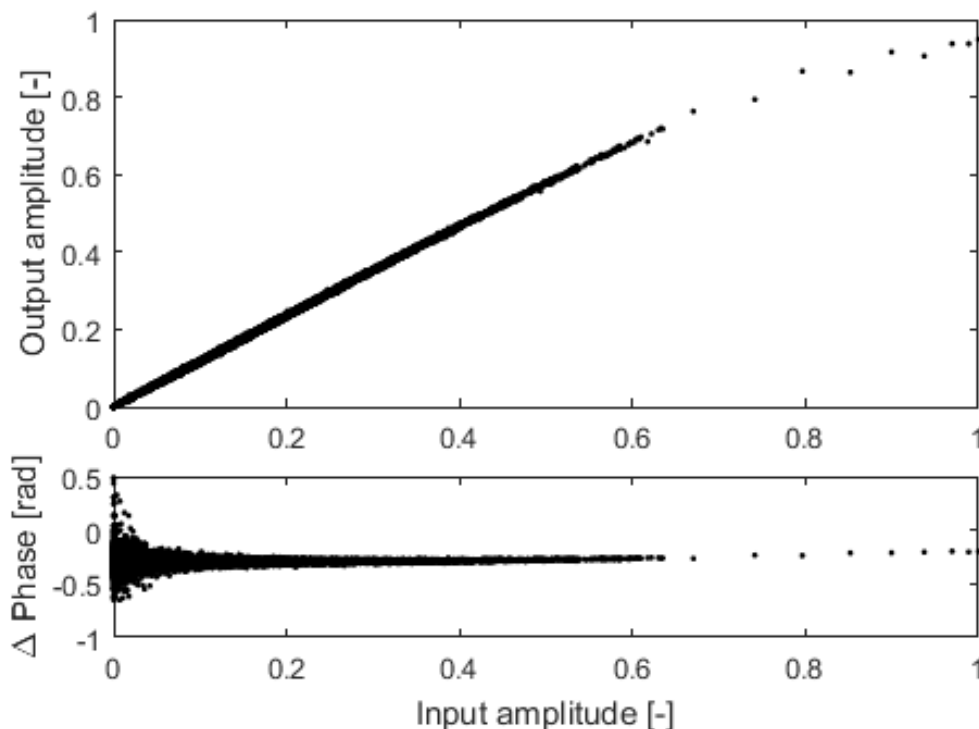
Figure 9.2: AM/AM charracteristics of measured power amplifier (top) and corresponding AM/PM characteristics.

For a nontrivial multi-objective optimization problem, there does not exist a single solution that simultaneously optimizes each objective. In that case, the objective functions are said to be conflicting, and there exists a (possibly infinite) number of Pareto optimal solutions. Pareto optimal solutions are considered equally good, therefore choice based on estimation trade-offs has to be chosen.

The crucial parameters have been chosen as a merits of proper modulator- power amplifier - demodulator link. As the criteria function, the EVM and ACPR (left) was chosen.

## 9.6 Results

The results have been obtained only through numerical system simulations. Yet we may expect the correspondence with measurements. In the Fig.9.3 we may see the Pareto plot with compromise between two criteria. The results have been obtained with genetic algorithm (build in procedure in Matlab) with population size (200). As we may see in Fig.9.4 and Fig.9.5, the filter function changes the distribution of symbols.

From the Fig.9.6 we may see, that the optimized filter inside FBMC modulator perform better in terms of adjacent channel power ($ACPR_L = -48dB$). The associated EVM was 0.31%.
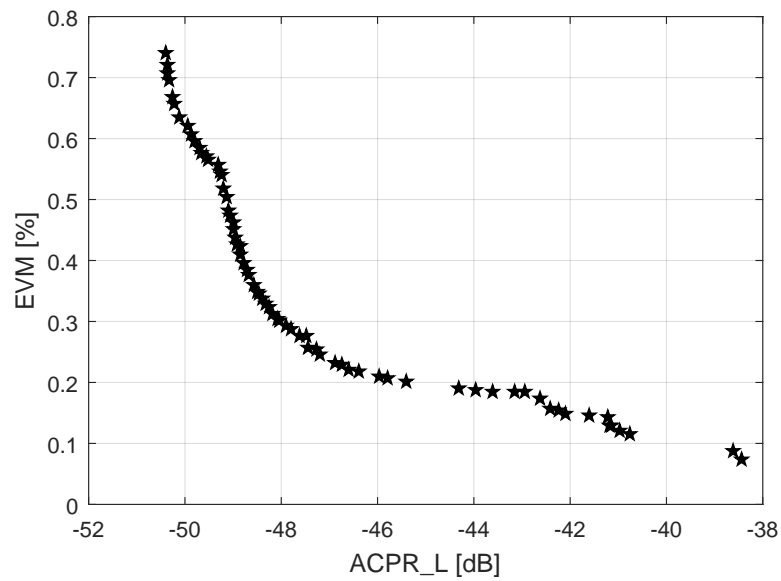
Figure 9.3: The pareto plot of two citeria: EVM [%] and $ACPR_L$ [dB].
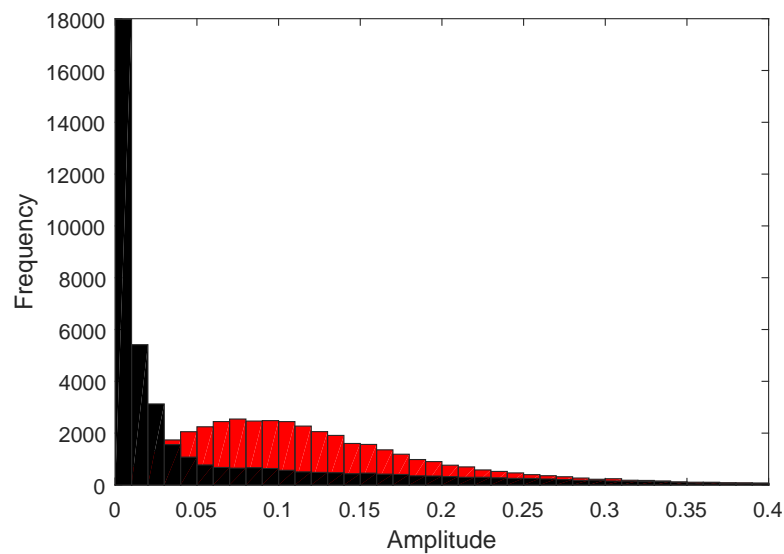


Figure 9.4: Histogram for input amplitude of PA fist standard filter design (black) and with optimized filter (red).

Using the optimization for our particular case the filter coefficients have been estimated as follows: $H_1 = -0.14819$, $H_2 = 0.14854$ and $H_3 = -0.13068$. The comparison of standard filter (PHYDAS) and optimized can be seen in the impulse response (Fig.9.7).
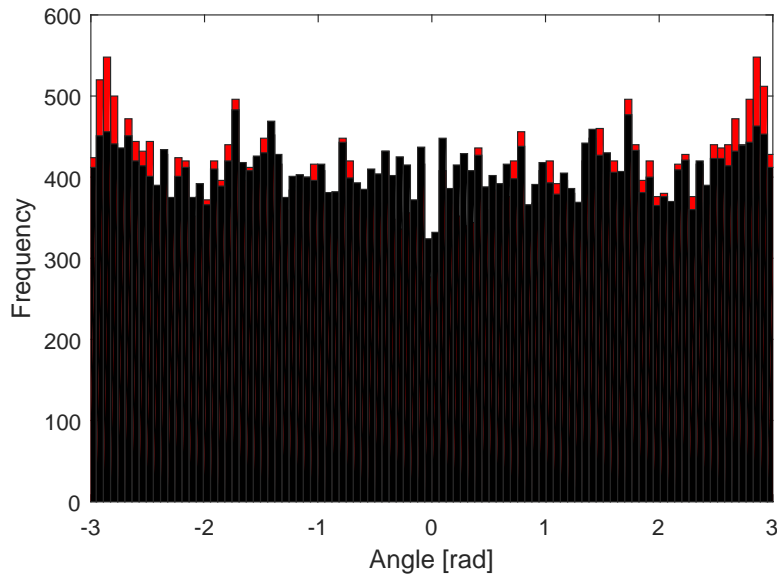
Figure 9.5: Histogram for input phase of PA fist standard filter design (black) and with optimized filter (red).
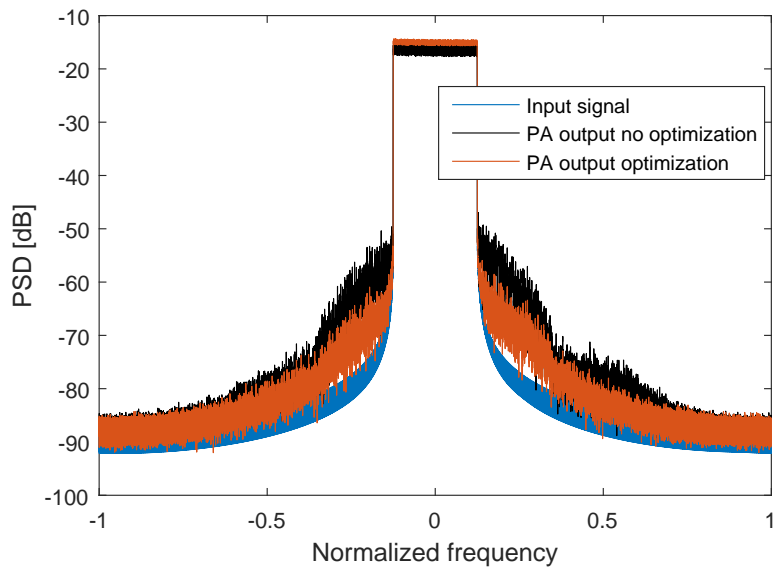


Figure 9.6: Power spectral density of FBMC for input signal (blue), output signal (black) and output signal with optimized filter(red).

## 9.7 Conclusion

The FBMC signals are resolutely candidates for future 5G systems. In this paper we have demonstrated, that proper optimization of filter inside FBMC modulator can improve the performance in the case of link with non-linear power amplifier.

We have demonstrated that proper calculation of coefficients could improve the merits
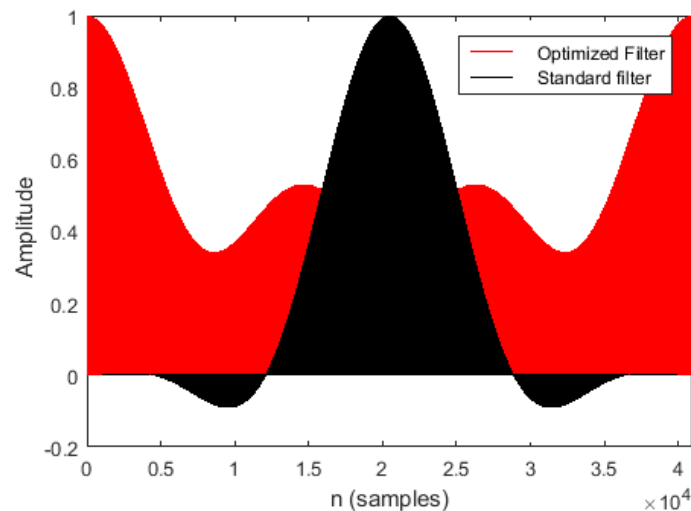
Figure 9.7: Impulse response of standard filter(black) and optimized (red).

significantly. As the results show, the filter optimization does not compensate non-linear effects or memory effects (as in the case of digital predistortion). The filter changes a distribution of symbols on order to compensate distortions.

Results have been obtained through numerical system simulations only. Yet we may expect the correspondence with measurements. If the readers have any further questions, please do not hesitate to contact the authors.

## 9.8 Bibliography

[1] H. Zhang, D. Le Ruyet, and M. Terre, "Spectral efficiency comparison between ofdm-oqam- and ofdm-based cr networks," *Wirel. Commun. Mob. Comput.*, vol. 9, no. 11, pp. 1487–1501, Nov. 2009. [Online]. Available: http://dx.doi.org/10.1002/wcm.v9:11

[2] J.-B. Dore, V. Berg, N. Cassiau, and D. Ktenas, "Fbmc receiver for multi-user asynchronous transmission on fragmented spectrum," *EURASIP Journal on Advances in Signal Processing*, vol. 2014, no. 1, p. 41, 2014. [Online]. Available: http://asp.eurasipjournals.com/content/2014/1/41

[3] H. Lin and P. Siohan, "Multi-carrier modulation analysis and wcp-coqam proposal," *EURASIP Journal on Advances in Signal Processing*, vol. 2014, no. 1, 2014. [Online]. Available: http://dx.doi.org/10.1186/1687-6180-2014-79

[4] J. Nadal, C. Abdel Nour, A. Baghdadi, and H. Lin, "Hardware prototyping of FBMC/OQAM baseband for 5G mobile communication systems," in *RSP 2014 : IEEE International Symposium on Rapid System Prototyping*, 2014, pp. 135 – 141.

[5] H. Bouhadda, H. Shaiek, D. Roviras, R. Zayani, Y. Medjahdi, and R. Bouallegue, "Theoretical analysis of ber performance of nonlinearly amplified fbmc/oqam and

ofdm signals," *EURASIP Journal on Advances in Signal Processing*, vol. 2014, no. 1, p. 60, 2014. [Online]. Available: http://asp.eurasipjournals.com/content/2014/1/60

[6]  Y. Medjahdi, M. Terre, D. Le Ruyet, D. Roviras, and A. Dziri, "Performance analysis in the downlink of asynchronous ofdm/fbmc based multi-cellular networks," *Wireless Communications, IEEE Transactions on*, vol. 10, no. 8, pp. 2630–2639, August 2011.

[7]  L. Varga and Z. Kollar, "Low complexity fbmc transceiver for fpga implementation," in *Radioelektronika (RADIOELEKTRONIKA), 2013 23rd International Conference*, April 2013, pp. 219–223.

[8]  Z. Kollár and P. Horváth, "Papr reduction of fbmc by clipping and its iterative compensation," *Journal of Computer Networks and Communications*, vol. 2012, 2012.

[9]  T. Ihalainen, A. Viholainen, T. Stitz, and M. Renfors, "Generation of filter bank-based multicarrier waveform using partial synthesis and time domain interpolation," *Circuits and Systems I: Regular Papers, IEEE Transactions on*, vol. 57, no. 7, pp. 1767–1778, July 2010.

[10]  T. Gotthans, R. Marsalek, J. Blumenstein, and G. Baudoin, "Experimental evaluation of digital predistortion with fbmc and ofdm signals," in *Wireless and Microwave Technology Conference (WAMICON), 2015 IEEE 16th Annual*, April 2015, pp. 1–3.

[11]  T. Gotthans, G. Baudoin, and A. Mbaye, "Comparison of modeling techniques for power amplifiers," in *Radioelektronika (RADIOELEKTRONIKA), 2013 23rd International Conference*, 2013, pp. 232–235.

# 10. Analytical Method of Fractional Sample Period Synchronisation for Digital Predistortion Systems

**Abstract**

As the data throughput is still increased in the wireless communication systems, it is required to efficiently utilise the radio frequency spectrum which usually requires linear transmitters. Consequently methods as a digital predistortion (DPD) are developed to linearise nonlinear power amplifiers. To extract precise parameters for the DPD it is essential to finely synchronise measured feedback signal with the known transmitted signal. In this paper we propose an analytical method for the fractional sample period time synchronisation suitable for DPD signals. Finally benefits of the proposed method are presented on results of its usage for the DPD linearisation using a measurement test-bed.

## 10.1 Introduction

As wireless communication systems develop higher demand is placed on data throughput and spectral and power efficiency. The higher data throughput and spectral efficiency is usually achieved using spectrally efficient modulations. The most of these modulations require usage of linear power amplifiers (PAs). These PAs are in principle low power efficient and in opposite high power efficient PAs are nonlinear. A technique solving this contradiction in modern communication systems is usage of a high power efficient nonlinear PA together with a digital predistorter (DPD). The DPD linearises characteristics of the nonlinear transmitter while preserving high power and spectral efficiency.

The typical implementation of the DPD is depicted by its baseband model in Fig. 11.1. The transmitter input and output signals are sampled, aligned, and processed to extract the DPD parameters that would be used to predistort the source signal before transmission to counteract the transmitter nonlinearities. However, the alignment accuracy in DPD is limited by nonideal electronic components and the associated circuitry which introduces unknown loop delay mismatch and thus degrades the overall linearisation performance as shown in Fig. 10.2 and in [1]. This paper analyses the influence of the accuracy of the timing of these signals on the performance of the predistorter. It considers the case of an integer and a fractional delay (less than the sampling period). It is shown that for a predistorter without memory, even very small fractional offset degrades

performance significantly. The theoretical analysis by Liu [2] reveals that performance degradation caused by the loop delay mismatch increases as well with the bandwidth of the orthogonal frequency-division multiplexing (OFDM) signal.
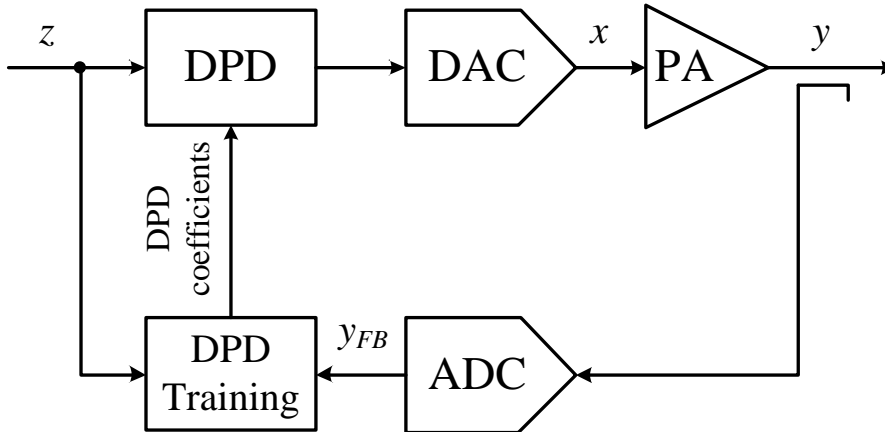


Figure 10.1: Baseband model of the digital predistorter

As a consequence of the delay mismatch degradation, a precise time synchronisation method is required for the DPD implementation. Time synchronisation and recovery have been already widely explored in the communication theory. An algorithm for symbol timing recovery using baud-rate sampling is described in [3]. Later Armstrong and Strickland presented an algorithm [4] to find a suitable strobe point and calculate signal values between the sample points by the interpolation. The Maximum-likelihood estimation theory also provides a general framework for developing near-optimum synchronisation schemes [5]. A synchronisation concept shown in [6] is based on a low-order polynomial approximation of the likelihood functions using the Farrow-based interpolator. Fu and Willson in [7], instead of approximating a continuous-time signal with a conventional (algebraic) polynomial and computing the synchronised samples using a Farrow structure, employed trigonometric polynomials.

In paper [8] there are presented two methods for signal alignment in a DPD system. A frequency multiplication method was used for the coarse alignment and subsequently the parabolic curve fitting method for the fine alignment.

In this paper we propose an analytical method for the fractional delay signal synchronisation and present results of its application in a DPD system. In the final section we provide experimental results of the proposed method.

## 10.2   Problem Observation

The described problem exists in all real systems. In coherent systems, where the clock signals in the feedback (FB) are exactly same as the clock signals in the direct path (DP), the clock phase skew can be well controlled by the design and is constant over time. The clock skew therein can be easily compensated. A different situation arises in incoherent systems where the clocks are not the same. It is to be noted that systems with clocks derived from a reference system clock by different phase-locked loops (PLLs) are
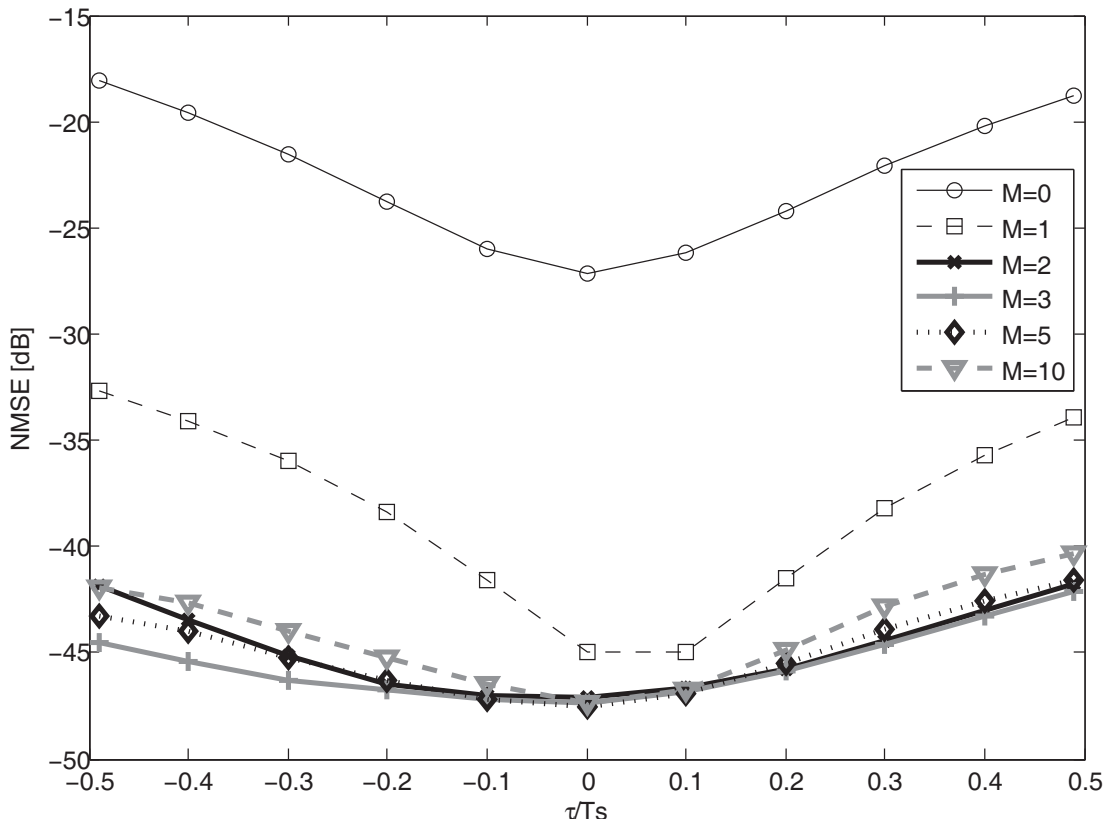
Figure 10.2: Effect of fractional delay for different memory length on normlised mean square error (NMSE) of the DPD with PA modelled by orthogonal polynomials with nonlinearity order $K = 7$ and the memory depth $M = 3$ [1]

considered as incoherent. A typical example of such system is an integrated transciever with separated PLLs in the transmitter and the receiver, or a measurement test-bed composed of a separated signal generator and an acquisition instrument. A simplified block diagram of such test-bed is depicted in Fig. 10.3.

The generator clock has phase skew with respect to the acquisition instrument clock. This skew is natural due to limited bandwidth of loop filters in PLLs and can vary over time. If the acquired length of the signal is relatively short with respect to the change of the clock phase skew, the phase skew can be assumed constant over the acquisition and appears as fractional sample time offset. Particularly we have observed this behaviour using high-end instruments from Rohde&Schwarz, the signal generator SMU 200A and the real-time spectrum analyser FSVR used for the acquisition. The clock phase skew spreads the amplitude-amplitude (AM/AM) characteristics as depicted in Fig. 10.4 and the amplitude-phase (AM/PM) characteristics as in Fig. 10.5. This spread can be easily misinterpreted as memory effect of the PA and it can be also partially compensated by a DPD with a memory as described in [1].
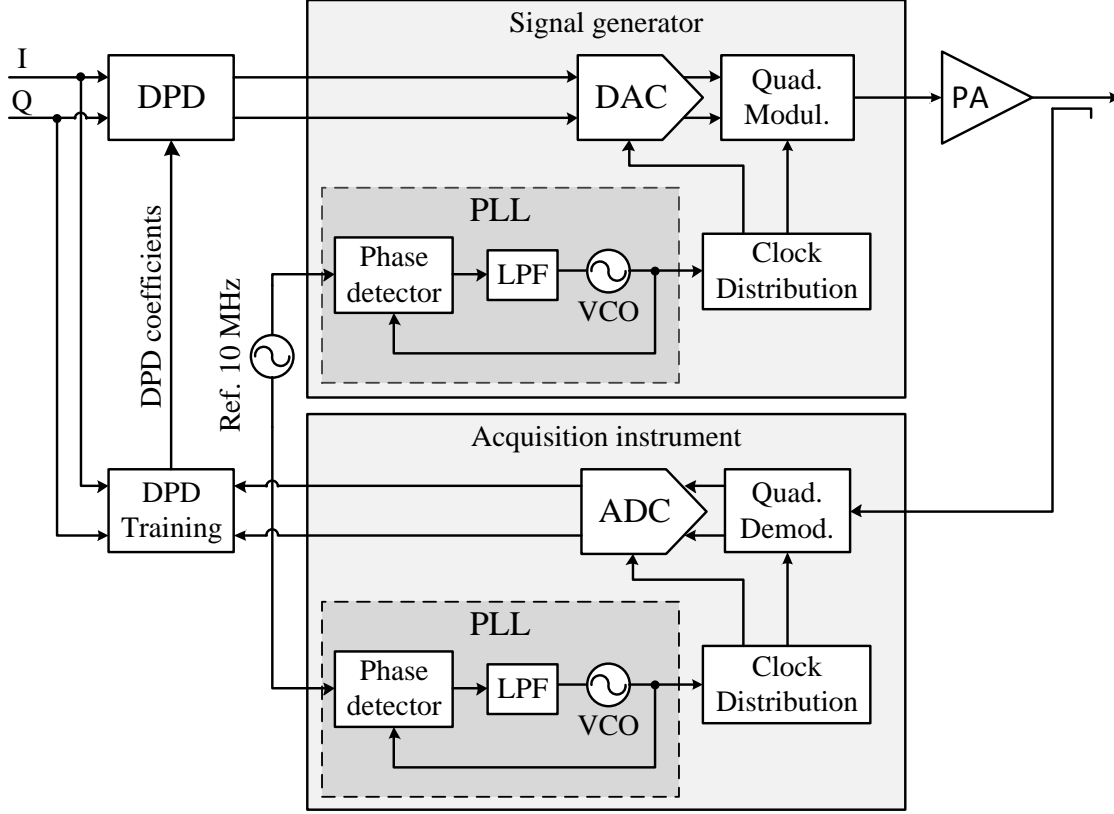
Figure 10.3: DPD test-bed with separated signal generator and acquisition instrument

## 10.3   Proposed Synchronisation Method

Let us assume that the PA is modelled by the polynomials and its baseband output $y(t)$ is given as

$$y(t) = \sum_{k=1}^{K} \sum_{q=0}^{Q} b_{k,q} x(t - qT_S) |x(t - qT_S)|^{k-1} \tag{10.1}$$

where $x(t)$ is the PA input signal, $T_S$ is the sampling period, $K$ and $Q$ represent the maximum PA nonlinear order and memory length respectively, and $b_{k,q}$ is a coefficient of the PA polynomial model. The obtained FB signal is

$$y_{FB}(t) = y(t - \tau) \tag{10.2}$$

where $\tau$ is a delay caused by the physical measurement setup and the clock skew of the instruments.

For these signals we define their Fourier transforms as

$$\mathcal{F}\{x(t)\} = X(j\omega) = |X(j\omega)|e^{j\varphi_x(\omega)} \tag{10.3}$$

and similarly $Y(j\omega)$ for $y(t)$ and $Y_{FB}(j\omega)$ for $y_{FB}(t)$. Based on Eq. 10.2 and the property of the Fourier transform it is possible to write

$$Y_{FB}(j\omega) = Y(j\omega)e^{-j\omega\tau}. \tag{10.4}$$
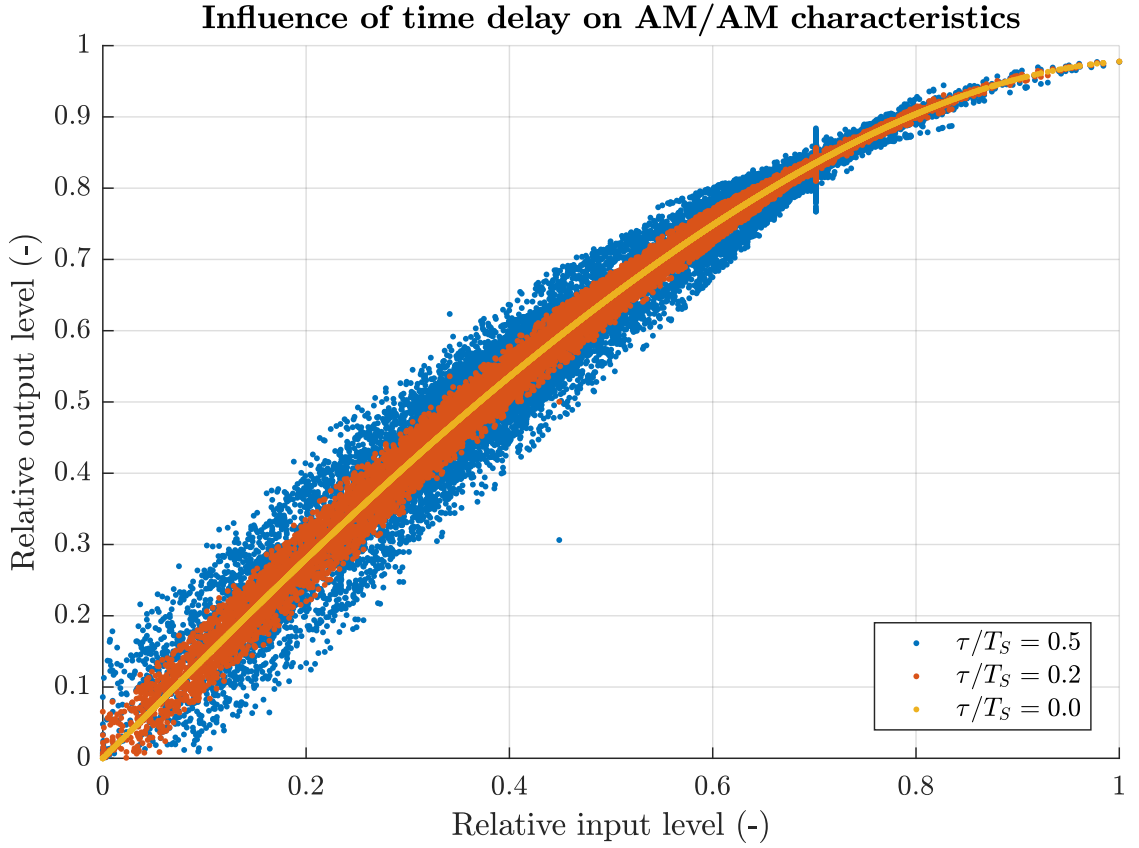
Figure 10.4: Influence of delay $\tau$ on AM/AM characteristics of PA using quadrature amplitude modulation (QAM) 16 signal with sampling period $T_S$

As the PA model (Eq. 10.1) contains only power of the magnitude, for $q = 0$ it preserves the phase of the original signal. If the memory effect of the PA is minimal and negligible, it can be shown using Eq. 10.4 that

$$\tau\omega = \varphi_x(\omega) - \varphi_{FB}(\omega). \tag{10.5}$$

For practical reasons the Eq. 10.5 is modified and the phase difference is taken from the interval $(-\pi, \pi\rangle$

$$\tau\omega = P(\varphi_x(\omega) - \varphi_{FB}(\omega)) \tag{10.6}$$

where $P(\cdot)$ is a function defined as

$$P(\varphi) = \begin{cases} \varphi \mod 2\pi, & \text{if } (\varphi \mod 2\pi) <= \pi \\ (\varphi \mod 2\pi) - 2\pi, & \text{otherwise.} \end{cases} \tag{10.7}$$

The left side of Eq. 10.6 represents a line going through the origin and with the direction $\tau$. For real signals, $\tau$ can be found using the method of least squares and for
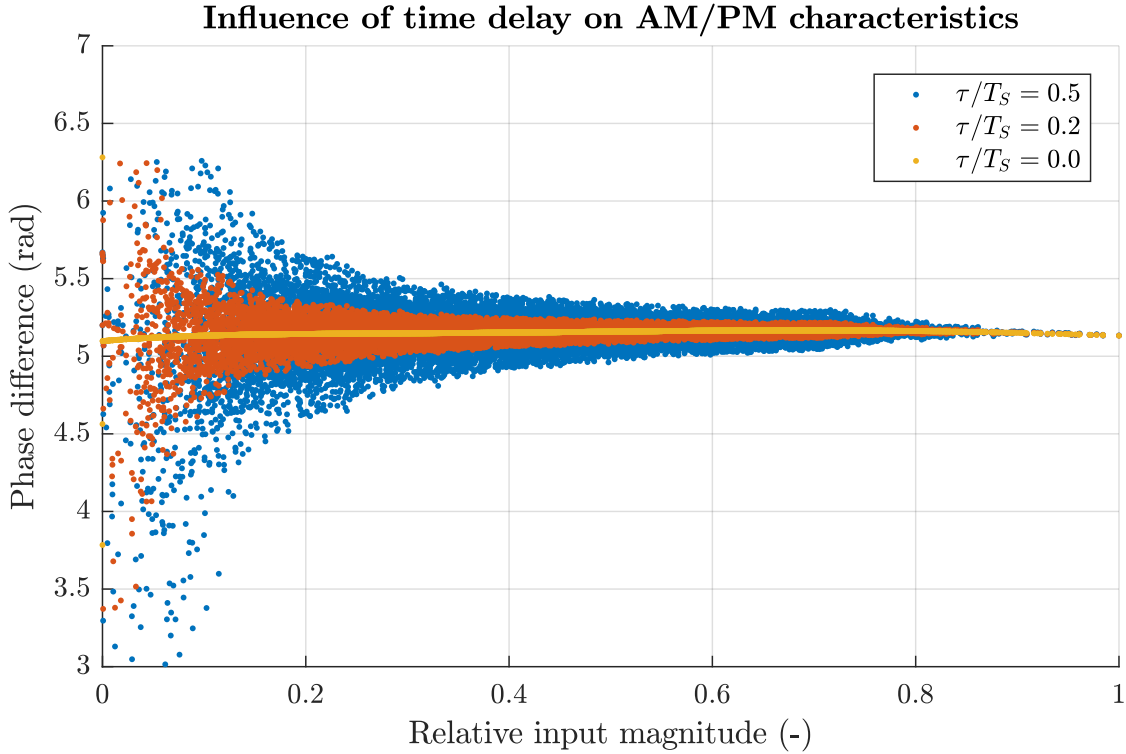
Figure 10.5: Influence of delay $\tau$ on AM/PM characteristics of PA using QAM16 signal with sampling period $T_S$

the discrete time signals is expressed as

$$\tau_0 = \frac{\sum\limits_{\omega_{min}}^{\omega_{max}} \omega P(\varphi_x(\omega) - \varphi_{FB}(\omega))}{\sum\limits_{\omega_{min}}^{\omega_{max}} \omega^2} \tag{10.8}$$

where $\omega_{min}$ and $\omega_{max}$ are lower and upper limits for least squares calculation. These limits should be set according to the frequency range of the signal $x(t)$. Eq. 10.8 expects $\tau \in \langle -T_S/2, T_S/2 \rangle$ which can be achieved by cross-correlation methods. The extension of the method for multiple $T_S$ is possible by unwrapping the phase difference.

When the time offset $\tau_0$ is obtained, the fractional sample time shift in spectrum domain is straightforward.

$$y(t) = \mathcal{F}^{-1}\{Y_{FB}(j\omega)e^{j\omega\tau_0}\} \tag{10.9}$$

The above describe approach does not change the shape of the AM/PM characteristics as Eq. 10.9 is not dependent on the magnitude of the input signal. It only improves the spread caused by the signal synchronisation offset. At the same time the method does not expect the IQ rotation of the signal phase which occurs due to the modulator and demodulator clock phase skew; therefore it is often convenient to determine $\tau_0$ for signal magnitudes instead of complex signals.

## 10.4 Experimental Results

The proposed method has been experimentally verified on our measurement test-bed shown in Fig. 10.6. The test-bed consists of the signal vector generator SMU 200A, real-time spectrum analyser FSVR, both from Rohde&Schwarz, and a radio-frequency power amplifier. The reference clock for both instruments is an internal oscillator of the signal generator.
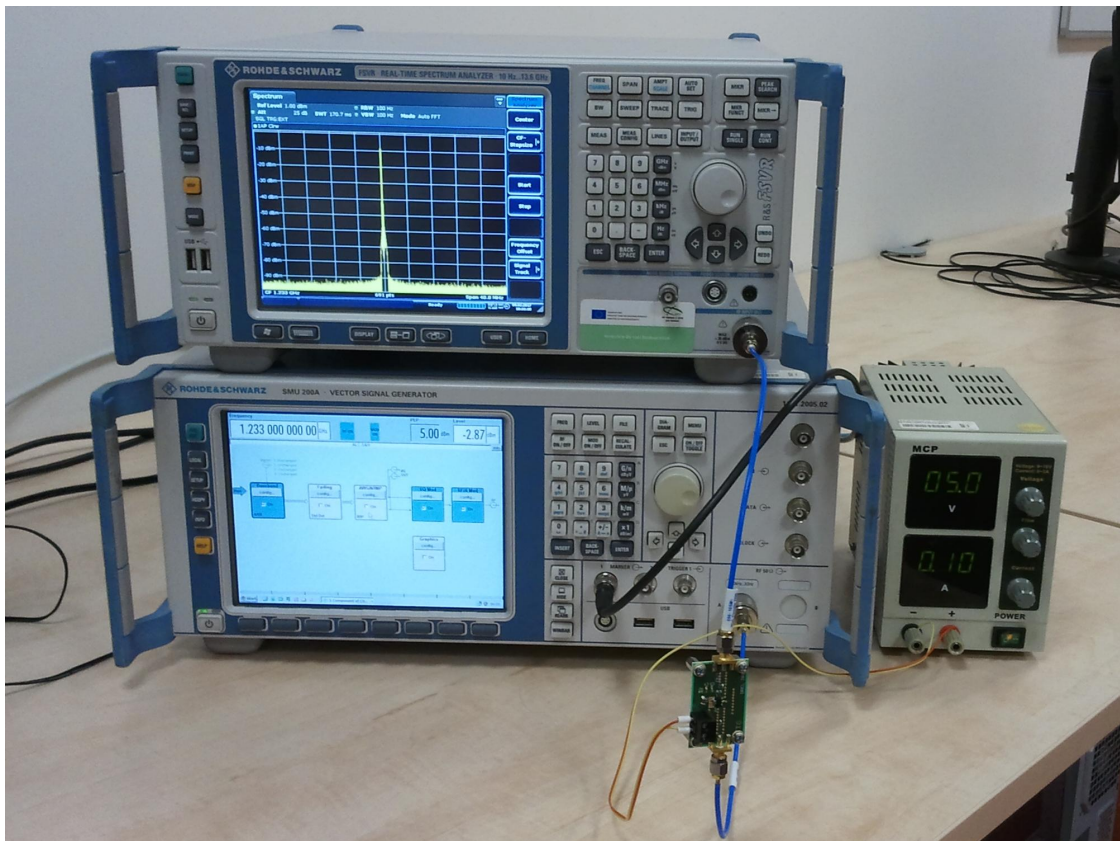


Figure 10.6: Photography of our test-bed for DPD measurements

The DPD used for the linearisation is based on the simplified $2^{\text{nd}}$-order dynamic

deviation reduction (DDR) based Voltera series model [9] and its output is given by

$$
\begin{aligned}
x(n) = &\sum_{k=0}^{\frac{K'-1}{2}} \sum_{q=0}^{Q'} b'_{2k+1,1,q} |z(n)|^{2k} z(n-q) \\
&+ \sum_{k=1}^{\frac{K'-1}{2}} \sum_{q=1}^{Q'} b'_{2k+1,2,q} |z(n)|^{2(k-1)} z^2(n) z^*(n-q) \\
&+ \sum_{k=1}^{\frac{K'-1}{2}} \sum_{q=1}^{Q'} b'_{2k+1,3,q} |z(n)|^{2(k-1)} z(n) |z(n-q)|^2 \\
&+ \sum_{k=1}^{\frac{K'-1}{2}} \sum_{q=1}^{Q'} b'_{2k+1,4,q} |z(n)|^{2(k-1)} z^*(n) z^2(n-q)
\end{aligned}
\tag{10.10}
$$

where $z(n)$ is an input signal to be predistored, $K'$ and $Q'$ are the maximum DPD nonlinear order and memory length respectively, and $b'_{k,i,q}$ is a coefficient of the DPD model.

The measurements were performed first with coarse cross-correlation synchronisation only and later with application of the proposed method. The maximum nonlinear order of the DPD was set $K' = 7$ and memory length $Q' = 0$. Fig. 10.7 shows the improvement of the AM/AM characteristics for the PA before and after linearisation by usage of the proposed method. The improvement of the AM/PM characteristics of the linearised PA is shown in Fig. 10.8.

Fig. 10.9 shows the phase difference (Eq. 10.6) and fitting of a line with direction $\tau_0$. The vertical lines in this picture depict the frequency interval $\langle \omega_{min}, \omega_{max} \rangle$ which is used for the calculation of $\tau_0$ using Eq. 10.8.

## 10.5   Power Amplifiers with Phase Distortion

Presence of phase distortion of the PA does not influence the performance of the proposed synchronisation method. Phase distortion in spectrum domain spreads the signals phase difference, but it preserves the direction of the fitted line. The time delay obtained using least squares is therefore insensitive to the phase distortion. Fig. 10.10 depicts a result of the synchronisation on the AM/PM characteristics of a PA with phase distortion. These characteristics were obtained by simulations only as there was no real suitable PA available for measurements.

## 10.6   Conclusion

In this paper we have proposed the analytical method for fractional sample period time synchronisation using spectrum domain. It has been presented that the method, due to its properties, is suitable for time synchronisation in DPD systems suffering from incoherent sampling, e.g. integrated transcievers with separated PLLs in receiver and transmitter. The main advantage of the proposed method is that it is analytical and thus much faster than optimisation methods. We have shown application of our method
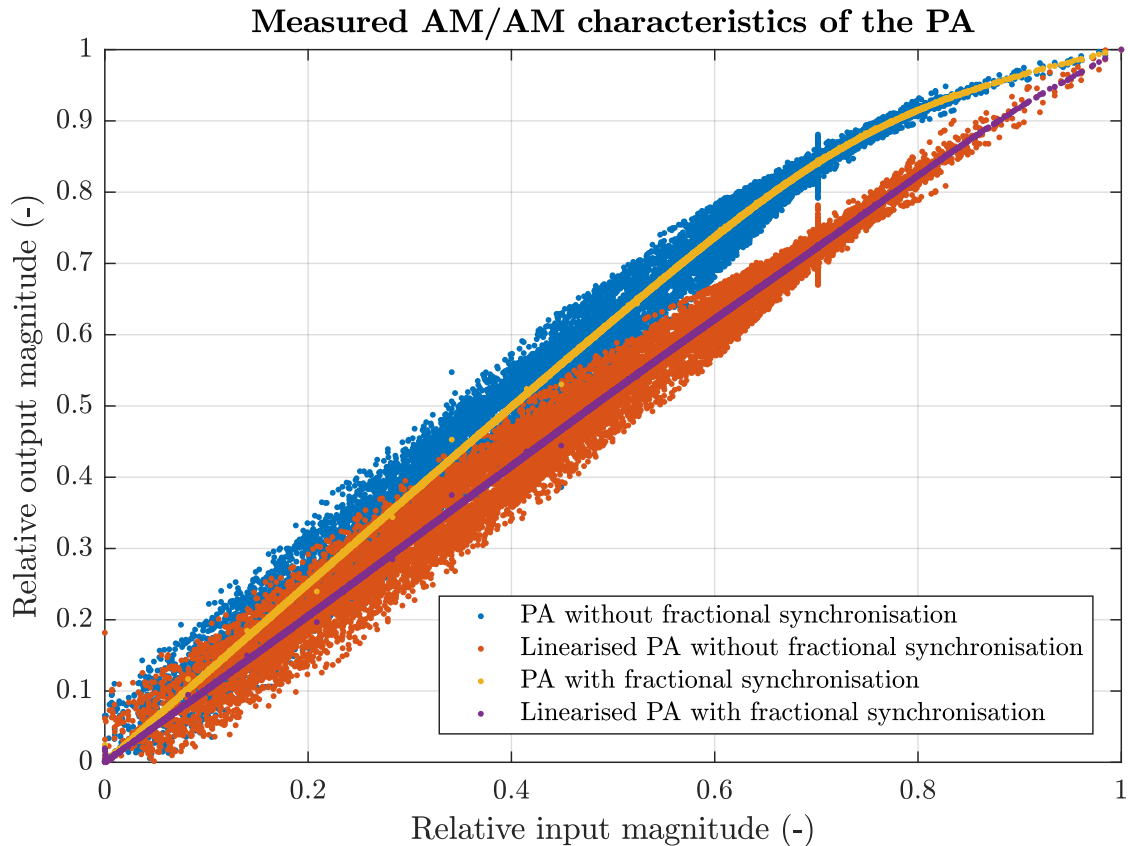
Figure 10.7: Measured AM/AM characteristics of the PA before and after linearisation with and without fractional sample period time synchronisation

in linearisation process using laboratory instruments and a real PA. The experimental measurements have shown its very good synchronisation capabilities. The simulation results have shown its outstanding performance in synchronisation of the phase distorted signals. The method is provided as a Matlab function on `github.com/jankralx/fract_tsync`.

## 10.7 Bibliography

[1] T. Gotthans, G. Baudoin, and A. Mbaye, "Influence of delay mismatch on digital predistortion for power amplifiers," in *Proceedings of the 20th International Conference Mixed Design of Integrated Circuits and Systems - MIXDES 2013*, June 2013, pp. 490–493.

[2] Y. Liu, X. Quan, W. Pan, S. Shao, and Y. Tang, "Performance Analysis of Direct-Learning Digital Predistortion With Loop Delay Mismatch in Wideband Transmitters," *IEEE Transactions on Vehicular Technology*, vol. 65, no. 9, pp. 7078–7089, Sept 2016.

## Measured linearised AM/PM characteristics of the PA
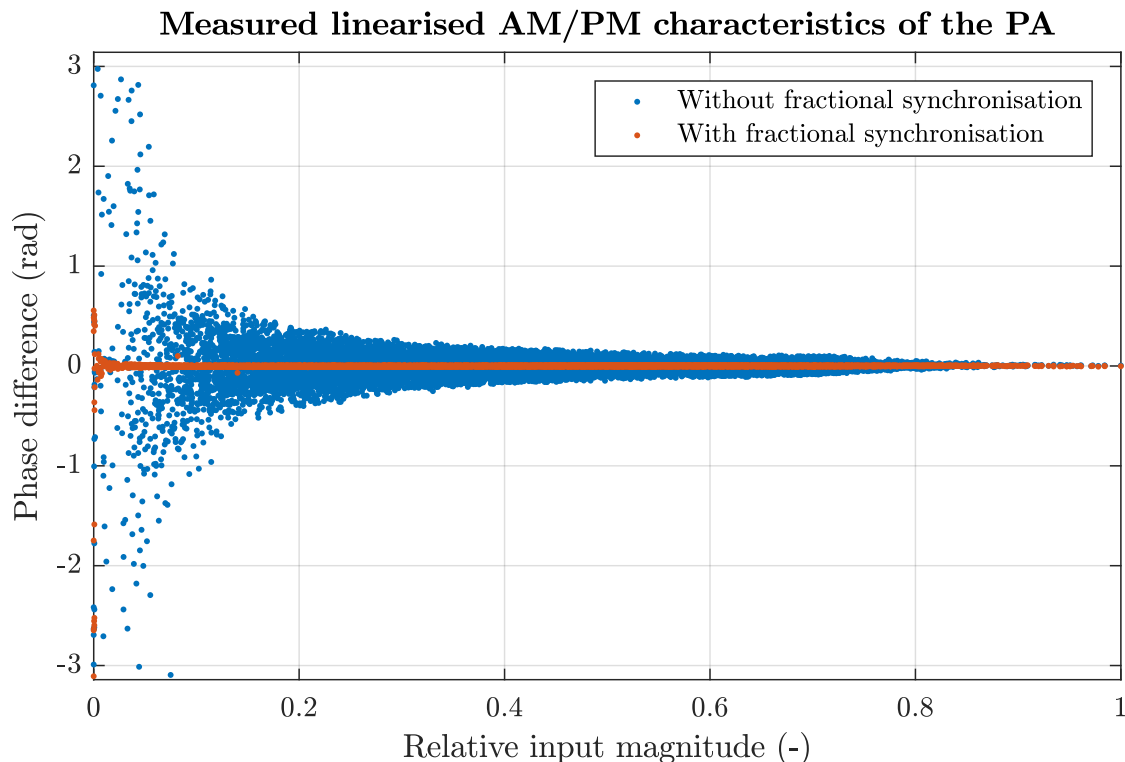


Figure 10.8: Measured AM/PM characteristics of the linearised PA with and without fractional sample period time synchronisation

[3]   J. Armstrong, "Symbol synchronization using baud-rate sampling and data-sequence-dependent signal processing," *IEEE Transactions on Communications*, vol. 39, no. 1, pp. 127–132, Jan 1991.

[4]   J. Armstrong and D. Strickland, "Symbol synchronization using signal samples and interpolation," *IEEE Transactions on Communications*, vol. 41, no. 2, pp. 318–321, Feb 1993.

[5]   L. Lin, J. Zhang, M. Ma, and H. Yan, "Time synchronization for molecular communication with drift," *IEEE Communications Letters*, vol. PP, no. 99, pp. 1–1, 2016.

[6]   R. Hamila, J. Vesma, and M. Renfors, "Polynomial-based maximum-likelihood technique for synchronization in digital receivers," *IEEE Transactions on Circuits and Systems II: Analog and Digital Signal Processing*, vol. 49, no. 8, pp. 567–576, Aug 2002.

[7]   D. Fu and A. N. Willson, "Trigonometric polynomial interpolation for timing recovery," *IEEE Transactions on Circuits and Systems I: Regular Papers*, vol. 52, no. 2, pp. 338–349, Feb 2005.
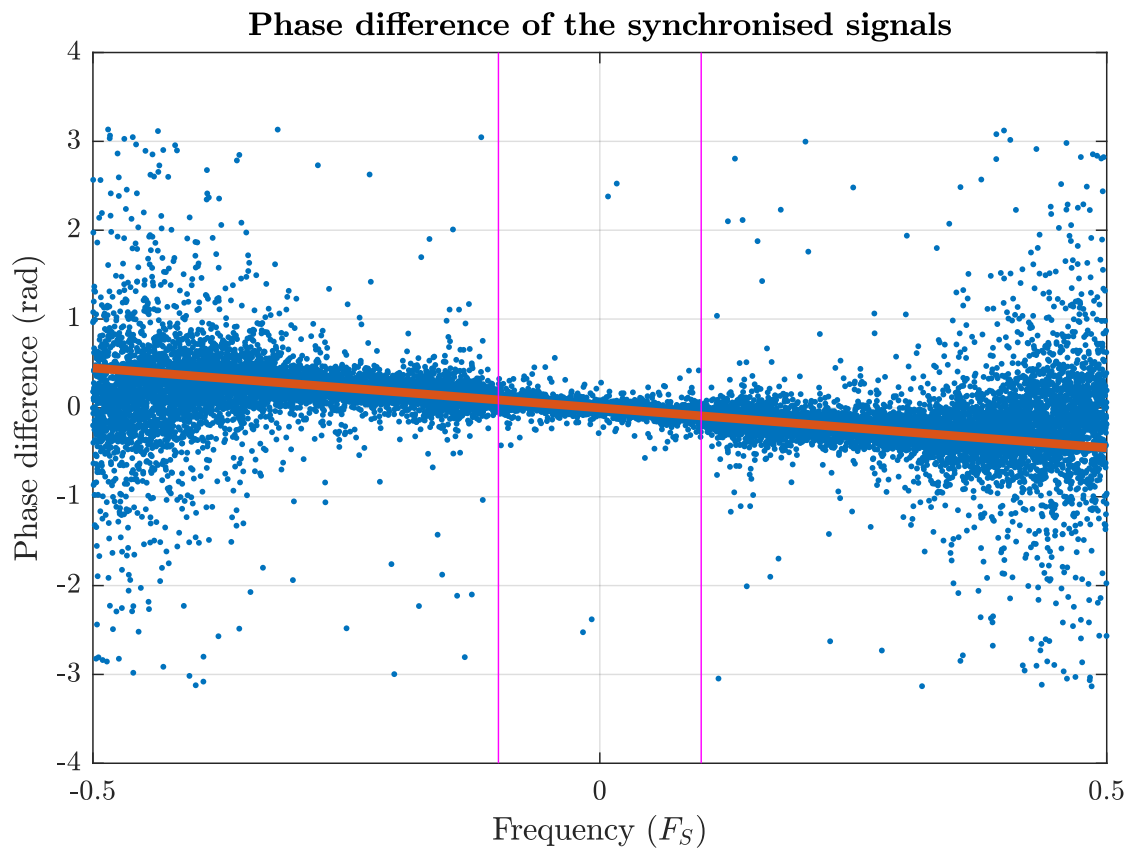
Figure 10.9: Phase difference of the synchronised signals with the fitted line representing the time offset $\tau_0$

[8]   H. Wang, W. Xue, and H. Ma, "Fast algorithms for the delay estimation in digital predistortion system," *IEEE Microwave and Wireless Components Letters*, vol. 25, no. 3, pp. 202–204, March 2015.

[9]   L. Guan and A. Zhu, "Simplified dynamic deviation reduction-based Volterra model for Doherty power amplifiers," in *2011 Workshop on Integrated Nonlinear Microwave and Millimetre-Wave Circuits*, April 2011, pp. 1–4.
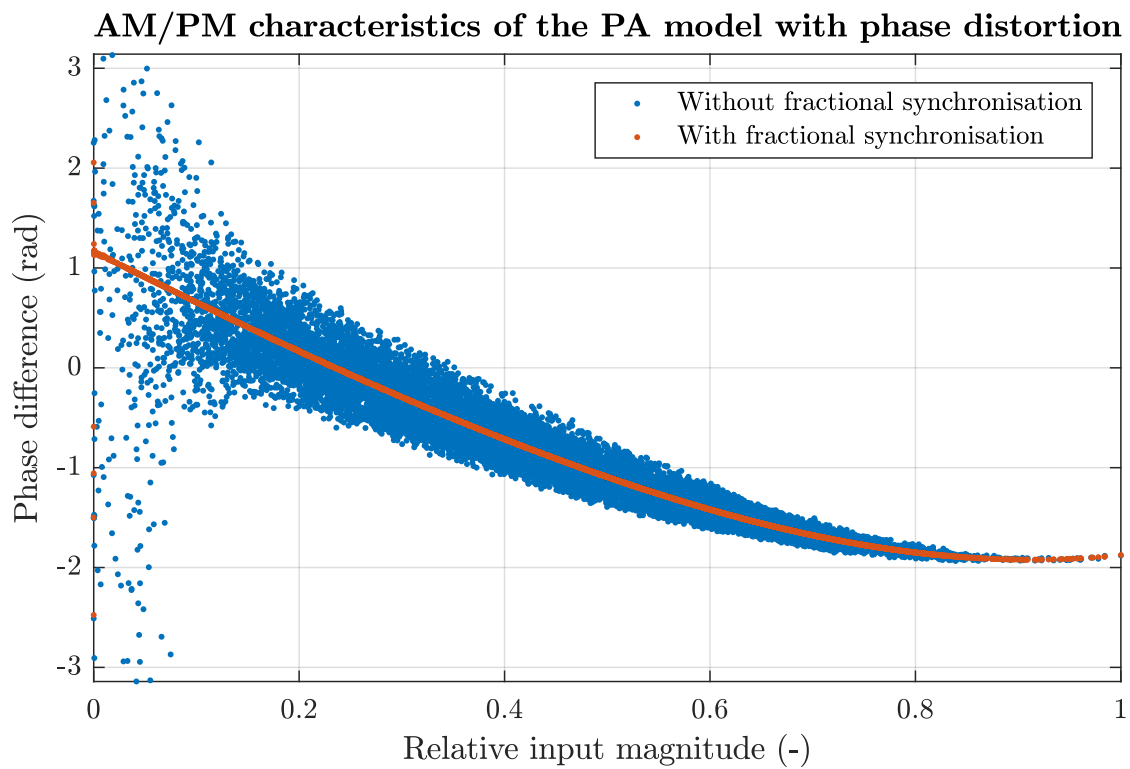
Figure 10.10: AM/PM characteristics of the PA model with phase distortion with and without fractional sample period time synchronisation. Signals without synchronisation are mutually shifted in time by $\tau/T_S = 0.48$.

# 11. Digital Predistorter with Real-Valued Feedback Employing Forward Model Estimation

**Abstract**

Digital predistorters (DPD) are used in modern communication systems to linearise nonlinear power amplifiers (PA) and maximise power efficiency. For their function, a feedback signal from the PA output is required. A conventional DPD uses a quadrature mixer and two analogue-to-digital converters (ADC) which consume additional power and increase system complexity. In this paper we have proposed an innovative technique which allows to use a nonquadrature RF mixer with one ADC in the feedback path. The DPD adaptation is noniterative and based on favoured indirect learning architecture. Firstly, the forward PA model is estimated and subsequently it is used to train DPD coefficients. We have verified and compared the proposed method with other DPD architectures in simulations. The results show that the proposed architecture can achieve the same results as a DPD with complex feedback samples and the other real-valued feedback architectures.

## 11.1 Introduction

Modern communications systems are evolved to fulfil still increasing demand for data throughput. Designers of these systems need to use higher frequency bandwidths, efficient modulations schemes, and at the same time they are required to minimise power consumption of the transceivers. Nowadays efficient modulations schemes are mostly linear, as the orthogonal frequency-division multiplexing (OFDM), the filter bank multicarrier (FBMC), and all their variants, require usage of linear power amplifiers (PA). The PAs are most power efficient when they operate close to saturation in nonlinear region where they cause degradation of the transmitted signal quality and interference in neighbours channels induced by the frequency spectrum regrowth.

One of the technique commonly used to allow PA operation in nonlinear region is utilisation of a baseband digital predistorter (DPD). Typical configuration of the transmitter with the DPD is depicted in Fig. 11.1. The DPD uses a local feedback to identify characteristics of the PA nonlinearity and introduces a nonlinear inverse to the transmitted signal. The PA nonlinearity cancels the intentionally introduced nonlinear inverse and the transmitted signal is very close to the desired.
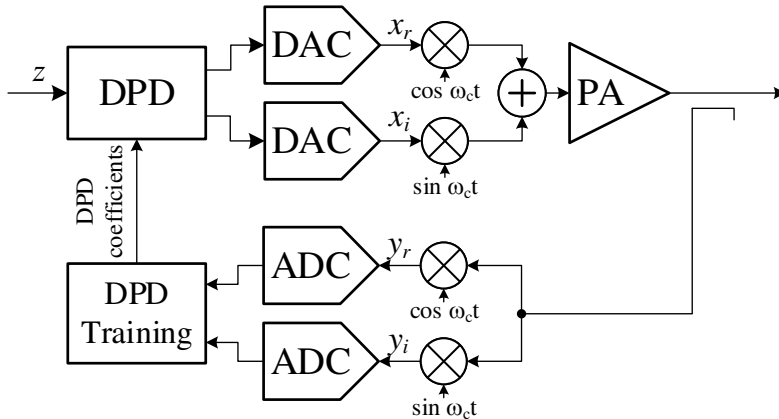
Figure 11.1: The diagram of the conventional baseband DPD

The correct function of the DPD is conditioned by a sufficient system bandwidth which has to be at least three times up to five times the communication bandwidth [1, 2]. In wideband communication systems this requirement implies need for two high-speed analogue-to-digital converters (ADCs) in the feedback path. These high-speed ADCs are usually power hungry and increase design complexity and price. The last research in the field shows the interest to relax demands on these ADCs. Liu [3], and Huang [4] focused on lowering of the ADC sampling frequency. Wang in the papers [5, 6] and Zhang in [7] extended the undersampling DPD for multiband and wideband transmitters. Zhang et al. followed different approach in their papers [8, 9] and presented a DPD with the feedback ADCs replaced by high-speed digital-to-analogue converters (DACs) accompanied with high-speed comparators which allowed them to reduce system power consumption.

Chani-Cahuana et al. in the paper [10] proposed an architecture with a single ADC and an RF mixer instead two ADCs with a quadrature mixer. Their DPD is based on a real-valued feedback and uses the iterative learning control (ILC) algorithm which they had presented in [11]. Besides the reduced power consumption and system complexity, the real-valued feedback provides an advantage of reduced sensitivity to in-phase and quadrature (IQ) imbalances of the feedback quadrature mixer [12].

In this paper we propose an innovative DPD architecture with real-valued feedback path based on work of Morgan [13] and Landin [14]. Firstly a forward PA model is extracted using real-valued feedback and subsequently the DPD with the indirect learning architecture (ILA) is trained using the forward PA model. We compare the proposed approach with a real-valued feedback DPD based on the iterative direct learning architecture (DLA), because it usually provides better performance than ILA [15]. The most recent paper [16] by Guan partially covers the DLA DPD with a real-valued feedback. Additionally our paper provides some comparisons for the DLA which Guan did not covered in [16].

## 11.2 DPD with Real Valued Feedback Using Forward PA Model

Consider a PA modeled by memory polynomial model (MP) [17]. The discrete baseband PA output $y$ is given as [17]

$$y(n) = \sum_{k=1}^{K} \sum_{q=0}^{Q} b_{k,q} x(n-q)|x(n-q)|^{k-1} \tag{11.1}$$

where $x$ is the PA input, $b_{k,q}$ is a coefficient of the PA model, and $P$ and $Q$ represent the maximum PA nonlinearity order and memory length respectively. The product $x(n-q)|x(n-q)|^{k-1}$ is often called a basis waveform or a basis function. We denote it as

$$\phi_{k,q}^{(x)}(n) = x(n-q)|x(n-q)|^{k-1}. \tag{11.2}$$

The input samples $x$, model coefficients $b_{k,q}$, and the basis waveforms $\phi_{k,q}(n)$ can be arranged into vectors and a matrix

$$\mathbf{\Phi}_{k,q}^{(x)} = \begin{bmatrix} \phi_{k,q}^{(x)}(0) & \phi_{k,q}^{(x)}(1) & \dots & \phi_{k,q}^{(x)}(N) \end{bmatrix}^T$$

$$\mathbf{x} = \begin{bmatrix} x(0) & x(1) & \dots & x(N) \end{bmatrix}^T$$

$$\mathbf{y} = \begin{bmatrix} y(0) & y(1) & \dots & y(N) \end{bmatrix}^T$$

$$\mathbf{b} = \begin{bmatrix} b_{1,0} & b_{1,1} & \dots & b_{1,Q} & b_{2,0} & \dots & b_{K,Q} \end{bmatrix}^T$$

$$\mathbf{U}_x = \begin{bmatrix} \mathbf{\Phi}_{1,0}^{(x)} & \mathbf{\Phi}_{1,1}^{(x)} & \dots & \mathbf{\Phi}_{1,Q}^{(x)} & \mathbf{\Phi}_{2,0}^{(x)} & \dots & \mathbf{\Phi}_{K,Q}^{(x)} \end{bmatrix}^T$$

where $\mathbf{b}$ is column vector with $K(Q+1)$ rows, and the size of the matrix $\mathbf{U}_x$ is $N \times K(Q+1)$. Eq. 11.1 can be rewritten into matrix form

$$\mathbf{y} = \mathbf{U}_x \mathbf{b}. \tag{11.3}$$

Eq. 11.3 can be split into the real and imaginary parts, denoted as $(.)_r$ and $(.)_i$ respectively, as

$$\mathbf{y}_r + j\mathbf{y}_i = (\mathbf{U}_{xr} + j\mathbf{U}_{xi})(\mathbf{b}_r + j\mathbf{b}_i)$$

$$\mathbf{y}_r + j\mathbf{y}_i = \mathbf{U}_{xr}\mathbf{b}_r + j\mathbf{U}_{xi}\mathbf{b}_r + j\mathbf{U}_{xr}\mathbf{b}_i - \mathbf{U}_{xi}\mathbf{b}_i$$

$$\mathbf{y}_r = \mathbf{U}_{xr}\mathbf{b}_r - \mathbf{U}_{xi}\mathbf{b}_i \quad \wedge \quad \mathbf{y}_i = \mathbf{U}_{xi}\mathbf{b}_r + \mathbf{U}_{xr}\mathbf{b}_i$$

and by matrix reordering we get two matrix equations

$$\mathbf{y}_r = \begin{bmatrix} \mathbf{U}_{xr} & -\mathbf{U}_{xi} \end{bmatrix} \begin{bmatrix} \mathbf{b}_r \\ \mathbf{b}_i \end{bmatrix} \quad \wedge \quad \mathbf{y}_i = \begin{bmatrix} \mathbf{U}_{xi} & -\mathbf{U}_{xr} \end{bmatrix} \begin{bmatrix} \mathbf{b}_r \\ \mathbf{b}_i \end{bmatrix}. \tag{11.4}$$

To get the PA coefficients $\mathbf{b}$, it is sufficient to solve only one of the two equations in Eq. 11.4. Advantageously each equation requires only real or imaginary samples of the amplifier output $\mathbf{y}$. Since the matrix $\mathbf{X}$ is fully known, as it consists of samples given by transmitted signal $x$, $\mathbf{b}$ can be obtained as the Least Squares (LS) solution of Eq. 11.4 using real feedback samples

$$\begin{bmatrix} \mathbf{b}_r \\ \mathbf{b}_i \end{bmatrix} = (\mathbf{A}_x^H \mathbf{A}_x)^{-1} \mathbf{A}_x^H \mathbf{y}_r \tag{11.5}$$

or imaginary feedback samples

$$\begin{bmatrix} \mathbf{b}_r \\ \mathbf{b}_i \end{bmatrix} = (\mathbf{B}_x^H \mathbf{B}_x)^{-1} \mathbf{B}_x^H \mathbf{y}_i \tag{11.6}$$

where

$$\mathbf{A}_x = \begin{bmatrix} \mathbf{U}_{xr} & -\mathbf{U}_{xi} \end{bmatrix} \qquad \mathbf{B}_x = \begin{bmatrix} \mathbf{U}_{xi} & \mathbf{U}_{xr} \end{bmatrix}. \tag{11.7}$$

Once the PA model is obtained, we can use it to calculate PA model output $\tilde{\mathbf{y}}$ [13, 14] as

$$\tilde{\mathbf{y}} = \mathbf{U}_x \mathbf{b} \tag{11.8}$$

and by application of ILA, doing the post-inverse to the PA output, we get the DPD coefficients in the vector $\mathbf{b}'$, of the same dimension as $\mathbf{b}$, as LS solution of

$$\mathbf{x} = \mathbf{U}_{\tilde{y}} \mathbf{b}' \tag{11.9}$$

which yields

$$\mathbf{b}' = (\mathbf{U}_{\tilde{y}}^H \mathbf{U}_{\tilde{y}})^{-1} \mathbf{U}_{\tilde{y}}^H \mathbf{x} \tag{11.10}$$

where the matrix $\mathbf{U}_{\tilde{y}}$ is given by samples $\tilde{y}$ in the same way as the matrix $\mathbf{U}_x$ is given by samples $x$.

Further, we will denote the proposed method as real-valued forward model indirect learning architecture (R-FM-ILA) and its complex variant using conventional DPD architecture (Fig. 11.1) as forward model indirect learning architecture (FM-ILA).

## 11.3 Real Valued Feedback DPD Using DLA

DLA is an iterative method which tries to directly solve $G(D(z)) = y$ with $G$ being a transfer function of the PA and $D$ a transfer function of the DPD. The solution $D(z) = A^{-1}(y)$ is a nonlinear problem and can be solved by the Gauss-Newton method which can be defined for DPD as [18]

$$\mathbf{b}'(m+1) = \mathbf{b}'(m) - \mu \mathbf{e}(m) \tag{11.11}$$

where $m$ is the iteration cycle, $\mathbf{b}'(m)$ and $\mathbf{b}'(m+1)$ are current and new DPD coefficients, $\mu$ is the iteration step size, and $\mathbf{e}(m)$ is the coefficient error vector for the $m$-th iteration given as the LS solution of

$$\mathbf{z} - \mathbf{y} = \mathbf{U}_z \mathbf{e}. \tag{11.12}$$

Following similar steps of splitting real and imaginary parts of Eq. 11.12 as in Section 11.2 a vector $\mathbf{e}$ can be obtained using only real samples of the PA output $y_r$ as

$$\begin{bmatrix} \mathbf{e}_r \\ \mathbf{e}_i \end{bmatrix} = (\mathbf{A}_z^H \mathbf{A}_z)^{-1} \mathbf{A}_z^H (\mathbf{z}_r - \mathbf{y}_r) \tag{11.13}$$

or imaginary feedback samples

$$\begin{bmatrix} \mathbf{e}_r \\ \mathbf{e}_i \end{bmatrix} = (\mathbf{B}_z^H \mathbf{B}_z)^{-1} \mathbf{B}_z^H (\mathbf{z}_i - \mathbf{y}_i) \tag{11.14}$$

with $\mathbf{A}_x$ and $\mathbf{B}_x$ defined in Eq. 11.7. Back substitution of the vector $\mathbf{e}$ into Eq. 11.11 yields the new DPD coefficients

$$\begin{bmatrix} \mathbf{b}'_r(m+1) \\ \mathbf{b}'_i(m+1) \end{bmatrix} = \begin{bmatrix} \mathbf{b}'_r(m) \\ \mathbf{b}'_i(m) \end{bmatrix} - \mu(\mathbf{A}_z^H \mathbf{A}_z)^{-1} \mathbf{A}_z^H (\mathbf{z}_r - \mathbf{y}_r). \tag{11.15}$$

DLA using only real feedback samples will be further referred as real-valued direct learning architecture (R-DLA).

## 11.4 Simulation Procedures

We have implemented and simulated various DPD architectures to evaluate their linearisation performance. Compared architectures are ILA, DLA, FM-ILA, R-DLA, R-FM-ILA, and system without DPD. For ILA, DLA and FM-ILA we have used the model depicted in Fig. 11.1 and for real-valued variants the model from Fig. 11.2. At both cases the PA has been modeled by memory polynomial model (Eq. 11.1) with $P = 7, Q = 1$ and coefficients extracted from measurements of a real PA. We have used FBMC signal with 1024 subcarriers, 18 frames in one transmission window, further referred as iteration. Sampling frequency has been set 6 times higher than the communication channel bandwidth $B$.
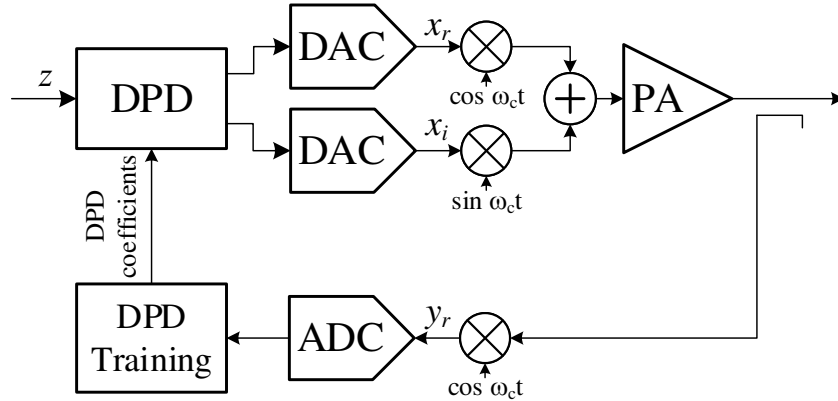


Figure 11.2: The diagram of the baseband DPD with real-valued feedback

All the architectures have been used in the iterative way which means that the DPD coefficients were trained on a signal after transmission through the PA without the possibility to use the PA twice – first for DPD coefficients training and second for linearised transmission.

For all the architectures one iteration consists of:

1. generation of a random-data FBMC signal $z$ (same signal for all DPD architectures),

2. predistortion of the desired signal $z$ with current DPD coefficients $\mathbf{b}'(m)$ to get the PA input $x$,

3. amplitude signal adjustment to set the desired PA output power,

4. modelling the PA and calculating its output $y$,

5. evaluation of the output metrics,

6. calculation of new DPD coefficients $\mathbf{b}'(m+1)$.

The critical operation is setting of the PA reference gain. Maximum signal amplitude in the system without DPD was set that the PA provided the same output power in the communication channel as the system with ILA. As this topic is out of the context, we will rather refer the interested reader into work of Jardin and Baudoin [19] where this problem is analysed. The calculation of new DPD coefficients (last step) varies based on the architecture.

The brief procedure for ILA (Fig. 11.3) is:

1. adjusting the maximum Euclidean norm of the $x$ and $y$ as $||x|| \leq 1$, $||y|| \leq 1$ for the following calculations,

2. solving coefficients $\mathbf{b}'(m+1)$ of the post-distorter as
   $\mathbf{b}'(m+1) = (\mathbf{U}_y^H \mathbf{U}_y)^{-1} \mathbf{U}_y^H \mathbf{x}$.

3. coefficients of the post-distorter are used as the DPD coefficients in the next iteration.
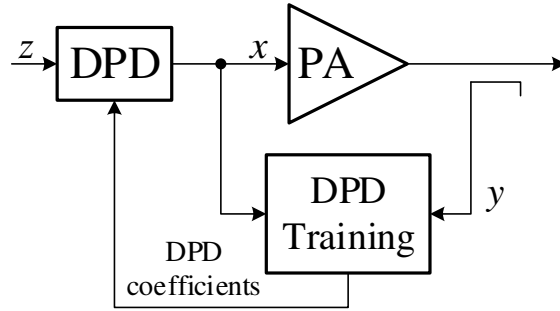


Figure 11.3: Schematic diagram of the ILA DPD

The procedure for DLA (Fig. 11.4) is:

1. adjusting the maximum Euclidean norm of the $z$ and $y$ as $||z|| \leq 1$, $||y|| \leq 1$ for the following calculations,

2. compensation of the phase part of the PA complex gain,

3. solving new DPD coefficients using the desired signal $z$ and the feedback $y$ as
   $\mathbf{d}(t+1) = \mathbf{d}(t) - \mu(\mathbf{U}_z^H \mathbf{U}_z)^{-1} \mathbf{U}_z^H (\mathbf{z} - \mathbf{y})$.

The compensation of of the phase part of the PA complex gain in the $2^{nd}$ step improves DLA convergence for selected PA. We compensate by a constant phase for the selected PA. If the initial coefficients are set close to the optimum, the phase IQ the phase part of the PA complex gain compensation is not required. However we have achieved reasonable convergence speed with the phase IQ rotation correction, initial coefficients set to $\mathbf{b} = \begin{bmatrix} 0.5 & 0 & 0 & \ldots \end{bmatrix}^T$ and initial step size $\mu = 0.8$. The step size is lowered after the DPD coefficients converged close to the solution.
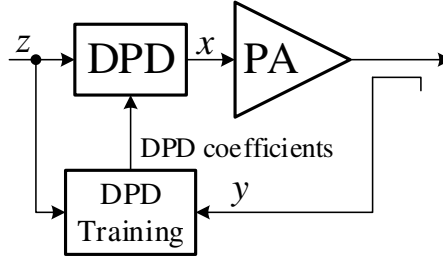


Figure 11.4: Schematic diagram of the DLA DPD

Finally the procedure for FM-ILA (Fig. 11.5) is:

1. adjusting the maximum Euclidean norm of the $x$ and $y$ as $||x|| \leq 1$, $||y|| \leq 1$ for the following calculations,

2. estimating the forward PA model coefficients as
   $\mathbf{b} = (\mathbf{U}_x^H \mathbf{U}_x)^{-1} \mathbf{U}_x^H \mathbf{y}$

3. calculating the forward model output as $\tilde{\mathbf{y}} = \mathbf{U}_x \, \mathbf{b}$

4. solving coefficients $\mathbf{b}'(m+1)$ of the post-distorter which distorts the forward model output $\tilde{\mathbf{y}}$ to get the PA input $\mathbf{x}$ as $\mathbf{b}'(m+1) = (\mathbf{U}_{\tilde{y}}^H \mathbf{U}_{\tilde{y}})^{-1} \mathbf{U}_{\tilde{y}}^H \mathbf{x}$.

5. coefficients of the post-distorter $\mathbf{b}'(m+1)$ are used as the DPD coefficients in the next iteration.

Procedures for the Real-valued feedback methods R-DLA and R-FM-ILA are slightly modified as described in Section 11.3 and 11.2.

All related Matlab source codes are provided at `www.github.com/jankralx/rfm_ila`.

## 11.5 Simulation Results

The linearisation performance has been qualified based on the normalised mean square error (NMSE) and the adjacent channel power ratio (ACPR). We evaluated NMSE as $NMSE = 10 \log_{10}[(\mathbf{z} - \mathbf{y})^H (\mathbf{z} - \mathbf{y}) (\mathbf{z}^H \mathbf{z})^{-1}]$ and ACPR for the $1^{st}$ adjacent channel which is $1B$ wide and with $1.1B$ offset, and for the $2^{nd}$ adjacent channel which is $1B$ wide too and with $2.2B$ offset. ACPRs from the left and right channels are averaged separately for the $1^{st}$ and $2^{nd}$ adjacent channels and presented as a single value per the adjacent channel.
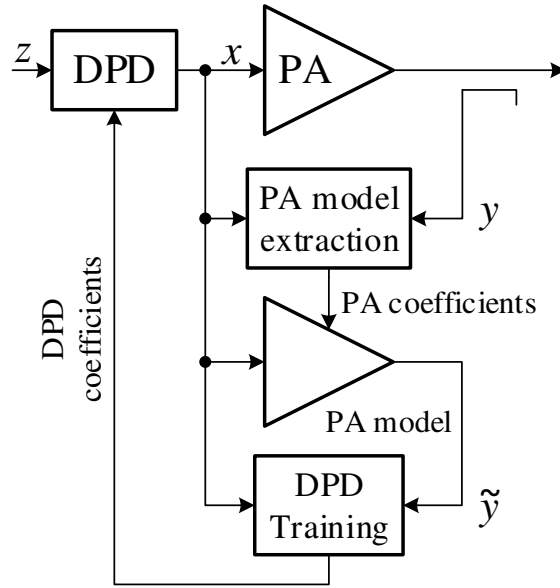
Figure 11.5: Schematic diagram of the FM-ILA DPD

We have simulated all architectures with the DPD modelled by the MP model. Although we have tried also the simplified $2^{nd}$-order dynamic deviation reduction (DDR2) based Voltera series model [20], for our simulation setup, MP model outperformed DDR2. We believe that DDR2 basis functions, given as a product of the signal with its delayed copy, and increased DDR2 sensitivity to the magnitudes of signals greater than one cause suboptimal linearisation compared to the MP model.

Provided results are thus for the MP model with $K = 7$, $Q = 3$. The simulation executed 220 iterations. Average frequency spectrum, NMSE and ACPR have been evaluated after 20 iterations, after the DLA and R-DLA converged.

Fig. 11.6 shows AM/AM characteristics for the R-FM-ILA with the trained DPD coefficients. Blue circles represents the characteristics of the PA got from the feedback signal and orange dots stand for the characteristic of the estimated forward PA model. Reader can see that the PA has a certain memory which is mostly compensated by the predistorter.

Average frequency spectra of PA outputs are shown in Fig. 11.7. The spectra for all the DPD architectures are almost the same and well improved due to the spectrum for the system without the DPD.

NMSE evolution in iteration cycles is depicted in Fig. 11.8. In the first iteration ILA, FM-ILA, and R-FM-ILA (further together denoted as ILA-based systems) are not trained yet and therefore provide the same NMSE as the system without DPD. DLA and R-DLA start with lower NMSE which is caused by the lowered output power given by first coefficient set to 0.5. In the second iteration ILA, FM-ILA and R-FM-ILA achieve almost the optimum predistortion. The output power of the system without the DPD is lowered to be the same as for the system with the ILA DPD. In the third step we would like to point out a little improvement for ILA-based systems. This improvement is caused by better estimation of DPD coefficients using a linearised PA and a predistorted PA
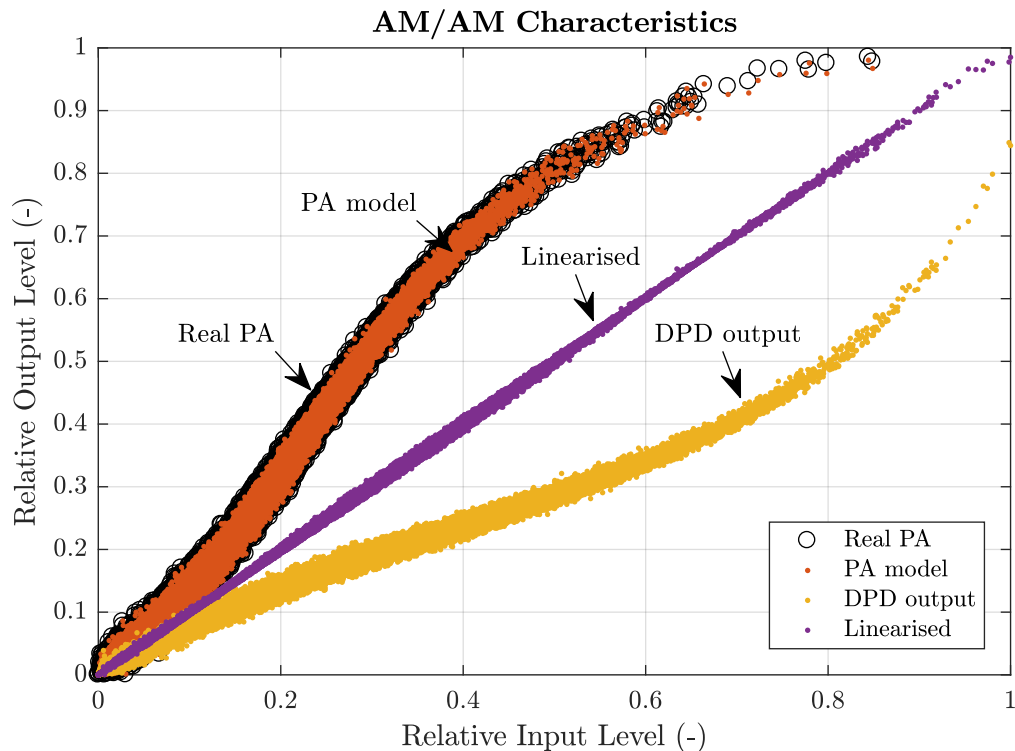
Figure 11.6: AM/AM characteristics for R-FM-ILA DPD

input. We have verified this assumption in the FM-ILA and R-FM-ILA system. If the post-distorter in the ILA part of FM-ILA or R-FM-ILA was trained using the desired signal $z$ instead of predistorter output $x$, obtained NMSE would be $\approx 1.5$ dB higher. Note the NMSE-evolution peak for DLA and R-DLA which the optimisation process needs to pass in order to achieve the solution. Convergence speed of DLA and R-DLA highly depends on the initial coefficients, step size $\mu$ (set as described in Section 11.4) and the desired signal $z$. Higher convergence speed could be achieved but with lower probability of convergence.

Detailed comparison of average NMSE and ACPR for all architectures is given in Tab. **??**. ILA-based systems provide the same linearisation performance based on the evaluated metrics. DLA and R-DLA are slightly better than ILA-based.

## 11.6 Conclusion

In this paper we have proposed an innovative DPD architecture using real-valued feed-back samples and employing forward PA model estimation denoted as R-FM-ILA. The proposed method has been verified and compared to the state-of-the-art DPD methods in the simulations. We have shown that the R-FM-ILA can achieve the same linearisation performance as its complex variant and the ILA DPD and very similar results as complex DLA and R-DLA. Its main advantage over the DLA and R-DLA is noniterative calculation and related unnecessary setting of the initial solution and step size. Additionally
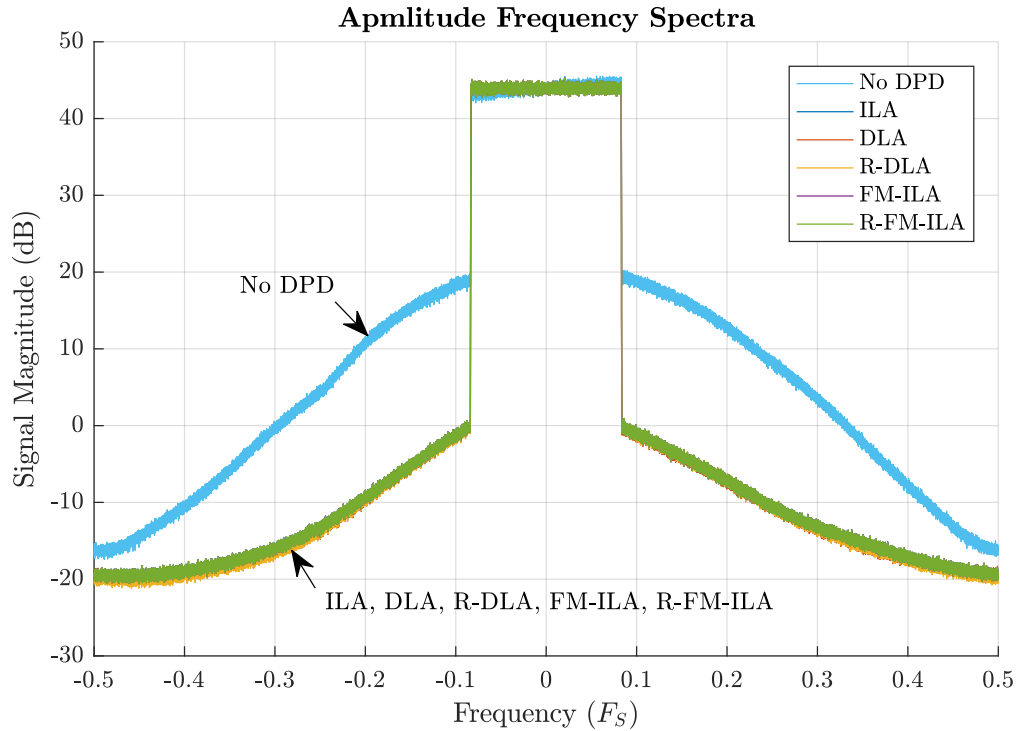
Figure 11.7: Frequency spectra of the PA output signal

Table 11.1: NMSE and ACPR in 1st and 2nd adjacent channels

| DPD architecture | NMSE (dB) | ACPR-1st (dB) | ACPR-2nd (dB) |
|:---:|:---:|:---:|:---:|
| No DPD | -19.9 | -29.6 | -46.5 |
| ILA | -40.5 | -49.6 | -60.3 |
| DLA | -40.8 | -49.8 | -60.7 |
| R-DLA | -40.7 | -49.7 | -60.7 |
| FM-ILA | -40.5 | -49.6 | -60.3 |
| R-FM-ILA | -40.5 | -49.6 | -60.3 |

it allows usage of an RF mixer and one ADC instead of a quadrature mixer with two
ADCs which decreases power consumption, system complexity and transmitter price.

## 11.7   Bibliography

[1]   F. M. Ghannouchi and O. Hammi, "Behavioral Modeling and Predistortion," *IEEE
Microwave Magazine*, vol. 10, no. 7, pp. 52–64, Dec 2009.

[2]   J. Zhao, Y. Liu, C. Yu, J. Yu, and S. Li, "A Modified Band-Limited Digital Predis-
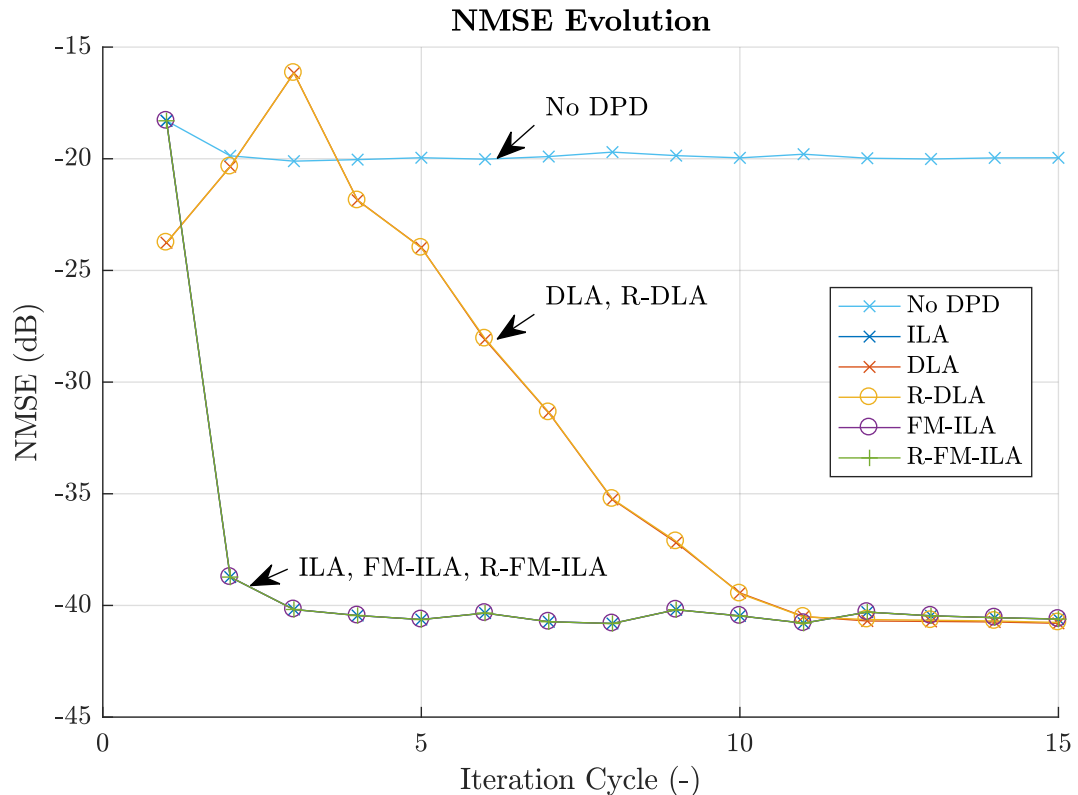
Figure 11.8: Evolution of the NMSE in the first iteration cycles

tortion Technique for Broadband Power Amplifiers," *IEEE Communications Letters*, vol. 20, no. 9, pp. 1800–1803, Sept 2016.

[3] Y. Liu, J. J. Yan, H. T. Dabag, and P. M. Asbeck, "Novel Technique for Wideband Digital Predistortion of Power Amplifiers With an Under-Sampling ADC," *IEEE Transactions on Microwave Theory and Techniques*, vol. 62, no. 11, pp. 2604–2617, Nov 2014.

[4] H. Huang, P. Mitran, and S. Boumaiza, "Digital Predistortion Function Synthesis using Undersampled Feedback Signal," *IEEE Microwave and Wireless Components Letters*, vol. 26, no. 10, pp. 855–857, Oct 2016.

[5] Z. Wang, L. Guan, and R. Farrell, "Compact Undersampled Digital Predistortion for Flexible Single-chain Multi-band RF Transmitter," in *2017 IEEE MTT-S International Microwave Symposium (IMS)*, June 2017, pp. 1542–1545.

[6] ——, "Undersampling Observation-Based Compact Digital Predistortion for Single-Chain Multiband and Wideband Direct-to-RF Transmitter," *IEEE Transactions on Microwave Theory and Techniques*, vol. 65, no. 12, pp. 5274–5283, Dec 2017.

[7] Q. Zhang, W. Chen, Z. Wang, and G. Su, "A Single Feedback Architecture for Dual-Band Digital Predistortion With Under-Sampling Technique," in *2016 IEEE MTT-S International Wireless Symposium (IWS)*, March 2016, pp. 1–4.

[8] H. Wang, G. Li, Y. Zhang, F. Liu, and A. Zhu, "Forward Modeling Assisted 1-bit Data Acquisition Based Model Extraction for Digital Predistortion of RF Power Amplifiers," in *2017 IEEE Topical Conference on RF/Microwave Power Amplifiers for Radio and Wireless Applications (PAWR)*, Jan 2017, pp. 59–62.

[9] H. Wang, G. Li, C. Zhou, W. Tao, F. Liu, and A. Zhu, "1-bit Observation for Direct-Learning-Based Digital Predistortion of RF Power Amplifiers," *IEEE Transactions on Microwave Theory and Techniques*, vol. 65, no. 7, pp. 2465–2475, July 2017.

[10] J. Chani-Cahuana, M. Özen, C. Fager, and T. Eriksson, "Digital Predistortion Parameter Identification for RF Power Amplifiers Using Real-Valued Output Data," *IEEE Transactions on Circuits and Systems II: Express Briefs*, vol. 64, no. 10, pp. 1227–1231, Oct 2017.

[11] J. Chani-Cahuana, P. N. Landin, C. Fager, and T. Eriksson, "Iterative Learning Control for RF Power Amplifier Linearization," *IEEE Transactions on Microwave Theory and Techniques*, vol. 64, no. 9, pp. 2778–2789, Sept 2016.

[12] T. Gotthans, R. Maršálek, M. Pospíšil, T. Urbanec, J. Král, and J. Blumenstein, "On the Lower I/Q Imbalance Sensitivity Using Real-valued Feedback of Digital Predistortion," in *2018 IEEE Topical Conference on RF/Microwave Power Amplifiers for Radio and Wireless Applications (PAWR)*, 2018, pp. 79–82.

[13] D. R. Morgan, Z. Ma, and L. Ding, "Reducing Measurement Noise Effects in Digital Predistortion of RF Power Amplifiers," in *Communications, 2003. ICC '03. IEEE International Conference on*, vol. 4, May 2003, pp. 2436–2439 vol.4.

[14] P. N. Landin, A. E. Mayer, and T. Eriksson, "MILA - A Noise Mitigation Technique for RF Power Amplifier Linearization," in *2014 IEEE 11th International Multi-Conference on Systems, Signals Devices (SSD14)*, Feb 2014, pp. 1–4.

[15] H. Paaso and A. Mammela, "Comparison of Direct Learning and Indirect Learning Predistortion Architectures," in *2008 IEEE International Symposium on Wireless Communication Systems*, Oct 2008, pp. 309–313.

[16] N. Guan, N. Wu, and H. Wang, "Digital Predistortion of Wideband Power Amplifier With Single Undersampling ADC," *IEEE Microwave and Wireless Components Letters*, vol. 27, no. 11, pp. 1016–1018, Nov 2017.

[17] J. Kim and K. Konstantinou, "Digital predistortion of wideband signals based on power amplifier model with memory," *Electronics Letters*, vol. 37, no. 23, pp. 1417–1418, Nov 2001.

[18] Z. Yu, H. Xie, and E. Zhu, "Wide-band Linear Characteristic Compensation for DPD Systems with Direct Learning," in *2013 Asia-Pacific Microwave Conference Proceedings (APMC)*, Nov 2013, pp. 790–793.

[19] P. Jardin and G. Baudoin, "Filter Lookup Table Method for Power Amplifier Linearization," *IEEE Transactions on Vehicular Technology*, vol. 56, no. 3, pp. 1076–1087, May 2007.

[20] L. Guan and A. Zhu, "Simplified dynamic deviation reduction-based Volterra model for Doherty power amplifiers," in *2011 Workshop on Integrated Nonlinear Microwave and Millimetre-Wave Circuits*, April 2011, pp. 1–4.

# 12. Influence of Filter-bank RF Transceiver Chain Imperfections on Digital Predistortion Performance

**Abstract**

Novel multicarrier waveforms, such as, Filter Bank Multi Carrier promise lower out-of-band emissions compared to the currently used Orthogonal Frequency Division Multiplex technique. Unfortunately, the power amplifier nonlinearity in the transmitter can significantly degrade the FBMC spectrum wiping-out the differences between these two approaches. In order to compensate for nonlinearities and memory effects introduced by power amplifiers, the digital predistortion is a widely used technique, but also the predistortion itself can significantly be influenced by the transceiver imperfections. This paper thus laid great emphasis on the evaluation of transceiver imperfections and uncertainties on the overall performance of digital predistortion driven with FBMC signals.

## 12.1 Introduction

Communication signals with high order modulations and non-constant envelope are used to fulfill ever-increasing demands for high data rates in contemporary communication systems. Such modulation formats are sensitive to various transmitter imperfections, such as, the power amplifier (PA) nonlinearities. Meanwhile, in order to achieve high transmitter efficiency, it is desirable to operate the power amplifiers close to their saturation point. Combination of these circumstances results in significant nonlinear distortion of the transmitted signals resulting in increased bit error rate and spurious transmission into adjacent channels.

One of the candidate waveforms for the fifth generation (5G) of communication systems is the Filter Bank Multi Carrier (FBMC) modulation, that is supposed to replace currently used Orthogonal Frequency Division Multiplexing (OFDM) technology. The impact of PA nonlinearity on FBMC signals has been investigated with the use of Bussgang theorem in [1] considering a widely accepted Saleh PA model. There, it has been established that OFDM and FBMC lead to similar performance in case of amplitude distortions, but a serious FBMC performance decrease is observed under phase distortions.

Digital predistortion (DPD) is one of the most commonly used technique for the compensation of PA nonlinearities. the principle of DPD consists in distorting the transmitted signal with a nonlinearity corresponding to PA inverse characteristic. The inverse function can be implemented in several ways differing in complexity as well as in linearization performance.

In order to account for memory effects, many approaches derived from Volterra series have been proposed such as polynomials with memory or generalized memory polynomials. Predistortion of FBMC signals is a very recent topic. In [2], the authors propose a DPD modeled by a multilayer perceptron neural network. In [3], we have performed experiments with DPD based on orthogonal polynomials for three different PA's. Similarly to other multi-carrier techniques, FBMC suffers from a high Peak to Average Power Ratio (PAPR) of the signal to transmit. In the last two decades, many methods for PAPR reduction have been proposed for the OFDM case [4]. These can be, with necessary modifications [5] due to the overlapping symbol structure of FBMC, tailored to the FBMC case. To ease-up the work of DPD, the combination of DPD with PAPR reduction is advantageous, [6].

The predistortion performance is affected by impairments of other RF components, such as, the IQ modulators, filters or the coupler in the feedback path of DPD. Several papers have discussed the effects of individual impairments and described methods for their compensation, e.g. [7] in the case of IQ mismatch. The pre-correction of anti-aliasing filter has been proposed in [8]. In those studies, the effect of RF transmitter impairments to DPD performance have been investigated and described for the case of individual impairments [9]. in this paper, we summarize their joint effect for practical values of RF impairments. We also investigate the influence of other uncertainties in the transmitter/feedback chain of DPD system, such as, the fractional sampling mismatch or unknown gain in the feedback path. Moreover, these analysis are done for FBMC input signals and direct conversion transmitter architectures. The paper is structured as follows. In section II, we briefly discuss the problem statement, i.e. the basics of FBMC and DPD techniques with the parameters used. In section III we point out the considered RF impairments and mismatches and we present the simulation results of their effect on DPD method applied to FBMC modulated signals. The conclusion then rounds up the paper.

## 12.2   Problem statement

### 12.2.1   Filter Bank Multi Carrier modulator

In the general multicarrier modulator, the output time-domain signal can be expressed as [10]:

$$x(t) = \sum_{n=-\infty}^{\infty} \sum_{s=0}^{S-1} X_{n,s} g_{n,s}(t), \tag{12.1}$$

where $X_{n,s}$ are symbols located on the $s$-th subcarrier at time instant $n$ and $g_{n,s}(t)$ is a basis (synthesis) function derived from a prototype filter $p(t)$ by the frequency and the time shift, such as:

$$g_{n,s}(t) = p(t - nT)e^{j2\pi sF(t-nT)}e^{j\frac{\pi}{2}(n+s)}. \tag{12.2}$$

Here $F$ and $T$ denote for the frequency and time separation.

Various prototype filters, including raised cosine, Hermite polynomials or PHYDYAS filters have been proposed. Similarly to the case of its predecessor, widespread in the 4-th generation of mobile communications - OFDM, the main part of the FBMC transmitter is the IFFT block. The filtering is then usually implemented using a polyphase network. Comparative study of various prototype filters have been published in [11], where the influence of the filter impulse response on the performance in doubly dispersive channels has been analyzed and compared to the case of OFDM, corresponding to the rectangular prototype filter. Due to the non-rectangular filtering operation, FBMC signals provide much lower adjacent channel emissions than is the case of OFDM (rectangular prototype filter corresponds to *sinc* in the frequency domain).

In order to deal with the overlapping of neighboring subcarriers caused by FBMC prototype filter, the information is sent in the interleaved way on the real/imaginary parts of IFFT inputs. Such approach is denoted as O-QAM/FBMC [12]. Similarly to OFDM, in this case it holds that $TF = 1$ and thus O-QAM/FBMC achieves the same spectral efficiency as OFDM, but with basis pulses localized in both time and frequency domain. Throughout our experiments, O-QAM/FBMC signal employing PHYDYAS filter with coefficients $p_1 = 0.972$, $p_2 = \frac{\sqrt{(2)}}{2}$ and $p_3 = 0.235$ [12] was used.

Recently [13, 14], several implementations of FBMC links based on the low-cost software defined radios, such as USRP, have been set-up, although the front-end parameters of the devices used (low dynamic range, nonlinearity, quadrature modulator imbalances) do not allow to fully exploit the FBMC advantages.

### 12.2.2  Digital predistortion subsystem

The typical digital predistortion chain consists of following main components: digital-to-analog (DAC) and analog-to-digital (ADC) data converters, filters and up/down converters. The signal is amplified over non-linear PA. Current technology and software radio in particular, can be used for digital predistortion implementation. Such radios usually use direct-conversion approach, also known as a homodyne receiver. Although the simplification by performing only a single-frequency conversion reduces the basic circuit complexity, other issues emerge. Unfortunately the IQ imbalance is one of the most performance-limiting issues in such a concept.

As stated above, in this paper we investigate the influence of various imperfections and uncertainties on digital predistortion (IQ imbalance, gain mismatch, fractional delay, number of bits of data converters, etc.) applied in the direct-conversion-based software defined radios as illustrated on Fig. 12.1.

For the consecutive simulations, a PA model and DPD model based on the orthogonal polynomial memory series (OMPS) [15] has been extracted from the measurements of a PA driven with FBMC signal described above. More details regarding DPD can be found in [15, 18]. The output of PA modeled using OMPS with nonlinear order $K$ and memory $M$ can be expressed as:
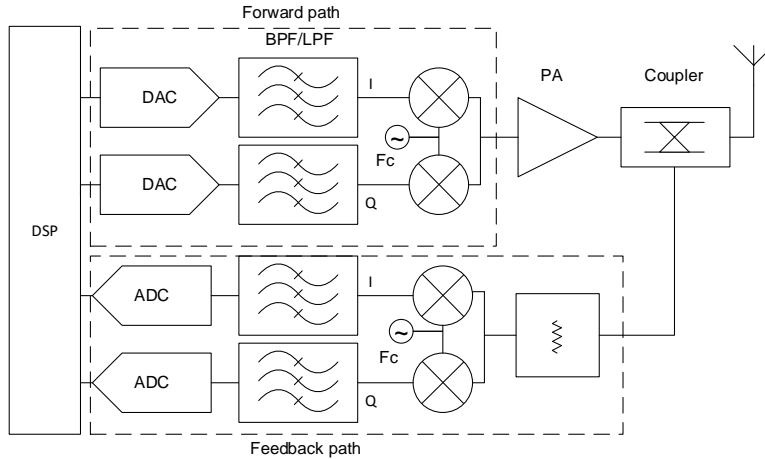
Figure 12.1: Overview of DPD implemented in the direct-conversion transceiver.

$$
\begin{aligned}
y(t) \;=\; & \sum_{k=1}^{K} \sum_{m=0}^{M} b_{k,m} \sum_{l=1}^{k} (-1)^{l+k} \cdot \\
& \cdot \; \frac{(k+l)!}{(l-1)!(l+1)!(k-l)!} |x(t-m)|^{k-1} x(t-m),
\end{aligned}
\tag{12.3}
$$

where $K$ is polynomial order, $M$ is memory depth, $y$ is the baseband output of PA and $x$ is the baseband input.

In our case, the complex coefficients $b_{k,m}$ were estimated using least-squares criterion considering order $K = 5$ and memory depth $M = 0$. This lead to OMPS coefficients $b_{PA} = [0.5 + 1.1i; -0.1 - 0.2; -0.03 - 0.03i; -0.004 - 0.002i; 0.003 - 0.004i]$. Note that the OMPS were used for digital predistortion as well.

In order to evaluate the performance of DPD we used difference between Adjacent Channel Power Ratio (ACPR) of power amplifier output without DPD and ACPR of PA output with DPD. The adjacent channel power ratio of a wireless communication signal describes the ratio between the integrated power in the carrier channel relative to the adjacent channel. If the bandwidth of the signal is $BW$ then the adjacent channel can be defined as $\pm \frac{BW}{2} \pm BW$. In the following we denote such difference as *ACPR Improvement*. To achieve the best linearization performance, the structure of DPD, i.e. its nonlinearity order and memory depth, were individually adjusted by exhaustive search for each imperfection under investigation.

## 12.3 Digital Predistortion Chain Imperfections

In the architecture of DPD shown in Fig. 12.1, several analogue circuit components are necessary. Due to the technological constraints, the imperfections of such components are the source of signal distortions leading to DPD performance degradation. In the

following paragraphs we would like to investigate sensitivity of predistortion as a whole to the imperfections of RF components used in the homodyne architecture.
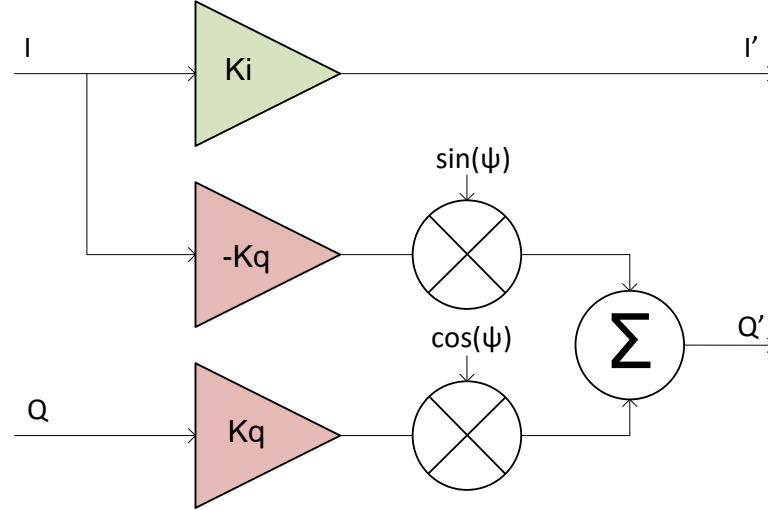


Figure 12.2: IQ Imbalance model.

### 12.3.1 Forward/Feedback path IQ Imbalance

IQ imbalances occur due to mismatch between the parallel sections processing the In-phase (I) and Quadrature (Q) signal paths. The IQ mismatch with cross-mixing component can be modeled similarly to a real-valued model used in [16]:

$$\begin{bmatrix} I' \\ Q' \end{bmatrix} = \begin{bmatrix} K_i & 0 \\ -K_q sin(\psi) & K_q cos(\psi) \end{bmatrix} \begin{bmatrix} I \\ Q \end{bmatrix},$$

(12.4)

where $K_i$ and $K_q$ represent the mismatched gains (amplitude imbalance - can be put either inside I or Q branch), $\psi$ is a phase imbalance, $I$ and $Q$ are non-distorted in-phase and quadrature signals and $I'$, $Q'$ are distorted signals. The visual representation of such model can be seen in Fig. 12.2.

As shown in Fig. 12.1, DPD contains the quadrature up- and down-conversion in the forward and feedback path, respectively. In Fig. 12.3 and Fig. 12.4 we have evaluated DPD system sensitivity on the gain imbalance. In fact the $K_i = 1\ dB$ means that the gain $K_i$ is 1 $dB$ higher than $K_d$. The performance of DPD degrades significantly with increasing gain imbalance, but as expected, it does not depend whether we model the gain mismatch in I or Q branch and the results shown in both figures are similar. In the Fig. 12.5 there is a phase imbalance influence. For the sake of simplicity the DC offset is omitted.

As can be seen, the low gain imbalance is important. For the phase imbalance, higher tolerance is allowed. Nevertheless, ACPR degradation of almost 20 dB can be expected for current IQ converters with the phase imbalance values close to 0.1 degrees.
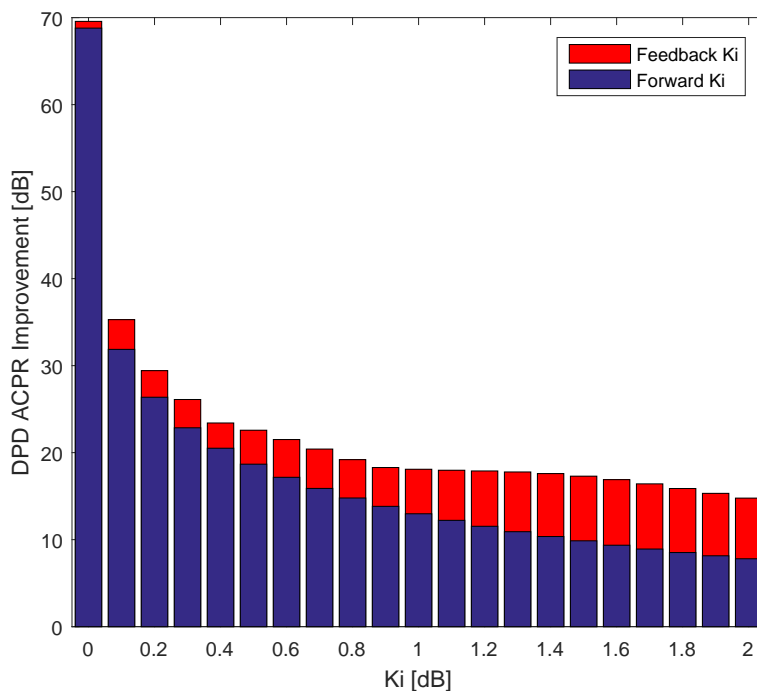
Figure 12.3: Influence of gain $K_i$ on DPD performance.
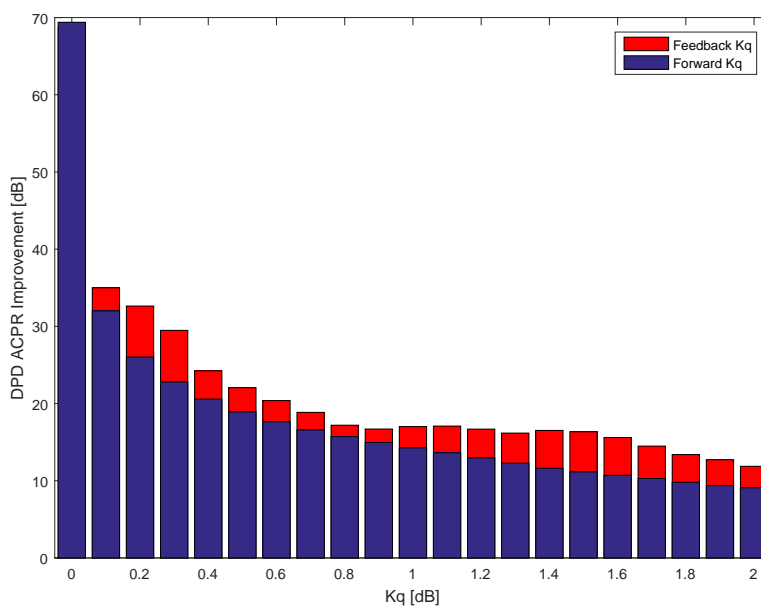


Figure 12.4: Influence of gain $K_q$ on DPD performance.

### 12.3.2   Forward/Feedback path Gain

The forward gain $G_f$ represents the scaling due to the DAC in the DPD forward path and $G_{fb}$ represents the improper attenuation and scaling of the signal in DPD feedback path. In practical systems, there is a back-off corresponding at least to PAPR of the
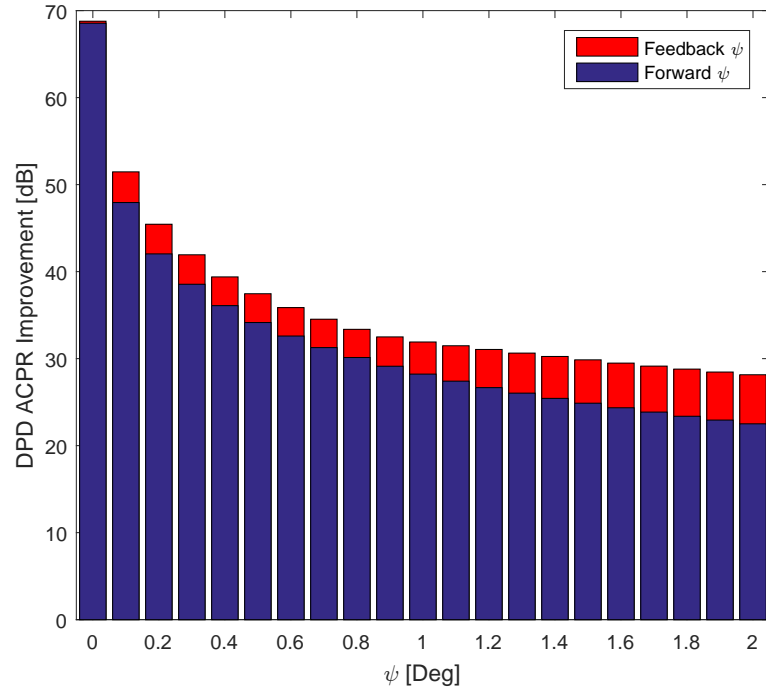
Figure 12.5: Influence of phase imbalance $\psi$ on DPD performance.

transmitted signal. On the contrary, when using simulations, the signals are usually normalized to $|1|$, guaranteeing the optimal values for DPD adaptation. The gain error of an ADC or DAC indicates how well the slope of an actual transfer function matches the slope of the ideal transfer function.

The gain mismatch effect on DPD is evaluated in Fig. 12.6. The improper gain choice leads to wrong PA output power, therefore the difference between the main channel power of the system without DPD and the system with DPD is also compared here.

As demonstrated, the proper gain selection in the feedback and forward paths is crucial to maintain DPD performance and to guarantee the required nominal PA output power.

### 12.3.3 Forward/Feedback path Number of Bits

The impact of data converters precision was also investigated. For the picture of effect, the selected bit precision is represented by additive white Gaussian noise (AWGN) corresponding to system dynamics only. As the amplitude of the AWGN is increased, the signal-to-noise ratio decreases. This results in increased uncertainty in time domain. From the results shown on Fig. 12.7 we may observe that the bit precision of the feedback ADC is less affecting DPD performance than in the case of the forward DAC.

### 12.3.4 Fractional delay in the DPD chain

In order to extract OMPS coefficients for a model from eq. 14.12, the baseband samples at the PA input $x$ have to be perfectly time-matched to the samples of PA output $y$.
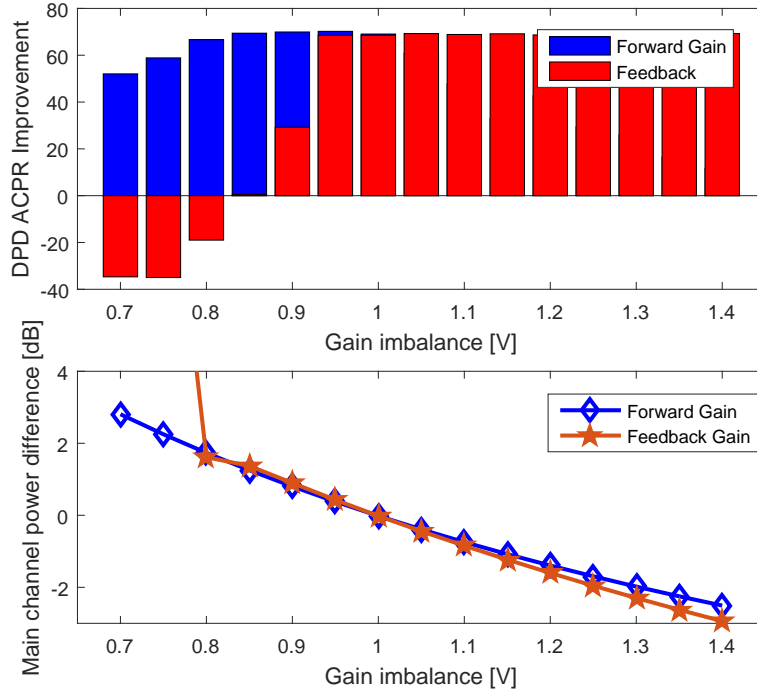
Figure 12.6: Influence of improper gains $G_f$ - forward and $G_{fb}$ - feedback (top) and resulting deviation of the main channel signal power (bottom).
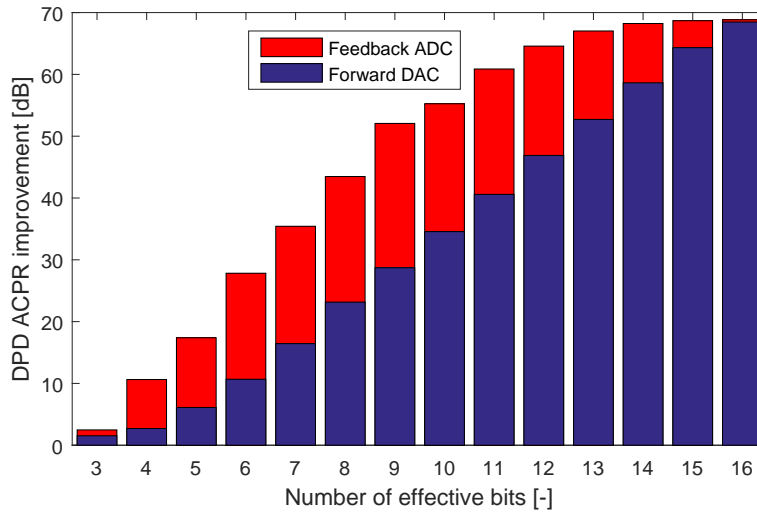


Figure 12.7: Influence of data converters resolution.

The same condition holds for the DPD adaptation as well. The fractional delay (in the meaning of irrational multiples of sampling period $T_s$) can be introduced by mismatch of digital to analog and analog to digital converters and by the physical delay of the analogue components, such as the power amplifier. The effect of fractional delay was introduced in our simulation model by the interpolation using Farrow filters [17].
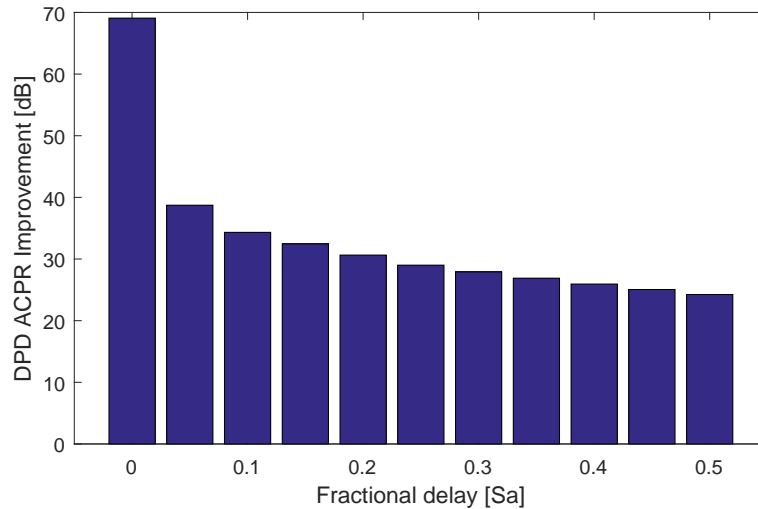
Figure 12.8: Influence of fractional delay on DPD performance.

The system sensitivity to fractional delay is displayed in Fig. 12.8. Note also that we expected that the integer delay between the signals can be perfectly estimated and compensated using e.g. well-known correlation techniques [18].

### 12.3.5 Power spectrum densities in the typical scenario

Even considering the excellent typical values (for example of state-of-the-art direct quadrature modulator STQ-2016) imperfections as $K_i = 0.2\ dB$, $K_q = 0\ dB$, $\psi = 0.5\ Deg$, perfectly compensated fractional delay $\tau_{fra} = 0$, no uncertainty in the forward gain $G_f = 1$ nor feedback gain $G_{fb} = 1$ and the use of 16 *bits* ADC and DAC converters, DPD performance degrades significantly. In such a case, DPD using OMPS ($K = 17$, $M = 0$) will gain only 25 $dB$ of ACPR improvement instead of ideal achievable improvement of 65 $dB$ in case of no imperfections. In Fig. 12.9 we may see power spectrum density comparison of ideal (green) and such a typical (violet) DPD system.

## 12.4 Conclusion

In this brief paper we have evaluated the influence of imperfections (IQ imbalances, data converters resolutions) and uncertainties (fractional delay in the feedback path, unknown gains) present in the direct-conversion-based transceivers on the performance of the Digital Pre Distortion system driven with a typical Filter Bank Multi Carrier signal. As we may see from the simulations, the sensitivity of DPD to imperfections is extensive. For our configuration, we have demonstrated that tuned homodyne system can improve only 25 $dB$ of ACPR and the advantage of FBMC approach over OFDM, i.e., the lower out-of-band emissions, can rapidly be smeared-out. Note that although such ACPR improvement surely depends on many factors, the results presented give a picture about the main limitations.
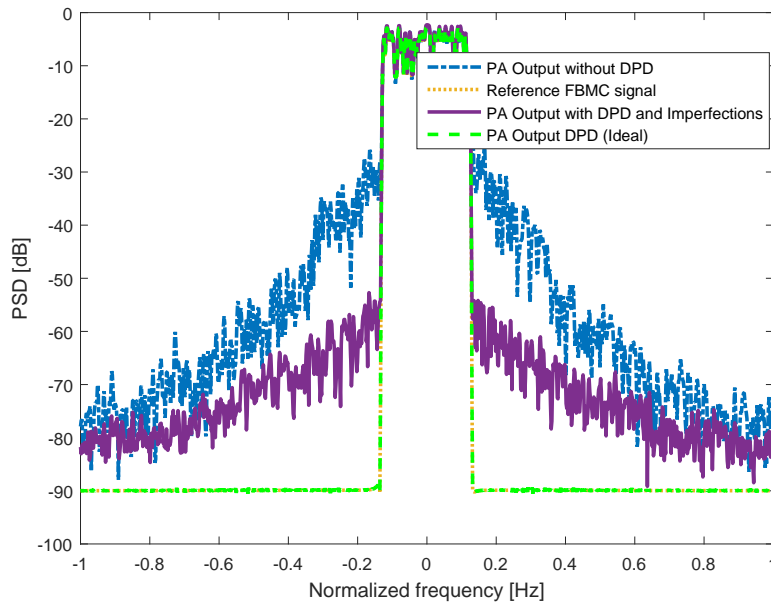
Figure 12.9: Power spectrum density of: blue - Output of PA without DPD, orange - reference transmitted FBMC signal, green output of PA with ideal DPD and violet - PA output with typical values of chain imperfections.

One solution to overcome the detrimental effects of transceiver imperfections to DPD performance would be precise imperfection compensation. Alternatively, the transceiver would drive the power amplifier directly with the signal just after D/A conversion and the feedback path would directly use A/D converted RF signal. Such idealized scheme is unfortunately not completely realizable due to the contemporary technology limits and can be currently employed hardly even for frequencies below 2 $GHz$. As an example 16 $bits$, 2.8 $GSPS$ DAC (AD9135) and 12 $bits$, 2 $GSPS$ ADC (AD9625) are available on the market. Such setup would provide ACPR improvement of 41 $dB$, that already outperforms the homodyne architecture.

## 12.5 Bibliography

[1] Bouhadda, H. and Shaiek, H. and Medjahdi, Y. and Roviras, D. and Zayani, R. and Bouallegue, R., Sensitivity analysis of FBMC signals to non linear phase distortion, IEEE International Conference on Communications Workshops (ICC 2014), June 2014, p. 73-78.

[2] Zayani, R. and Medjahdi, Y. and Bouhadda, H. and Shaiek, H. and Roviras, D. and Bouallegue, R., Adaptive Predistortion Techniques for Non-Linearly Amplified FBMC-OQAM Signals, IEEE 79th Vehicular Technology Conference (VTC Spring 2014), May 2014, p. 1-5.

[3] T. Gotthans and R. Marsalek and J. Blumenstein and G. Baudoin, Experimental evaluation of digital predistortion with FBMC and OFDM signals, 16th Annual

IEEE Wireless and Microwave Technology Conference (WAMICON 2015), April 2015, p. 1-3.

[4] Marsalek, R. and Fedra, Z., Reduced Complexity Adaptive Symbol Selection Method for OFDM PAPR Reduction, 7th Nordic Signal Processing Symposium (NORSIG), June 2016, p. 286-289.

[5] S. S. Krishna Chaitanya Bulusu, Hmaied Shaiek; Daniel Roviras, Potency of trellis-based SLM over symbol-by-symbol approach in reducing PAPR for FBMC-OQAM signals, IEEE International Conference on Communications (ICC) 2015, p. 4757 - 4762.

[6] Gouba, O.A. and Louet, Y., Adding signal for peak-to-average power reduction and predistortion in an orthogonal frequency division multiplexing context, IET Signal Processing, Vol. 7, No. 9, Dec 2013, p. 879-887.

[7] Antilla, L. et al., Recursive learning-based joint digital predistorter for power amplifier and I/Q modulator impairments, *International Journal of Microwave and Wireless Technologies*, 2010, 2(2), p. 173–182.

[8] Gettings, K.; Bolstad, A.; Chen, S.-Y.S.; Ericson, M.; Miller, B.A.; Vai, M., Low Power Sparse Polynomial Equalizer (SPEQ) for Nonlinear Digital Compensation of an Active Anti-Alias Filter, in *2012 IEEE Workshop on Signal Processing Systems (SiPS)* ,p. 249-253.

[9] Gotthans, T.; Baudoin, G.; Mbaye, A., Influence of delay mismatch on digital pre-distortion for power amplifiers, in *20th International Conference Mixed Design of Integrated Circuits and Systems (MIXDES)*, 2013, p. 490-493.

[10] R. Nissel and M. Rupp, On pilot-symbol aided channel estimation in FBMC-OQAM, International Conference on Acoustics, Speech and Signal Processing (ICASSP), Shanghai, 2016, p. 3681-3685.

[11] Sahin, A., Guvenc, I., Arslan, H., A comparative Study of FBMC Prototype Filters in Doubly Dispersive Channels, In Proceedings of The 8th Broadband Wireless Access Workshop, GlobeCom 2012, p. 1-7.

[12] M. Bellanger, Filter banks and OFDM-OQAM for high throughput wireless LAN, Communications, in *3rd International Symposium on Control and Signal Processing, 2008*. ISCCSP 2008. , St Julians, 2008, pp. 758-761.

[13] A. Dziri, C. Alexandre, R. Zakaria and D. Le Ruyet, SDR based prototype for filter bank based multi-carrier transmission, 2014 11th International Symposium on Wireless Communications Systems (ISWCS), Barcelona, 2014, pp. 878-882.

[14] B. Horvath and P. Bakki, Implementation of FBMC transmission link using SDR, 23rd International Conference Radioelektronika, Pardubice, 2013, pp. 320-323.

[15] Raich et al., Orthogonal Polynomials for Power Amplifier Modeling and Predistorter Design,IEEE Trans. on Vehicular Technology, vol.53, No.5, 2004

[16] M. Petit and A. Springer, Analysis of a Properness-Based Blind Adaptive I/Q Filter Mismatch Compensation, IEEE Transactions on Wireless Communications, vol. 15, no. 1, pp. 781-793, Jan. 2016.

[17] F. M. Gardner, Interpolation in digital modems,Part I: Fundamentals, IEEE Trans. Commun., vol. 41, pp. 501-507, 1993

[18] H. Li, D. H. Kwon, D. Chen and Y. Chiu, A Fast Digital Predistortion Algorithm for Radio-Frequency Power Amplifier Linearization With Loop Delay Compensation, in IEEE Journal of Selected Topics in Signal Processing, vol. 3, no. 3, pp. 374-383, June 2009.

# 13. Reduced Feedback Complexity MIMO Digital Predistortion of Power Amplifiers for FBMC Systems

**Abstract**

In this paper we presented a reduced complexity digital predistortion of multiple power amplifiers. The reduction was based on using only one feedback path. First the theoretical basics were presented. Then the experiment in this paper was trying to give an answer whether the predistortion can be used with limited number of feedback paths. As a test signal we have used a FBMC which was considered as a potential candidate for future 5G systems.

## 13.1   Introduction

For the future radio systems where the amount of transfered data rises, the requirements for more efficient technologies arises. In modern communication systems orthogonal frequency division multiplexing signals (OFDM) with cyclic prefix are established as the most popular type of multi carrier modulation [1]. But using cyclic prefix e.g. for LTE 10MHz loses of data-rates are about 16%. It was proved that using multi-carrier modulations (MCM) is an efficient way of transmission [2] and has better resistance to multi-path channels than single carrier modulations. The key technologies that have been lately discussed for the future 5G networks are: non-orthogonal multiple access, millimeter frequencies, 3D massive MIMO, cognitive spectrum radio sensing, ultra wide-band signals, ultra dense networks (UDN) with heterogeneous cells (HetNet), multiple technology carrier aggregation and filtered bank multi-carrier (FBMC) signals [3], [4].

FBMC systems are basically a subclass of multicarrier (MCM) systems. While its basic principle, dividing frequency spectrum into many narrow subchannels, may not be new, MCM systems have seen wide adoption in recent years (LTE, WLAN). FBMC modulation can be considered as an evolved OFDM. While FBMC is a step in the right direction it is still not optimal as many issues are arising when applying practical system settings [5]. Unfortunately MIMO extension is still not straightforward if maximal spectral efficiency is desired.

One of problems of MIMO digital predistortion (DPD) is its required complexity of feedback path. We can expect that the power amplifiers in the transmission path are quite similar, but yet we need the same number of feedback paths as the number of channels. This paper deals with reduced complexity of feedback path even when one of the power amplifier shows failure in the terms of reduced gain.

The paper is organized as follows: the first section brings the introduction to FBMC modulation, then we present the digital predistortion followed by a problem of multiple transmission channels statement. The forthcoming section presents the tested power amplifiers ensued by experimental evaluation. Finally we conclude in the last section.

## 13.2   FBMC Modulation

There exists several types of FBMC, but so-called staggered multi-tone (SMT) exhibits higher spectral efficiency and is more heavily promoted. To achieve a time-frequency efficiency of 1 SMT needs to stagger the multi-carrier symbols in time, therefore offset-QAM (OQAM) has to be applied. Filtering functionality is based on a per subcarrier basis. Which means, the frequency response of the filter needs to be rather tight, requiring long filter lengths (relative to the length of a single symbol). Typically filter lengths of three or four times the symbol [6]. The general modulation can be described as:

$$x[t] = \sum_{m=-\infty}^{+\infty} \sum_{k=0}^{N-1} (\theta^k \Re\{X_k[m]\} h[t - m\ N] +$$

$$\theta^{k+1} \Im\{X_k[m]\} h[t - m\ N - \frac{N}{2}]) \ e^{j\frac{2\pi}{N}k(t-mN)}, \tag{13.1}$$

where $X_k$ is a modulation part of a symbol, $\theta^{k+1}$ is real part phase rotation vector for the imaginary part $\theta^k$ respectively, $h[.]$ is general prototype filter for each sub-carrier with impulse response length $L = KN$ with $K$ so-called overlapping factor and $N$ number of sub-carriers. The filter impulse response of fourth order overlap (taken from the PHYDAS [7]) can be written as:

$$h(1+i) = 1 \quad - \quad 2H_1 \cos(\frac{\pi i}{2N}) + 2H_2 \cos(\frac{\pi i}{N})$$

$$- \quad 2H_3 \cos(\frac{3\pi i}{2N}), \tag{13.2}$$

where filter coefficients are $H_1 = 1$, $H_2 = 0.972$, $H_3 = \frac{\sqrt{(2)}}{2}$ and $H_4 = 0.235$.

Due to filtering properties, the dynamical range (adjacent channel power ratio resp.) of FBMC signal is huge. We may expect to have the the ACPR corresponding to dynamical range of DACs. The general difference and compatibility with OFDM systems can be seen in Fig. 13.1.
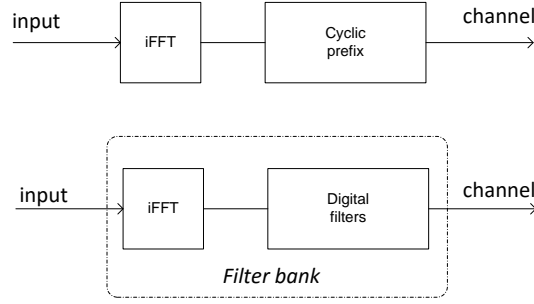
Figure 13.1: General difference between Orthogonal frequency division multiplexing signals (OFDM) with cyclic prefix (Top) and Filter Bank based Multicarrier (FBMC) transmitter (Bottom).

## 13.3 Digital predistortion

Digital predistortion is one of the techniques used for overcoming the non-linear behavior of PA [8]. As already published in [9] the non-linear regime is related with PA efficiency, but also with spectrum widening, memory effects, etc. Generally as predistorters the Volterra based models are used. Demonstrating the DPD and overcoming the complexity of the general Volterra series, an effective model pruning method, called dynamic deviation reduction (DDR) [10, 11, 12] was used. A simplified version of the model is defined by:

$$
\begin{aligned}
z(t) = & \sum_{k=0}^{\frac{K-1}{2}} \sum_{i=0}^{M} g_{2k+1,1}(i) \, |x(t)|^{2k} x(t-i) \\
& + \sum_{k=1}^{\frac{K-1}{2}} \sum_{i=1}^{M} g_{2k+1,2}(i) \, |x(t)|^{2(k-1)} x^2(t) x^*(t-i) \\
& + \sum_{k=1}^{\frac{K-1}{2}} \sum_{i=1}^{M} g_{2k+1,3}(i) |x(t)|^{2(k-1)} \, x(t) |x(t-i)|^2 \\
& + \sum_{k=1}^{\frac{K-1}{2}} \sum_{i=1}^{M} g_{2k+1,4}(i) |x(t)|^{2(k-1)} \, x^*(t) x^2(t-i).
\end{aligned}
\tag{13.3}
$$

With the DPD input $x(t)$ matrices can be arranged as follows:

$$
\begin{aligned}
\Phi_{k,i}(x(t)) & = [|x(t)|^{2k} x(t-i), \\
& \dots \quad |x(t)|^{2(k-1)} x^2(t) x^*(t-i), \\
& \dots \quad |x(t)|^{2(k-1)} \, x(t) |x(t-i)|^2, \\
& \dots \quad |x(t)|^{2(k-1)} \, x^*(t) x^2(t-i)], \\
\mathbf{g} & = [g_{1,0}, g_{2,0}, \dots, g_{1,1}, \dots, g_{1,M}, \dots, g_{K,M}]^T \\
\Phi & = [\Phi_{1,0}(u(t)), \dots, \Phi_{K,M}(u(t))].
\end{aligned}
$$

Their structure is determined by 2 parameters: $K$ the non-linearity order and $M$ the memory length. The number of coefficients $g$ is $2MK + (\frac{K+1}{2})) - M$. The problem can be expressed in matricial notations with:

$$
\begin{aligned}
\mathbf{z} &= [z(0), z(1), ..., z(S-1)]^T \\
\mathbf{x} &= [x(0), x(1), ..., x(S-1)]^T \\
\mathbf{e} &= [e(0), e(1), ..., e(S-1)]^T.
\end{aligned}
$$

Using the indirect learning architecture of [REF] DPD the criteria can be written as:

$$
J = \min_{g} ||\hat{\mathbf{z}} - \mathbf{z}||^2, \tag{13.4}
$$

where $\hat{\mathbf{z}}$ is feedback path and the forward is similarly arranged as:

$$
\mathbf{z} = \mathbf{U}\mathbf{g}. \tag{13.5}
$$

Then the Least-squares (LS) solution of (13.5) can be written:

$$
\mathbf{g} = (\mathbf{U}^H\mathbf{U})^{-1}\mathbf{U}^H\mathbf{z} = \mathbf{U}^+\mathbf{z}, \tag{13.6}
$$

where $(.)^H$ represents Hermitian transpose and $\mathbf{U}^+$ denotes Moore - Penrose pseudo-inverse.

## 13.4 Problem statement

In the case of multiple transmitters (that are especially involved in the MIMO systems) the problem complexity with DPDs increase linearly with number of transmitters, because with standard architecture of DPD the same number of feedback channels have to employed as displayed in the Fig.13.2. Each channel have to have at least 3 times larger bandwidth (meaning increased sampling frequency) for capturing the non-linear phenomenas. Each channel coefficients have to be estimated separately which is not an easy task on FPGAs. Such criteria drastically increase the overall complexity. The practical question related with MIMO DPD is if we could reduce the number of feedback paths assuming certain similarities between PAs. Therefore we would like to investigate the case where only one feedback path is employed and taken as a reference as shown in Fig.13.3.

The knowledge of PA gain is important. The gain of PA with feedback $s_{21FB}$ is considered as a reference. Then we may calculate using the gain of actual predistorted PA scattering parameters $s_{21act}$, the difference $s_\Delta$ to a reference $s_{21FB}$:

$$
s_\Delta(f_c) = \frac{s_{21FB}(f_c)}{s_{21act}(f_c)}, \tag{13.7}
$$

because the scattering parameters are a function of frequency, we have chosen only $f_c$ - a carrier frequency. Then the estimation yields to:

$$
\mathbf{g} = s_\Delta(f_c)\mathbf{U}^+\mathbf{z}. \tag{13.8}
$$

It is obvious from (13.8) that the coefficients for PAs without feedback $\mathbf{g}_{mod}$ can be calculated as:

$$
\mathbf{g}_{mod} = \frac{1}{s_\Delta(f_c)}\mathbf{g}. \tag{13.9}
$$
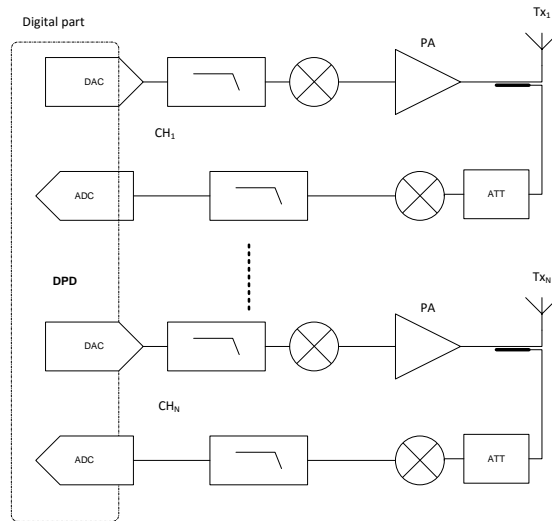
Figure 13.2: Standard layout for MIMO digital predistortion transmitter with $N$ channels.
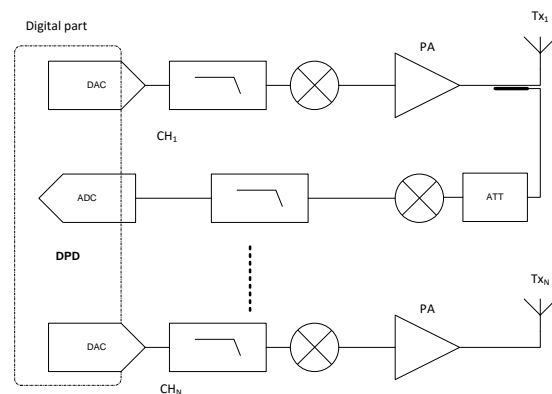


Figure 13.3: Proposed simplified layout for MIMO digital predistortion transmitter with $N$ channels.

## 13.5 Power Amplifier

Concerning the evaluation of proposed simplification, five power amplifiers have been designed. Each PA is made of the ADL5610, a single-ended RF/IF gain block amplifier, that provides broadband operation from 30 MHz to 6 GHz. The ADL5610 provides a low noise figure of 2.2 dB with a very high OIP3 (at 900 MHz) of more than 38 dBm simultaneously, which delivers a high dynamic range. The one-dB compression point is 20.4 dBm at 900 MHz.

The ADL5610 provides a gain of 18 dB, which is stable over frequency, temperature, and power supply, and from device to device. The amplifier is offered in the industry-standard SOT-89 package and is internally matched to 50 $\Omega$ at the input and output, making the ADL5610 easy to implement in a wide variety of applications. The only

external parts required are the input and output ac coupling capacitors, power supply decoupling capacitors, and bias inductor.

In order to guarantee dispersion of designing process, the components have been ordered from three different suppliers. The PA with failure is made with much higher capacitive load at the output that should simulate capacitive short circuit. It can be seen in the measured $S_{21}$ parameters, where the capacitive load behaves for higher frequencies as a short circuit. We believe, that such process is a good example of practical performance degradation.

## 13.6  Experimental evaluation

In order to prove the concept, the experimental test-bench was assembled. First the gain characteristics of PAs have been measured network analyzer E5071C (with E-Cal set N4433A) in the range of 50 MHz to 6 GHz as shown in Fig.13.6. The signal-processing and additional post-processing has been done with MATLAB that was communicating with Rohde&Schwarz generator SMU200A and with real-time spectrum analyzer Rohde&Schwarz FSVR. The generator was synchronized with analyzer using external 10 MHz reference signal and the beginning of test sequence was triggering the acquisition with signal marker. Then in PC additional processing using MATLAB have been done (such as integer synchronization based on correlation, fractional synchronization based on Farrow filters, etc.). The generated FBMC signal had 1024 sub-carriers and prototype filter of fourth order was used [7]. The total generated data sequence had 16384 samples. The signal had oversampling ratio 2, sampling frequency $f_s = 100\ MHz$, with carrier frequency $f_c = 2.4\ GHz$, and with inner OQAM modulation level $M = 4$. Therefore the total bandwidth of transmitted signals was $BW = 24\ MHz$. The equipment with high dynamical ranges and low noise figures had to be threated very carefully for taking advantage of FBMC properties [13, 14, 15].

In the Fig. 13.4 we may see the AMAM characteristics of measured power amplifiers. It also shows, that 4 PAs have nearly similar characteristics (alike shape of nonlinearities), but the one with the failure (violet). The same can be observed in the power spectrum density in the Fig.14.1.

At least the setup was assembled as in the Fig. 13.3. The PA1 was used as a reference PA with feedback. Then the predistortion of other PA have been done on blind having only the knowledge of $s_{21}$ parameters. The measured screenshot from spectrum analyzer can be found in the Fig.13.7. We may see, that the predistortion improve the ACPR for about 8 dB for all PAs.

## 13.7  Conclusion

In this paper we have presented a problem with multiple transmitting channels employing digital predistortion. Standard solution e.g. having feedback for each channel is complex and expensive. We have proposed a solution when the knowledge of scattering
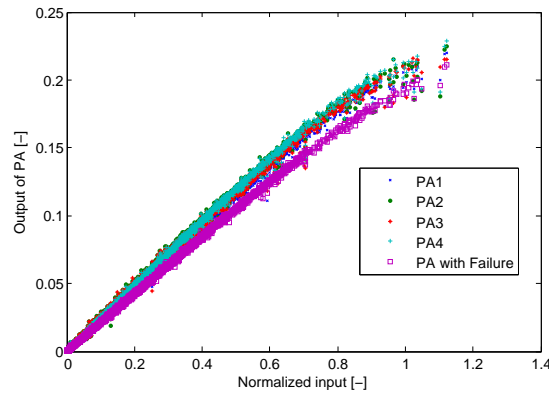
Figure 13.4: AMAM characteristics for four power amplifiers with similar parameters and one PA with degraded performance (violet curve).
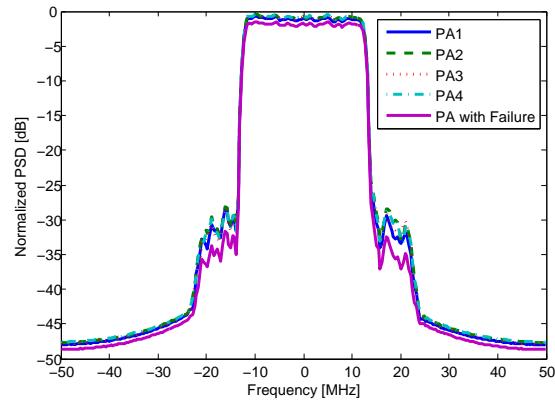


Figure 13.5: Normalized power spectrum density (PSD) for output of four non-linear power amplifiers with similar parameters and one PA with degraded performance (violet curve).
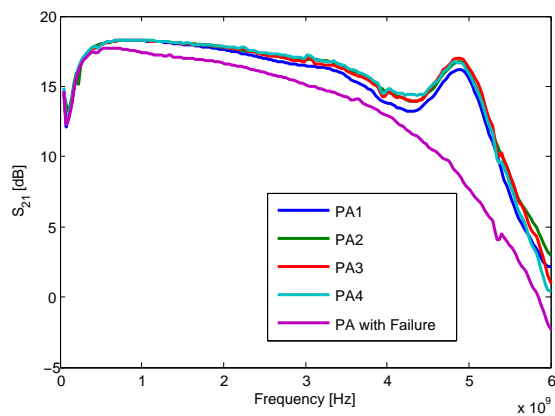


Figure 13.6: Scattering parameters (namely $S_{21}$) for four power amplifiers with similar parameters and one PA with degraded performance (violet curve).
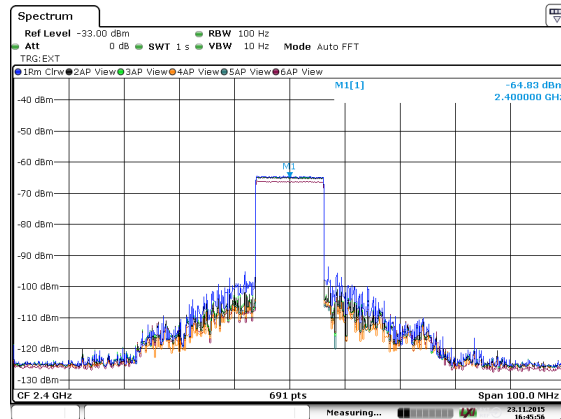
Figure 13.7: Screenshot of real-time spectrum analyzer FSVR with DPD (with feedback on the PA1) orders $K = 5$ and $M = 1$. Trace 1 is PA1 without DPD and traces with DPD are: trace 2 is PA1 (black), trace 3 is PA2 (green), trace 4 is PA3 (orange), trace 5 is PA4 (light blue) and trace 6 is PA with failure (violet).

parameters ($s_{21}$) of each amplifier can reduce the number of feedbacks. In order to prove the concept, we have build five different PAs using part from different suppliers providing an essential variance of properties. One PA was intensionally designed with capacitive load at the output simulating failure.

In this paper we have demonstrated that in the case of very close behavior of PAs we may reduce the complexity, keeping the performance of DPD quite high.

## 13.8  Bibliography

[1]  H. Zhang, D. Le Ruyet, and M. Terre, "Spectral efficiency comparison between ofdm-oqam- and ofdm-based cr networks," *Wirel. Commun. Mob. Comput.*, vol. 9, no. 11, pp. 1487–1501, Nov. 2009. [Online]. Available: http://dx.doi.org/10.1002/wcm.v9:11

[2]  J.-B. Dore, V. Berg, N. Cassiau, and D. Ktenas, "Fbmc receiver for multi-user asynchronous transmission on fragmented spectrum," *EURASIP Journal on Advances in Signal Processing*, vol. 2014, no. 1, p. 41, 2014. [Online]. Available: http://asp.eurasipjournals.com/content/2014/1/41

[3]  H. Lin and P. Siohan, "Multi-carrier modulation analysis and wcp-coqam proposal," *EURASIP Journal on Advances in Signal Processing*, vol. 2014, no. 1, 2014. [Online]. Available: http://dx.doi.org/10.1186/1687-6180-2014-79

[4]  J. Nadal, C. Abdel Nour, A. Baghdadi, and H. Lin, "Hardware prototyping of FBMC/OQAM baseband for 5G mobile communication systems," in *RSP 2014 : IEEE International Symposium on Rapid System Prototyping*, 2014, pp. 135 – 141.

[5]  T. Gotthans, R. Marsalek, J. Blumenstein, and G. Baudoin, "Experimental evaluation of digital predistortion with fbmc and ofdm signals," in *Wireless and Microwave Technology Conference (WAMICON), 2015 IEEE 16th Annual*, April 2015, pp. 1–3.

[6]  A. Sahin, I. Guvenc, and H. Arslan, "A survey on multicarrier communications: Prototype filters, lattice structures, and implementation aspects," *Communications Surveys Tutorials, IEEE*, vol. 16, no. 3, pp. 1312–1338, Third 2014.

[7]  T. Ihalainen, A. Viholainen, T. Stitz, and M. Renfors, "Generation of filter bank-based multicarrier waveform using partial synthesis and time domain interpolation," *Circuits and Systems I: Regular Papers, IEEE Transactions on*, vol. 57, no. 7, pp. 1767–1778, July 2010.

[8]  T. Gotthans, R. Marsalek, M. Pospisil, J. Blumenstein, and G. Baudoin, "Experimental verification and comparison of polynomials and luts predistortion techniques," in *Radioelektronika (RADIOELEKTRONIKA), 2015 25th International Conference*, April 2015, pp. 309–312.

[9]  J. K. Cavers, "Amplifier linearization using a digital predistorter with fast adaptation and low memory requirements," *Vehicular Technology, IEEE Transactions on*, vol. 39, no. 4, pp. 374–382, 1990.

[10] Z. Anding, J. C. Pedro, and T. J. Brazil, "Dynamic deviation reduction-based volterra behavioral modeling of rf power amplifiers," *Microwave Theory and Techniques, IEEE Transactions on*, vol. 54, no. 12, pp. 4323–4332, 2006.

[11] T. Gotthans, G. Baudoin, and A. Mbaye, "Comparison of modeling techniques for power amplifiers," in *Radioelektronika (RADIOELEKTRONIKA), 2013 23rd International Conference*, 2013, pp. 232–235.

[12] Z. Anding, P. Draxler, J. Yan, T. Brazil, D. Kimball, and P. Asbeck, "Open-loop digital predistorter for rf power amplifiers using dynamic deviation reduction-based volterra series," *Microwave Theory and Techniques, IEEE Transactions on*, vol. 56, no. 7, pp. 1524–1534, 2008.

[13] H. Bouhadda, H. Shaiek, D. Roviras, R. Zayani, Y. Medjahdi, and R. Bouallegue, "Theoretical analysis of ber performance of nonlinearly amplified fbmc/oqam and ofdm signals," *EURASIP Journal on Advances in Signal Processing*, vol. 2014, no. 1, p. 60, 2014. [Online]. Available: http://asp.eurasipjournals.com/content/2014/1/60

[14] Z. Kollár and P. Horváth, "Papr reduction of fbmc by clipping and its iterative compensation," *Journal of Computer Networks and Communications*, vol. 2012, 2012.

[15] L. Varga and Z. Kollar, "Low complexity fbmc transceiver for fpga implementation," in *Radioelektronika (RADIOELEKTRONIKA), 2013 23rd International Conference*, April 2013, pp. 219–223.

[16] Y. Medjahdi, M. Terre, D. Le Ruyet, D. Roviras, and A. Dziri, "Performance analysis in the downlink of asynchronous ofdm/fbmc based multi-cellular networks," *Wireless Communications, IEEE Transactions on*, vol. 10, no. 8, pp. 2630–2639, August 2011.

# 14. Wideband Digital Predistortion with Sub-Nyquist Nonuniform Sampling and Reconstruction of Feedback Path

**Abstract**

We consider the problem of periodic nonuniform sampling of a multiband signal and its reconstruction from samples in the feedback path of a digital predistortion system in order to decrease the sampling rate, hence to increase the bandwidth of digital predistortion system. Such considerations are particularly important in context of the wideband multiband linearization system design.

## 14.1 Introduction

There is a long history investigating sampling theory. The most fundamental work of Whittaker-Kotelnikov-Shannon is widely known and it states that a low-pass signal bandlimited to the frequency range $(-f_{max}, f_{max})$ can be perfectly reconstructed from its uniform time samples taken no less than on Nyquist rate $f_{nyq} = 2f_{max}$ [1]. Another pioneering work sets a lower bound of sampling density on the sampling scheme required for a perfect reconstruction [2]. For multiband signals this fundamental lower bound is given by the Lebesgue measure of spectral support of Fourier transform of the signal [3]. Landau's bound is often lower than Nyquist rate due to sparsity of such signals[4]. From the practical point of view, the sub-Nyquist sampling is very important in many applications such as magnetic resonance imaging, where it is impossible to collect many samples, synthetic aperture radars, or spectral sensing [5, 6] where the sparsity is successfully exploited.

In modern wireless communication systems, a demand for speed is rapidly growing. One of the solutions delivering higher data rates is to widen the bandwidth of signals. Broadening the bandwidth is usually connected with unwanted non-linear effects of power amplifiers (PA) [7]. An example of very high bandwidth system is the second-generation satellite digital video broadcast DVB-RCS2 return channel via satellite air interface, which can be used for supporting future demands for Tbit/s traffic requirements [8].

To mitigate the non-linearity and memory effects introduced by the power amplifiers (PA), the natural step is to use the digital predistortion (DPD) techniques. In

order to create an adaptive digital predistortion, the feedback path is used [9]. There exist a thumb rule, that the bandwidth of the feedback path should be at least three times larger than the bandwidth of the transmitted signal. There are works dealing with band-limited feedback path [10, 11]. In case of sparse wideband concurrent multiband signals, most conventional wideband digital predistortion techniques require the use of a very high-speed analog-to-digital converter (ADC) in the feedback path. We note that problem of reconstruction using sub-band filter banks is fundamentally different.

In the literature there are several works dealing with sparse signal reconstruction such as Xampling [12] using the modulated wideband converter which multiplies the analog signal by a bank of periodic waveforms resulting in overlayed spectrum and then digital reconstruction is performed. Over the recent years multi-coset (MC) sampling has gained fair popularity and several methods of implementing the MC sampling have been proposed. MC sampling is a periodic non-uniform sampling technique which samples the signal at a rate lower than the Nyquist rate [4]. The most famous architecture is composed of several parallel branches, each with a time shift followed by an uniform sampler operating at the sampling rate lower than the Nyquist rate [3, 4]. In [13], the authors used the Synchronous Mutlirate Sampling - the uniform samplers operating at different rates. Recently, the dual-sampling architecture has been presented for multi-coset sampling [14], where a subset of the synchronous mutlirate Samplers was used (in fact only two uniform samplers).

## 14.2 Multicoset sampling

Numerically the non-uniform sampling is realized as follows. The analog signal $x(t)$ is sampled at Nyquist rate. Then the Nyquist grid is divided into successive segments of $L$ samples each. In each segment only $p$ samples, described by the set $\Delta$, out of $L$ are kept. From the parallel structure described in [4] we may write the reconstruction formula from its multicoset samples as:

$$x(t) = \sum_{i=1}^{p} \sum_{j=-\infty}^{\infty} x((\Delta_i + Lj)T)\phi_i(t - ((\Delta_i + Lj)T), \tag{14.1}$$

where sampling period $Ts = LT$, and $\Delta_i$ represents shifting in time. Functions $\phi_i$ $(i = 1, ..., p)$ are the interpolation filters [4]. The Fourier transform, $Xi(e^{j2\pi fT})$ of the sampled sequence $y_i[n]$ is related to the Fourier transform, $X(f)$, of the unknown signal $x(t)$ by the following matrix form of under-determined system:

$$y(f) = \mathbf{A}_\Delta \mathbf{s}(f), f \in B_0 = \left[ -\frac{1}{2LT}, \ \frac{1}{2LT} \right]. \tag{14.2}$$

$y(f)$ is a vector of size $p$ x 1 whose $i$-th element is given by:

$$y_i(f) = Xi(e^{j2\pi fT}). \tag{14.3}$$

$\mathbf{A}_\Delta$ is a matrix of size $p$ x $L$ whose $(i, l)$-th element is given by:

$$[\mathbf{A}_\Delta]_{il} = \frac{1}{LT} e^{\frac{j2\pi l\Delta_i}{L}}, 1 \leq i \leq p, 0 \leq l \leq L - 1 \tag{14.4}$$

and $s(f)$ represents the unknown vector of size $L$ x 1 with $l$-th element given by:

$$s_l(f) = X(f + \frac{l}{LT}), f \in B_0, 0 \leq l \leq L - 1. \tag{14.5}$$

### 14.2.1 Multicoset reconstruction

For a given signal $x(t)$, its spectral support $\Gamma$ is defined as the set of frequencies where the Fourier transform $X(f)$ does not vanish. The spectral span $[\Gamma]$ is defined as the smallest interval containing $\Gamma$. The total number of spectral support is denoted as $q$ (the number of active cells). Spectral index $\mathbf{k}$ is a set of indexes of a sub-cells that are contained in $\Gamma$:

$$\mathbf{k} = [k_i, ..., k_q], 0 \leq i \leq q, \tag{14.6}$$

where the reduced signal vector of size $q$ x 1 with $i$-th element given by is:

$$\mathbf{z}_i(f) = X(f + \frac{k_i}{L}) \tag{14.7}$$

and the reduced measurement matrix of size $p$ x $q$ whose $(i, l)$-th element then can be expressed as:

$$[\mathbf{A}_\Delta(k)]_{il} = \frac{1}{LT} e^{\frac{j2\pi k_l \Delta_i}{L}}, 1 \leq i \leq p, 1 \leq l \leq q. \tag{14.8}$$

Similarly as in equation (14.2) we may write:

$$\mathbf{y}(f) = \mathbf{A}_\Delta(k)\mathbf{z}(f), \tag{14.9}$$

with the solution by Moore-Penrose pseudoinverse:

$$\mathbf{z}(f) = (\mathbf{A}_\Delta^H \mathbf{A}_\Delta)^{-1} \mathbf{A}_\Delta^H \mathbf{y}(f). \tag{14.10}$$

## 14.3 Digital predistortion and PA model

In order to compensate the non-linearities or to model the PA, the orthogonal polynomial memory series (OMPS) have been proposed in [15]. The output of DPD system using OMPS with nonlinear order $K$ and memory depth $M$ can be expressed as:

$$y(t) = \sum_{k=1}^{K} \sum_{m=0}^{M} b_{k,m} \sum_{l=1}^{k} (-1)^{l+k} \cdot \tag{14.11}$$
$$\cdot \frac{(k+l)!}{(l-1)!(l+1)!(k-l)!} |x(t-m)|^{k-1} x(t-m),$$

where $K$ is polynomial order, $M$ is memory depth, $x$ and $y$ are the baseband input and output of the DPD.

During our simulations described below, we have used the memory-less PA model based on OMPS (memory depth $M = 0$). The model of PA was extracted from the experimental measurements. In our case, the complex coefficients $b_{k,m}$ were estimated using the least-squares criterion considering polynomial order $K = 5$. This lead to OMPS coefficients $b_{PA} = [0.5 + 1.1i; -0.1 - 0.2; -0.03 - 0.03i; -0.004 - 0.002i; 0.003 - 0.004i]$.

## 14.4   Simulations

We have used the concurrent multiband signal with 4 sub-bands and the total bandwidth of 500 MHz, therefore the Nyquist sampling frequency is $f_{nyq} = 1$ GHz as shown in Fig. 14.1. Each sub-band has the bandwidth of 25 MHz. The optimal reconstruction assumes that the number of sub-bands and the maximum bandwidth the band can have, are known. The value of $L = 128$ was used.

In order to evaluate the performance of OMPS DPD and sensitivity to the sampling
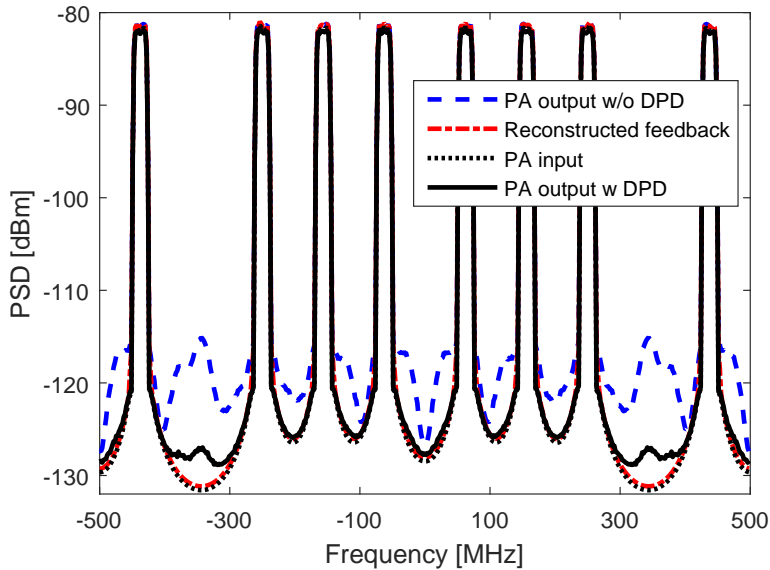


Figure 14.1: Power spectral densities for the proposed sub-Nyquist feedback DPD.

frequency, we used Adjacent Channel Power Ratio (ACPR) measured at center frequency 25 MHz with channel bandwidth 25 MHz. ACPR for PA output without DPD and ACPR for PA output with DPD is shown in Fig. 14.2 as a function of the sampling rate. ACPRs at different frequency allocations have also been simulated. The values have been similar to the case localized at 25 MHz. To achieve the best linearization performance, the structure of DPD, i.e., its nonlinearity order $K$ and memory depth $M$, were individually adjusted by exhaustive search for each sub-Nyquist sampling frequency under investigation. In Fig. 14.3, we show a normalized mean square error (NMSE) between the PA output signal and the signal reconstructed from its non-uniformly-spaced samples as a function of the sampling frequency.

## 14.5   Conclusion

We have proposed a new sub-Nyquist technique based on the multicoset non-uniform samplers for multiband Digital PreDistortion of the wideband sparse signals. The multicoset signal processing algorithm is used in the feedback path of DPD system. We have demonstrated its functionality and ACPR/NMSE performance on the case of the signal containing four sub-bands, each having 25 MHz bandwidth. Therefore the Landau
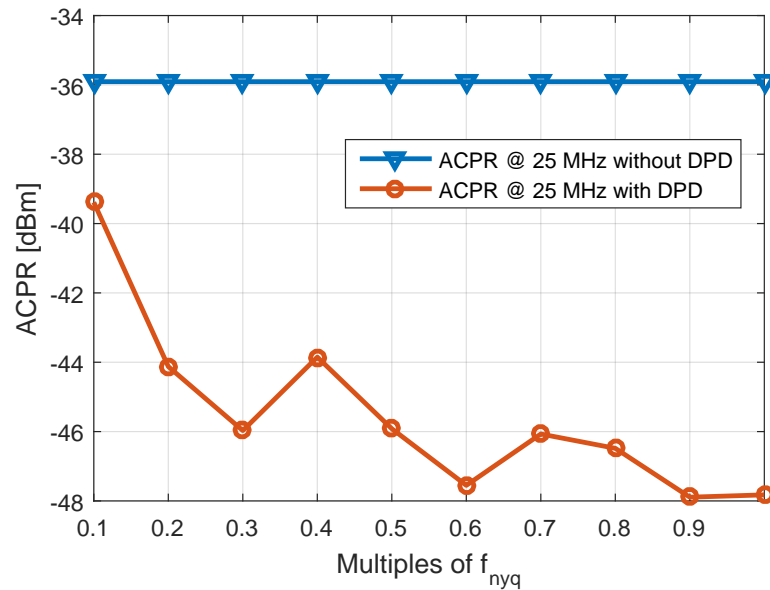
Figure 14.2: Simulated ACPR values under different multiples of $f_{nyq} = 1$ GHz.
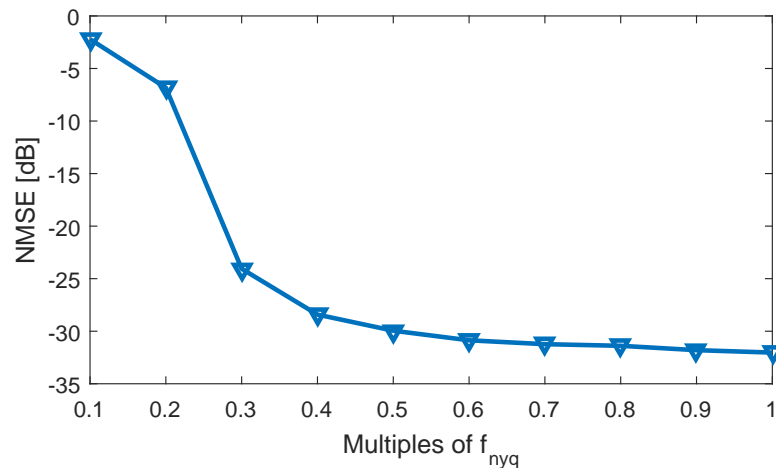


Figure 14.3: Normalized mean square error between PA output and reconstructed signal for different multiples of $f_{nyq} = 1$GHz.

sampling frequency is 100 MHz. Although in classical DPD systems, the signals have to sampled at least 3-times faster than the Nyquist rate is, in our experiment ACPR improvement of 12 dBm is achievable by OPMS DPD even for the sampling frequency of 0.6 $f_{nyq}$ (note that on the frequency 360 MHz the ACPR improvement would be more significant) .

## 14.6 Bibliography

[1] C. E. Shannon, "A mathematical theory of communication," *The Bell System Technical Journal*, vol. 27, no. 3, pp. 379–423, July 1948.

[2] H. J. Landau, "Sampling, data transmission, and the nyquist rate," *Proceedings of the IEEE*, vol. 55, no. 10, pp. 1701–1706, Oct 1967.

[3] R. Venkataramani and Y. Bresler, "Sub-nyquist sampling of multiband signals: perfect reconstruction and bounds on aliasing error," in *Acoustics, Speech and Signal Processing, 1998. Proceedings of the 1998 IEEE International Conference on*, vol. 3, May 1998, pp. 1633–1636 vol.3.

[4] ——, "Optimal sub-nyquist nonuniform sampling and reconstruction for multiband signals," *IEEE Transactions on Signal Processing*, vol. 49, no. 10, pp. 2301–2313, Oct 2001.

[5] M. Mishali and Y. C. Eldar, "Blind multiband signal reconstruction: Compressed sensing for analog signals," *IEEE Transactions on Signal Processing*, vol. 57, no. 3, pp. 993–1009, March 2009.

[6] D. D. Ariananda and G. Leus, "Compressive wideband power spectrum estimation," *IEEE Transactions on Signal Processing*, vol. 60, no. 9, pp. 4775–4789, Sept 2012.

[7] T. Gotthans, R. Maršálek, J. Blumenstein, and G. Baudoin, "Experimental evaluation of digital predistortion with fbmc and ofdm signals," in *Wireless and Microwave Technology Conference (WAMICON), 2015 IEEE 16th Annual*, April 2015, pp. 1–3.

[8] P. T. Mathiopoulos, E. A. Candreva, A. B. Awoseyila, V. Dalakas, D. Tarchi, B. G. Evans, A. Vanelli-Coralli, and G. E. Corazza, "Performance improvement techniques for the dvb-rcs2 return link air interface," *International Journal of Satellite Communications and Networking*, vol. 33, no. 5, pp. 371–390, 2015. [Online]. Available: http://dx.doi.org/10.1002/sat.1124

[9] L. Ding, G. T. Zhou, D. R. Morgan, Z. Ma, J. S. Kenney, J. Kim, and C. R. Giardina, "A robust digital baseband predistorter constructed using memory polynomials," *IEEE Transactions on Communications*, vol. 52, no. 1, pp. 159–165, Jan 2004.

[10] C. Yu, L. Guan, E. Zhu, and A. Zhu, "Band-limited volterra series-based digital predistortion for wideband rf power amplifiers," *IEEE Transactions on Microwave Theory and Techniques*, vol. 60, no. 12, pp. 4198–4208, Dec 2012.

[11] Q. Zhang, Y. Liu, J. Zhou, S. Jin, W. Chen, and S. Zhang, "A band-divided memory polynomial for wideband digital predistortion with limited bandwidth feedback," *IEEE Transactions on Circuits and Systems II: Express Briefs*, vol. 62, no. 10, pp. 922–926, Oct 2015.

[12] M. Mishali and Y. C. Eldar, "Sub-nyquist sampling," *IEEE Signal Processing Magazine*, vol. 28, no. 6, pp. 98–124, Nov 2011.

[13] M. E. Domínguez-Jiménez, N. González-Prelcic, G. Vazquez-Vilar, and R. López-Valcarce, "Design of universal multicoset sampling patterns for compressed sensing of multiband sparse signals," in *2012 IEEE International Conference on Acoustics, Speech and Signal Processing (ICASSP)*, March 2012, pp. 3337–3340.

[14] T. Moon, H. W. Choi, N. Tzou, and A. Chatterjee, "Wideband sparse signal acquisition with dual-rate time-interleaved undersampling hardware and multicoset signal reconstruction algorithms," *IEEE Transactions on Signal Processing*, vol. 63, no. 24, pp. 6486–6497, Dec 2015.

[15] R. Raich, H. Qian, and G. T. Zhou, "Digital baseband predistortion of nonlinear power amplifiers using orthogonal polynomials," in *Acoustics, Speech, and Signal Processing, 2003. Proceedings. (ICASSP '03). 2003 IEEE International Conference on*, vol. 6, April 2003, pp. VI–689–92 vol.6.

# Part IV

# Overview of Research Work II

# 15. New class of chaotic systems with circular equilibrium

**Abstract**

This paper brings a new mathematical model of the third-order autonomous deterministic dynamical system with associated chaotic motion. Its unique property lies in the existence of circular equilibrium which was not, by referring to the best knowledge of the authors, so far reported. Both mathematical analysis and circuitry implementation of the corresponding differential equations is presented. It is shown that discovered system provides a structurally stable strange attractor which fulfills fractal dimensionality, geometrical density and is bounded into a finite state space volume.

## 15.1  Introduction

It is well known that chaotic dynamics is not restricted only to complicated and strongly nonlinear vector fields [1] but can be observed also in the case of algebraically simple systems with six terms including nonlinearity [2]. Recent progress in overall performance of the personal computers and possibility of multi-grid calculation allows to implement fast-to-be-calculated quantifier of the dynamical motion inside a procedure for chaos or hyper-chaos localization [3]. Doing this we can start searching for irregular behavior of arbitrary-order nonlinear dynamical system. Such process begins with analytical definition of dimensionless mathematical models and continues with specification of the internal system parameters which are so far unknown. Since coexistence of multiple different attractors is possible in such systems the initial conditions are randomly and, more importantly, repeatedly chosen. Each time a routine come across vector field which provides the so-called folding and stretching mechanism the dynamical system is remembered for consequent numerical analysis.

This work has been primarily motivated by two recently published research papers where a group of dynamical systems with very specific properties have been presented. In paper [4] a class of the dynamical systems without equilibrium has been presented. Similarly paper [5] introduces several dynamical systems with a line equilibrium. Both works can be considered as a breakthrough idea since chaos is often put into the context of the singular saddle-type fixed points; the most common configuration of the vector field contains two [6] or three[7] of them. From this point of view a system with circular equilibrium (CES) represents somehow future logical progress.
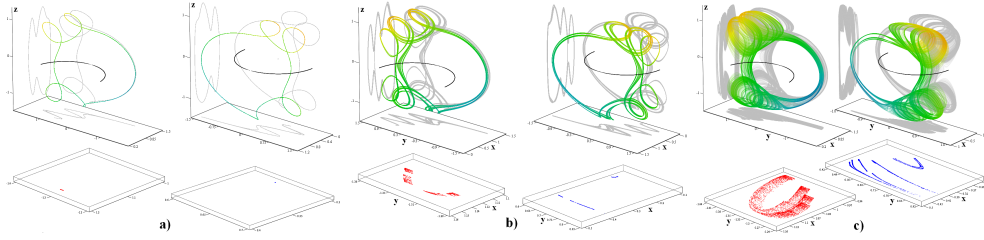
Figure 15.1: 3D perspective view of the chaotic attractor without initial transient motion and associated plane projections for a) $d = -0.15$, b) $d = -0.12$, c) $d = -0.10$ with equilibrium half-circle located in plane $z = 0$.
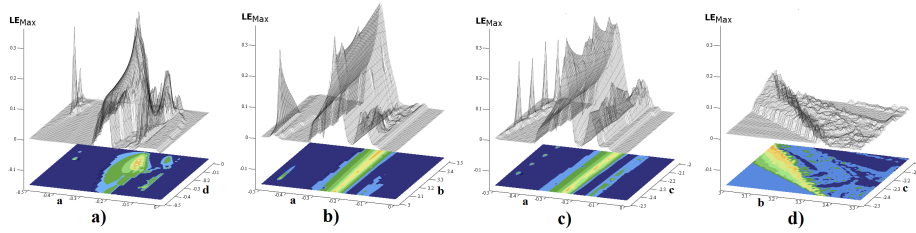


Figure 15.2: A contour-surface plots of the largest Lyapunov exponent (LE) for two variable parameters while remaining two are fixed at default values (15.3). The positive value of LE stands for chaotic solution.
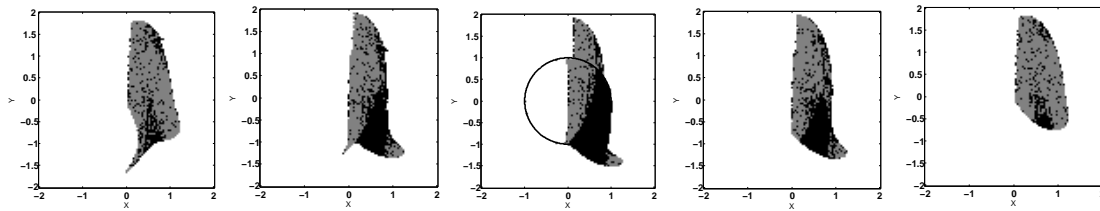


Figure 15.3: Cross-sections of basin of attraction, from left to right $z = -1$, $z = -0.5$, $z = 0$, $z = 0.5$, $z = 1$ (white color represent unbounded solutions, black areas are fixed points and gray regions denote chaotic motion).

## 15.2  Mathematical models under inspection

As previously mentioned first step towards discovery of new chaotic dynamics goes through a choice of dimension-less set of three first-order differential equations

$$
\begin{aligned}
\frac{dx}{dt} &= a \cdot z \\
\frac{dy}{dt} &= z \cdot f_1(x, y, z) \\
\frac{dz}{dt} &= x^2 + y^2 - r^2 + z \cdot f_2(x, y, z),
\end{aligned} \tag{15.1}
$$

where $r$ became radius of circular equilibrium and $a$ marks free parameter. Of course a predefined form (15.1) is not unique for CES; it is only the most straightforward realization of system containing fixed points which form a circle located on the plane

$z = 0$. The nonlinear functions $f_1$ and $f_2$ can contain a variety of terms; eventually it seems that several quadratic polynomials are sufficient to generate necessary geometrical structure of a vector field. In particular search routine reveals following smooth functions

$$
\begin{aligned}
f_1(x, y, z) &= b \cdot x + c \cdot z^2 \\
f_2(x, y, z) &= d \cdot x,
\end{aligned}
\tag{15.2}
$$

where $b$, $c$ and $d$ are remaining free constants. The numerical values of all free parameters are following

$$
a = -0.1 \quad b = 3 \quad c = -2.2 \quad d = -0.1 \quad r = 1,
\tag{15.3}
$$

for which a chaotic attractor evolves. To prove it Mathcad and build-in fourth-order Runge-Kutta integration method has been employed with final time 5000 and time step equals to 0.1 as demonstrated by means of Fig. 15.1.

The initial conditions can be taken as $\mathbf{x}_0 = (0, 0, 0)^T$. Typical property of this dynamical system is long spiral-type transient behavior and dissipative dynamical flow given by parameter $d$.

Figure 15.2 demonstrates the regions of chaotic solution in the hyper-space of the internal system parameters where a concept of the largest Lyapunov exponent (LE) is adopted. The LEs are calculated using Jacobi matrix (16.4) as presented in [8]. In order to get better insight into global dynamics only a fragments of this hyper-space are demonstrated. The dark blue color in the topographically-scaled graphs should be understood as limit cycle, green as a weakly chaotic system and yellow denotes chaotic motion. Discovered dynamical system possess several attractors, see the basins of attraction provided in Fig. 15.3.

Dynamical motion in the close neighborhood of the equilibrium circle is determined by the eigenvalues and associated eigenspaces established along this structure [9]. In the case of (15.1) and (15.2) a state-dependent linearization matrix can be established as

$$
\mathbf{J}(\mathbf{x}) = \begin{pmatrix} 0 & 0 & a \\ b \cdot z & 0 & b \cdot x + 3 \cdot c \cdot z^2 \\ 2 \cdot x + d \cdot z & 2 \cdot y & d \cdot x \end{pmatrix}
\tag{15.4}
$$

A local behavior along the equilibrium circle is determined by the so-called eigenvalues, i.e. roots of the parameterized characteristic equation

$$
\begin{aligned}
\lambda \quad (x) &= \lambda^3 - d \cdot x \cdot \lambda^2 - \\
&- 2 \cdot x \cdot \left( a \pm b \sqrt{r^2 - x^2} \right) \cdot \lambda = 0.
\end{aligned}
\tag{15.5}
$$

One eigenvalue is zero and the remaining two depend on a position on the equilibrium circle. Obviously there always exist a center manifold and dynamical motion in

127

the neighborhood of this circle can be decomposed into different configurations of the remaining two-dimensional subspace. Its nature can be clarified by means of Fig. 15.4.

After huge efforts it turns out that even simpler system without nonlinear function $f_2$ can get very close to the situation where it exhibit chaotic motion, in detail

$$\begin{aligned}
\frac{dx}{dt} &= z \\
\frac{dy}{dt} &= z \cdot f(x, y, z) \\
\frac{dz}{dt} &= x^2 + y^2 - r^2,
\end{aligned} \qquad (15.6)$$

and this expression can be marked as canonical polynomial CES.
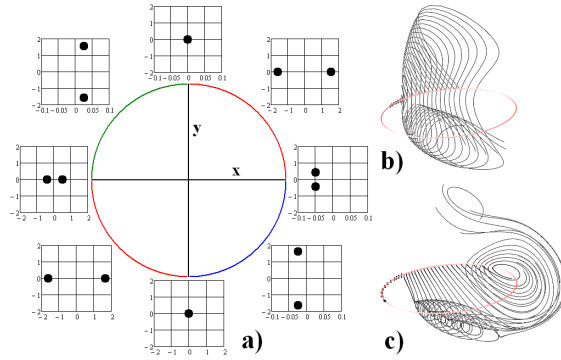


Figure 15.4: A local behavior of the discovered system: a) two remaining eigenvalues and the associated two-dimensional subspace: red (saddle-type), blue (stable spiral), green (unstable spiral), b) dynamical motion with initial conditions near equilibrium circle (outside), c) dynamical motion with initial conditions near equilibrium circle (inside).

## 15.3  Experimental verification

To illustrate that dynamical system (15.1) and (15.2) provides chaotic attractor with certain degree of the structural stability it has been implemented as a lumped electronic circuit. For network synthesis we choose a concept based on integrator block schematic [10], [11]. Final network is given in Fig. 15.5 where route-to-chaos scenario can be traced via a change of the external dc voltage supply $Vd$. Since desired chaotic attractor is bounded into relatively small state space volume the dynamical ranges of used active devices can be also reduced. Thus a four-channel four-quadrant analogue multiplier MLT04 has been chosen for implementation of the quadratic terms. The supply voltage for these devices is symmetrical $\pm 5\ V$. Voltage limitation of this active device occurs for values outside of $\pm 2.5\ V$ range. Thus strange attractors which occupy bigger volumes in the state space can not be realized by the proposed circuitry. For mathematical operations integration and summation a basic inverting voltage-mode two-ports with voltage feedback operational amplifier TL084 are utilized. In this case a supply voltage is raised to symmetrical $\pm 15\ V$. The time constant of the ideal integrators is chosen to be only

$\tau = RC = 10^{-4}s$ such that parasitic properties of the utilized active elements can be neglected. The individual state variables are easily measurable at the output nodes of the lossless integrators. Sixth multiplier is used in order to control bifurcation parameter $d$ via external dc voltage source and can be removed for further network simplification.



Figure 15.5: Circuitry realization of CES.

If active devices can be considered as close enough to ideal and by assumption of a fundamental transformation of the coordinates $(-x, y, -z) \rightarrow (u_1, u_2, u_3)$ the describing differential equations became

$$
\begin{aligned}
\frac{du_1}{dt} &= -\frac{u_3}{R_1 C} \\
\frac{du_2}{dt} &= \frac{u_3}{R_6 K_3 C}\left(\frac{R_2}{R_3}u_1 + \frac{R_2}{R_5 K_1}u_3^2\right), \\
\frac{du_3}{dt} &= \frac{1}{C}\left(\frac{u_1^2}{R_7 K_2} + \frac{u_2^2}{R_8 K_4} - \frac{V_r}{R_9} - \frac{u_1 u_3 V_d}{R_4 K_5 K_6}\right)
\end{aligned}
\tag{15.7}
$$

where $K_i = 5/2$ is internally trimmed scaling factor of $i$-th multiplier. The set of values for circuit realization can be calculated by a comparison of the individual terms of (15.7) with system (15.1) having functions (15.2) with numerical values (15.3), in detail

$$
\begin{aligned}
V_r &= r^2 = 1V & V_d &= -d \\
R_1 &= \frac{-R}{a} = 10k\Omega & R_2 &= R_9 = R = 1k\Omega \\
R_3 &= \frac{R}{b} = 333\Omega & R_4 &= \frac{R}{K_5 K_6} = 160\Omega \\
R_5 &= \frac{-R}{K_1 c} = 182\Omega & R_6 &= \frac{R}{K_3} = 400\Omega \\
R_7 &= \frac{R}{K_2} = 400\Omega & R_8 &= \frac{R}{K_4} = 400\Omega.
\end{aligned}
\tag{15.8}
$$

If natural frequency components of the chaotic waveforms need to be moved behind 1 MHz the non-ideal and parasitic properties of the used active elements need to be analyzed. Unlike others especially input and output admittances in the form of a parallel combination of resistor and capacitor as well as roll-off nature of a transfer function typical for both MLT04 and TL084 should be respected. These unwanted features can introduce several error terms into describing differential equations causing deformation of the desired chaotic attractor or its geometrical collapse. Note that only three integrated circuits are required for design of the proposed chaotic oscillator. The circuit was evaluated by circuit simulator Orcad Pspice and the voltage spectrum and plane projections can be seen in Fig. 15.6.

The circuit was designed on breadboard and in experimental setup digital oscilloscope HP54603B was used for attractor visualization, see Fig. 15.7. Based on the computed riddled basins of attraction serious problems have to be expected during measurement. Before documentation of each particular routing-to-chaos scenario predefined initial conditions needs to be imposed into the oscillator. However this additional circuitry is not provided.

## 15.4   Conclusion

In this short paper a novel dynamical system with circular equilibrium is uncovered, numerically confirmed as well as experimentally measured. Brief nature of this paper leaves the place for upcoming deeper investigation of the class of dynamical system with circular equilibrium. It is believed that brute-force method which combines stochastic search routine with objective function in the form of precise motion quantifier is powerful tool which can be utilized for discovering interesting dynamical systems with prescribed features. As indicated by new publications [6], [12] research in this particular area will proceed in the near future.

## 15.5   Bibliography

[1]   Wei Z., Yang Q.: Dynamical analysis of the generalized Sprott C system with only two stable equilibria. Nonlinear Dynamics **68**(4):543–554 (2012)
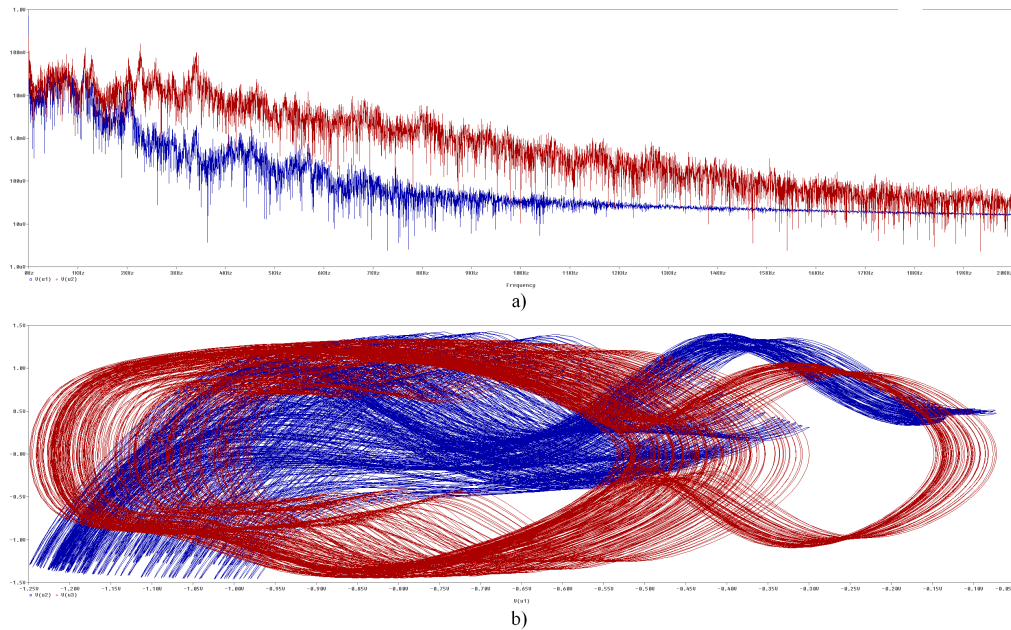
Figure 15.6: Time-domain analysis of designed chaotic oscillator by using Orcad Pspice circuit simulator: a) power spectra of $u_1$ and $u_2$ signals, b) $xy$ (blue) and $xz$ (red) plane projections.
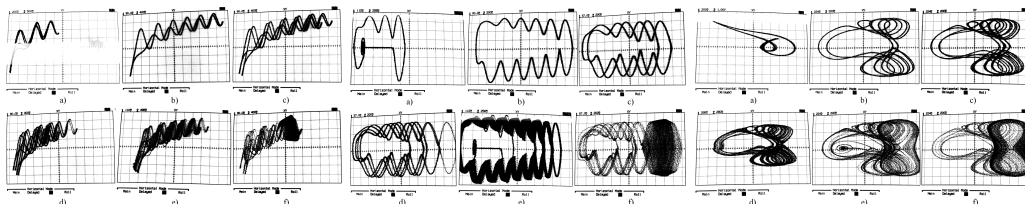


Figure 15.7: Oscilloscope traces of the chaotic attractors. Projection of the chaos evolution onto (upper left:xy, upper right: xz, bottom: yz) plane: a) Vd = 800 mV, b) Vd = 500 mV, c) Vd = 480 mV, d) Vd = 420 mV, e) Vd = 400 mV, f) Vd = 250 mV.

[2] Sprott J.C.: Elegant Chaos: Algebraically Simple Chaotic Flows. World Scientific (2010)

[3] Gotthans T., Petrzela J., Hrubos Z.: Advanced parallel processing of lyapunov exponents verified by practical circuit. 21st International Conference Radioelektronika: 1–4 (2011)

[4] Jafari S., Sprott J., Golpayegani S.M.R.H.: Elementary quadratic chaotic flows with no equilibria. Physics Letters A **377**(9):699 – 702 (2013)

[5] Jafari S., Sprott J.: Simple chaotic flows with a line equilibrium. Chaos, Solitons & Fractals **57**: 79 – 84 (2013)

[6] Li C., Sprott J.: Chaotic flows with a single nonquadratic term. Physics Letters A **378**(3):178 – 183 (2014)

[7] Spany V., Galajda P., Guzan M., Pivka L., Olejar M.: Chua's singularities: Great miracle in circuit theory. I J Bifurcation and Chaos **20**(10):2993–3006 (2010)

[8] Wolf A., Swift J.B., Swinney H.L., Vastano J.A.: Determining Lyapunov exponents from a time series. Physica D **16**:285 (1985)

[9] Sprott J.C.: Chaos and Time-Series Analysis. Oxford University Press (2003)

[10] Petrzela J., Gotthans T., Hrubos Z.: Modeling deterministic chaos using electronic circuits. Radioengineering **20**:438–444 (2011)

[11] Ma J., Wu X., Chu R., Zhang L.: Selection of multi-scroll attractors in jerk circuits and their verification using Pspice. Nonlinear Dynamics **76**(4):1951–1962 (2014)

[12] Shen C., Yu S., Lu J., Chen G.: Generating hyperchaotic systems with multiple positive Lyapunov exponents. 9th Asian Control Conference (ASCC): 1–5 (2013)

# 16. Simple Chaotic Flow with Circle and Square Equilibrium

**Abstract**

It is recognized that simple systems of third-order autonomous nonlinear differential equations can exhibit behavior known as chaos. In this paper we present a new class of chaotic flow with square shaped equilibrium. This unique property referring to the best knowledge of the authors was not yet described. Such system belong to a newly introduced category of chaotic systems that could be important and potentially interesting in engineering applications. The mathematical model is provided with its circuitry equivalent proving its structural stability of strange attractors. First the circuit is simulated with PSpice and subsequently is assembled measured.

## 16.1   Introduction

Over past three decades, finding chaotic systems is attracting attention of many researchers. Generating chaotic attractors may help to understand better dynamics of real world systems. After many years of intensive research, several chaotic systems have been revealed. The recent development in the chaotic domain have presented systems without any equilibrium points [9], rare flows with a stable equilibrium [12], systems with line equilibrium points [3], systems without equilibrium [2] or more system with circular equilibrium [1]. In fact recently many chaotic systems with unique equilibrium points have been presented [5], [14], [10], [13]. Yet many undiscovered systems exists. The goal of this work is not only present a new system with unique property, but mainly to extend the general knowledge. In this paper we introduce unpresented rare category with infinite number of equilibrium points - system with square equilibrium. This category due to PWL (piecewise linear) vector field is a challenging topic [4], [7]. According to paper [11] our system satisfies at least two conditions from three of novelty. Our goal was to focus on systems with Euclidean dimension equal to three.

## 16.2   Mathematical Model

As presented in the paper [1] possible simpler mathematical model with circle equilibrium may exist. One of simple flows can be expressed as follow

$$
\begin{aligned}
\dot{x} &= z \\
\dot{y} &= -z\left(ay + by^2 + xz\right) \\
\dot{z} &= x^2 + y^2 - 1,
\end{aligned}
\tag{16.1}
$$

where $a$ and $b$ are constants. Setting $a = 5$, $b = 3$ and with initial condition $i_c = (0, 0, 0)^T$ a chaotic motion can be observed. Linearizing system by pieces (PWL) proposed in (16.1) a system with square equilibrium can be obtained. Despite the novelty of the system with the circle equilibrium was already published, we will further focus on the linearized version that have unique properties. The equations can be rewritten as

$$
\begin{aligned}
\dot{x} &= z \\
\dot{y} &= -z\left(ay + b|y|\right) - x|z| \\
\dot{z} &= |x| + |y| - 1,
\end{aligned}
\tag{16.2}
$$

where $a$ and $b$ have same values as in the system described by (16.1). The proposed system (16.2) is a set of linear equation and therefore an analytical solution for each linearized region could be obtained. Then if the solution reaches a boundary region, it can be used as initial condition for a next analytical solution. Unfortunately such approach is unpractical due to its complexity. It is obvious that such system (16.2) could be modified in order to have rectangular equilibrium by modifying the last state equation as $\dot{z} = |\frac{x}{\alpha^2}| + |\frac{y}{\beta^2}| - 1$. It is not our goal, due to higher complexity than (16.2), to analyze such enhancement.

The fix points of system (16.2) can be obtained by solving $\dot{x} = 0$, $\dot{y} = 0$, and $\dot{z} = 0$, that is

$$
\begin{aligned}
x &= \mathbb{R} \\
y &= \begin{cases}
-1 - x, & \text{if } -1 < x \le 0 \\
1 + x, & \text{if } -1 < x \le 0 \\
1 - x, & \text{if } 0 < x < 1 \\
-1 + x, & \text{if } 0 < x < 1
\end{cases} \\
z &= 0
\end{aligned}
\tag{16.3}
$$

Dynamical motion in the close neighborhood of the equilibrium circle is determined by the eigenvalues and associated eigenspaces established along this structure [1]. In order to estimate the Jacobian matrix, the derivatives of state variables are necessary. The derivation of $|.|$ can be obtained in many ways, for example as condition statement (step function), or $\frac{x}{|x|}$. Alternatively for the simplicity we use sgn(.) where for 0 the function is not differentiable. Note that in the equations the statements can be always substituted. In the case of (16.2) a state-dependent linearization matrix can be established as
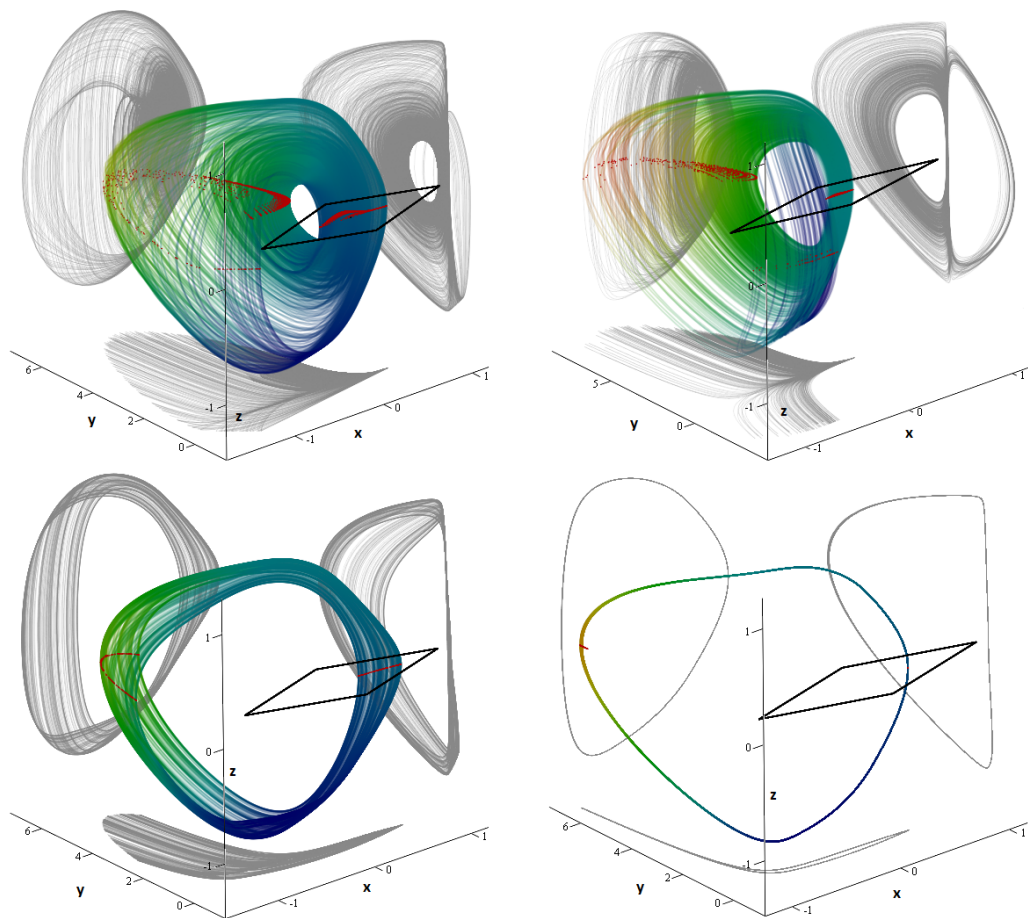
Figure 16.1: Numerical integration. The individual state projections (corresponding to top left: $a = 5$ and $b = 3$, top right: $a = 10$ and $b = 3$, bottom left: $a = 3.5$ and $b = 3$ and bottom right: $a = 5$ and $b = 4$). The black quadrangle represents a square equilibrium. In the figures, there are also marked Poincare sections (Red).

$$\mathbf{J} = \begin{pmatrix} 0 & 0 & 1 \\ -|z| & -a \cdot z - b \cdot z \cdot \text{sgn}(y) & -a \cdot y - b \cdot |y| - x \cdot \text{sgn}(z) \\ \text{sgn}(x) & \text{sgn}(y) & 0 \end{pmatrix} \quad (16.4)$$

A local behavior along the equilibrium circle is determined by the so-called eigenvalues, i.e. roots of the parameterized characteristic equation

$$det(\mathbf{J} - \lambda) = -\lambda^2(a \cdot z + \lambda) + sgn(x) \cdot [a \cdot z + \lambda + b \cdot z \cdot sgn(y)] -$$
$$sgn(y) \cdot \{b \cdot \lambda |y| + |z| + \lambda [a \cdot y + b \cdot z \cdot \lambda + x \cdot sgn(z))]\} = 0. \quad (16.5)$$

Considering the plane of equilibrium lies in the plane $z = 0$. The eigenvalues are as follow

$$\lambda_1 = 0$$
$$\lambda_{2,3} = \pm\sqrt{\text{sgn}(x) - a \cdot y \cdot \text{sgn}(y) - b \cdot |y| \cdot \text{sgn}(y))}$$

$$(16.6)$$

The behavior along square equilibrium located as noted in 16.3 can be seen on the figure 16.2. Pure pair of imaginary eigenvalues represents a unstable center equilibrium. That means there are concentric periodic orbits around the equilibrium lines. Such phenomena can be also observed in Fig.16.3. The pair of two purely real eigenvalues can be referred as unstable saddle. Three dimensional Bogdanov-Takens equilibrium ($\lambda_{1,2,3} = 0$) are also present and are located at $(x, y, z) = (0.5, -0.5, 0)$ and $(x, y, z) = (0.825, 0.175, 0)$.
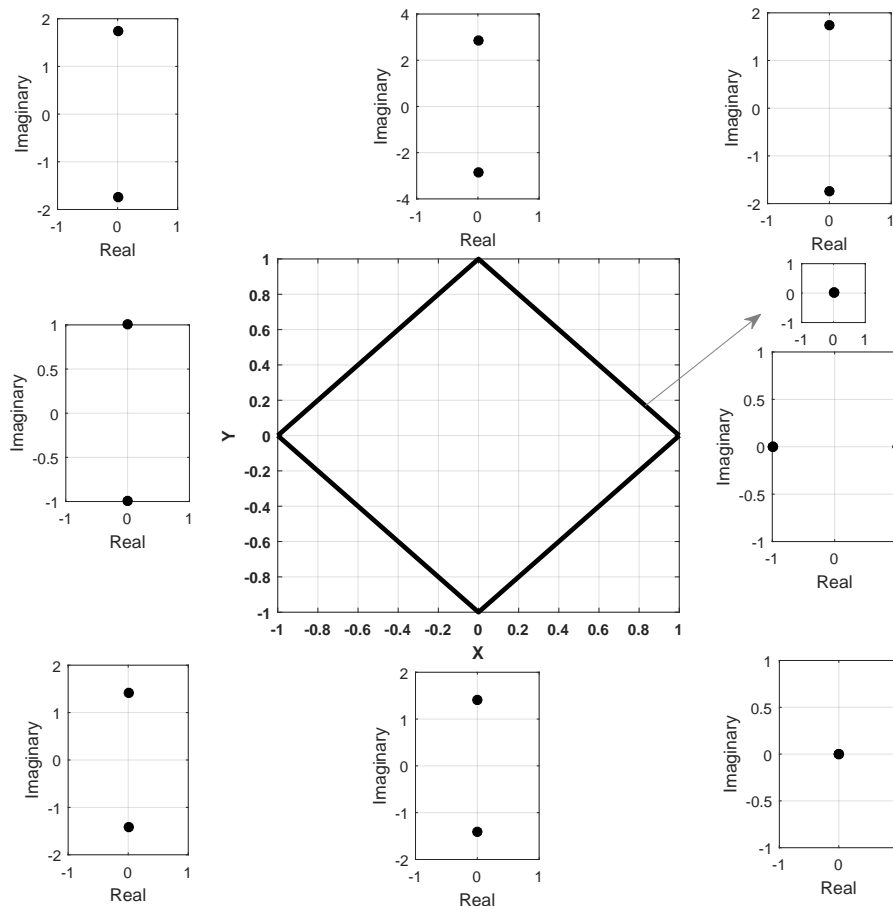


Figure 16.2: For the values $a = 5$ and $b = 3$ with $i_c = (0, 0, 0)^T$ the behavior of eigenvalues $\lambda_{2,3}$ along the square equilibrium.

The dynamical motion near equilibrium square can be seen in the Fig.16.3. We may see that the negative value of state variable $x$ creates periodic motion along the

equilibrium. After reaching some point, chaotic motion can be observed (it can be considered as a very long transient). Therefore initial conditions have to be chosen carefully.
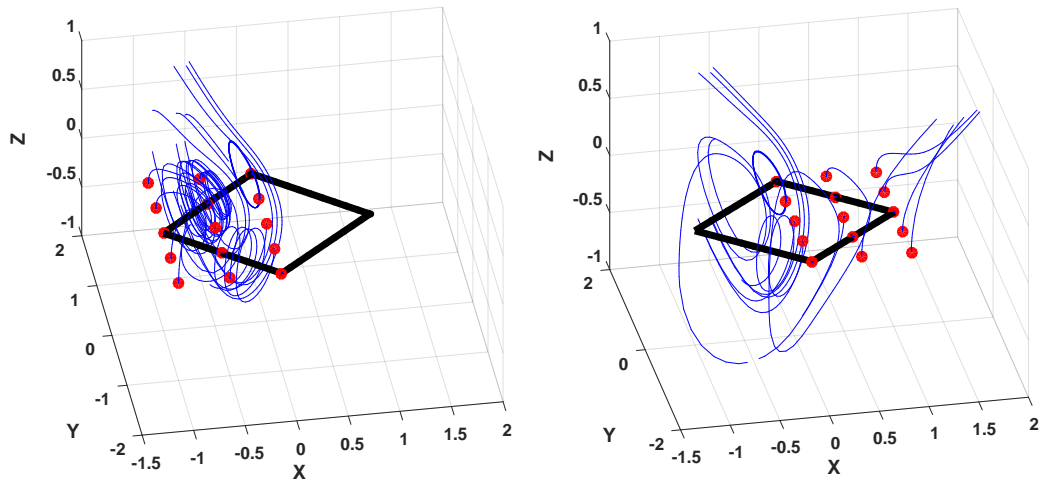


Figure 16.3: Dynamical motion (blue curve) with initial conditions (red dots) near equilibrium square (black).

The dynamics of the new system (16.2) is discovered by varying the parameter $a$ while fixing other parameter $b = 3$. The bifurcation diagram and the corresponding largest Lyapunov exponent (LLE) and Kaypan-Yorke dimension are displayed in Fig. 16.4 varying the variable $a$ in the range $< 3, 10 >$. They indicate that the new system can generate chaotic behavior for quite large range of $a$.

## 16.3 Experimental Verification

It has been widely accepted to demonstrate structural stability of proposed dynamical system with lumped circuit synthesis and measurements. Synthesis of the electronic circuits is not only a way how to accurately model the nonlinear dynamical systems, but also a way how to evaluate overall structural stability of examined system.

There exist several ways how to practically realize chaotic oscillators [8]. Most of these techniques unambiguous and have been already published. To synthesize circuit from differential equations system (reference), integrator synthesis was chosen. After thinking about how to reduce the complexity of the nonlinear network a very simple circuitry has been revealed. Only few basic building blocks are necessary: inverting integrators (TL084), summing amplifier (TL084), three multipliers (AD633) and diodes (1N4148) (for absolute value modeling). The analog multiplier has all nodes not displayed in the Fig. 16.6 connected to ground. First the proposed topology is verified with PSpice 16.0 circuit simulator and then it is experimentally measured as seen in Fig.16.5.
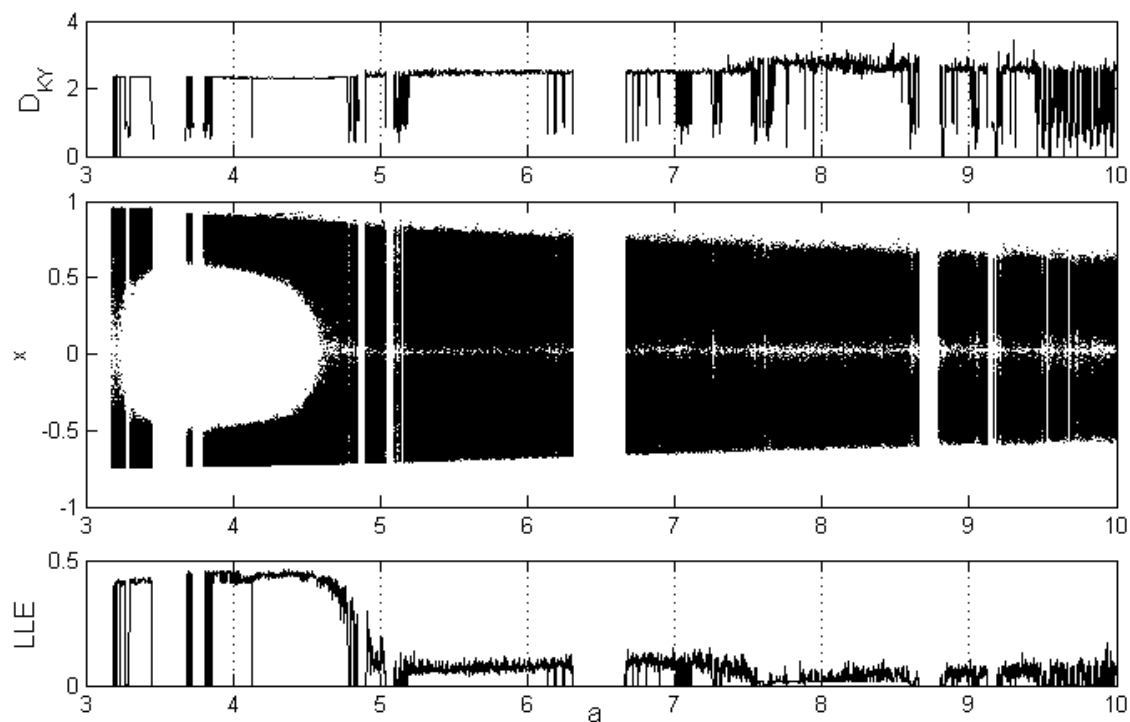
Figure 16.4: Kaplan-Yorke dimension (top), biffurcation diagram of parameter $a$ (middle) and it corresponding LLE.
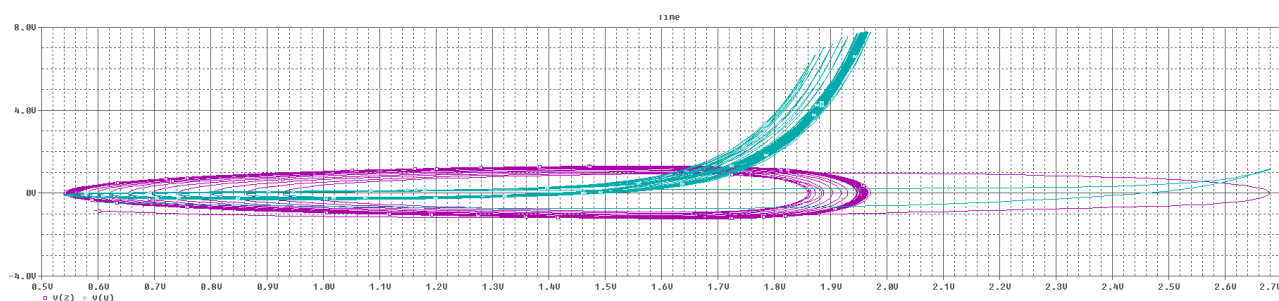


Figure 16.5: PSpice simulated Monge's projections for the proposed circuit (-X Y blue curve and -X Z violet curve).

The individual state variables are easily measurable at the output nodes of the lossless integrators.

The state variables represented by voltages have been measured by Rohde&Schwarz RTM 1052 oscilloscope. The screenshots can be found in Fig. 16.7, 16.8 and 16.9.
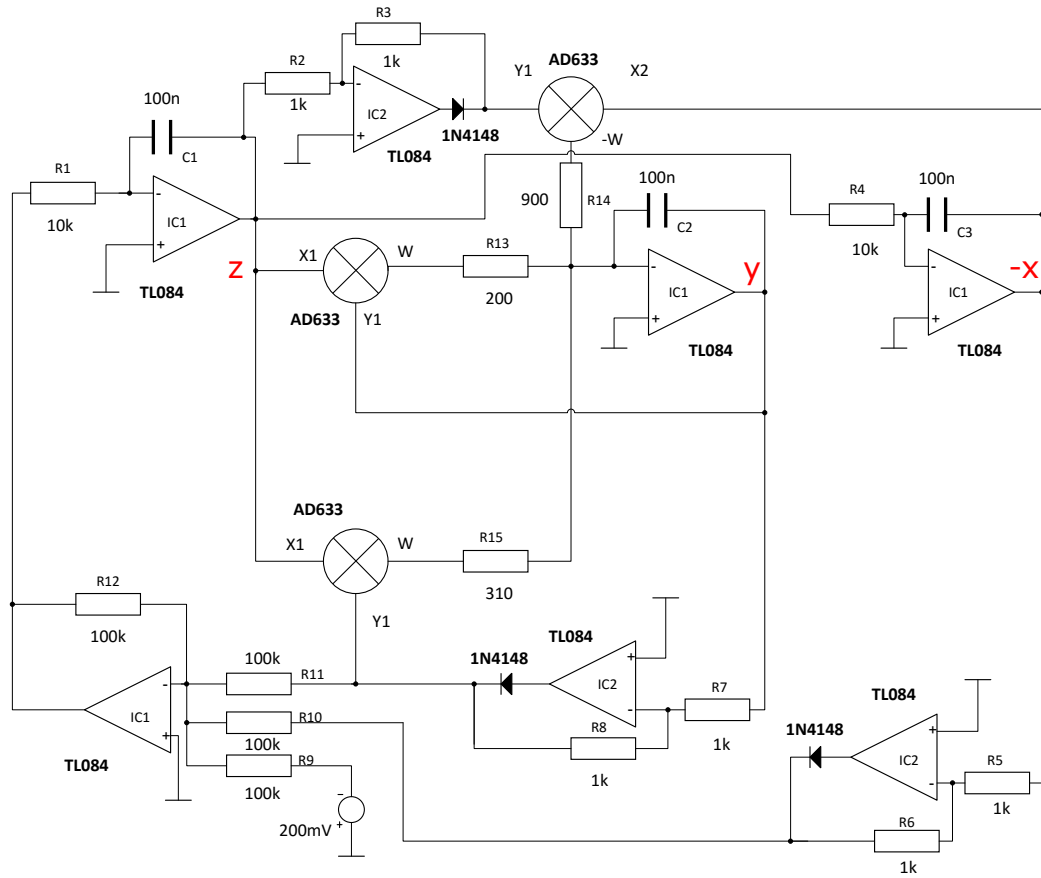
Figure 16.6: Circuitry realization of proposed system.
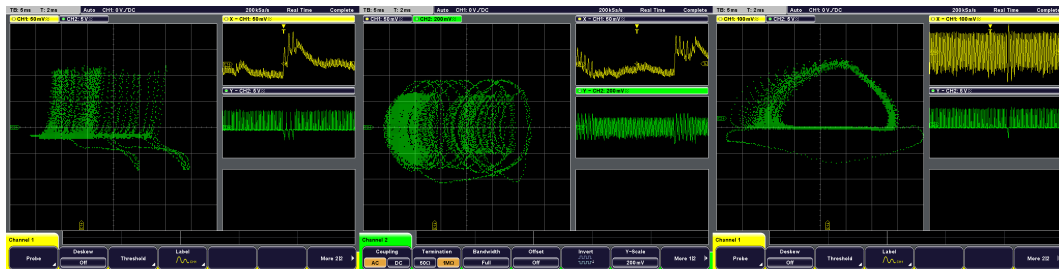


Figure 16.7: Measurements on individual state variables. (corresponding to $a = 5$ and $b = 3$).

## 16.4 Conclusion

In this paper first the three-dimensional system with circular equilibrium was presented as a initial system. Applying PWL a system with square equilibrium was presented (its version with rectangular equilibrium was outlined). From the computational point of view the system is quite interesting mainly in the regions of interest. After providing
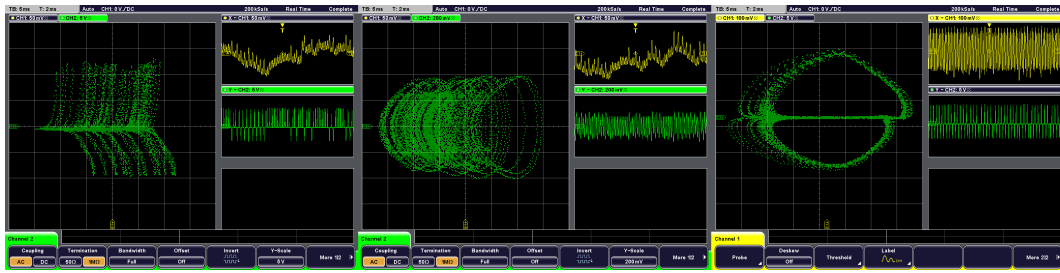
Figure 16.8: Measurements on individual state variables. (corresponding to $a = 5$ and $b = 2.2$).
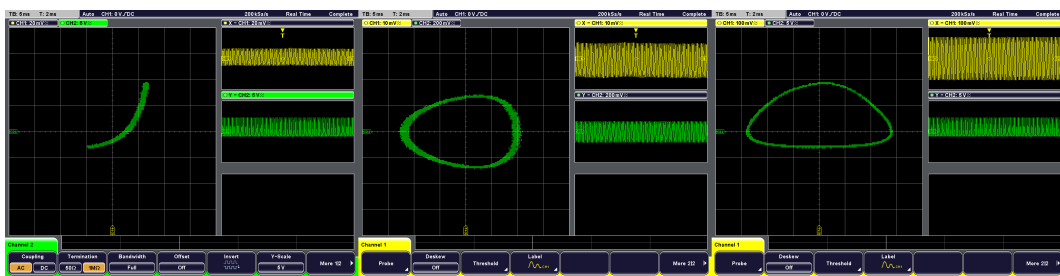


Figure 16.9: Measurements on individual state variables. (corresponding to $a = 5$ and $b = 4$).
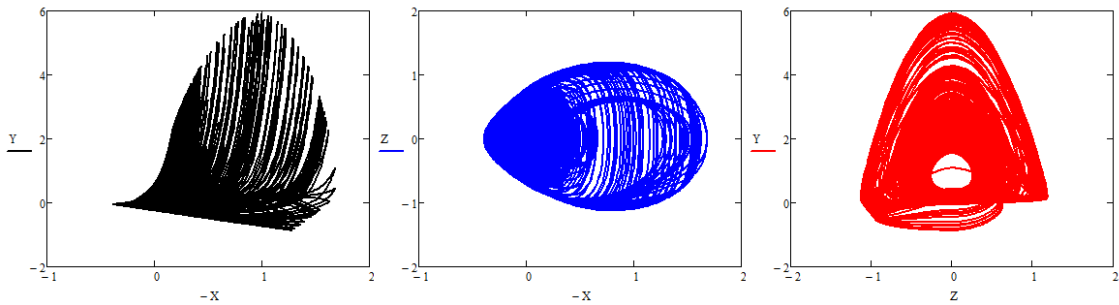


Figure 16.10: Numerical integration. The individual state projections (corresponding to $a = 5$ and $b = 3$).

the numerical analysis we present the behavior around regions of square equilibrium. Then the calculations of Lyapunov exponents, Kaplan-Yorke dimension together with bifurcation analysis is provided.

Finally we present analog circuit in order to evaluate structural stability of proposed system. The circuit was first simulated, assembled and then measured. By comparing the measurements with numerical simulations we may see that there is quite agreement.

Authors believe that system with square equilibrium was never presented and is pre-
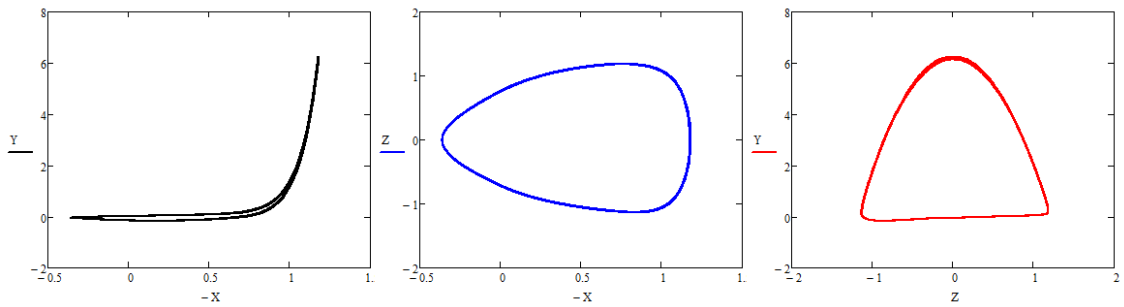
Figure 16.11: Numerical integration. The individual state projections (corresponding to $a = 5$ and $b = 4$).

sented in it's simplest form. If the reader have any questions, please do not hesitate to contact the authors.

## 16.5 Bibliography

[1] Gotthans, T. & Petrzela, J. [2015] "New class of chaotic systems with circular equilibrium", *Nonlinear Dynamics* **81**, 1143–1149.

[2] Jafari, S., Sprott, J. C. & Golpayeaggani, M., [2013] "Elementary quadratic chaotic flows with no equilibria", *Physics Letters A* **377**, 699–702.

[3] Jafari, S., Sprott, J. C., [2013] "Simple chaotic flows with a line equilibrium", *Chaos, Solitons & Fractals* **57**, 79–84.

[4] Li, C., Sprott, J.C., Thio, W., [2015] "Linearization of the Lorenz system", *Physics Letters, Section A: General, Atomic and Solid State Physics* **379**, 888-893.

[5] Molaie, M., Jafari, S., Sprott, J. C., Golpayeagani, S., [2013] "Simple chaotic flows with one stable equilibrium", *International Journal of Bifurcation and Chaos* **23**, 135–188.

[6] Munmuangsaen, B., Sprott, J.C., Thio, W., Buscarino, A., Fortuna, L., [2015] "A Simple Chaotic Flow with a Continuously Adjustable Attractor Dimension", *International Journal of Bifurcation and Chaos* **25**.

[7] Petrzela, J. [2012] "Optimal piecewise-linear approximation of the quadratic chaotic dynamics", *Radioengineering* **21**, 20–28.

[8] Petrzela, J., Gotthans, T., Hrubos, Z., [2011] "Modeling deterministic chaos using electronic circuits", *Radioengineering* **20**, 438–444.

[9] Pham, V., Vaidyanathan, S., Volos, C. Jafari, S., Kingni, S. T., [2016] "A no-equilibrium hyperchaotic system with a cubic nonlinear term", *Optik-International Journal for Light and Electron Optics* **127**, 3259–3265.

[10] Sprott, J. C. [2010] *Elegant Chaos Algebraically Simple Chaotic Flows*, (World Scientific).

[11] Sprott, J. C. [2011] "A proposed standard for the publication of new chaotic systems", *International Journal of Bifurcation and Chaos* **21**, 2391–2394.

[12] Sprott, J. C. [2015] "Strange attractors with various equilibrium types", *The European Physical Journal Special Topics* **224**, 1409–1419.

[13] Sprott, J. C., Jafari, S., Pham, V., Hosseni, Z. S., [2015] "A chaotic system with a single unstable node", *Physics Letters A* **379**, 2030–2036.

[14] Wei, Z., Sprott, J. C., Chen, H., [2015] "Elementary quadratic chaotic flows with a single non-hyperbolic equilibrium", *Physics Letters, Section A: General, Atomic and Solid State Physics* **379**, 2184–2187.

# 17. Current-mode network structures dedicated for simulation of dynamical systems with plane continuum of equilibrium

**Abstract**

This review paper describes different lumped circuitry realizations of the chaotic dynamical systems having equilibrium degeneration into a plane object with topological dimension of the equilibrium structure equals one. This property has limited amount (but still increasing, especially recently) of third-order autonomous deterministic dynamical systems. Mathematical models are generalized into classes to design analog networks as universal as possible capable to model rich scale of associated dynamics including the so-called chaos. Reference state trajectories for the chaotic attractors are generated via numerical analysis. Since used active devices can be precisely approximated by using third-level frequency dependent model it is believed that computer simulations are close-enough to capture real behavior. These simulations are included to demonstrate existence of chaotic motion.

## 17.1  Introduction

Different configurations of lumped analog circuits capable to model continuous chaotic dynamics attract significant interest of researchers and engineers for the last four decades. The reason for this can be found in several unique properties of a strange attractor such as complex geometrical structure, fractal dimension, attractor is dense in a finite state space volume while chaotic waveforms are extremely sensitive to changes of internal system parameters. Since there is no closed-form analytic solution of the describing differential equations chaotic behavior can be predicted towards neither near nor far future. All these mentioned features cause chaotic oscillators much harder to be practically implemented if compared to conventional analog networks such as amplifiers, modulators, converters, mixers, harmonic or functional generators, etc.

Most existing papers dealing with construction of chaotic oscillators utilize general design approach based on concept of analog computers. This method is universal, can be applied to arbitrary set of the ordinary differential equations and was successfully tested

on mathematical model of jerk function [1]-[3], simplified model of isolated neuron [4], general class of autonomous nonlinear systems with smooth and piecewise-linear vector field [5], n-scroll spiral attractors [6], four-dimensional [7] and hyperchaotic systems [8]. Integrator-based design approach can be easily combined with single or multiple digital feedback two-ports (supplemented by A/D and D/A converters) that implements complex nonlinear transfer function, see paper [9] for realization of labyrinth chaos. Another type of chaotic oscillators represents interconnection of higher-order admittance two-terminal element with nonlinear resistor. Pioneering studies in this area has been done on famous Chua´s oscillator where admittance network is fully passive [10]-[12] and individual state variables are voltages across grounded capacitors and current flowing through inductor. Generalization of this design process leads to assumption that structure of the admittance network can realize non-positive real function if contains various active elements, check examples given in [13]-[15]. Chaotic signals can be successfully generated by coupling two harmonic oscillators with the common LC tank [16]-[18] as well as tank composed of parallel resonant combination of a linear resistor and a frequency dependent negative resistor [19]. Since fundamental component for evolution of strange attractor is harmonic waveform chaotic oscillator can be constructed by slight modification (only single diode is included) of standard oscillator having frequency-dependent passive feedback two-port with losses compensated by amplifier such as Wien-bridge concept [20]. As consequence chaos can be observed as unwanted oscillations in high-Q analog frequency filters like KHN biquadratic filtering section [21]. Nonlinearity naturally missing in a mathematical description of functional block (filter, amplifier, etc.) can be very simple [22], sometimes in the form of amplitude stabilization mechanism. Signum-type nonlinearity responsible for evolution of chaos can be realized by the logic elements as demonstrated in [23].

To simplify experimental verification procedure voltage-mode circuits are preferred over current-mode flow-equivalents. Reason for this is not only in fact that node voltages can be easily captured by oscilloscope. There is also a much bigger platform of integrated active elements that process voltages; are cheap and widespread over the market stocks. Besides dynamical systems designed by using discrete components there were successful efforts to construct chaotic oscillators fully- or partially-integrated using available MOS technology [24]-[27]. Interesting implementation of grid spiral attractors using Arduino open source integrated development environment is presented in paper [28] together with application of chaos in the selected secure communication issues.

Early ideas about emergence of chaotic oscillations were closely related to harmonic oscillators where losses in resonant sub-circuit are compensated by using one or several negative resistance elements [29]. Such structures have single or multiple fixed points with saddle-spiral local vector field geometry and stability index lower than dynamical system dimension. From the viewpoint of chaos generation, it was long time believed that there are always two mechanisms acting in a continuous vector field exhibiting chaos. The so-called stretching property is responsible for the exponential divergence rate of the neighborhood state orbits and is generated by an unstable hyperbolical fixed point; this property creates waveform sensitivity. Second mechanism is trajectory folding and keeps attractor inside a finite volume of the state space. Thus, local instability together with at least one nonlinear scalar function of some state variable should be incorporated into the describing mathematical model. However, this statement has been recently violated by several interesting papers where chaotic systems with completely different formations

144

of equilibrium structure and vector field geometry have been discussed. Please remember that upcoming list of the references is by no way complete survey; it should only help the readers to start their own study on this emerging topic.

The best way how to proceed with this study is provided in fundamental paper [30] where many simple chaotic flows are discussed. It is shown that complex dynamical motion is not restricted to the complex mathematical models with many algebraic terms. Paper [31] presents possibility to interchange saddle-spiral equilibrium with saddle-node without qualitative change of global behavior. Chaotic dynamical system having only one unstable node fixed point is discussed in [32] and chaotic flow with one non-hyperbolic fixed point is a topic of paper [33]. Further intensive research demonstrates that chaos is not restricted to dynamical systems with several saddle-type fixed points but also systems having single fixed point with associated real-valued eigenvalues which corresponds to three eigenvectors in the local vector filed geometry. Surprisingly chaotic attractors can be hidden also in the case of the deterministic dynamical systems without equilibrium as shown in work [34]-[40]. Even more interesting discoveries are chaotic systems having only a stable fixed point; for further study consult papers [41]-[43]. One step forward reveals that scenario for strange attractor evolution can be achieved in dynamical flows with several stable fixed points; see [44]. Surprisingly, deformation of the singular fixed points into higher-dimensional objects does not preclude evolution of a strange attractor. A significant number of research articles have been devoted to mathematical model with chaotic behavior and equilibrium in form of surface objects such as one or several lines (two parallel) [45]-[47], hyperbola [48], circle [49] and ellipse, square [50], other conic-sectioned equilibrium [51] or a general curve equilibrium [52]-[54]. However, it seems that only portion of line, circle or square is responsible for chaos generation. Based on these recent discoveries in the field of nonlinear dynamic theory it is not a breath-taking fact that three-dimensional equilibrium structure such as cube can also lead to evolution of chaos [55]. Systematic procedure towards the chaotic dynamics with any number of equilibria is described in [56]. Different route-to-chaos scenarios can be observed in the mathematical model of chaotic system with a variable equilibrium [57]. To end this part of review procedure for finding arbitrary-dimensional dynamical systems with the chaotic nature can be algorithmized. Suitable form of a starting mathematical model is briefly described in paper [58] together with some examples. Chaotic attractors associated with dynamical system with degenerated equilibria are often referred as the hidden attractors [59]-[61]. It is because basin of attraction does not include vicinity of equilibrium.

The main motivation for this work is to extend and complete list of the current-mode realizations of chaotic systems published in [62]. Simplicity of models predestinates them for the circuit realizations dedicated for various exhibitions, educational or basic research purposes (for example bifurcation sequences can be traced and captured).

## 17.2   Mathematical Background

As already mentioned the most often configuration of vector field with associated chaotic motion is composed of single, two or three fixed points. Typical situation for multi-scroll and multi-grid spiral attractors is symmetrical vector field composed by repetition of the several affine segments. Trajectory in each segment spirals away from saddle-focus fixed point; there is just one such point per region. Some special cases of mathematical models

describing thermo-dynamical systems and chemical reactions do not exhibit fixed points at all. Since system is closed without external driving forces it always contains a nonzero energy for time evolution. The main aim of this paper is to address question if the chaotic dynamics with a non-conventional equilibrium formation can be implemented as hybrid-mode or the fully current-mode electronic circuits (where all state variables are currents). Evidently, strange attractor must be structurally stable and robust to be experimentally observable. Asked question about robustness of dynamical system remains unanswered in the case of the electronic circuits for signal processing applications (masking, modulation and demodulation) since these do not naturally exhibit equilibrium degenerations.

Consider general mathematical description of a third-order autonomous deterministic dynamical system in the form of first-order ordinary differential equations, namely

$$\frac{d}{dt} = f(x), x = (x \ y \ z)^T, x \in \Re^3, \tag{17.1}$$

where x represents a state vector and f(x) is a continuous smooth nonlinear function. Expected degeneration of the fixed points means that nonlinear problem f(x)=0 does not lead to the singular solutions but to some plane object; curve that can be parameterized.

New chaotic dynamical systems can be discovered by using a three-step brute-force numerical procedure. First step is definition of a mathematical model which belongs to general class (1), has prescribed form of equilibrium and contains only polynomial terms. Second step is declaration of free parameters of analyzed mathematical model which will be adjusted during a stochastic optimization routine. Last step is stochastic optimization sometimes replaced by tabularized calculation of fitness function. However, dimension of scanned space directly corresponds to the amount of free system parameters and can be significant. Due to the possibility of existence of several attractors (including non-chaotic and trivial solution) the initial conditions should be generated randomly and many times. This approach is capable to uncover attractors excited by equilibrium as well as hidden attractors. Search routine employs repeated computation of some precise and fast-to-be-calculated chaos quantifier such as the largest Lyapunov exponent (LE) obtained from differential equations or small data sets [63]-[65], metric dimension like Kaplan-Yorke or capacity. Nevertheless, the latter case is time consuming and should be applied if parallel processing/computing becomes available. Gradient algorithms are useless because there is no analytic formula for chaos detection. A successive application of this algorithm is demonstrated via few examples in papers [66]-[68]. Proposed algorithm can be used for detection of chaotic motion in real physical system; both continuous [69] and discrete.

### 17.2.1 System with line equilibrium

Speaking in terms of the dynamical motion of lumped electronic circuit these systems are evolutionary insensitive if the initial conditions accurately satisfy known line equation. This situation leads to the state variables which are frozen with no further time changes of the network quantities. If covering mathematical model is unbalanced by at least one constant term this line generally need not to cross over zero, i.e. origin of the state space. If we look on the individual points of this line the associated eigenvalues, the stability indexes and the local geometry can change along this line. Of course, a requirement for dynamical flow to be dissipative is still working.

Two known members form this group of the dynamical systems in which formula for equilibrium represents a line segment. First can be described by expression

$$\frac{dx}{dt} = az, \frac{dy}{dt} = z \ f_1(x), \frac{dz}{dT} = z \ f_2(x) + \Psi(x), \tag{17.2}$$

together with a line equation substitution $\psi(\text{x})$=b· x-y+c leading to a chaotic system with line equilibrium with so far hypothetical form of the scalar functions f1(x) and f2(x). Slightly less general but for upcoming analog circuit design more convenient form is canonical, i.e. without function f2(x)

$$\frac{dx}{dt} = az, \frac{dy}{dt} = z \ f_1(x), \frac{dz}{dT} = \Psi(x), \tag{17.3}$$

Line equilibrium is primary subject of interest in contribution [45]. Presented systems represent alternatives to dynamics given by equations (2) and (3) in the sense there is no linear transformation of coordinates which can form a bridge between these two groups. These dynamical systems can be generalized into class

$$\frac{dx}{dt} = y, \frac{dy}{dt} = -x + y \ f_1(x), \frac{dz}{dT} = -x + y \ f_1(x) - y \ f_3(x), \tag{17.4}$$

Equilibrium line is given implicitly as one of the coordinate axes of the state space and can be expressed as $xe = (00z)^T$. Let's pick up for example first two dynamical systems from a group in paper [45]. These can be characterized by (4) together with functions

$$f_1(x) = z, f_2(x) = 1 + ay + bz, f_3(x) = 0, \tag{17.5}$$

and the numerical values of the system parameters equal a=15 and b=1. Typical strange attractor can be observed for the initial conditions $x0 = (0.200)^T$ and is demonstrated by means of Fig. 1. Second dynamical system with line equilibrium can be expressed as

$$f_1(x) = z, f_2(x) = ay + bz, f_3(x) = 1, \tag{17.6}$$

with the internal system parameters equal $a = 17$ and $b = 1$. Corresponding strange attractor generated by using initial conditions $x0 = (00.40)^T$ is given in Fig. 2.

Other member that belongs to this class of the dynamical systems with a single line equilibrium and associated chaotic behavior has auxiliary functions

$$f_1(x) = z, f_2(x) = -x + ay + bz, f_3(x) = 1, \tag{17.7}$$

with the internal system parameters a=18, b=1 and the initial conditions $x0 = (0 - 0.40.5)^T$. Strange attractor is visualized in Fig. 3. Similarly, line equilibrium is obtained for

$$f_1(x) = z, f_2(x) = ay + bz, f_3(x) = z, \tag{17.8}$$

and chaotic attractor can be observed for choice of the system parameters $a = 4$, $b = 0.6$ and a set the initial conditions $x0 = (0.20.70)^T$ as demonstrated in Fig. 4.

Finally, following choice of auxiliary functions
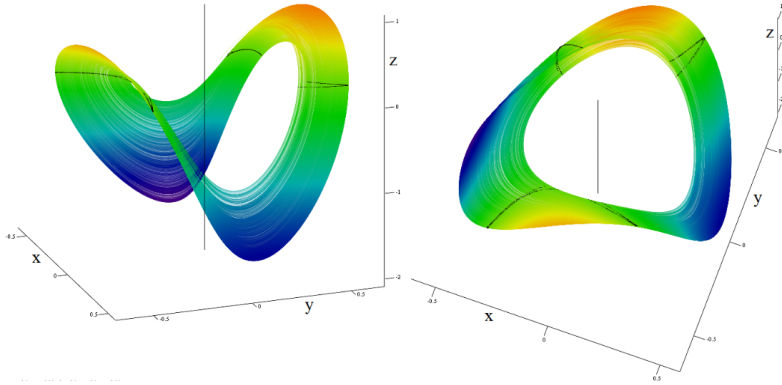
Figure 17.1: Three-dimensional perspective projections of a typical chaotic attractors observed in system with line equilibrium given by functions (5a), visualization of equilibrium line and Poincaré section defined by z=0.
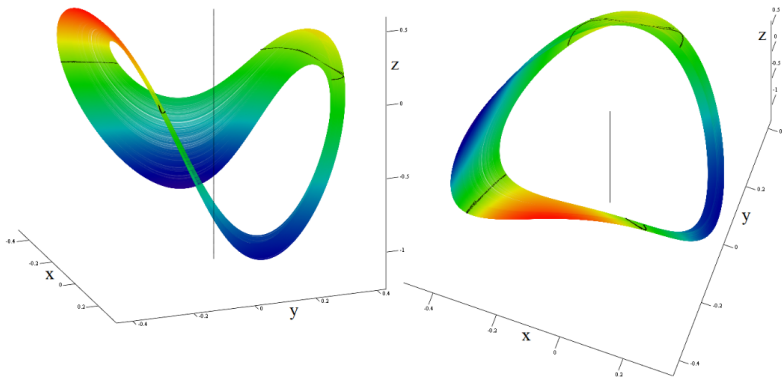


Figure 17.2: 3D rainbow-scaled projections of a typical chaotic attractors observed in dynamical system with line equilibrium given by functions (5b), visualization of equilibrium line and Poincaré section given by z=0.

$$f_1(x) = z, f_2(x) = y + bz, f_3(x) = -ay, \tag{17.9}$$

also leads to chaos if system parameters are fixed on the numerical values $a = 0.04$, $b = 0.1$ and a set of the initial conditions is $x0 = (0.80.80)^T$, see Fig. 5 for attractor visualization.

Geometrical structures of the chaotic attractors produced by the dynamical systems with line equilibrium mentioned above are similar. Note that mathematical model defined by (4) with the additional functions (5a-e) are also closely related. It is because all cases are discovered using the same numerical approach with the same starting mathematical model with many quadratic terms [70]. From the viewpoint of practical realization of (4) with terms (5) universal circuit with few switchable linear feedbacks can be constructed. In paper [45] there are few dynamical systems that do not directly fit into mathematical model with general description (4) but still preserves line equilibria located on plane z=0. However, it can be shown that circuit implementations, either voltage-mode or current-mode, have the same number of the active elements and a final network complexity.
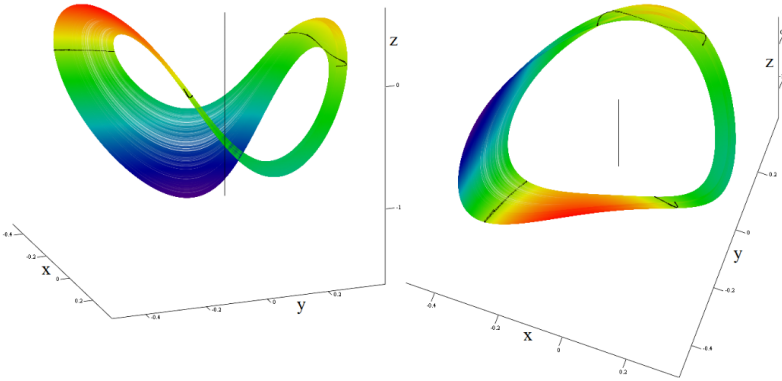
Figure 17.3: 3D perspective projections of a typical chaotic attractor observed in system with line equilibrium given by functions (5c), visualization of equilibrium line and Poincaré sections defined by plane z=0.
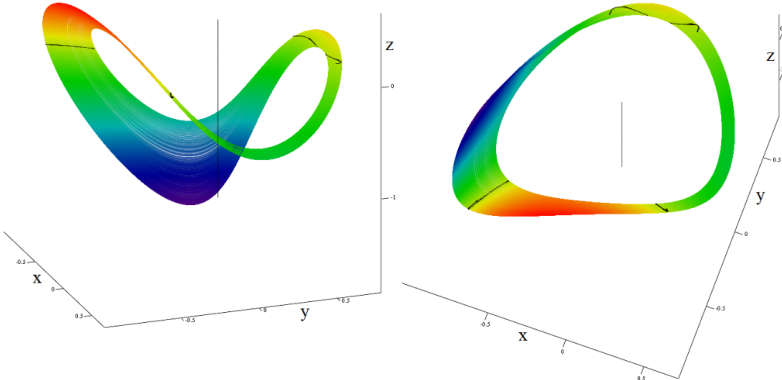


Figure 17.4: Three-dimensional perspective projections of a typical chaotic attractor observed in dynamical system with line equilibrium given by functions (5d), visualization of equilibrium line and Poincaré sections z=0.
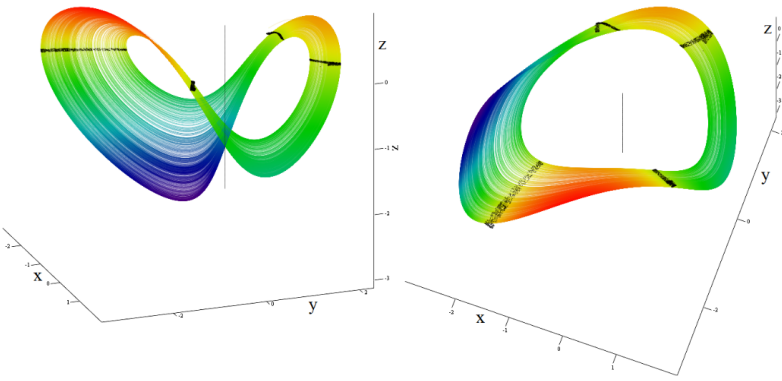


Figure 17.5: Three-dimensional perspective projections of a typical chaotic attractor observed in dynamical system with line equilibrium given by functions (5e), visualization of equilibrium line and Poincaré sections z=0.

All dynamical systems defined above are dissipative, i.e. associated dynamics is not time reversible. Divergence of the flow can be calculated as

$$\Delta V = f_1(x) + y\frac{\delta f_1(x)}{\delta y} - +x\frac{\delta f_2(x)}{\delta z} - y\frac{\delta f_3(x)}{\delta z} \qquad (17.10)$$

For system having auxiliary functions (5) we get following volume element exponential contraction rates $\nabla V \approx z-b \cdot x$ for (5a-c,e) and $\nabla V \approx z-b \cdot x-y$ for (5d). Examples of the chaotic time-reversible flows are provided in [71].

Quite recently, chaotic mathematical models with multiple line equilibrium have been proposed. One such example can be found in report [47] and can be described in general form (2) together with the following functions

$$f_1(x) = by^2 + cxz, f_2(x) = -xy, \Psi(x) = y^2 - 1, \qquad (17.11)$$

and the internal parameters a=0.6, b=0.3 and c=0.5. Solution dx/dt=0 considering (2) and (7) leads to a couple of parallel equilibrium lines located at xe=(x ±1 0)T, corresponding attractor is shown in Fig. 6 where a set of the initial condition was equal to x0=(1 0 0)T. Note that these lines are infinite in state space while strange attractor is bounded in small volume element such that only fraction of these lines is responsible for its formation.

Divergence of flow can be established using formula

$$\Delta V = z\frac{\delta f_1(x)}{\delta y} + f_2(x) + z\frac{\delta f_2(x)}{\delta z} + \frac{\Psi(x)}{\delta z} = 2byz - xy, \qquad (17.12)$$

Numerical integrations demonstrated in this paper were done by using Mathcad and build-in fourth-order Runge-Kutta method. Final time was chosen to be tmax=10000 with a time step t$\Delta$=0.01. Initial conditions can be chosen accordingly to relevant publications where also the bifurcation diagrams, different plots of the Lyapunov exponents vs system parameter and calculated Kaplan-Yorke dimensions can be found. These papers reveal possibility to see route-to-chaos scenarios via a continuous change of a single constant term. In circuit practice, this term can be represented by external dc voltage or current control source. By performing this change the regions of chaos alternate with windows characterized by periodic solution.

### 17.2.2 Model with hyperbolic and parabolic equilibrium

One logical step further in searching for the chaotic systems with equilibrium located on plane is hyperbolic and parabolic equilibrium structure. Both cases are provided in [47] and a comprehensive study of another different "hyperbolic" case can be found in [48]. First one can be expressed as (2) with the auxiliary functions

$$f_1(x) = z^2 - 1, f_2(x) = y^2 - z^2, f_3(x) = x^2 - y^2 - 1, \qquad (17.13)$$

and internal parameter a=-1. Corresponding strange attractor arise for a set of the initial conditions x0=(0 -0.6 0)T and is illustrated in Fig. 7.

Second dynamical system can be described by general expression (2) with functions

$$f_1(x) = -z^2, f_2(x) = z - xy, \Psi(x) = x^2 + y, \qquad (17.14)$$
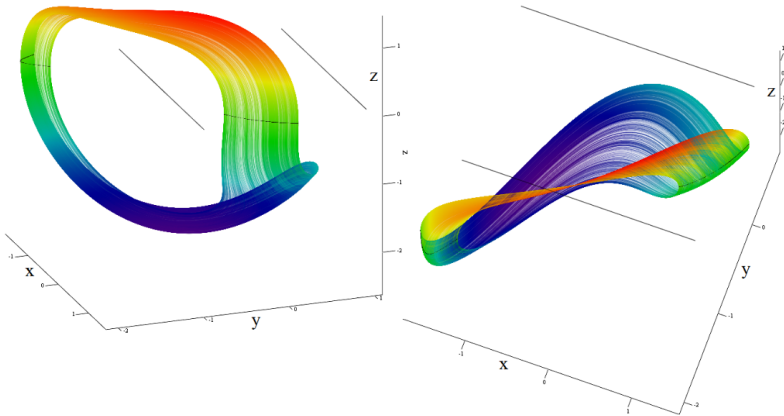
Figure 17.6: Chaotic attractor observed in system characterized by functions (7), i.e. with a pair of line equilibrium.

and parameter a=-2 where interesting strange attractor can be observed if set of the initial conditions equals x0=(0 10 0)T. Geometrical structure of a corresponding strange attractor is demonstrated using perspective view in Fig. 8. For both systems equilibrium curve is located on the horizontal plane z=0. Note that state attractor of this "parabolic" system occupies large state space volume which can cause problems for circuitry implementation due to the limited dynamical ranges of used active elements.
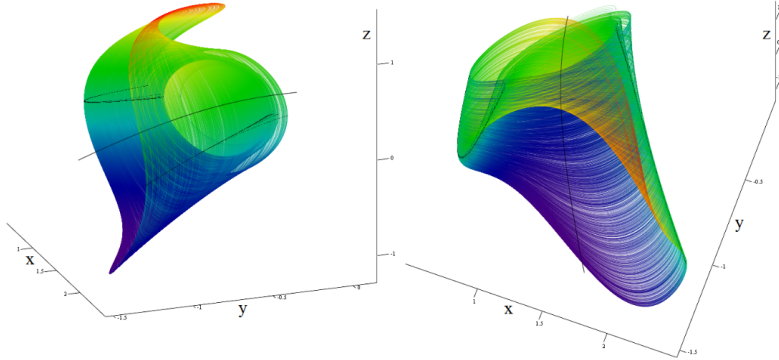


Figure 17.7: Three-dimensional rainbow-scaled projections of a typical chaotic attractors observed in system having hyperbolic equilibrium, visualization of equilibrium curve and Poincaré section defined by plane z=0.

### 17.2.3 Model having circular and elliptical equilibrium

Very first example which belongs into class of autonomous dynamical systems having a circular equilibrium has been discovered recently [49] and can be expressed in form (2). First equation defines a two-dimensional subspace (z=0) where degenerated equilibrium structure can be found; it is z=0 plane again. Equilibrium circle can be unfolded and local bifurcations along this circle can be examined. Third equation covers the implicitly given formula for equilibrium geometry $\psi(x)$ extended by additional vector field deformation
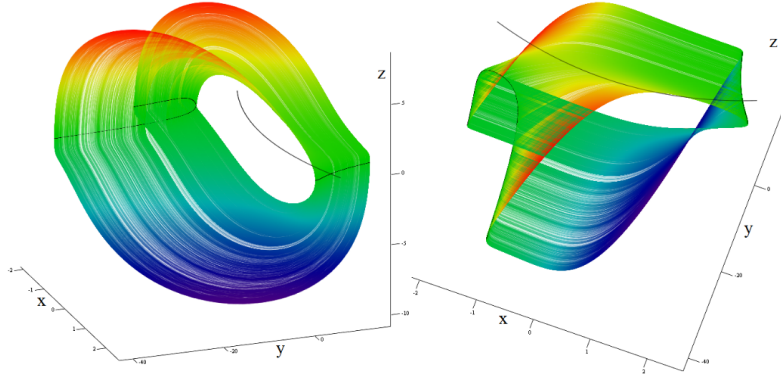
Figure 17.8: Three-dimensional color-scaled projections of a typical chaotic attractors observed in dynamical system with parabolic equilibrium, visualization of equilibrium curve and Poincaré section given by plane z=0.

and/or scaling factor f2(x). Desired equilibrium is achieved if $\psi(x)$ is equation of a circle and chaotic behavior can be observed for the remaining functions

$$f_1(x) = bx - cz^2, f_2(x) = -dx, \Psi(x) = x^2 + y^2 - r, \qquad (17.15)$$

Obviously, this mathematical model possesses complementary pair of chaotic attractors. Original one can be observed for a value choice a=-0.1, b=3, c=2.2, d=0.1 and radius of equilibrium circle r=1. Mirrored attractor appears after the trivial inversions of the system coordinates. Note that a vector field ready for evolution of the chaotic attractor becomes strongly polynomial (up to cubic term) and five four-quadrant analog multipliers will be necessary for design of this chaotic oscillator. Typical strange attractor generated by this dynamical system in the case of the initial conditions x0=(0.3 0 0)T is shown in Fig. 9.

In order to define canonical (algebraically simplest) system a deformation factor can be assumed zero reducing the dynamical system (2) into a more practical expression with a single scalar function f1(x) covering polynomial nonlinear terms. Thus, we return to (3). One such example can be described by following set of auxiliary functions

$$f_1(x) = -bxy - yz + cz^2, \Psi(x) = x^2 + y^2 - r, \qquad (17.16)$$

where chaotic motion can be observed for the parameters a=0.4, b=0.8, c=1.3 and set of the initial conditions x0=(0.3 0 0)T, check Fig. 10 for shape of this strange attractor.

Another example of dynamical system with circle equilibrium can be found in [47]. This system belongs into class (2) with functions

$$f_1(x) = -y^2 - xz, f_2(x) = y^2 - bz^2 + x, \Psi(x) = x^2 + y^2 - r, \qquad (17.17)$$

and parameters a=1, b=2 and radius r=1. Corresponding strange attractor for the initial conditions x0=(0 0.9 0.4)T is provided in Fig. 11. Both attractors are small in the state space and can be easily realized as the lumped electronic circuits. It should be noted that above mentioned systems with circular equilibrium can produce completely dissimilar chaotic attractors with completely different cross-sections.

Since circle is a special case of ellipse dynamical system described by expression (2) needs only a minor modification to possess elliptical equilibrium, namely

$$f_1(x) = bx - cz^2, f_2(x) = -dx, \Psi(x) = \left(\frac{x}{r_1}\right)^2 + \left(\frac{y}{r_2}\right)^2 - r, \qquad (17.18)$$

where variables r1 and r2 state for minor and major semi-radius of an equilibrium ellipse respectively. Let introduce symmetrical ellipse deformation ratio $\sigma = 1/r1 = r2$ as arbitrary real positive number. Then we can make a nonsingular transformation of the coordinates which changes system (2) with functions (10) into same system (2) with functions (13); x→x´·σ, y→y´/σ, z→z´ where x´, y´, z´ are the new state variables. Values of the internal parameters associated with (2) and (13) needs to be recalculated using simple formulas (results provided for choice $\sigma = 5$) a=-0.1/σ=-0.02, b=3·σ2=75, c=2.2·σ=11, d=0.1·σ=0.5.
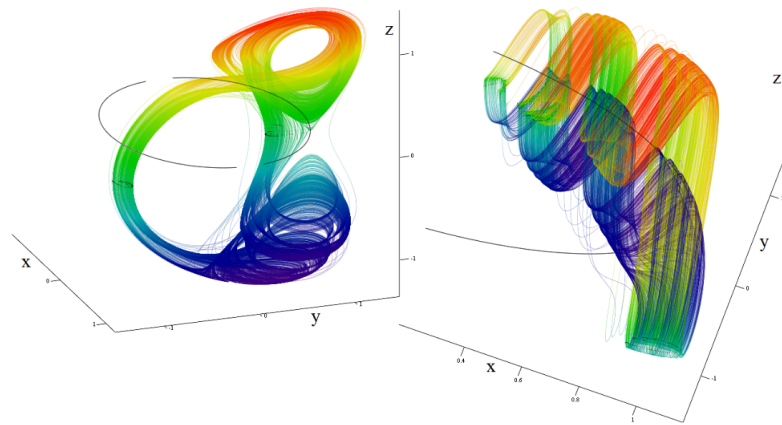


Figure 17.9: Perspective rainbow-scaled projections of a typical chaotic attractor observed in dynamical system taken from paper [49] with circular equilibrium, visualization of equilibrium line and Poincaré section given by z=0.
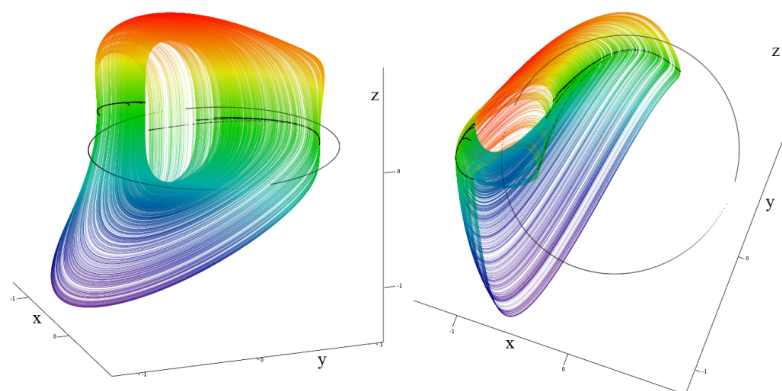


Figure 17.10: 3D color-scaled visualization of a typical chaotic attractor observed in system with circular equilibrium taken from [47], equilibrium structure (black curve) and return map with cross-section z=0 (black dots).

For such values chaotic attractor is provided by means of Fig. 12 for the initial conditions shifted towards new basin of attraction, lets pick for example x0=(0 4.5 0)T.

Circuit-level simulations again uncover possibility to see the route-to-chaos scenarios via continuous change of a single model/network parameter; and its value can be adjusted by external dc voltage or current control source. By performing this change the regions of chaos wanders with the windows showing limit cycles having various shapes and periods. The main problem here is that initial conditions should be precisely adjusted and imposed into the chaotic oscillator; all three state variables at the same time.
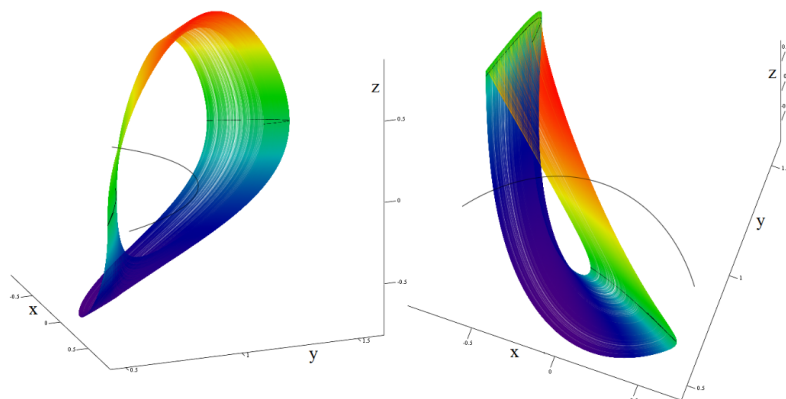


Figure 17.11: 3D plot of a typical chaotic attractor observed in a system with circular equilibrium taken from [47], equilibrium structure (black curve) and return map with cross-section defined by plane z=0 (black dots).
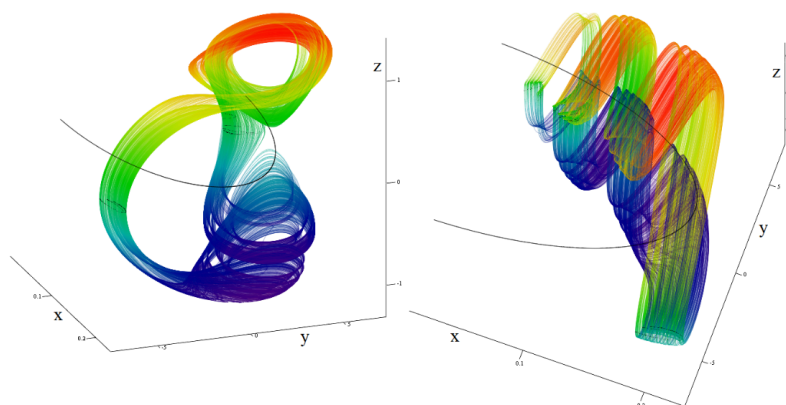


Figure 17.12: Perspective rainbow-scaled projections of a typical chaotic attractor observed in a dynamical system with elliptical equilibrium, compare the horizontal axis scales with state space shown in Fig. 9.

## 17.3 Circuitry Implementation and Verification

The proposed circuit design procedure is based on first Kirchhoff's law applied on nodes with the grounded linear capacitors. This means that each differential equation de-facto represents sum of the currents. Necessary mathematical operations are realized by using

active building blocks capable to process currents instead of voltages. Advantage of such concept is that sum of the individual terms in the differential equations can be done by a single node. Typical property of a current-mode realization is low input and high output impedances of used active devices. Some commercially available as well as promising but so far hypothetical active elements dedicated for current-mode signal processing are provided in overview article [72].

The most promising active element is a second-generation current conveyor (CCII±) described by three terminal equations VX=VY, IY=0 and IZ=±IX. Positive type CCII+ is commercially available under notation AD844 and package also contains output voltage buffer. This device was already implemented for design of analog chaotic oscillator, see examples [73]-[75]. Negative variant CCII- can be found in the markets under notation EL2082; current gain of this device can be adjusted in range between zero (Vgain=0V) and two (Vgain=2V) using external dc voltage source Vgain. Multiple-output second generation current conveyors (MOCCII) will be implemented by using appropriate number of CCII+ (each current output requires one active element) to preserve dynamical system ready for immediate design; on the contrary to a brief paper [62] where these devices were used without hesitation. Well established operational trans-admittance amplifiers with single (OTA) or multiple (MOTA) current outputs are other examples of handy active devices. Currently both are commercially available (unfortunately limited offer) as the integrated circuits under various denotations such as LM13600, LM13700, CA3080, LT1228, MAX435, MAX436, OPA660 and OPA860 (both with voltage buffer), etc. Last but not least, differential voltage current conveyor (DVCC) can be used if multiple mathematical operations are needed. This device has three inputs with the circuit quantities satisfying IY1=IY2=0, VX=VY1–VY2 and a single output terminal characterized by IZ=IX. More current outputs can be achieved by connection of several CCII± as it is in the case of MOCCII. Thanks to publications [76]-[78] where DVCC has been both designed and applied this device is no longer hypothetical; although probably not supposed for mass fabrication in the near future. Basic behavior of DVCC can be modeled by input buffers, and standard differential amplifier. Output of this sub-circuit forms node X where some load is supposed to be connected. Current passing through this load can be copied into output Z terminal by using single CCII+. To date, very few research papers have been dedicated to design of the chaotic oscillators with last promising current-mode active element named accordingly to fundamental operation as current differencing transconductance amplifier (CDTA) [79]-[81].

Reason why modern devices should be considered for design is that it can simplify final network (level of simplification depends on the mathematical model), make one-to-one-correspondence between mathematical model parameter and circuit parameter or to provide external electronical adjustability of system parameter. The latter advantage will be considered as essential requirement for final realization of chaotic oscillator. In other words, if network topology is chosen correctly a smooth change of external dc voltages can be used to trace different route-to-chaos scenarios. Moreover, it is still believed that a current-mode signal processing is advantageous from the viewpoint of better frequency response. Although only theoretically, high frequency currents can be processed without spurious attenuation (without filtering effect of the active elements). In most cases supply voltage of the current-mode integrated circuits is symmetrical.

The active devices will be firstly considered close-enough to the ideal which means in the case of current signal processing that input impedance is zero and output impedance is

infinite. It means that output current is distributed into the rest of circuit no matter what kind of load is involved. Next step is that input impedance is modeled by basic resistance connected in series with inductance while output impedance is composed by resistance with high-frequency value degradation caused by capacitor connected in parallel.

It should be noted that many upcoming network realizations does not contain resistors and are suitable for full on-chip implementations using common CMOS technology.

### 17.3.1 Chaotic oscillators

Circuit synthesis belongs to tasks having multiple correct solutions. Design engineer can construct many completely different analog circuits that behave identically as a given mathematical model. Some of these realizations can be celebrated because of simplicity, the others can benefit from minimal number of elements and the rest of realizations can have the one-to-one relations between model parameters and circuit variables. Remember that we are focused on the current-mode circuits only; it means that all state variables are currents. In some realizations of chaotic oscillators initial conditions needs to be imposed into proper network branches. This requirement can be rather problematic to satisfy in the case of current-mode operational regime. Here, voltage-mode is probably the better idea.

**Oscillator with line equilibrium**

Dynamical system with general line equilibrium expressed as (2) can be modeled by a current-mode network provided in Fig. 13. Covering differential equations are following

$$\frac{d\,i_x}{dt} = \frac{g_{m1}}{C_1}i_z, \frac{d\,i_y}{dt} = \frac{g_{m2}}{C_2}\varepsilon_1 i_z f_1(i_x, i_y, i_z),$$
$$\frac{d\,i_z}{dt} = \frac{g_{m3}}{C_3}\left[\varepsilon_2 i_z f_2(i_x, i_y, i_z) + \gamma_1 i_x - i_y + \frac{V_c}{R_c}\right] \tag{17.19}$$

where $f_1(i_x, i_y, i_z)$ and $f_2(i_x, i_y, i_z)$ are fully current-mode nonlinear scalar transfer functions, $\varepsilon k$ is transfer factor of k-th current multiplier and$\gamma$i is multiplication factor of i-th CCII-. Quite common situation is that required current gain factor $\gamma$i of some multiplier is much bigger than it is allowed by a manufacturer of EL2082. This obstacle can be removed simply by a cascading sufficient number of CCII-. This interconnection is done by using Z→X current terminals. Simultaneously it is assumed that reaching output-Z current saturation is out of question for the employed conveyors finishing cascade similarly as going out of dynamical range for linear operation which is allowed for input-X current. Since integrated analog multiplier EL4083 has balanced current outputs and only one is actually used circuit designer should take care of remaining output; i.e. connect optimal-valued resistor to terminate unused output.

For each designed oscillator working capacitors can be chosen the same C1=C2=C3 as well as resistors R1=R2=R3 without the loss of generality; for the frequency components falling into acoustic range time constant $\tau$=R·C=10410-7=1ms has been chosen. External dc voltage Vc represents equilibrium line offset and can be both positive and negative. However, a slight change of an equilibrium structure can dramatically influence observed state attractor. Of course, Vc and Rc together with associated CCII+ can be interchanged by dc source of a constant current.
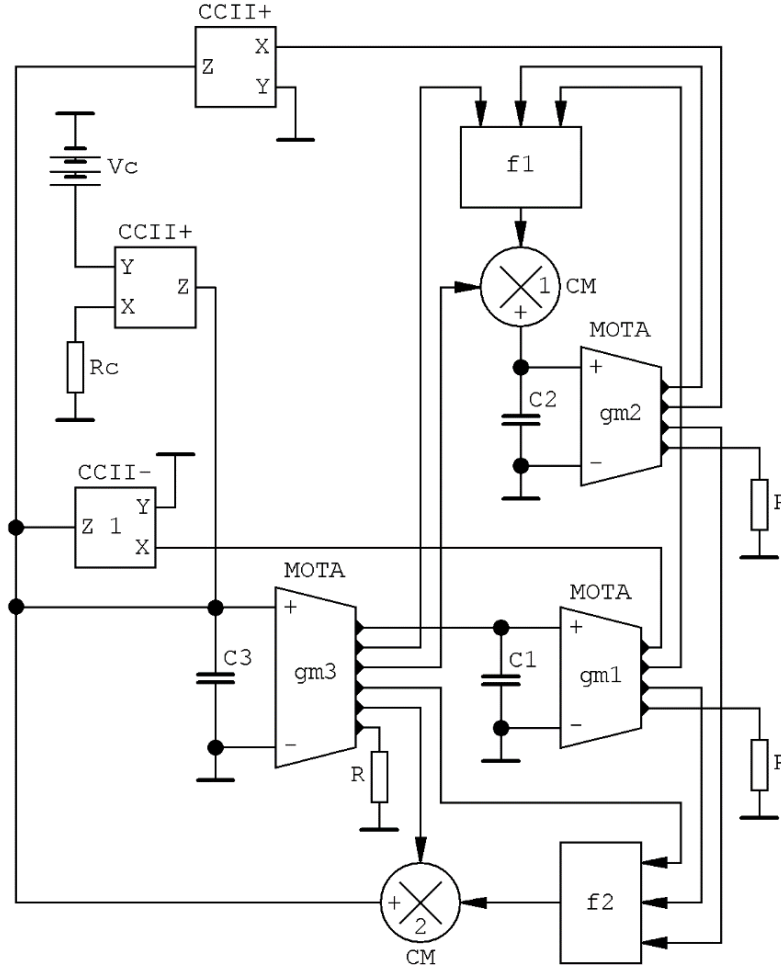
Figure 17.13: Current-mode implementation of a general dynamical system having line equilibrium expressed as (2) using three MOTA, three CCII± and two black-boxes with desired current-mode transfer characteristics.

Circuit conception of a dynamical system (3) is illustrated in Fig. 14 and following state equations can be derived leading to canonical realization with line equilibrium

$$\frac{d\,i_x}{dt} = \frac{1}{C_1 R_1} i_z, \frac{d\,i_y}{dt} = \frac{1}{C_2 R_2} \varepsilon_1 i_z f_1(i_x, i_y, i_z)$$

$$\frac{d\,i_z}{dt} = \frac{1}{C_3 R_3 R_c} \left[ R_x i_x - R_y i_y + V_c \right], \tag{17.20}$$

where the gain factors of CCII- are set to be unity. Obviously, a voltage source Vc cannot be replaced by dc current source and designed chaotic oscillator contains only one black-box with a prescribed nonlinear current transfer function. Note that MOCCII+ is realized by four CCII± and whole circuit can be directly constructed and experimentally verified.

Mathematical models provided in [45] have slightly different circuit representations; for clarification compare formulas (5), structure given in Fig. 15 and the state equations
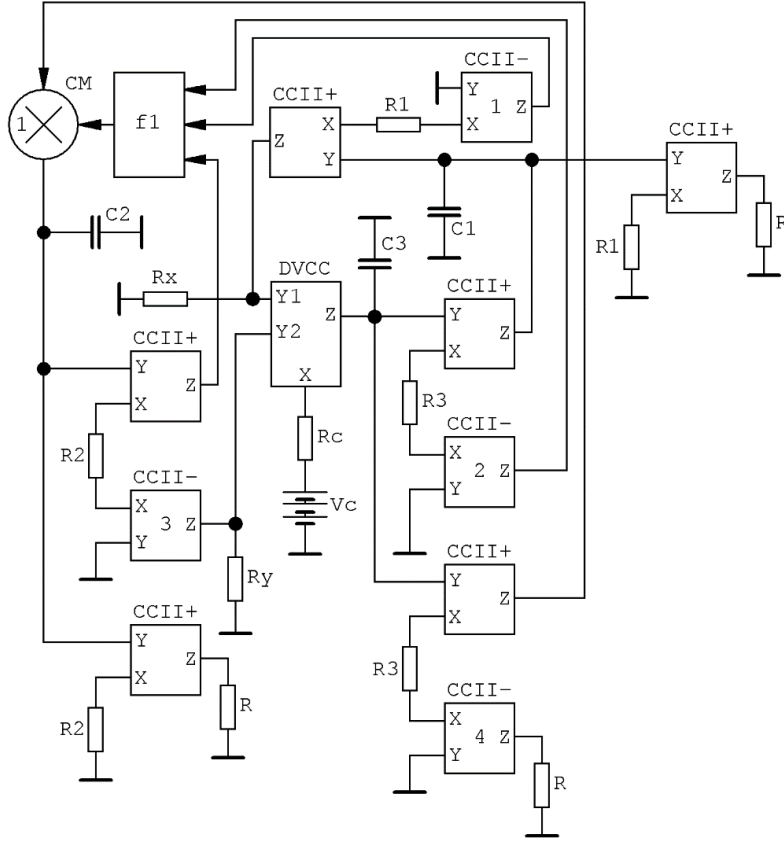
Figure 17.14: Canonical current-mode realization of a dynamical system (15) using six CCII+, four CCII- and single DVCC; two-port with transfer function f1 can be arbitrary still preserving line equilibrium.

in the upcoming form

$$\frac{d\ i_x}{dt} = \frac{1}{C_1 R_1} i_y, \frac{d\ i_y}{dt} = \frac{1}{C_2 R_2} \left[ -\gamma_1 i_x + \epsilon_1 i_y i_z \right]$$
$$\frac{d\ i_z}{dt} = \frac{-1}{C_3 R_3} \varepsilon_2 i_x \left( \gamma_2 i_y + \gamma_3 i_z \frac{V_c}{R_c} \right). \tag{17.21}$$

During simulations the circuit parameters was set to following constant values

$$\tag{17.22}$$

$$gamma_1 = gamma_3 = 1, \gamma_2 = 15, \varepsilon_1 = \varepsilon_2 = 1, V_c = 1, R_c = 10k\Omega \tag{17.23}$$

From experimental perspective these values should not represent a realization problem. Individual state variables are, as in previous cases, currents flowing through resistors R. This complete analog chaotic oscillator requires seven CCII+, four CCII- and two four-quadrant current multipliers. Remember that current gain 15 needs to be implemented by a cascading additional four CCII-.

By taking concrete form of a dynamical system (4) network provided in Fig. 16 can be constructed where only three MOTA, a couple of CCII- and a pair of the current-mode multipliers are utilized. The corresponding state equations are following

$$\frac{d\,i_x}{dt} = \frac{gm_1}{C_1}i_y + \frac{1}{R_{in}^1 C_1}, \frac{d\,i_y}{dt} = \frac{gm_2}{C_2}\left[-i_x + \varepsilon_1 i_y i_z\right] + \frac{1}{R_{in}^2 C_2}i_x,$$

$$\frac{d\,i_z}{dt} = \frac{gm_3}{C_3}\left[-\varepsilon_2 i_x(\gamma_1 i_y + \gamma_2 i_z) - i_y\right] + \frac{1}{R_{in}^3 C_3}i_z, \qquad (17.24)$$

where Rink represents input resistance of k-th OTA (for upcoming analysis of the parasitic features). During simulations the circuit parameters was set to following constant values

$$gm_1 = gm_2 = gm_3 = 100\mu S \gamma_1 = 17, \gamma_2 = 1, \varepsilon_1 = \varepsilon_2 = 1. \qquad (17.25)$$

Since maximum gain of EL2082 equals two a cascade of five these active devices should be utilized to achieve desired current gain $\gamma 1$; in such case, total theoretical gain of 32 can be reached. Of course, in the case of on-chip implementation high current gain is not a big problem since transfer constants of the current mirrors can be adjusted simply by the aspect ratios (W/L) of employed mosfet transistors. Be aware that CCII- as well as OTA blocks must operate in linear regime; nonlinear part of the vector field must be generated in prescribed form only by the current multipliers. Note that if parameter b of original mathematical model is fixed to unity and only parameter a is supposed to be variable second CCII- can be completely removed further simplifying final oscillator. Also, note that parasitic properties of the active elements have not been considered. In practice their influences need to be minimized.
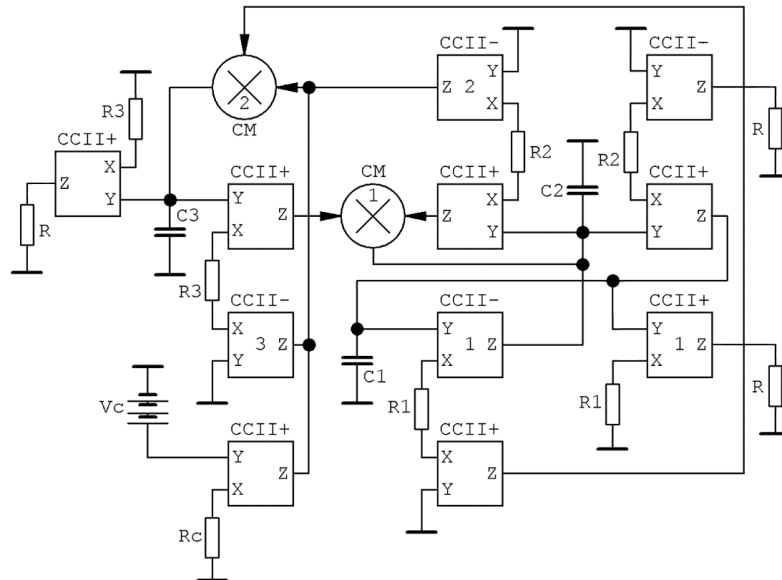


Figure 17.15: Current conveyor based current-mode network topology described by set of differential equations (16).
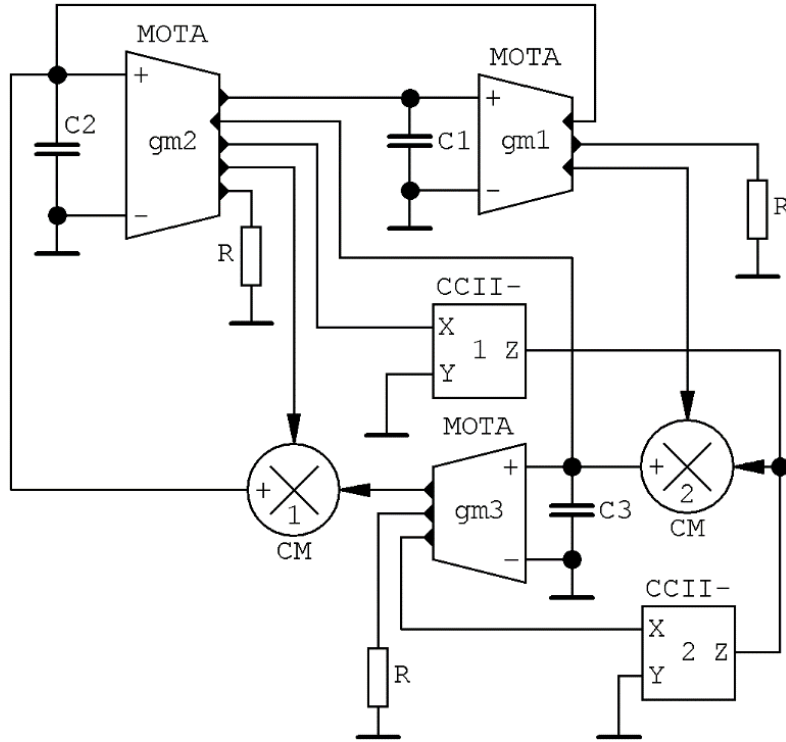
Figure 17.16: OTA based representation of a second chaotic dynamical system taken from publication [45].

## Oscillators with conical-shaped equilibrium

Algebraic complexity of the describing mathematical model (9a) implies that circuitry implementation will be complicated as well, see Fig. 17. This analog oscillator is covered by the following ordinary differential equations

$$\frac{d\,i_x}{dt} = \frac{-\gamma_1}{C_1 R_1}i_z, \frac{d\,i_y}{dt} = \frac{\varepsilon_2}{C_2 R_2}i_z\left(\varepsilon_1 i_z^2 - \gamma_5\frac{V_d}{R_d}\right),$$
$$\frac{d\,i_z}{dt} = \frac{1}{R_3 C_3}\varepsilon_5\gamma_2 i_z(\varepsilon_1 i_z^2 + \varepsilon_3\gamma_4 i_y^2) + \varepsilon_3\gamma_3 i_x^2 - \varepsilon_4\gamma_4 i_y^2 - \gamma_6\frac{V_c}{R_c}, \qquad (17.26)$$

where state variables can be considered both voltages and currents, i.e. $i_x = u_z/R_1$, $i_y = u_y/R_2$ and $i_z = u_z/R_3$. External voltages $V_c$ and $V_d$ can be used as natural bifurcation parameters. Note that eleven CCII$\pm$ and five current multipliers are necessary for a chaotic oscillator.

Mathematical model (9b) can be realized analogically using the same building blocks as shown in Fig. 18. Set of the differential equations can be derived directly from this analog system in the form

$$\frac{d\,i_x}{dt} = \frac{-\gamma_1}{C_1 R_1}i_z, \frac{d\,i_y}{dt} = -\frac{\varepsilon_1\varepsilon_2}{C_2 R_2}i_z^3,$$
$$\frac{d\,i_z}{dt} = \frac{1}{R_3 C_3}\varepsilon_4\varepsilon_5\gamma_2 i_x i_y i_z + \varepsilon_3\gamma_3 i_x^2 + \gamma_4 i_y + \varepsilon_1 i_z^2, \qquad (17.27)$$
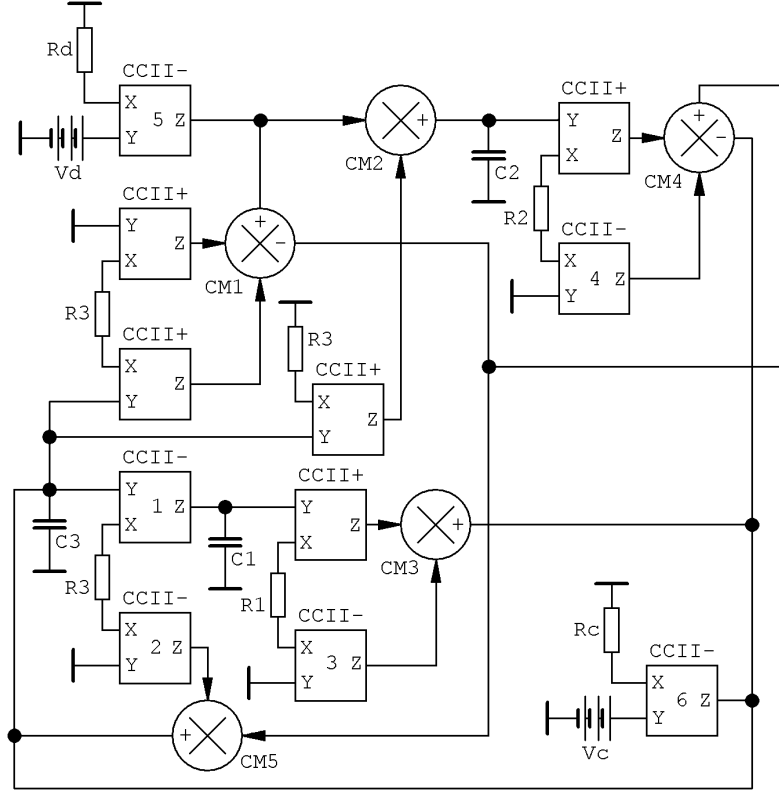
Figure 17.17: Current conveyor based current-mode network topology capable to model chaotic behavior associated with dynamical system (20) having hyperbolic equilibrium, one bipolar output current multiplier is required.

where external voltages $V_c$ and $V_d$ can be used as suitable bifurcation parameters. Typical strange attractor can be observed for example for the choice

$$R_1 = R_2 = R_3 = R_r = 10k\Omega, V_r = 1V, \gamma_1 = 0.1, \gamma_2 = 0.03$$
$$\gamma_3 = 0.5, \gamma_4 = 2, \varepsilon_1 = 0.35, \varepsilon_2 = 12.5, \varepsilon_3 = \varepsilon_4 = \varepsilon_5 = 1. \tag{17.28}$$

Note that proposed collection of values should not represent serious realization problems. If directly unreachable constant $\varepsilon_2$ can be lowered to 1.25 while $R_2$ changes to $1k\Omega$.

**Electronic system with elliptical-type equilibrium**

Similarly, describing state equations of autonomous analog network capable to model dynamical system with circular equilibrium are following

$$\frac{d\,i_x}{dt} = \frac{-\gamma_1}{C_1 R_1}i_z, \frac{d\,i_y}{dt} = -\frac{\varepsilon_1 \varepsilon_2}{C_2 R_2}\varepsilon_1 i_z(i_x + \varepsilon_2 i_z^2)$$
$$\frac{d\,i_z}{dt} = \frac{1}{R_3 C_3}\left[\varepsilon_3 i_x i_z + \varepsilon_4 i_x^2 + \varepsilon_5 i_y^2 - \gamma_1 \frac{V_r}{R_r}\right], \tag{17.29}$$
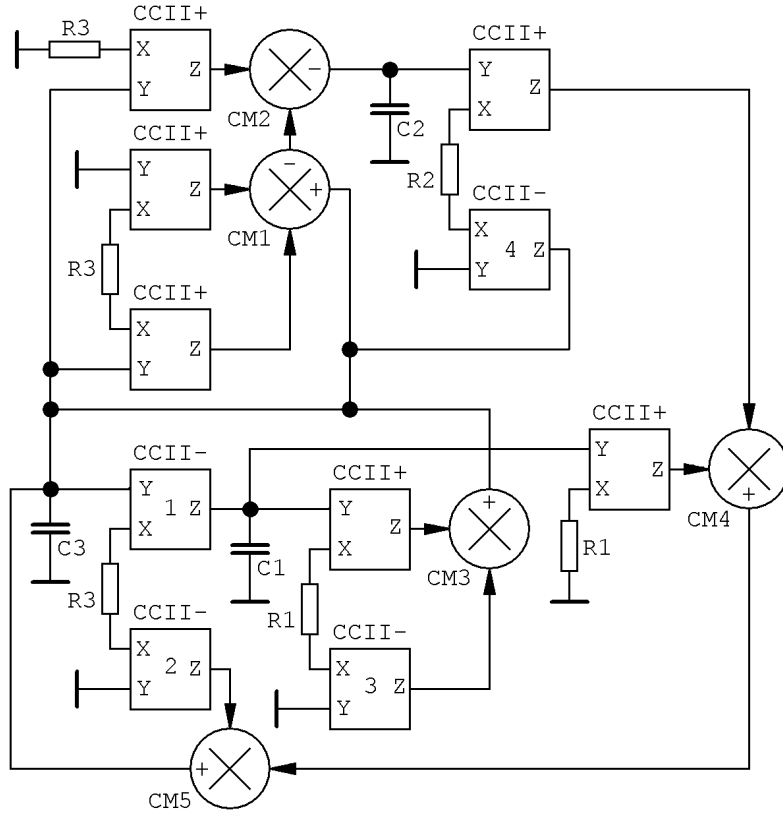
Figure 17.18: Current conveyor based current-mode chaotic circuit capable to model
behavior associated with system (21) having parabolic equilibrium, single bipolar output
current multiplier is need.

where circle radius can be changed directly by the external voltage Vr or, more
precisely, by transfer gain $\gamma 1$. Careful adjustment is required here since global behavior
is extremely sensitive to this value. Corresponding network can be found in Fig. 19.
Unfortunately, MOCCII+ is not off-the-shelf active component; thus, previous design
cannot be used for immediate laboratory experimentation and transformation into CCII±
only based network is necessary. After a slight modification, a chaotic oscillator shown
in Fig. 20 has been achieved. This circuit is covered by a set of the ordinary differential
equations

$$\frac{d\,i_x}{dt} = \frac{-gm_1}{C_1}i_z, \frac{d\,i_y}{dt} = -\frac{gm_2}{C_2}\varepsilon_1 i_z(i_x + \varepsilon_2 i_z^2)$$
$$\frac{d\,i_z}{dt} = \frac{1}{R_3 C_3}\left[\varepsilon_3 i_x i_z + \varepsilon_4 i_x^2 + \varepsilon_5 i_y^2 - \gamma_1 \frac{V_r}{R_r}\right], \qquad (17.30)$$

For computer-aided verification most circuit can be fixed on circuit-reasonable numerical
values such as

$$gm_1 = 10\mu S, gm_2 = 4\mu S, gm_3 = 100\mu S, R_y = R_r = 1k\Omega$$
$$R_x = 10k\Omega, \varepsilon_1 = \varepsilon_3 = \varepsilon_4 = 1, \varepsilon_2 = 0.1, \varepsilon_5 = 0.8, V_r = 1V. \qquad (17.31)$$

For these values the ratio between minor/major axes of ellipse r1/r2 is enhanced to 1/3. In any case, only a fraction of ellipse provides a vector field geometry responsible for evolution of this strange attractor. However, such fraction still represents infinite number of the equilibrium points. Major and minor radius of an equilibrium ellipse equals inverse square root of current gain factors $\varepsilon 3$ and $\varepsilon 4$ respectively. Numerical studies reveal that global behavior of this dynamical system is extremely sensitive to both radiuses and chaos quickly disappears for values far away from unity; a solution became unbounded leading to the state space attractor limited only by the saturation levels of the used active devices (in fact applied supply voltages).

Note that only transfer factors of the used current multipliers are supposed to control chaotic motion. Since EL4083 is the only commercially available current multiplier so far (but without chance to adjust gain) this circuit should be considered for on-chip CMOS realization and fabrication. Extreme sensitivities of a specific strange attractor to external currents can turn to be advantageous if these circuit quantities are generated by some sort of sensors; for example, caused by the chemical changes in some liquid.

Canonical dynamical system having elliptical equilibrium can be also implemented in various current-mode conceptions. One of them can be described by state equations

$$\frac{d\, i_x}{dt} = \frac{gm_1}{C_1}i_z, \frac{d\, i_y}{dt} = -\frac{gm_2}{C_2}\varepsilon_1 i_z f_1(i_x, i_y, i_z)$$
$$\frac{d\, i_z}{dt} = \frac{gm_3}{C_3}\left(\gamma_1\varepsilon_2 i_x^2 + \gamma_2\varepsilon_3 i_y^2 - \frac{V_r}{R_r}\right), \tag{17.32}$$

where Vr=1V is fixed constant and value Rr should be chosen accordingly to impedance normalization factor. Major and minor radius of an equilibrium ellipse equals inverse square root of current gain factors $\varepsilon 2$ and $\varepsilon 3$ respectively. This so far unfinished analog circuit where two-port with arbitrary transfer function is given as black-box is provided by means of Fig. 21.

Finally, network structure with only CCII± and current multipliers can be derived as shown in Fig. 22. Straightforward analysis leads to the following describing formulas

$$\frac{d\, i_x}{dt} = \frac{-\gamma_1}{C_1 R_1}i_z, \frac{d\, i_y}{dt} = \frac{\varepsilon_2 i_z}{C_2 R_2}\left(\varepsilon_1 i_z^2 + i_x\right)$$
$$\frac{d\, i_z}{dt} = \frac{1}{C_3 R_3}\left(\varepsilon_3\varepsilon_5\gamma_2 i_x i_z + \varepsilon_4\gamma_4 i_x^2 + \varepsilon_3\gamma_3 i_y^2 - \gamma_1\frac{V_r}{R_r}\right). \tag{17.33}$$

Numerical values of the circuit parameters leading to the evolution of a typical strange attractor can be chosen as follows

$$R_1 = R_2 = R_3 = R_r = 10k\Omega\gamma_1 = 0.07, \gamma_2 = 1, V_r = 1V$$
$$\varepsilon_1 = 0.5, \varepsilon_2 = 4, \varepsilon_3 = 0.66, \varepsilon_4 = 1.52, \varepsilon_5 = 0.1. \tag{17.34}$$

### 17.3.2   Orcad Pspice circuit simulations

Orcad Pspice simulator has been utilized for demonstration that chaotic solution is neither numerical artifact nor transient motion but regular solution. To preserve a limited
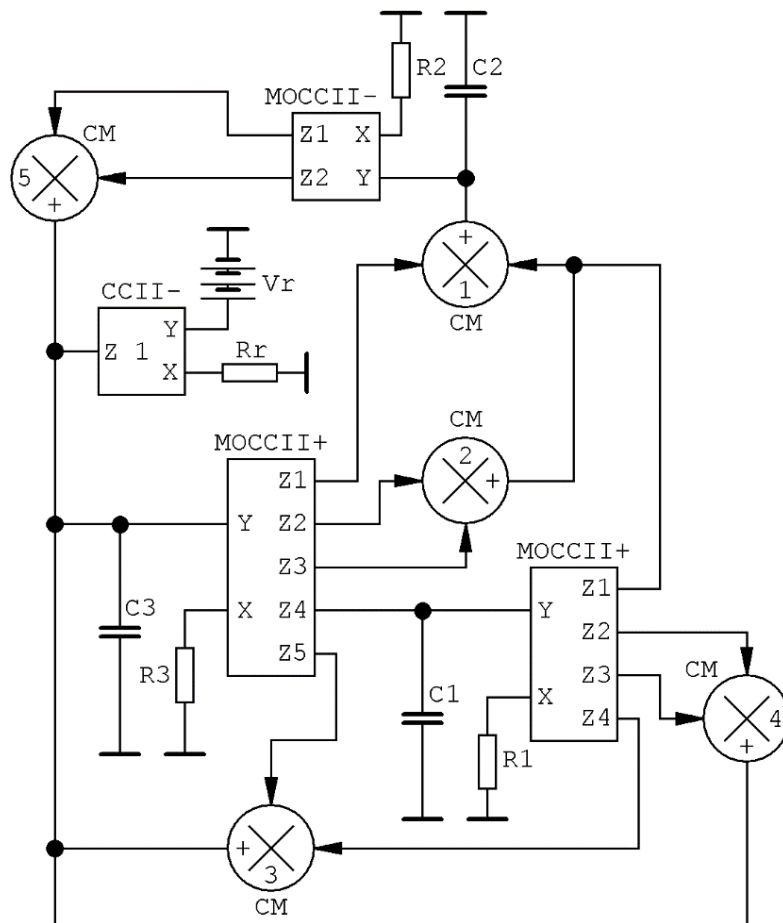
Figure 17.19: Current-mode circuit realization of system (23) with circular equilibrium using MOCCII+ elements.

length of this paper only strange attractors are visualized. These are in a very good accordance with the theoretical expectations, i.e. with the numerically integrated state trajectories. Since chaotic oscillators are always nonlinear circuits simulation scenarios are restricted to time-domain analysis; final time was chosen to be 100ms and maximum step size $1\mu$s with respect to a time constant. Achieved waveforms are sufficiently smooth and long enough such that the calculated frequency spectra of the generated signals (using fast Fourier transform) have required resolution.

First simulation results given in this section are related to dynamical system with line equilibrium (16) with values (17). Chaotic waveforms in time and frequency domain are provided in Fig. 23 (up to frequency component 150kHz) and selected plane projections of a typical strange attractor are shown in Fig. 24.

Second simulation results are bounded to a dynamical system with a line equilibrium; namely which is described by the differential equations (18) together with the numerical values (19). Generated chaotic signals in time and frequency domain are shown by means of Fig. 25 while corresponding plane projections of a state attractor are given in Fig. 26. The state variables are naturally currents but for attractor visualization purpose voltages across grounded capacitors are considered. Note that the chaotic waveforms generated
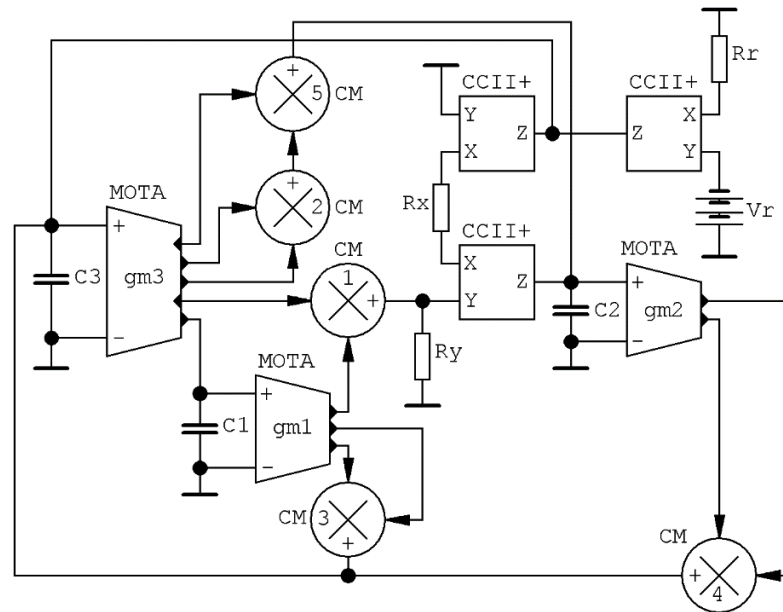
Figure 17.20: Current-mode circuit realization of a dynamical system (24) with circular equilibrium structure.

by this dynamical system have several dominant peaks in the frequency domain.

Third circuit which was verified by simulation is specified by the equations (24) with the numerical values (25). Resulting chaotic waveforms plotted in time and frequency domain (visualization provided up to 2kHz) are shown in Fig. 27. Corresponding Monge projections can be found in Fig. 28.

Fourth analog chaotic oscillator which undergoes verification through simulation is given by the differential equations (27) together with a parameter choice (28). Generated chaotic signals in time and frequency domain (wideband linear-scaled axis 0 to 200kHz is visualized) are shown in Fig. 29. Same waveforms plotted as the plane projections are provided by means of Fig. 30.

## 17.4   Concept of Generalized Parasitic and Its Analysis

Fast dynamical motions and short transients can be found quite problematic in the case of circuit implementation of prescribed dynamics. Mathematically speaking such situation corresponds to a right-hand-side of the differential equations multiplied by a big number. If considering parasitic properties of the used active elements error terms will necessarily appear in a set of describing differential equations. This can also cause nasty phenomena such as significant increase of a network order, reducing degrees of freedom by bounding two accumulation elements, it can lead to a structural instability of a chaotic attractor or completely damage prescribed state attractor. Since chaotic orbit is typically surrounded in hyperspace of the internal system parameters by unbounded solution (i.e. solution going to $\pm$ infinity) this attractor collapses into a large limit cycle with a squared quasi-radius defined by the saturation levels of used active devices (these ranges are slightly reduced supply voltages). Deep inspection of published papers dealing with
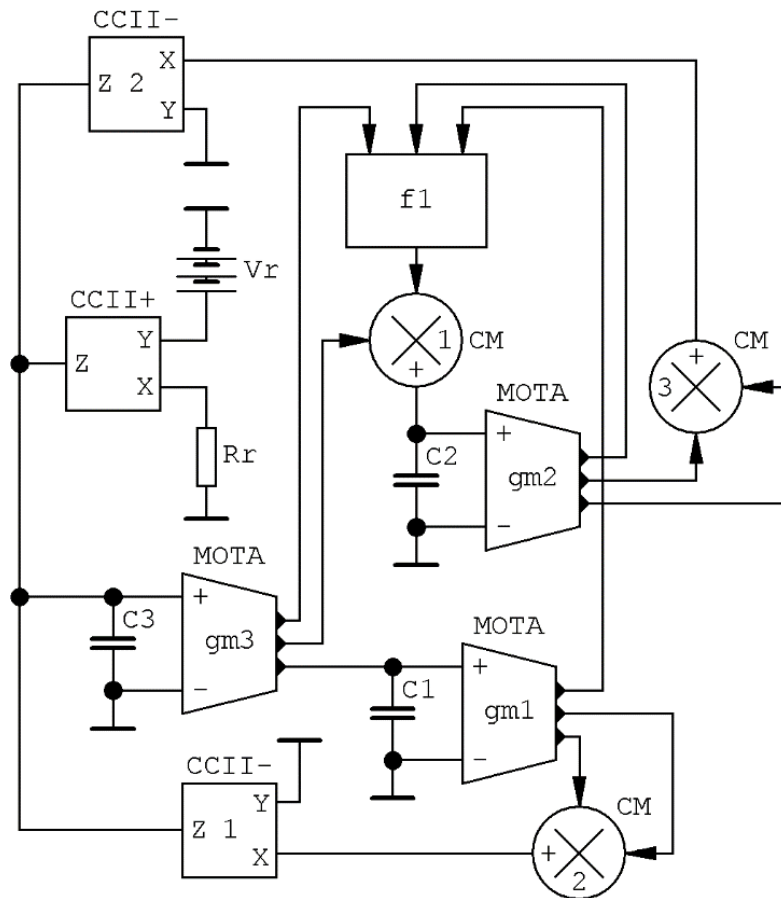
Figure 17.21: General concept of a chaotic oscillator with elliptical equilibrium where
function f1 can be arbitrary.

continuous-time chaotic oscillator design reveals that authors usually little care about
the parasitic properties of used active elements and how these factors influence expected
strange attractor. Of course, there are few exceptions like [75] where authors nicely
explain how frequency limitations of AD844 affects construction and verification of the
multi-scroll chaotic oscillator. Anyhow theoretically such qualitative analysis can solve
this problem: Is desired chaotic pattern structurally stable such that generated wave-
forms have potential for the practical applications? If such stability cannot be satisfied
to some degree desired chaotic attractor is not experimentally observable. The major
problem here is that neither largest LE nor geometrical dimension is monotonic function
with respect to the parasitic element values. Considering this it means that common
worst-case analysis or systematic gradient optimization methods do not represent cor-
rect approach to determine structural stability of the state space attractors in the case
of the nonlinear vector field.

Let's imagine that parasitic properties of the individual active devices are considered
separately. Each such parameter has unknown value and forms one edge of hyperspace
scanned by optimization routine. This idea is wrong both from viewpoint of visualization
and enormous time demands required for calculation. To quantify influence of non-ideal
properties of the active devices on the desired strange attractors a new term generalized
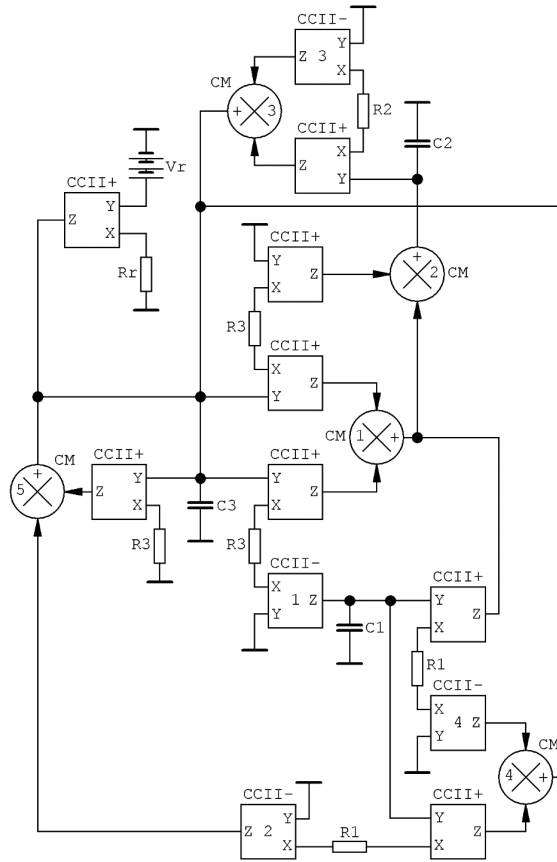
Figure 17.22: Fully current-mode chaotic oscillator with elliptical equilibrium ready for experimental measurement; design requirements are eight CCII+, four CCII- and five current-mode multipliers.
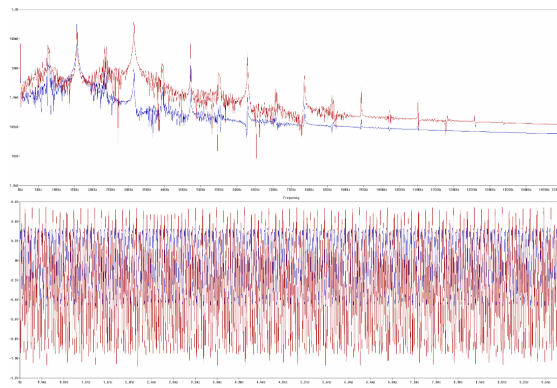


Figure 17.23: Chaotic signals in time domain (lower picture) and calculated frequency components (upper picture).

parasitic can be defined. It means that parasitic effects which have the same nature are swept and applied on mathematical model of chaotic dynamical system together in group. The most important generalized parasitic effect is additional dissipation (caused by finite
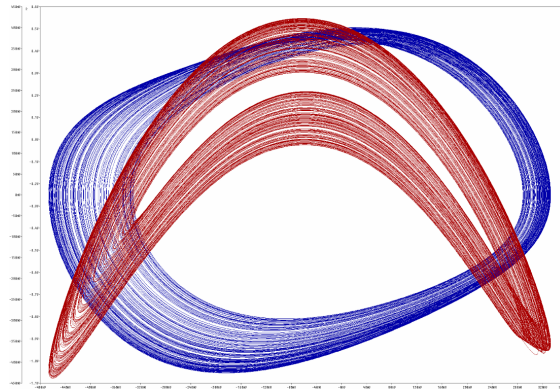
Figure 17.24: Plane projections iy and iz vs ix of typical chaotic attractor generated by analog circuit given in Fig. 15, described by differential equations (16) with numerical values (17).
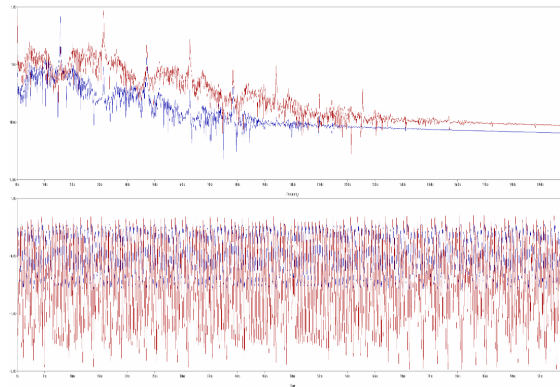


Figure 17.25: Chaotic signals in time domain (lower picture) and calculated frequency components (upper picture).
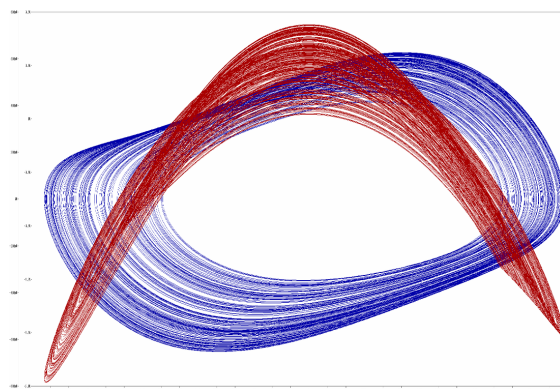


Figure 17.26: Plane projections iy and iz vs ix of a typical chaotic attractor generated by circuit provided in Fig. 16, described by the differential equations (18) with numerical values (19).

input resistances of CCII±, OTA, DVCC blocks or output resistances of these elements),
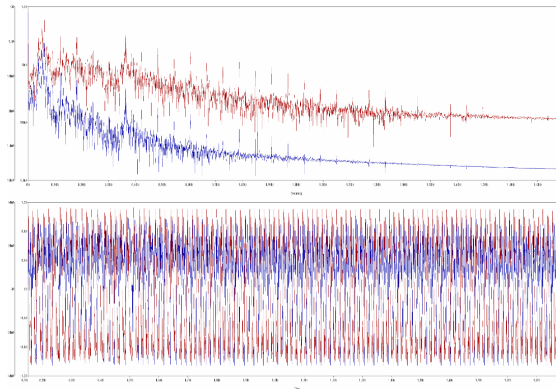
Figure 17.27: Chaotic signals in time domain (lower picture) and calculated frequency components (upper picture).
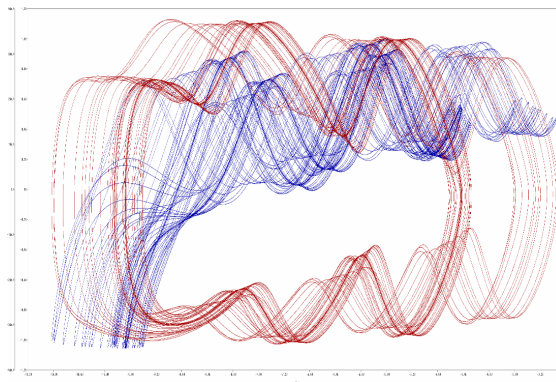


Figure 17.28: Plane projections iy and iz vs ix of a typical chaotic attractor generated by circuit given in Fig. 20, described by the differential equation (24) with numerical values (25).
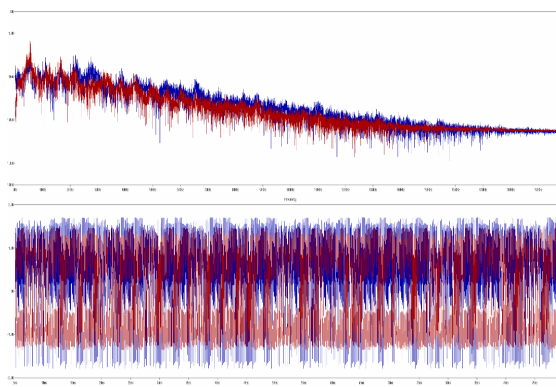


Figure 17.29: Chaotic signals in time domain (lower picture) and calculated frequency components (upper picture).

parameter uncertainty, roll-offs (caused by low-pass nature of CCII± or OTA transfers) and component tolerances. Demonstration example how to deal with mentioned reality
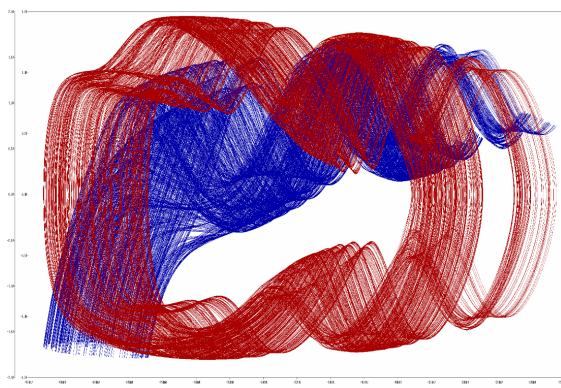
Figure 17.30: Monge projections iy and iz vs ix of a typical chaotic attractor generated by the analog circuitry depicted in Fig. 22, described by the differential equations (27) and using numerical values (28).

is provided in Fig. 31 where generalized parasitic analysis is put into the context with the so-called Kaplan-Yorke dimension of observed state attractor. In this plot, colored points are rainbow-scaled such that red denote strongly chaotic attractor, yellow represents weakly chaotic system, green and blue stands for limit cycles. Horizontal grid is sparse such that it is easy to recognize nominal (ideal) system state. This idea is applied on the selected state equations. Note that this method is capable to find "more chaotic" system.

Since one basic error term never compensate the other analyzed parasitic properties tend to have accumulating nature. For example, each OTA block connected to a working capacitor enlarges time constant by associated parasitic input capacitance while its input resistance is responsible for increased dissipation of dynamical flow. If dissipation is too high (above critical value) desired strange attractor collapse into the simpler geometrical structure, i.e. limit cycle or fixed point. In CCII based chaotic oscillators input resistance of X-terminal is connected in series with working resistor causing again a time constant enlargement effect. Roll-off effect of each OTA trans-conductance as well as each CCII current transfer constant (both should be ideally constant over full frequency scale) also has a devastating impact on a desired state attractor.

## 17.5   Conclusions

First part of this contribution can be considered as a comprehensive review showing process of discovering mathematical models with exotic types and shapes of equilibrium; beginning with the simplest dissipative flows [82] to the hyperchaotic systems with three-dimensional equilibrium structures or a chaotic dynamic where attractor can be changed from hidden to self-excited [83] by changing values of the internal system parameters.

Main part of this paper is focused on current-mode circuit realizations and consequent simulations of the hidden chaotic oscillators with the degenerated equilibrium structures. It completes current research studies where voltage-mode operational regime is preferred over current-mode designs. It is also for the first time when fully current-mode circuitry realization of a dynamical system with circular and elliptical equilibrium is reported;
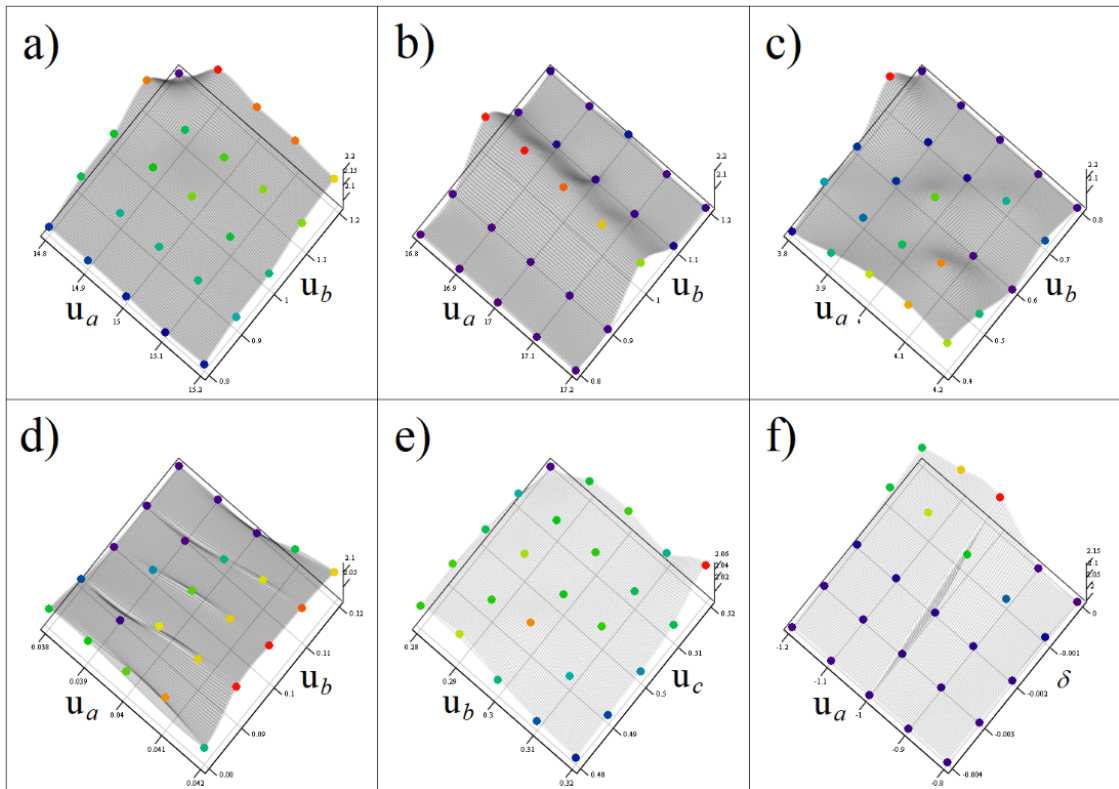
Figure 17.31: Graphical illustration of a generalized parasitic concept for a system (2) with functions: a) choice (5a), b) choice (5b), c) set (5d), d) set (5e), e) set (7), f) uncertainty of parameter a and additional dissipation for (9a).

although existence of a desired strange attractor is proved only by Orcad Pspice circuit simulations using datasheet-based level-three models of the active devices.

Last idea behind this paper is suggestion to adopt a concept of one-dimensional LE (used for calculation of a metric dimension of state attractor) for case-specific sensitivity analysis: to determine robustness of the designed chaotic oscillator to preserve prescribed strange attractor. The most devastating parasitic properties of utilized active elements are specified and proposed procedure is demonstrated via example.

## 17.6 Bibliography

[1] J. C. Sprott, A new class of chaotic circuit, Physics Letters A 266 (2000) 19–23.

[2] J. R. Piper and J. C. Sprott, Simple autonomous chaotic circuits, IEEE Transactions on Circuits and Systems II: Express Briefs 57 (2010) 730–734.

[3] J. C. Sprott, A new chaotic jerk circuit, IEEE Transactions on Circuits and Systems II: Express Briefs 58 (2011) 240–243.

[4] J. Petrzela, Modeling deterministic chaos using electronic circuits, Radioengineering 20 (2011) 438–444.

[5] M. Itoh, Synthesis of electronic circuits for simulating nonlinear dynamics, International Journal of Bifurcation and Chaos 11 (2001) 605–653.

[6] S. Yu, J. Lu, H. Leung and G. Chen, Design and implementation of n-scroll chaotic attractors from a general jerk circuit, IEEE Transactions on Circuits and Systems I: Fundamental Theory and Applications 52 (2005) 1459–1476.

[7] J. E. Varrientos and E. Sanchez-Sinencio, A 4-D chaotic oscillator based on a differential hysteresis comparator, IEEE Transactions on Circuits and Systems I: Fundamental Theory and Applications 45 (1998) 3–10.

[8] X. S. Yang, Q. Li and G. Chen, A twin-star hyperchaotic attractor and its circuit implementation. International Journal of Circuit Theory and Applications 31 (2003) 637–640.

[9] T. Gotthans and J. Petrzela, Experimental study of the sampled labyrinth chaos, Radioengineering 20 (2011) 873–879.

[10] L. Chua and G. N. Lin, Canonical realizations of Chua´s circuit family, IEEE Transactions on Circuits and Systems I: Fundamental Theory and Applications 37 (1990) 885–902.

[11] M. Gotz, U. Feldman and W. Schwarz, Synthesis of higher dimensional Chua circuits, IEEE Transactions on Circuits and Systems I: Fundamental Theory and Applications 40 (1993) 854–860.

[12] W. K. S. Tang, G. Q. Zhong, G. Chen and K. F. Man, Generation of N-scroll attractors via sine function, IEEE Transactions on Circuits and Systems I: Fundamental Theory and Applications 48 (2001) 1369–1372.

[13] S. O. Scanlan, Synthesis of piecewise-linear chaotic oscillators with prescribed eigenvalues, IEEE Transactions on Circuits and Systems I: Fundamental Theory and Applications 46 (1999) 1057–1064.

[14] J. Petrzela and J. Slezak, Conservative chaos generators with CCII+ based on mathematical model of nonlinear oscillator. Radioengineering 17 (2008) 19–24.

[15] R. Trejo-Guerra, E. Tlelo-Cuautle, C. Cruz-Hernandez and C. Sanchez-Lopez, Chaotic communication system using Chua´s oscillators realized with CCII+s, International Journal of Bifurcation and Chaos 19 (2009) 4217–4226.

[16] A. S. Elwakil and S. Ozoguz, On the generation of higher order chaotic oscillators via passive coupling of two identical or nonidentical sinusoidal oscillators, IEEE Transactions on Circuits and Systems I: Fundamental Theory and Applications 53 (2006) 1521–1532.

[17] A. S. Elwakil and M. P. Kennedy, Construction of classes of circuit-independent chaotic oscillators using passive-only nonlinear devices, IEEE Transactions on Circuits and Systems I: Fundamental Theory and Applications 48 (2001) 289–307.

[18] A. S. Elwakil and A. M. Soliman, Current conveyor chaos generators, IEEE Transactions on Circuits and Systems I: Fundamental Theory and Applications 46 (1999) 393–398.

[19] A. S. Elwakil and M. P. Kennedy, Chaotic oscillator configuration using a frequency dependent negative resistor, International Journal of Circuit Theory and Applications 28 (2000) 67–76.

[20] A. S. Elwakil and M. P. Kennedy, A family of Wien-type oscillators modified for chaos, International Journal of Circuit Theory and Applications 25 (1997) 561–579.

[21] J. Petrzela, On the existence of chaos in the electronically adjustable structures of the state variable filters, International Journal of Circuit Theory and Applications 44 (2016) 1779–1797.

[22] J. Petrzela, Chaotic behavior of state variable filters with saturation-type integrators, Electronics Letters 51 (2015) 1159–1161.

[23] H. Li, Ch. Li, Z. Yuan, W. Hu and X. Zhen, A new class of chaotic circuit with logic elements, Journal of Circuits, Systems and Computers 24 (2015) 1550136.

[24] R. Trejo-Guerra, E. Tlelo-Cuautle, J. M. Jimenez-Fuentes, C. Sanchez-Lopez, J. M. Munoz-Pacheco, G. Espinosa-Flores-Verdad and J. M. Rocha-Perez, Integrated circuit generating 3- and 5-scroll attractors, Communications in Nonlinear Science and Numerical Simulation 17 (2012) 4328–4335.

[25] A. G. Radwan, A. M. Soliman and A. L. El-Sedeek, Low-voltage MOS chaotic oscillator based on the nonlinearity of gm, Journal of Circuits, Systems and Computers 13 (2004) 101.

[26] R. Trejo-Guerra, E. Tlelo-Cuautle, J. M. Jimenez-Fuentes, J. M. Munoz-Pacheco and C. Sanchez-Lopez, Multiscroll floating gate based integrated chaotic oscillator, International Journal of Circuit Theory and Applications 41 (2013) 831–843.

[27] J. C. Nunez, E. Tlelo, C. Ramirez and J. M. Chimenez, CCII+ based on QFGMOS for implementing Chua´s chaotic oscillator, IEEE Latin America Transactions 13 (2015) 2865–2870.

[28] A. D. Pano-Azucena, J. J. Rangel-Magdaleno, E. Tlelo-Cuautle and A. J. Quintas-Valles, Arduino-based chaotic secure communication system using multi-directional multiscroll chaotic oscillators. Nonlinear Dynamics 87 (2017) 2203–2217.

[29] B. Kumari and N. Gupta, Realization of chaotic circuits using lambda diode, Journal of Circuits, Systems and Computers 26 (2017) 1750189.

[30] J. C. Sprott and S. J. Linz, Algebraically simple chaotic flows, International Journal of Chaos Theory and Applications 5 (2000) 1–20.

[31] P. Bartissol and L. Chua, The double hook, IEEE Transactions on Circuits and Systems 35 (1988) 1512–1522.

[32] J. C. Sprott, S. Jafari, V. T. Pham and Z. S. Hoseini, A chaotic system with a single unstable node, Physics Letters A 379 (2015) 2030–2036.

[33] Z. Wei, J. C. Sprott and H. Chen, Elementary quadratic chaotic flows with a single non-hyperbolic equilibrium, Physics Letters A 377 (2015) 2184–2187.

[34] S. Jafari, J. C. Sprott and S. M. R. H. Golpayegani, Elementary quadratic chaotic flows with no equilibria, Physics Letters A 377 (2013) 699–702.

[35] Z. Wei, Dynamical behaviors of a chaotic system with no equilibria, Physics Letters A 376 (2011) 102–108.

[36] F. R. Tahir, S. Jafari, V. T. Pham, C. Volos and X. Wang, A novel no-equilibrium chaotic system with multiwing butterfly attractors, International Journal of Bifurcation and Chaos 25 (2015) 1550056.

[37] V. T. Pham, C. Volos, S. Jafari, Z. Wei and X. Wang, Constructing a novel no-equilibrium chaotic system, International Journal of Bifurcation and Chaos 24 (2014) 1450073.

[38] Z. Wang, A. Akgul, V. T. Pham and S Jafari, Chaos-based application of novel no-equilibrium chaotic system with coexisting attractors, Nonlinear Dynamics 89 (2017) 1877–1887.

[39] V. T. Pham, S. Vaidyanathan, C. Volos, S. Jafari and S. T. Kingni, A no-equilibrium hyperchaotic system with a cubic nonlinear term, Optik 127 (2016) 3259–3265.

[40] Z. Wang, S. Cang, E. Oketch Ochola and Y. Sun, A hyperchaotic system without equilibrium, Nonlinear Dynamics 69 (2012) 531–537.

[41] V. T. Pham, X. Wang, S. Jafari, C. Volos and T. Kapitaniak, From Wang-Chen system with only one stable equilibrium to a new chaotic system without equilibrium, International Journal of Bifurcation and Chaos 27 (2017) 1750097.

[42] M. Molaie, S. Jafari, J. C. Sprott, S. M. R. H. Golpayegani, Simple chaotic flows with one stable equilibrium, International Journal of Bifurcation and Chaos 23 (2013) 1350188.

[43] X. Wang and G. Chen, A chaotic system with only one stable equilibrium, Communications in Nonlinear Science and Numerical Simulation 17 (2012) 1264–1272.

[44] Z. Wei and Q. Yang, Dynamical analysis of the generalized Sprott C system with only two stable equilibria, Nonlinear Dynamics 68 (2012) 543–554.

[45] S. Jafari and J. C. Sprott, Simple chaotic flows with a line equilibrium, Chaos, Solitons & Fractals 57 (2013) 79–84.

[46] C. Li, J. C. Sprott and W. Thio, Bistability in a hyperchaotic system with a line equilibrium, Journal of Experimental and Theoretical Physics 118 (2014) 494–500.

[47] S. Jafari, J. C. Sprott and M. Molaie, A simple chaotic flow with a plane of equilibria, International Journal of Bifurcation and Chaos26 (2016) 1650098.

[48] J. Petrzela and T. Gotthans, New chaotic dynamical system with a conic-shaped equilibrium located on the plane structure, Applied Sciences 7 (2017) 976–988.

[49] T. Gotthans and J. Petrzela, New class of chaotic systems with circular equilibrium, Nonlinear Dynamics 81 (2015) 1143–1149.

[50] T. Gotthans, J. C. Sprott and J. Petrzela, Simple chaotic flow with circle and square equilibrium, International Journal of Bifurcation and Chaos 26 (2016) 1650137.

[51] S. T. Kingni, V. T. Pham, S. Jafari and P. Woafo, A chaotic system with an infinite number of equilibrium point located on a line and on a hyperbola and its fractional-order form, Chaos, Solitons & Fractals 99 (2017) 209–218.

[52] K. Barati, S. Jafari, J. C. Sprott and V. T. Pham, Simple chaotic flows with a curve of equilibria, International Journal of Bifurcation and Chaos 26 (2016) 1650034.

[53] V. T. Pham, C. Volos, T. Kapitaniak, S. Jafari and X. Wang, Dynamics and circuit of a chaotic system with curve of equilibrium points, International Journal of Electronics 6 (2017) 1–13.

[54] S. Jafari, J. C. Sprott, V. T. Pham, C. Volos and C. Li, Simple chaotic 3D flows with surfaces of equilibria, Nonlinear Dynamics 86 (2016) 1349–1358.

[55] V. T. Pham, C. Volos, S. Jafari and T. Kapitaniak, A novel cubic-equilibrium chaotic system with coexisting hidden attractors: analysis and circuitry implementation, Journal of Circuits, Systems and Computers 27 (2017) 1850066.

[56] X. Wang and G. Chen, Constructing a chaotic system with any number of equilibria, Nonlinear Dynamics 71 (2013) 429–436.

[57] V. T. Pham, S. Jafari, C. Volos and T. Kapitaniak, Different families of hidden attractors in a new chaotic system with variable equilibrium, International Journal of Bifurcation and Chaos 27 (2017) 1750138.

[58] V. T. Pham, C. Volos, S. Jafari, S. Vaidyanathan, T. Kapitaniak and X. Wang, A chaotic system with different families of hidden attractors, International Journal of Bifurcation and Chaos 26 (2016) 1650139.

[59] D. Dudkowski, S. Jafari, T. Kapitaniak, N. V. Kuznetsov, G. A. Leonov and A. Prasad, Hidden attractors in dynamical systems, Physics Reports 637 (2016) 1–50.

[60] G. A. Leonov, N. V. Kuznetsov and V. I. Vagaitsev, Localization of hidden Chua´s attractors, Physical Letters A 375 (2011) 2230–2233.

[61] G. A. Leonov, N. V. Kuznetsov and V. I. Vagaitsev, Hidden attractors in smooth Chua system, Physica D 241 (2012) 1482–1486.

[62] J. Petrzela and M. Guzan, Analog implementations of dynamical systems with equilibria degenerated into plane objects, Proceedings International Conference Telecommunications and Signal Processing, Wien, 2016, pp. 243–249.

[63] J. C. Sprott, Chaos and Time Series Analysis (Oxford University Press, Oxford, 2003), p. 507.

[64] S. Kodba, M. Perc and M. Marhl, Detecting chaos from a time series, European Journal of Physics 26 (2005) 205–215.

[65] A. Wolf, J. B. Swift, H. L. Swinney and J. A. Vastano, Determining Lyapunov exponents from a time series, Physica D 16 (1985) 285–317.

[66] J. Petrzela, Optimal piecewise-linear approximation of the quadratic chaotic dynamics, Radioengineering 21 (2012) 20–28.

[67] T. Gotthans, J. Petrzela and Z. Hrubos, Advanced parallel processing of Lyapunov exponents verified by practical circuit, Proceedings International Conference Radioelektronika, Brno, 2011, pp. 405–408.

[68] L. G. de la Fraga and E. Tlelo-Cuautle, Optimizing the maximum Lyapunov exponent and phase space portraits in multi-scroll chaotic oscillators, Nonlinear Dynamics 76 (2014) 1503–1515.

[69] J. Petrzela, T. Gotthans and Z. Hrubos, Behavior identification in the real electronic circuits, Proceedings International Conference Mixed Design of Integrated Circuits and Systems, Lodz, 2011, pp. 438–441.

[70] Ch. Li, J. C. Sprott, Chaotic flows with a single nonquadratic term, Physics Letters A 378 (2014) 178–183.

[71] J. C. Sprott, Symmetric time-reversible flows with a strange attractor, International Journal of Bifurcation and Chaos 25 (2015) 1550078.

[72] D. Biolek, R. Senani, V. Biolkova and Z. Kolka, Active elements for analog signal processing: classification, review, and new proposals, Radioengineering 17 (2008) 15–32.

[73] C. Sanchez-Lopez, R. Trejo-Guerra, J. M. Munoz-Pacheco and E. Tlelo-Cuautle, N-scroll chaotic attractors from saturated functions employing CCII+s, Nonlinear Dynamics 61 (2010) 331–341.

[74] A. S. Elwakil and M. P. Kennedy, Improved implementation of Chua´s chaotic oscillator using current feedback op amp, IEEE Transactions on Circuits and Systems I: Fundamental Theory and Applications 47 (2000) 76–79.

[75] J. M. Munoz-Pacheco, E. Tlelo-Cuautle, I. Toxqui-Toxqui, C. Sanchez-Lopez and R. Trejo-Guerra, Frequency limitations in generating multi-scroll chaotic attractors using CFOAs, International Journal of Electronics 101 (2014) 1559–1569.

[76] T. M. Hassan and S. A. Mahmoud, New CMOS DVCC realization and applications to instrumentation amplifier and active-RC filters, AEU - International Journal of Electronics and Communications 64 (2010) 47–55.

[77] A. Imran, D. Arora and R. Kumar, Dual DVCC based voltage-mode digitally programmable biquadratic filter, Circuits and Systems 5 (2014) 1–6.

[78] J. Petrzela, Utilization of DVCC element for modeling driven nonlinear dynamics, Proceedings International Conference Telecommunications and Signal Processing, Prague, 2015, pp. 1–5.

[79] A. Lahiri and A. Chowdhury, A novel first-order current-mode all-pass filter using CDTA, Radioengineering 18 (2009) 300–305.

[80] A. U. Keskin and D. Biolek, Current mode quadrature oscillator using current differencing transconductance amplifiers (CDTA), IEE Proceedings – Circuits, Devices and Systems 153 (2006) 214–218.

[81] D. Prasad, D. R. Bhaskar and A. K. Singh, New grounded and floating simulated inductance circuits using current differencing transconductance amplifiers, Radioengineering 19 (2010) 194–197.

[82] J. C. Sprott, Simplest dissipative chaotic flow, Physics Letters A 228 (1997) 271–274.

[83] R. Karthikeyan, A. Akgul, S. Jafari, A. Karthikeyan and I. Koyuncu, Chaotic chameleon: dynamical analysis, circuit implementation, FPGA design and fractional-order form with basic analysis, Chaos, Solitons & Fractals 103 (2017) 476–487.

# Part V

# Education

# 18. Educational Activities

Education is an inseparable part of an academic career. Having the opportunity of give knowledge to students in my everyday work is a great honor and privilege that I truly appreciate. In this Chapter, I will describe my activities in education of the university students, high school students and even retired listeners.

## 18.1  Education in Bachelor's, Master's and Docrotal's Courses

During my career, I have been involved in teaching different courses at the Faculty of Electrical Engineering and Communication, Brno University of Technology.

- Communication Systems (BKSY) - 2012

- Theory of Electronic Circuits (MTEO) - 2013

- Field Programmable Gate Arrays (MPLD) - 2014–2016

- Advanced Radio Communication Systems and Their Components (MARC) - 2014–2018

- Measurements in Radioelectronics (MREM) - 2016–2017

- ARM Microprocessors (MPOA) - 2016–2017

- Modern Wireless Digital Communication (DRE2) - 2014–2018

## 18.2  Other activities

The following subsections summarize educational activities beyond regular Bachelor or Master level courses.

### 18.2.1  Lectures at High Schools

The Department of Radio Electronics has been working hard to increase the awareness of the attractive study program Electronics and Communication among high school students. Due to the decrease of the number of applicants in recent years, the obvious target is to approach the students in person and reveal a part of the topics they can study at Brno University of Technology.

In frame of these activities, I gave lectures following high schools in the years 2014–2017 (school names in Czech) and motivating students (as well teachers) in being interested in software defined radios:

- Střední průmyslová škola Třebíč;

181

- Střední průmyslová škola Olomouc;

- Střední škola technická a ekonomická Brno;

### 18.2.2 Lectures for the University of 3rd Age

Since 2016, I have been involved in the courses offered by Brno Univerisity of Technology to pensioners. I joined prof. Václav Říčný during fall 2016 in lecturing the course Car Electronics, intended as an overview of the operation principles, parameters and recommendations for modern vehicles (electronics standards, communication protocols, radars, etc.). Out of several topics of the course, I have been lecturing:

- Hybrid Cars;

- Electric and Sport Cars;

- Future Car Technologies;

- Final Discussion.

All the lectures have been very interactive due to the nature of students – their keen attitude and many times a deep knowledge is a strong motivation for the lecturer himself.

### 18.2.3 Student Competition Golden Transistor

At Brno University of Technology, department of Radioelectronics we are organising regular student competition. The principle is simple. Students (one or team) can submit their work and compete against their colleges. The jury, representatives from companies and academic institutions, is subsequently named. Then the team should present and defend their work (same principle as an faire show) to individual members of committee as well as to regular spectators.

I am responsible for founding this event and I am regularly organising together with Dr. Jiří Miloš, Dr. Peter Barcík and with support of prof. Tomáš Kratochvíl, this beautiful competition (since 2016). On top of expert knowledge and gaining an engineering experience, I believe this event allows to students practising their presentations skills and can enrich their partnering activities. If the reader is interested, more about this competition can be found in `http://zlatra.sdelovacka.cz`.

### 18.2.4 Open Day Events

At university open day events I am usually actively joining the exhibition showing and promoting the genius of software defined radios. Severally I have prepared some sample exhibits (such as LTE Mobile Cell, GPS Hijack, Air traffic monitoring, Listening to wireless microphone, etc.). This event gives me feedback about general knowledge (and I am usually surprised with high level) about wireless technologies.